GIULIA MARCUCCI

COMPLEX EXTREME NONLINEAR WAVES: CLASSICAL AND QUANTUM THEORY FOR NEW COMPUTING MODELS

COMPLEX EXTREME NONLINEAR WAVES: CLASSICAL AND QUANTUM THEORY FOR NEW COMPUTING MODELS

GIULIA MARCUCCI

Ph. D. Thesis

SAPIENZA
UNIVERSITÀ DI ROMA

Physics Department
Faculty of Mathematical, Physical and Natural Sciences
Sapienza University of Rome

Supervisor: Prof. Claudio Conti

31st October 2019

Dedicated to the loving memories of
Francesco M. and Giorgio T.,
who left us still with the hunger
for their hugs.

DECLARATION

This thesis is a presentation of my original research work. Wherever contributions of others are involved, every effort is made to indicate this clearly, with due reference to the literature, and acknowledgement of collaborative research and discussions.

The work was done under the unvaluable guidance of Professor Claudio Conti, at Sapienza University of Rome, Physics Department, and was carefully reviewed by Dr. Andrea Aiello & Prof. Robert Boyd.

Rome, 31st October 2019

Giulia Marcucci

ABSTRACT

The historical role of nonlinear waves in developing the science of complexity, and also their physical feature of being a widespread paradigm in optics, establishes a bridge between two diverse and fundamental fields that can open an immeasurable number of new routes.

In what follows, we present our most important results on nonlinear waves in classical and quantum nonlinear optics. About classical phenomenology, we lay the groundwork for establishing one uniform theory of dispersive shock waves, and for controlling complex nonlinear regimes through simple integer topological invariants. The second quantized field theory of optical propagation in nonlinear dispersive media allows us to perform numerical simulations of quantum solitons and the quantum nonlinear box problem.

The complexity of light propagation in nonlinear media is here examined from all the main points of view: extreme phenomena, recurrence, control, modulation instability, and so forth. Such an analysis has a major, significant goal: answering the question *can nonlinear waves do computation?* For this purpose, our study towards the realization of an all-optical computer, able to do computation by implementing machine learning algorithms, is illustrated. The first all-optical realization of the Ising machine and the theoretical foundations of the random optical machine are here reported.

We believe that this treatise is a fundamental study for the application of nonlinear waves to new computational techniques, disclosing new procedures to the control of extreme waves, and to the design of new quantum sources and non-classical state generators for future quantum technologies, also giving incredible insights about all-optical reservoir computing. *Can nonlinear waves do computation?* Our random optical machine draws the route for a positive answer to this question, substituting the randomness either with the uncertainty of quantum noise effects on light propagation or with the arbitrariness of classical, extremely nonlinear regimes, as similarly done by random projection methods and extreme learning machines.

PUBLICATIONS

[1] D. Pierangeli, V. Palmieri, G. Marcucci, C. Moriconi, G. Perini, M. De Spirito, M. Papi and C. Conti, "Deep Optical Neural Network by Living Tumour Brain Cells", (2019), to be submitted, *ArXiv*: 1812.09311

[2] G. Marcucci, P. Cala, W. Man, D. Pierangeli, C. Conti and Z. Chen, "Anisotropic Optical Shock Waves in Isotropic Media with Giant Nonlocal Nonlinearity", (2019), submitted to *Phys. Rev. Lett.*, *ArXiv*: 1909.04506

[3] G. Marcucci, D. Pierangeli, P. Pinkse, M. Malik and C. Conti, "Programming Multi-level Quantum Gates in Disordered Computing Reservoirs via Machine Learning", (2019), submitted to *Phys. Rev. A*, *ArXiv*: 1905.05264

[4] G. Marcucci, S. Montangero, T. Calarco and C. Conti, "Quantum Control of Quantum Soliton Entanglement", (2018), to be submitted to *Phys. Rev. A*

[5] G. Marcucci, C. Conti and M. Materassi, "Metriplectic Structure of a Radiation-Matter Interaction Toy Model", (2018), *ArXiv*: 1804.00526

[6] G. Marcucci and C. Conti, "Simulating general relativity and noncommutative geometry by non-paraxial quantum fluids", (2019), accepted by *New J. Phys.*, *ArXiv*: 1805.03600

[7] G. Marcucci, D. Pierangeli, A. J. Agranat, R. K. Lee, E. DelRe and C. Conti, "Topological Control of Extreme Waves", *Nat. Commun.* **10**, 5090 (2019), featured by N. Meinzer in *Nat. Phys.* **15**, 1210 (2019), *ArXiv*: 1908.05212

[8] G. Marcucci, D. Pierangeli, S. Gentilini, N. Ghofraniha, Z. Chen and C. Conti, "Optical Spatial Shock Waves in Nonlocal Nonlinear Media", *Adv. Phys. X* **4**, 1662733 (2019) *ArXiv*: 1907.02823

[9] D. Pierangeli, G. Marcucci and C. Conti, "Large-scale Photonic Ising Machine by Spatial Light Modulation", *Phys. Rev. Lett.* **122**, 213902 (2019), Selected as Editor's Suggestion, featured by C. Roques-Carmes and M. Soljačić in *Physics* **12**, 61 (2019), August 2019 issue of *Focus Laser World*, *ArXiv*: 1905.11548

[10] D. Pierangeli, M. Flammini, L. Zhang, G. Marcucci, A.J. Agranat, P.G. Grinevich, P.M. Santini, C. Conti and E. DelRe, "Observation of Fermi-Pasta-Ulam-Tsingou Recurrence and Its Exact Dynamics", *Phys. Rev. X* **8**, 041017 (2018)

[11] L. Pilozzi, F. Farrelly, G. Marcucci and C. Conti, "Machine Learning Inverse Problem for Topological Photonics", *Commun. Phys* **1**, 57 (2018), *ArXiv*: 1803.02875

[12] L. Di Mauro Villari, G. Marcucci*, M.C. Braidotti and C. Conti, "Sine-Gordon soliton as a model for Hawking radiation of moving black holes and quantum soliton evaporation", *J. Phys. Commun.* **2**, 055016 (2018), (*Corresponding Author), *ArXiv*: 1703.02891

[13] G. Marcucci, M.C. Braidotti, S. Gentilini and C. Conti, "Time Asymmetric Quantum Mechanics and Shock Waves: Exploring the Irreversibility in Nonlinear Optics", *Ann. Phys.* **529**, 1600349 (2017)

[14] G. Marcucci and C. Conti, "Irreversible evolution of a wave packet in the rigged-Hilbert-space quantum mechanics", *Phys. Rev. A* **94**, 052136 (2016), *ArXiv*: 1607.08109

[15] M.C. Braidotti on behalf of S. Gentilini, G. Marcucci, E. DelRe and C. Conti, "Nonlinear Gamow vectors in nonlocal optical propagation", *Nuovo Cimento* **39 C**, 281 (2016)

[16] S. Gentilini, M.C. Braidotti, G. Marcucci, E. DelRe and C. Conti, "Physical realization of the Glauber quantum oscillator", *Sci. Rep.* **5**, 15816 (2015)

[17] S. Gentilini, M.C. Braidotti, G. Marcucci, E. DelRe and C. Conti, "Nonlinear Gamow vectors, shock waves, and irreversibility in optically nonlocal media", *Phys. Rev. A* **92**, 023801 (2015), Selected as Editor's Suggestion, *ArXiv*: 1508.00692

[18] M.C. Braidotti, G. Marcucci, S. Gentilini and C. Conti, "Irreversibility and Squeezing of Shock Waves", Book *Nonlinear Guided Wave Optics*, Chapter **3**, IOP Publishing (2017)

CONTENTS

ACRONYMS

AAH	Aubry-Andre-Harper
AI	Artificial Intelligence
ANN	Artificial Neural Network
API	Application Program Interface
BEC	Bose-Einstein Condensation
BPM	Beam Propagation Method
CCD	Charged Coupled Device
CRAB	Chopped Random-Basis
CW	Continuous Wave
DSW	Dispersive Shock Wave
FPE	Fokker-Planck Equation
FPUTR	Fermi-Pasta-Ulam-Tsingou Recurrence
FT	Fourier Transform
GV	Gamow Vector
GVD	Group Velocity Dispersion
Hb	Hemoglobin
HO	Harmonic Oscillator
KdVE	Korteweg-de Vries Equation
KLTN	Potassium-Lithium-Tantalate-Niobate $K_{0.964}Li_{0.036}Ta_{0.60}Nb_{0.40}O_3$
IST	Inverse Scattering Transform
MI	Modulation Instability
ML	Machine Learning

NE Von Neumann (or Quantum Liouville) Equation

NLO Nonlinear Optics

NLSE Nonlinear Schrödinger Equation

ODE Ordinary Differential Equation

P-SVEA Paraxial and Slowly Varying Envelope Approximation

PDE Partial Differential Equation

PDF Probability Density Function

PUF Physically Unclonable Function

QKD Quantum Key Distribution

QM Quantum Mechanics

QNLSE Quantum Nonlinear Schrödinger Equation

QPR Quantized Phase-Retrieval

RhB Rhodamine B

RHS Rigged Hilbert Space

RHO Reversed Harmonic Oscillator

RW Rogue Wave

RWA Rotating Wave Approximation

SG Soliton Gas

SLM Spatial Light Modulator

SNLSE Stochastic Nonlinear Schrödinger Equation

SPDE Stochastic Partial Differential Equation

TAQM Time Asymmetric Quantum Mechanics

TF TensorFlow™

Part I

INTRODUCTION

Thesis Outline

This thesis aims at introducing new methods for studying complex nonlinear dynamics in optical systems, for classical and quantum evolution. It also aims at using these methods for novel computational models (currently involving only linear optical propagation), as an in-depth, preliminary study to the future goal of doing computation through nonlinear waves. Although this work is theoretical and numerical, we include many experimental results, in which the new methods have been applied, and the computational devices have been realized.

After a general introduction to the topic here in Part i, the work is organized as follows.

Part ii is about classical nonlinear dynamics. We deal with new theoretical models for shock waves, rogue waves, Fermi-Pasta-Ulam-Tsingou recurrence, and soliton gas generation. Experimental results in thermal media and photorefractive crystals confirm the theory.

Part iii is about quantum nonlinear regimes described in a nonperturbative framework. We introduce the positive $\mathcal{P}$representation and apply the resulting numerical methods for studying quantum effects in solitons and rogue wave generation.

Part iv is about the use of waves for novel computational devices, which solve complex optimization problems, like Ising machines and random optical neural networks.

Conclusions are drawn in Part v. Different sections are described in detail at the beginning of each Part.

1

WAVES & COMPLEXITY

INTRODUCTION

The complexity science is based on a new way of thinking, which stands in sharp contrast to the philosophy underlying the Newtonian science, based on reductionism, determinism, and objective knowledge. Systems theory replaced reductionism by a scientific holism, namely, by the idea that systems (physical, biological, chemical, social, economic, mental, linguistic) and their properties should be viewed as wholes, not just as a collection of parts. Determinism was challenged by Quantum Mechanics (QM) and chaos theory. Cybernetics and postmodern social science showed that knowledge is intrinsically subjective, by focusing the attention on how anything processes information, reacts to information, and changes or can be changed to accomplish these tasks better.

Nowadays, complexity is perhaps the most essential characteristic of our society. As technology and global economy advance, transport and communication are every day more efficient, we interact with ever more people, organizations, systems, and objects. This network of interactions continuously grows and spreads around the globe. We take an active part in different economic, social, technological, and ecological systems that ceaselessly become more interdependent. The result is an ever more complex “system of systems", where a change in any component may affect virtually any other component unpredictably [19].

The traditional scientific method, which is based on analysis, isolation, and the gathering of complete information about a phenomenon, is incapable of dealing with such complex interdependencies. For centuries, the world view underlying science has been deterministic. Over the past century, several scientific developments have challenged the Newtonian promise of a complete, objective, and absolute knowledge of the past and future. This simplistic - although fundamental in various fields of science - the picture was gradually replaced by another, profoundly different view of reality, complex at its core. First, Heisenberg’s uncertainty principle in QM, followed by the notion of chaos in nonlinear dynamics, showed that the world is intrinsically unpredictable. Then, systems theory, cybernetics, postmodern social science, together with the theories of self-organization and biological evolution, made us aware that regularity or organization is not something taken for granted, but emerges dynamically out of a

tangle of conflicting forces and random fluctuations, that is, a process called "order out of chaos" [20]. All the previously listed different approaches are now starting to become integrated under the heading complexity science. Its central paradigm is the multi-agent system: a collection of autonomous components whose local interactions give rise to global order. Agents are intrinsically subjective and uncertain about the consequences of their actions, but they generally manage to self-organize into an emergent, adaptive system. For this reason, uncertainty and subjectivity should no longer be viewed negatively, as the loss of the absolute order of mechanicism, but positively, as factors of creativity, adaptation, and evolution.

Complexity science emerged as a new approach to the study of reality as an assembly of multi-agent systems in the 1980's [21–24]. Although its origins are largely independent of systems science and cybernetics, complexity science offers the promise to extend and integrate their ideas, and thus to develop a radical, yet workable alternative to the Newtonian paradigm. The roots of the complexity movement are diverse, including:

NONLINEAR DYNAMICS AND STATISTICAL MECHANICS, which noted that the modeling of more complex systems required new mathematical tools that can deal with randomness and chaos;

COMPUTER SCIENCE, which allowed the simulation of systems too large or too complex to be modeled mathematically;

BIOLOGICAL EVOLUTION, which explains the appearances of complex forms through the intrinsically unpredictable mechanism of blind variation and natural selection;

SOCIAL SCIENCES, such as stock markets, the internet, or insect societies, where there is no predefined order, although there are emergent structures.

In fact, the signature of complexity science is its focus on phenomena that are characterized neither by order (like those studied in Newtonian mechanics and systems science), nor by disorder (like those investigated by statistical mechanics and postmodern social science), but that are situated somewhere in between, in the zone that is commonly called the "edge of chaos" [25]. We already know how to model order, since we can predict everything once we know the initial conditions and the constraints. We already know how to model disorder as well, to some extent: while we cannot predict the behavior of individual components, statistical independence allows us to predict their average behavior accurately. In a genuinely complex system, on the other hand, components are, to a

certain degree, independent, and thus autonomous in their behavior, while undergoing various direct and indirect interactions. This makes the global behavior of the system very difficult to predict, although it is not truly random.

However, a conceptual framework, able to examine whatever complex phenomenon, belonging to whichever field of knowledge, in its entirety and to establish the methodological structure to analyze the system as a whole, is still lacking. Currently, complexity science is little more than an amalgam of methods, models, and metaphors from a variety of disciplines rather than an integrated science. Applications of complexity science use either very specialized, technical formalisms - such as network clustering algorithms, computer simulations, and nonlinear Partial Differential Equations (PDEs) - or rather vaguely defined ideas and metaphors.

A possible - and promising - first step towards the construction of complexity science foundation may be an exhaustive physical model, supported by experimental proofs, of a self-analyzing multi-agent system: finding a field that can be represented as an ensemble of nonlinear complex phenomena, that is, a complex “system of systems", whose self-organization and adaptation to the environment can be used to describe and predict the behavior of the ensemble itself, could open the way to a new scientific paradigm and allow to reach new unthought-of frontiers, where *complexity explains complexity*.

Physically, what does “complex" mean? A complex physical system is a system with a high number of degrees of freedom, which are governed by a nonlinear evolution. It is not a particle in gas, because particles belonging to gas do not have long-term interactions. We need nonlinearity to make the system’s components to be highly interacting. For all these reasons, complexity in physics finds its true expression in the inevitable need of a high amount of information for any mathematical description of the system, and its numerical simulation [26].

If we turn the gaze to Nonlinear Optics (NLO), namely, to the multiple possible undulatory phenomena that a laser beam can experience or realize in a nonlinear medium, we can ask if it is the feasible complex “system of systems" we are looking for. Optical nonlinear waves have many interesting features:

NLWS ARE COMPLEX, indeed, recent experiments showed that a non trivial regime of nonlinear waves is now completely accessible; just until a few decades ago, scientists could not go beyond the study of few solitons, while today we are able to access extremely nonlinear and multi-modal regimes, from hydrodynamics to Bose-Einstein Condensation (BEC), to classical and quantum NLO [4, 7, 8, 10];

NLWS ARE CONTROLLABLE, we show that we can control transitions from Dispersive Shock Waves (DSWs) to Rogue Waves (RWs) in classical NLO, and the propagation of quantum solitons in quantum NLO;

CAN NLWS DO COMPUTATION? At a linear regime, many efforts have been made in quantum technology - without a decisive success - but new computational models, such as the Ising machine, have been solved classically through optical free propagation [9].

Can nonlinear waves do computation? This question is still open, but the scientific community is making a great effort to answer it, and several signs of progress have already been reached [1, 27]. Whenever we will be able to answer that question positively, that is, whenever we will prove that nonlinear waves can do computation and we will build an *all-optical nonlinear computer*, we will not only have found the first self-analyzing multi-agent system, demonstrating that *complexity does explain complexity*, but we will have proven that *complexity does explain complexity at the speed of light*.

OPTICAL NONLINEAR WAVES

When we deal with waves in dispersive media, we are facing specific mathematical objects, that is, dispersive PDEs. A linear PDE is dispersive when it has a solution $\psi(x,t) = Ae^{i[kx+\omega(k)t]} + c.c.$, i.e., a monochromatic wave, for which $k \in \mathbb{R} \Rightarrow \omega(k) \in \mathbb{R}$ and $\exists k \in \mathbb{R} \ : \ \omega''(k) \neq 0$. For a linear dispersive PDE, we can define a leading wave number as $k_0 \in \mathbb{R} \ : \ \partial_k \phi|_{k_0} = 0$, a group velocity $v_g = \omega'(k_0)$, and a phase velocity $v_p = \frac{\omega(k_0)}{k_0}$. The same definitions remain valid also for nonlinear PDE, by looking at their linearized versions (neglecting the nonlinear terms), or by looking at which model equation they correspond through the multiscale method [28]. The multiscale method consists in a weakly pertubative approach, where a general class of solutions of a specific PDE is modified by introducing new spatiotemporal coordinates (or scales) in order to get rid of secular terms - oscillating solutions whose amplitude grows with time - and hold the asymptotic expansion true. The result is a chain of PDEs, each one at an increasing perturbative order. In one-dimensional problems, for example, a model equation for the continuity laws is the Hopf equation:

$$\partial_t \psi + \psi \partial_x \psi = 0. \tag{1.1}$$

If we consider modifications of continuity laws, by adding a dissipative or a dispersive term, we attain two other model equations, respectively, the Burgers equation

$$\partial_t \psi + \nu \partial_x^2 \psi + \psi \partial_x \psi = 0, \text{with} \nu \in \mathbb{R}, \tag{1.2}$$

and the Korteweg-de Vries Equation (KdVE)

$$\partial_t \psi + \partial_x^3 \psi + 6\psi \partial_x \psi = 0. \tag{1.3}$$

The model equation that rules third-order nonlinear phenomena in optics is the Nonlinear Schrödinger Equation (NLSE)

$$\imath \partial_t \psi + \frac{1}{2} \partial_x^2 \psi + |\psi|^2 \psi = 0. \tag{1.4}$$

It belongs to the same class of the KdVE, that is, it is a dispersive PDE. Its three-dimensional version is equivalent to the Gross-Pitaevskii in condensed-matter problems, or to a Klein-Gordon equation for a complex field in high-energy models. The NLSE set of solutions is ample and varied, with features covering a large spectrum of cases: NLSE solutions can be very simple, as one soliton propagating shape-invariantly, or can be extremely complex, as DSWs generating RWs, or a Soliton Gas (SG).

To go into much deeper details about what complexity means in NLO, let us recall the definition of physical complexity: a complex physical system is a system with a high number of degrees of freedom, which are governed by a nonlinear evolution, and it finds its true expression in a high amount of information for any mathematical (or numerical) description. Optically, it is the number of modes that determines the complexity of any scenario. As the number of modes grows, the complexity arises. This appears very clear when one considers the propagation of a Nth-order soliton under Eq. (1.4). In the Inverse Scattering Transform (IST) method, the scattering problem associated with Eq. (1.4) is [29]

$$\begin{aligned} \imath \partial_x \nu_1 + \psi \nu_2 &= \zeta \nu_1, \\ \imath \partial_x \nu_2 + \psi^* \nu_1 &= -\zeta \nu_2, \end{aligned} \tag{1.5}$$

where $\nu_{1,2}$ are the amplitudes of the two waves scattered by the potential $\psi(x,t)$, and ζ is the IST eingevalue, similar to the frequency for the Fourier Transform (FT). Following the IST method, in order to obtain the initial scattering data for a given initial condition $\psi(x,0)$, namely, the reflection coefficient $r(\zeta)$, its N complex poles ζ_j and their residues c_j ($j = 1 \dots N$), Eqs. (1.5) are solved. The solution $\psi(x,t)$ is reconstructed from the evolved scattering data using the IST as sketched in Fig. 1.1. The

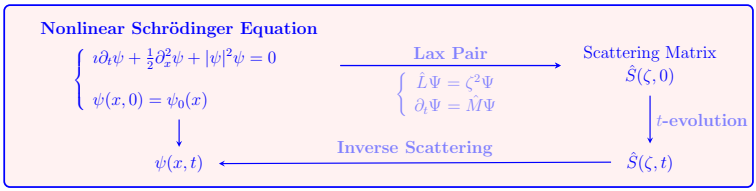

Figure 1.1: Pictorial representation of the IST method.

general solution can be written as [30]

$$\psi(x,t) = -2\sum_{j=1}^{N} \lambda_j^* \psi_{2j}^*, \tag{1.6}$$

with $\zeta_j = \frac{1}{2}\delta_j + \frac{\imath}{2}\eta_j$ ($\delta_j, \eta_j \in \mathbb{R}$), and

$$\begin{aligned} \lambda_j - \sqrt{c_j} e^{\imath\zeta_j x + \imath\zeta_j^2 t} &= 0, \\ \psi_{1j} + \textstyle\sum_{k=1}^{N} \frac{\lambda_j \lambda_k^*}{\zeta_j - \zeta_k^*} \psi_{2j}^* &= 0, \\ \psi_{2j}^* - \textstyle\sum_{k=1}^{N} \frac{\lambda_j^* \lambda_k}{\zeta_j^* - \zeta_k^*} \psi_{1k}^* &= \lambda_j^*. \end{aligned} \tag{1.7}$$

The first-order soliton corresponds to the case of a single eigenvalue, that is, $N = 1$. It propagates without changing its shape and its mathematical expression is [31]

$$\psi(x,t) = \eta \operatorname{sech}\left[\eta(x - x_s + \delta t)\right] e^{\frac{\imath}{2}(\eta^2 - \delta^2)t - \imath\delta x + \imath\phi_s)}, \tag{1.8}$$

with η the soliton amplitude, δ the frequency, x_s the position and ϕ_s the phase. Without loss of generality [for Eq. (1.4), $\eta\psi(\eta x, \eta^2 t)$ is also a solution], we treat the simpler form with $\eta = 1, x_s = \delta = \phi_s = 0$:

$$\psi(x,t) = \operatorname{sech}(x)\, e^{\frac{\imath}{2}t}. \tag{1.9}$$

The higher-order solitons can be found by imposing initial data $\psi(x,0) = N\operatorname{sech}(x)$, $N \in \mathbb{N}$, and they correspond to N pure imaginary eigenvalues $\zeta_j = \frac{\imath}{2}\eta_j$. The explicit solution at the second order is

$$\psi(x,t) = 4\frac{\cosh(3x) + 3\cosh(x)\, e^{4\imath t}}{\cosh(4x) + 4\cosh(2x) + 3\cos(4t)} e^{\frac{\imath}{2}t}, \tag{1.10}$$

it is t-periodic, with period $t_0 = \pi/2$, property true for all solitons with $N \geq 2$. Calculations become more and more complicated for increasing values of N. Whereas fundamental solitons are usually rather stable, higher-order solitons can break up into fundamental solitons under the

influence of various effects, such as higher-order dispersion, Raman scattering, or two-photon absorption [32]. In a few words, the higher the soliton order is, the more complex its propagation can be.

Solitons are not the only kind of nonlinear waves that can be solution of NLSE, namely, that can be generated by a laser beam propagating into a Kerr medium. Another important effect conveyed by NLSE is the Modulation Instability (MI). The MI is a phenomenon whereby deviations from a Continuous Wave (CW) are strengthen by nonlinearity, leading to a linear single-mode amplification and multi-solitons generation [31, 33]. When we consider a strongly nonlinear regime, light can experience a damping after the amplification, which means that the MI has reached a nonlinear stage [34]. The nonlinear MI induces RWs emergence, like Akhmediev breathers or Peregrine solitons, and if the damping is followed again by linear amplification, the RWs occurrence becomes recurrent [10, 35–37].

Equation (1.4) is called *focusing* NLSE, because it is derived by the focusing Kerr effect, but studying its *defocusing* version is worthwhile as well. It reads

$$\imath\partial_t\psi + \frac{1}{2}\partial_x^2\psi - |\psi|^2\psi = 0, \tag{1.11}$$

and the main important types of nonlinear waves generated by Eq. (1.11) are dark solitons [31] and DSWs [13, 38]. DSWs, RWs, SGs and other NLSE solutions are very complex, nonlinear phenomena, and their description has already required a great effort, albeit there is still much to be done. The non-trivial nature of these undulatory events, their complicated modal distribution and their heterogeneous intensity landscape, composed by high peaks, flat plateau, fast oscillations, phase discontinuities, and so on and so forth, lead us to define these nonlinear waves as *extreme*.

A NOVEL PERSPECTIVE

We have just argued that extreme nonlinear waves are complex phenomena. Can they be a new tool to analyze/interpret other fields of complexity science? In a nutshell, again the same question: *can nonlinear waves do computation?* This thesis does not answer this question definitively but makes a special effort to draw the route to follow in order to attain a positive response.

At first, almost every main class of optical nonlinear waves is analyzed, and, in particular, the ones generated by propagation in Kerr or Kerr-like media. DSWs are presented in Chapter 2, with specific reference to their demonstrated intrinsically irreversible evolution in thermal media. In

Chapter 3, we experimentally demonstrate a recent theory on nonlinear MI and RW recurrent emergence made by *P. G. Grinevich and P. M. Santini* [35, 36]. Chapter 4 is about the control, by topological tools, of light propagation in the multimodal regime, that is, the box problem - an initial waveform with an infinite number of modes- in a photorefractive crystal.

Major complexity arises when one considers the quantum version of the previously treated NLSE solutions. Quantization of NLSE is conveyed in Chapter 5. In the process that leads to an exact - neither approximated, nor given by perturbation theory - description of nonlinear waves at a quantum regime, that is, at low photon number, the uncertainties due to the Heisenberg principle are mapped into a stochastic white noise through phase-space methods. The result is an equivalence between the Quantum Nonlinear Schrödinger Equation (QNLSE) and a system of two coupled Stochastic Nonlinear Schrödinger Equations (SNLSEs). The numerical simulations of the solution of such a stochastic PDEs system let us study the quantum realization of the aforementioned optical nonlinear waves. Chapter 6 reports the study of quantum solitons and their quantum control along propagation. The quantum nonlinear box problem is treated in Chapter 7.

Once we analyzed both classical and quantum nonlinear waves, we can move to computation. Our attempt to draw the mentioned route is to develop linear all-optical devices, able to solve paradigmatic computational problems and to mimic Machine Learning (ML) algorithms. After a brief introduction to computational complexity and the related classification of decision problems, followed by an overview of the Ising Hamiltonian models and the quantum annealing, in Chapter 8, the first all-optical realization of an Ising machine is illustrated in its details in Chapter 9. In Chapter 10, the class of ML algorithms are reviewed, and a specific application of a supervised ML regression technique - implemented by the use of TensorFlow™ (TF) routines - to the inverse problem for a topological laser design is reported. Last but not least, in Chapter 11, we establish the theoretical foundation of the random optical machine. We prove that light transmission in a random medium generates an Artificial Neural Network (ANN) - as deep as the amount of system perturbations - that performs reservoir computing. This represents one of the first conceptual fulfilments of an all-optical computer, of which experimental realization is designed in what follows, treating the application of the random optical machine to the implementation of quantum gates.

Finally, Chapter 12 concludes the thesis, unveiling the way to a possible *all-optical nonlinear computer*.

Part II

COMPLEXITY IN CLASSICAL NONLINEAR WAVES

Outline of Part ii

This Part deals with complex classical nonlinear optical waves.

- Chapter 2 is a general introduction to theory and experiments on optical shock waves, with emphasis on nonlocal media.
- Chapter 3 describes the onset of complex regimes by nonlinear modulation instability. Fermi-Pasta-Ulam-Tsingou recurrence is described as the leading mechanism towards non-trivial nonlinear dynamics, starting from a simple periodical wave. Theory and experiments in photorefractive media are reported.
- Chapter 4 describes the fully developed complex nonlinear regime starting from a box-shaped wave. The roles of shock waves, rogue waves, and soliton gases are outlined in a phase-diagram, which enables the interpretation of new experiments about the control of this highly nonlinear regime.

Synopsis

Chapter 1 presents the role of nonlinear waves in developing the science of complexity, and also illustrates what nonlinear waves are, their paradigmatic model in optics, i.e., the nonlinear Schrödinger equation, and why we are interested in them, from both fundamental and applied perspectives.

In what follows, we present our most important results on classical nonlinear waves in nonlinear optics: the model of dispersive shock wave intrinsic irreversibility by time asymmetric quantum mechanics, in the context of the nonlocal Kerr nonlinearity, the optical realization of Fermi-Pasta-Ulam-Tsingou recurrence, and the topological control of extreme waves, included the supervised transition from dispersive shock waves to rogue waves, ending in a soliton gas.

We believe that this treatise is not only a fundamental study for application of nonlinear waves to new computational techniques, but can also be a further step towards a complete description of dispersive nonlinear phenomena, where inverse scattering transform, Whitham modulation, hydrodynamic approximation and time asymmetric quantum mechanics cooperate in establishing one uniform theory of dispersive shock waves, and towards the control of complex nonlinear regimes through simple integer topological invariants.

2 DISPERSIVE SHOCK WAVES

INTRODUCTION

The intent of Part ii is to show our study on nonlinear waves in classical coherent light propagation by the alternation of general introductions to topics of broad interest in NLO, and of analysis in details of our original results in the related area. We start illustrating DSWs in defocusing nonlocal nonlinearity, which allows a simpler description than its local counterpart.

DSWs are rapidly oscillating solutions of hyperbolic partial differential equations that contrast the generation of multivalued regions through the formation of undular bores [13, 39–49]. This class of phenomena was investigated in several physical fields, initially in shallow water waves [50] and ion-acoustic waves [51], then in oceanography [52], pulses propagation in photonic fibers [53, 54], BEC [55–60], quantum liquids [61], photorefractive media [62], plasma physics [63], viscous fluids [64], and diffracting optical beams [16, 17, 43, 65–78].

In 1967 Gardner, Greene, Kruskal and Miura developed a method to solve the KdVE equation, called IST [79]. Among all the equations solvable by IST, which allowed to find the mathematical formulation of exact solutions of such nonlinear models, KdVE and the NLSE belong to the case with dispersive regularization of the aforementioned multivalued singularity. NLSE is a universal model that describes many phenomena, in particular a third-order nonlinear phenomenon in optics: the Kerr effect [80], a refractive index perturbation linearly scaling with the light intensity. Kerr effect can be generalized to the nonlocal case when the nonlinear response in a specific point depends on entire beam transverse profile. This occurs, e.g., in thermal media [42, 49, 66, 71, 81–95]. In these materials, light propagation is affected by a highly nonlocal Kerr nonlinearity, ruled by nonlocal NLSE.

Unfortunately, IST is still of little use for the nonlocal NLSE and other theoretical approaches must be conceived, despite some recent progress in 2D media [96, 97]. For many years, Whitham modulation and hydrodynamic approximation have predominated in solving the nonlocal NLSE [40, 66]. However, hydrodynamic approximation cannot describe light propagating beyond the shock point, and two new techniques have been developed, one coming from nuclear physics, the Time Asymmetric

Quantum Mechanics (TAQM) [2, 13, 14, 98–107], which models the nonlinear wave intrinsically irreversible propagation as a superposition of decaying resonances, and the wave turbulence theory [70, 74, 76, 108–111], which uses a statistical interpretation of NLO.

This Chapter aims to summarize all the current theoretical models to describe wave breaking of nonlocal NLSE solutions in diffracting optical beam propagation, and to highlight some of the most recent experimental observations of DSWs in spatial nonlinear photonics.

After an introductory section about the derivation of nonlocal NLSE in Sec. 2.2, we report the main theoretical approaches and results related to DSWs. Section 2.2.1 explains in details the difference between the wave breaking due to local Kerr effect, which causes shock both in phase and in intensity, and the one in nonlocal Kerr media, where the beam intensity follows the phase singularity adiabatically [66]. The most recent theoretical models of nonlinear wave propagation in highly nonlocal nonlinear media are treated in Secs. 2.2.2, 2.2.3. Section 2.2.2 treats DSWs generated by laser beams and gives an analytical description of their intrinsic irreversibility, due to the complexity of the dynamics rather than losses [13]. Section 2.2.3 applies this model to a novel kind of DSWs, which simultaneously presents two diverse singularities: the annular collapse singularity and the zero-singularity. Nonlocality has strong impact also in random dispersive waves nonlinear interaction, where it produces giant collective incoherent shock waves [74, 76, 110]. However, this thesis is limited to the analysis of initially coherent beams propagation, but one can refer to [8, 110] for further details.

The second part of the Chapter is a collection of experiments on DSW generation in thermal media. Sec. 2.3 reports observations in Rhodamine solutions [66]. Output beam intensity profiles in Sec. 2.3.1 are modeled by TAQM both in two dimensional experiments, where decaying states describe the longitudinal propagation [16, 17], and in the one dimensional approximation, having the proof that TAQM is an excellent approach also to analyze transverse intensity profiles beyond the shock point [75]. The interplay of nonlinearity and disorder is illustrated in Sec. 2.3.2. There, observations in Rhodamine with silica spheres [69] and in silica aerogel [72] exhibit the competition between randomness and nonlocal Kerr effect. DSW generation processes in chemical [73] and biological solutions [78] are illustrated in Sec. 2.3.3, while observations of anisotropic DSWs in M-Cresol/Nylon are in Sec. 2.3.4.

THE NONLOCAL NONLINEAR SCHRÖDINGER EQUATION

From Maxwell's equations, considering a region with zero charge, current and magnetization, we obtain the following electric field wave equation

$$-\nabla^2 \boldsymbol{E} + \frac{1}{c^2}\partial_t^2 \boldsymbol{E} = -\frac{1}{\epsilon_0 c^2}\partial_t^2 \boldsymbol{P}, \tag{2.1}$$

with $\boldsymbol{E}$ the electric field and $\boldsymbol{P}$ the medium polarization [38].

The relation between $\boldsymbol{P}$ and $\boldsymbol{E}$ depends on the material properties. Including all the nonlinear terms, we have

$$\boldsymbol{P} = \epsilon_0 \sum_{n\geq 1} \boldsymbol{\chi}^{(n)} \cdot \boldsymbol{E}^{\otimes n} = \boldsymbol{P}^{(L)} + \boldsymbol{P}^{(NL)}, \tag{2.2}$$

where $\boldsymbol{E}^{\otimes n}$ is the vector Kronecker product, which maps a vector into an n-order tensor: $\left[\boldsymbol{E}^{\otimes n}\right]_{i_1 \ldots 1_n} = E_{i_1} \ldots E_{i_n}$. In other terms, $P_j^{(L)} = \epsilon_0 \sum_k \chi_{jk}^{(1)} E_k$ is the linear polarization j-th component, and the same for the nonlinear polarization is $P_j^{(NL)} = \epsilon_0 \left[\sum_{k,l} \chi_{jkl}^{(2)} E_k E_l + \sum_{k,l,m} \chi_{jklm}^{(3)} E_k E_l E_m + \ldots\right]$, with $1 + \chi^{(1)} = n_0^2$ when $\boldsymbol{\chi}^{(1)} = \chi^{(1)} \mathbb{1}$ (in case of isotropic medium - our assumption hereafter - $\mathbb{1}$ is the identity matrix), n_0 the medium refractive index, $\boldsymbol{\chi}^{(2)}$ and $\boldsymbol{\chi}^{(3)}$ tensors denoted as second and third order susceptibility, respectively.

One must take into account the temporal delay between the instant when the electric field reaches the medium and the medium response. For this reason, this radiation-matter interaction is more properly represented by the following non instantaneous superposition of linear and nonlinear polarization [38]:

$$\boldsymbol{P}(t) = \epsilon_0 \Big(\left[\tilde{\boldsymbol{\chi}}^{(1)} * \boldsymbol{E}\right](t) + \left[\tilde{\boldsymbol{\chi}}^{(2)} * \boldsymbol{E}^{\otimes 2}\right](t) + \left[\tilde{\boldsymbol{\chi}}^{(3)} * \boldsymbol{E}^{\otimes 3}\right](t) + \ldots \Big), \tag{2.3}$$

where $*$ is the convolution product

$$\begin{aligned} &\left[\tilde{\boldsymbol{\chi}}^{(n)} * \boldsymbol{E}^{\otimes n}\right]_j (t) = \int_{-\infty}^{t} \mathrm{d}t_1 \cdots \int_{-\infty}^{t} \mathrm{d}t_n \\ &\sum_{i_1,\ldots,i_n} \tilde{\chi}_{ji_1\ldots i_n}^{(n)} (t - t_1, \ldots, t - t_n) E_{i_1}(\boldsymbol{R}, t_1) \ldots E_{i_n}(\boldsymbol{R}, t_n), \end{aligned} \tag{2.4}$$

and

$$\tilde{\boldsymbol{\chi}}^{(n)}(t_1, \ldots, t_n) = \frac{1}{(2\pi)^n} \int_{-\infty}^{+\infty} \mathrm{d}\omega_1 \cdots \int_{-\infty}^{+\infty} \mathrm{d}\omega_n \boldsymbol{\chi}^{(n)}(\omega_1, \ldots, \omega_n) e^{\imath \sum_{i=1}^{n} \omega_i t_i} \tag{2.5}$$

is the n-order susceptibility FT. If we have a third-order isotropic and centrosymmetric material, the nonlinear polarization is

$$\begin{aligned} \boldsymbol{P}^{(NL)}(\boldsymbol{R},t) &= \epsilon_0 \int_{-\infty}^{t} \mathrm{d}t_1 \int_{-\infty}^{t} \mathrm{d}t_2 \int_{-\infty}^{t} \mathrm{d}t_3 \\ &\quad \tilde{\boldsymbol{\chi}}^{(3)}(t-t_1, t-t_2, t-t_3)\boldsymbol{E}^{\otimes 3}(\boldsymbol{R}, t_1, t_2, t_3) \end{aligned} \tag{2.6}$$

and the related dielectric tensor changes as

$$\epsilon_{new} = \epsilon + \epsilon_2 \langle \boldsymbol{E} \cdot \boldsymbol{E} \rangle, \tag{2.7}$$

where $\langle \boldsymbol{E} \cdot \boldsymbol{E} \rangle = \frac{1}{2}|\boldsymbol{E}|^2$ is the square of the electric field time average. The final refractive index causes the Kerr effect [38], a phenomenon that consists in a perturbation of the medium refractive index, proportional to the field intensity:

$$n = \sqrt{\frac{\epsilon_{new}}{\epsilon_0}} = \sqrt{\frac{\epsilon + \epsilon_2 \langle \boldsymbol{E} \cdot \boldsymbol{E} \rangle}{\epsilon_0}} \approx n_0 + n_2 I, \tag{2.8}$$

with $I = |\boldsymbol{E}|^2$ the field intensity and n_2 the Kerr coefficient.

The nonlocal Kerr effect is a third-order phenomenon, but the radiation-matter interaction depends on the whole intensity profile, as occurs in thermal media. In these materials, when an optical beam propagates, it locally heats the medium, and the resulting temperature gradient generates a variation of the density distribution and a refractive index perturbation [66, 88, 94]:

$$\Delta n = \left(\frac{\partial n}{\partial T} \right)_0 \Delta T, \tag{2.9}$$

with $\left(\frac{\partial n}{\partial T}\right)_0$ the thermo-optic coefficient of the sample at the steady-state. It turns out that the nonlinear response induced at a specific spatial point is carried away to the surrounding region, and the size of this extended region determines the range of nonlocality. The heat conduction in optical thermal materials was termed "response with an infinite range of nonlocality" [86] until 2007, when A. Minovich *et al.* [88] demonstrated experimentally and proved theoretically that the nonlocal response of thermal optical media can be accurately described by a localized well function dependent only on the sample geometry, and not on the nature of the material. This property allows us to express the temperature variation, in a stationary limit, as governed by the following 3D heat equation [66, 81, 86–88, 94, 112, 113] with constant boundary conditions (at room temperature):

$$\left(\partial_X^2 + \partial_Y^2 + \partial_Z^2 \right) \Delta T(\boldsymbol{R}) = -\gamma |\boldsymbol{E}(\boldsymbol{R})|^2, \tag{2.10}$$

where $\gamma = (L_{loss}\rho_0 c_P D_T)^{-1}$, L_{loss} is the loss characteristic length, ρ_0 is the material density, c_P is the specific heat at constant pressure, D_T is the thermal diffusivity and $\boldsymbol{R} = (X, Y, Z) = (\boldsymbol{R}_\perp, Z)$. The solution can be written as

$$\Delta T(\boldsymbol{R}) = \int\int\int \mathrm{d}Z' \mathrm{d}\boldsymbol{R}_\perp' G(\boldsymbol{R}_\perp - \boldsymbol{R}_\perp', Z - Z')|\boldsymbol{E}(\boldsymbol{R}_\perp', Z')|^2, \quad (2.11)$$

with $G(\boldsymbol{R}_\perp)$ a Green function that depends only on the sample geometry and the boundary conditions, and expresses the nonlocality of the nonlinear effect. In principle, one can remove the Z-dependence by integrating along the longitudinal medium length Z_0 [88], but we are interested in the Green function itself, and the longitudinal behavior of G becomes as complicated as Z_0 becomes comparable to L_{loss}, getting smaller and strongly asymmetric near the boundaries [94]. Physically, the reason why this happens is due to the choice of heat equation to describe the nonlinear radiation-matter interaction: it works only in a neighborhood of the sample midpoint $\hat{Z} = Z_0/2$, not in proximity of the borders. Mathematically, this is deciphered in a longitudinal parabolic approximation with characteristic width $L_{nloc} = \sqrt{\frac{|n_2|}{\gamma\left|\frac{\partial n}{\partial T}\right|_0}} \propto \sqrt{L_{loss}}$:

$$\Delta T(\boldsymbol{R}) = \left[1 - \frac{(Z - \hat{Z})^2}{2L_{nloc}}\right] \Delta T_\perp(\boldsymbol{R}_\perp). \quad (2.12)$$

From Eqs. (2.10,2.12) we obtain the 2D heat equation

$$\left(\partial_X^2 + \partial_Y^2\right) \Delta T_\perp(\boldsymbol{R}_\perp) - L_{nloc}^{-2} \Delta T_\perp(\boldsymbol{R}_\perp) = -\gamma I_\perp(\boldsymbol{R}_\perp), \quad (2.13)$$

with $I_\perp(\boldsymbol{R}_\perp) = \frac{1}{Z_0}\int \mathrm{d}Z|\boldsymbol{E}(\boldsymbol{R}_\perp, Z)|^2$. Eq. (2.11) now reads

$$\Delta T_\perp(\boldsymbol{R}_\perp) = \int\int \mathrm{d}\boldsymbol{R}_\perp' G_\perp(\boldsymbol{R}_\perp - \boldsymbol{R}_\perp') I_\perp(\boldsymbol{R}_\perp'). \quad (2.14)$$

In low absorption regime ($Z_0 << L_{loss}$) $\Delta T(\boldsymbol{R}) \sim \Delta T_\perp(\boldsymbol{R}_\perp)$ and $\partial_Z I(\boldsymbol{R}) \sim 0$ (intensity longitudinal changes are negligible as for solitary wave packets), therefore we attain $n[I](\boldsymbol{R}) = n_0 + \Delta n[I](\boldsymbol{R}_\perp)$, with the refractive index nonlocal perturbation

$$\Delta n[I](\boldsymbol{R}_\perp) = n_2 \int\int \mathrm{d}\boldsymbol{R}_\perp' K(\boldsymbol{R}_\perp - \boldsymbol{R}_\perp') I(\boldsymbol{R}_\perp'), \quad (2.15)$$

and $n_2 K(\boldsymbol{R}_\perp) = \left(\frac{\partial n}{\partial T}\right)_0 G_\perp(\boldsymbol{R}_\perp)$.

By a comparison between the nonlocality length L_{nloc} and the beam waist diameter W_0, we can analyze two different limits: the standard Kerr effect in Eq. (2.8) when $L_{nloc} \ll W_0$ (local approximation), i.e.,

$K(\boldsymbol{R}_\perp - \boldsymbol{R}_\perp{}') \sim \delta(\boldsymbol{R}_\perp - \boldsymbol{R}_\perp{}')$, and the opposite case $L_{nloc} \gg W_0$, that is, the highly nonlocal approximation, where $K * I(\boldsymbol{R}) \sim K(\boldsymbol{R}_\perp)P(Z)$, with $P(Z) = \int \mathrm{d}\boldsymbol{R}_\perp I(\boldsymbol{R})$ the power.

For a monocromatic field $\boldsymbol{E}(\boldsymbol{R},\tau) = \hat{\boldsymbol{E}}_0 \Re\left[A(\boldsymbol{R})e^{-\imath\omega\tau}\right]$ in a third-order thermal medium, in paraxial and slowly varying envelope approximations, introducing the delayed time $\tau = t - \frac{n_0}{c}Z$ and adding a linear loss of characteristic length L_{loss}, from Eq. (2.1) we find that the propagation along Z is ruled by the nonlocal NLSE [66]:

$$2\imath k\partial_Z A + \left(\partial_X^2 + \partial_Y^2\right)A + 2k^2\frac{\Delta n[|A|^2]}{n_0}A = -\imath\frac{k}{L_{loss}}A, \tag{2.16}$$

with $k = \frac{2\pi n_0}{\lambda} = \frac{\omega n_0}{c}$ the wavenumber.

Spatial Dispersive Shock Waves in Nonlocal Kerr Nonlinearity

Spatial DSWs are rapidly oscillating waves which regularize an abrupt discontinuity in phase through diffraction, that is, through the formation of intensity undular bores on the beam borders. Scientific community paid close attention to the theoretical description [39, 40, 59] and experimental demonstration [51, 53, 55–58, 63, 64, 66, 67, 70] of optical DSWs. Here we summarize results on the defocusing DSWs in nonlocal media [66]. In such materials, the IST cannot describe the solutions, and we need other methods.

In next sections, we detail a specific methodology for DSWs in nonlocal media: the TAQM [13, 14, 98–107]. Such a theory also proves that DSWs are intrinsically irreversible.

Starting from Eq. (2.16), through the scaling $x = \frac{X}{W_0}$, $y = \frac{Y}{W_0}$, $z = \frac{Z}{L}$, $\psi(x,y,z) = \frac{A(X,Y,Z)}{\sqrt{I_0}}$, with I_0 the intensity peak, $L = \sqrt{L_{nl}L_d}$, $L_{nl} = \frac{n_0}{k|n_2|I_0}$ the nonlinear length scale associated to a local Kerr effect, $L_d = kW_0^2$ the diffraction length, one obtains the normalized nonlocal NLSE

$$\imath\epsilon\partial_z\psi + \frac{\epsilon^2}{2}\left(\partial_x^2 + \partial_y^2\right)\psi + \chi\theta\psi = -\imath\frac{\alpha}{2}\epsilon\psi, \tag{2.17}$$

with $\epsilon = \frac{L_{nl}}{L} = \sqrt{\frac{L_{nl}}{L_d}}$ a small quantity in strongly nonlinear (or weakly diffracting) regime, as the one we are considering, $\chi = \frac{n_2}{|n_2|}$, $\theta = \left|\frac{k\Delta n L_{nl}}{n_0}\right|$, $\alpha = \frac{L}{L_{loss}}$. From Eq. (2.13)

$$-\sigma^2\left(\partial_x^2 + \partial_y^2\right)\theta + \theta = |\psi|^2, \tag{2.18}$$

where $\sigma = \frac{L_{nloc}}{W_0}$ is the nonlocality degree, which expresses the nature of the Kerr effect through the limits we have previously discussed: if

$\sigma \ll 1$ we are considering the local limit $\theta \sim |\psi|^2$, instead, if $\sigma \gg 1$, by highly nonlocal approximation $\theta \sim \kappa(x,y)p(z)$, with $p(z) = \int \mathrm{d}x\mathrm{d}y\,|\psi(x,y,z)|^2 = \frac{P(Z)}{W_0^2 I_0}$.

The fundamental laser mode (Gaussian TEM_{00}) is described by an axisymmetric Gaussian input $\psi_0(r) = \exp(-r^2)$, with $r = \sqrt{x^2+y^2}$, which evolves in the WKB approximation [114] as $\psi(r,z) = \sqrt{\rho(r,z)}\exp\left[\imath\frac{\phi(r,z)}{\epsilon}\right]$. For $D = 2$ the transverse dimensionality and $u = \partial_r\phi$ the phase chirp, from Eqs. (2.17, 2.18) one obtains

$$\begin{aligned} \partial_z\rho + \left[\tfrac{D-1}{r}\rho u + \partial_r(\rho u)\right] &= -\alpha\rho, \\ \partial_z u + u\partial_r u - \chi\partial_r\theta &= 0, \\ -\sigma^2\left[\partial_r^2\theta + \tfrac{D-1}{r}\partial_r\theta)\right] + \theta &= \rho. \end{aligned} \tag{2.19}$$

Figure 2.1 reports phase chirp and field amplitude for $D = 1$, so for $\partial_y \sim 0$ and $r \to x$, in a defocusing medium ($\chi = -1$) without losses ($\alpha = 0$). The local case ($\sigma = 0$) is illustrated in Figs. 2.1a,c and follows from system (2.19):

$$\partial_z\rho + \partial_x(\rho u) = 0, \quad \partial_z u + u\partial_x u = -\partial_x\rho. \tag{2.20}$$

Eqs. (2.20) are equivalent to Euler and continuity equations, respectively, for a fluid of speed u, mass density ρ and pressure proportional to ρ^2. In the reported dynamics, the diffraction, initially of order ϵ^2, starts to play a relevant role in proximity of the wave breaking. In fact, it regularizes such a discontinuity by rapid oscillations of wavelength $\sim \epsilon$, which appear simultaneously in phase chirp u and intensity ρ. For large values of σ, the normalized refractive index variation, here expressed by $\theta(x)$, is wider than the Gaussian input. As shown in Figs. 2.1b,d the shock oscillations are essentially driven by the phase chirp u, while the intensity ρ adiabatically follows. Major details are given in [66].

An in-depth description of the difference between DSWs in local and nonlocal Kerr media is also provided by turbulence theory, in particular by the Vlasov formalism [8, 110]. Indeed, the analysis made for random optical waves is also relevant to the coherent problem considered here, since the reduced hydrodynamic equations derived from the Vlasov model [[74], Eqs. (3,4)] coincide with Eq. (2.19). Following this approach, DSWs in thermal nonlinearity were interpreted for the first time as an annular collapse singularity in [74]. By looking at the M-shaped field amplitude in Fig. 2.1d (and, in the following, at the intensity profiles in Fig. 2.4a, Fig. 2.8, Figs. 2.9D,E, and Figs. 2.11a,b), and comparing this to the fast oscillations in Fig. 2.1c [or Fig. 2 in [67]], the feature of the collapse singularity in nonlocality appears evident. Indeed, the

corresponding hydrodynamic model in the limit of a local nonlinearity [Eq. (2.20)] recalls the shallow water equations, which exhibit a pure shock without collapse.

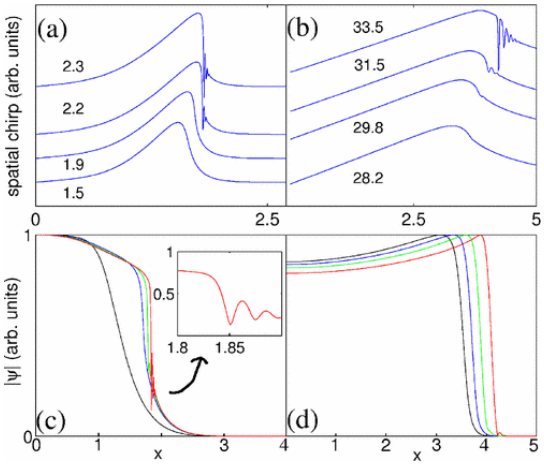

Figure 2.1: Phase chirp $u(x)$ (a,b), and amplitude $\sqrt{\rho(x,z)}$ (c,d) for transverse dimensionality $D = 1$ and different values of z, as indicated. (a,c) are obtained by Eqs. (2.20) with $\epsilon = 10^{-3}$. (b,d) are simulations of the result of the system (2.19) with $D = 1$, $\alpha = 0$, $\chi = -1$, $\sigma^2 = 5$. Reprinted from [66].

High Nonlocality and Time Asymmetric Quantum Mechanics

Let us consider the nonlocal NLSE in Eq. (2.16) with a medium response function $K(X,Y) = \exp\left[-(|X| + |Y|)/L_{nloc}\right]/(2L_{nloc})^2$. Being K separable, i.e., $K(X,Y) = \tilde{K}(X)\tilde{K}(Y)$, through the approximation $\partial_Y \sim 0$ (as in the previous section) we can consider only one transverse dimension, since analyzing propagation along Y is no more interesting for our purposes. We rewrite Eq. (2.16) in terms of $1+1$ dimensionless variables by using the same scaling of Eq. (2.17) and choosing I_0 such that $L_{nl} = L_d$:

$$\imath\partial_z\psi + \frac{1}{2}\partial_x^2\psi - \kappa * |\psi|^2\psi = -\imath\frac{\alpha}{2}\psi. \tag{2.21}$$

with $\kappa(x) = W_0\tilde{K}(xW_0) = \exp\left(-|x|/\sigma\right)/(2\sigma)$.

We take into account a medium where the nonlocality length is much larger than the beam waist diameter. By highly nonlocal approximation we have [90, 115]

$$\kappa * |\psi|^2 \sim \kappa(x)p(z), \tag{2.22}$$

where κ is a function no more depending on $|\psi|^2$. In a system without loss, that is, $\alpha = 0$, the normalized power p is conserved and the NLSE is mapped into a linear Schrödinger equation $\imath\partial_z\psi = \hat{H}\psi$, with the Hamiltonian $\hat{H} = \frac{1}{2}\hat{p}^2 + p\kappa(x)$ ($\hat{p} = -\imath\partial_x$). When we express the even function κ as its second order expansion, that is, $\kappa(x) = \kappa_0^2 - \frac{\kappa_2^2}{2}x^2$, where $\kappa_0^2 = \frac{1}{2\sigma}$ and $\kappa_2^2 = \frac{1}{\sqrt{\pi}\sigma^2}$, we obtain the Reversed Harmonic Oscillator (RHO) Hamiltonian [14, 103, 105]:

$$\hat{H} = p\kappa_0^2 + \hat{H}_{RHO}, \quad \hat{H}_{RHO} = \frac{\hat{p}^2}{2} - \frac{\gamma^2\hat{x}^2}{2}, \quad \gamma^2 = p\kappa_2^2. \tag{2.23}$$

If $\psi = \exp\left(-\imath\kappa_0^2 pz\right)\phi$, then $\imath\partial_z\phi = \hat{H}_{RHO}\phi$.

Figure 2.2 sketches the relation between the harmonic and the reversed oscillators. For a Harmonic Oscillator (HO), the spectrum is discrete and the corresponding eingenstates form a orthonormal basis (both a orthogonality and a completeness relations hold):

$$\begin{aligned} \hat{H}_{HO} &= \tfrac{\hat{p}^2}{2} + \tfrac{\omega^2}{2}\hat{x}^2 \\ \hat{H}_{HO}\psi(x) &= E\psi(x), \quad E_n = \omega\left(n + \tfrac{1}{2}\right), \\ \psi_n(x) &= \sqrt[4]{\tfrac{\omega}{\pi}}\tfrac{1}{\sqrt{2^n n!}}H_n\left(\sqrt{\omega}x\right), \end{aligned} \tag{2.24}$$

with $H_n(x) = (-1)^n x^2 \frac{d^n}{dx^n}e^{-x^2}$ the Hermite polynomials. On the other hand, RHOs has complete continuous spectrum, but one derives a generalized discrete spectrum from HO spectrum by a complex analytic prolongation in the Rigged Hilbert Space (RHS) [14, 102, 116] through the transformation $\omega \to \imath\gamma$, $\hat{x} \to e^{-\imath\frac{\pi}{4}}\hat{x}$, $\hat{p} \to e^{\imath\frac{\pi}{4}}\hat{p}$ [14, 105]. The new stationary Schrödinger equation is $\hat{H}_{RHO}\mathfrak{f}^{\pm}(x) = \imath\frac{\Gamma}{2}\mathfrak{f}^{\pm}(x)$, solved by the spectrum $\frac{\Gamma_n}{2} = \gamma\left(n + \frac{1}{2}\right)$ and the non normalizable eigenfunctions

$$\mathfrak{f}_n^{\pm}(x) = \frac{\sqrt[4]{\pm i\gamma}}{\sqrt{2^n n!\sqrt{\pi}}}H_n(\sqrt{\pm i\gamma}x)\exp(\mp i\frac{\gamma}{2}x^2), \tag{2.25}$$

namely, the RHOs Gamow Vectors (GVs) [117, 118].

We can express every wavefunction as a truncated superposition of GVs added to a background function, which dispersively oscillates at infinite as a polynomials [14]:

$$\phi(x) = \phi_N^G(x) + \phi_N^{BG}(x) \tag{2.26}$$

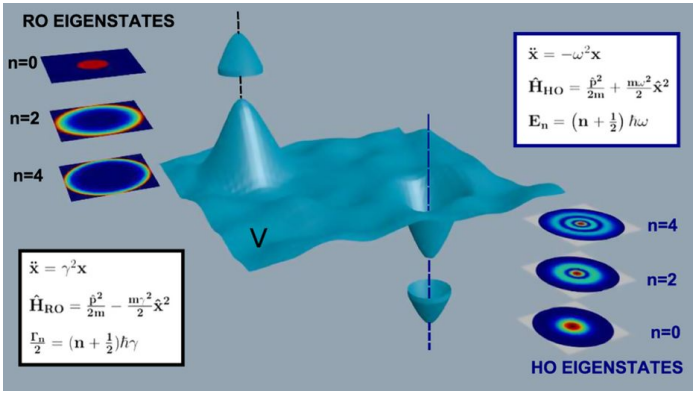

Figure 2.2: Pictorial representation of an energy landscape. When the system is in proximity of a local maximum it obeys the RHOs Hamiltonian, in figure $\hat{H}_{RO}$. In proximity of the minimum the system obeys the Hamiltonian of a HO, in figure $\hat{H}_{HO}$. The two Hamiltonians are explicitly written in the two the corresponding text boxes, with the related dynamical systems and the discrete eingenvalues. Insets show the transverse profiles of the respective eigenfunctions, bounded on right hand side for the HO, unbounded on the left hand side for the RHOs.

with

$$\phi_N^G(x) = \sum_{n=0}^{N} \mathfrak{f}_n^-(x)\langle \mathfrak{f}_n^+ | \phi(x,0)\rangle. \tag{2.27}$$

Figure 2.3 shows the GV square norms (Fig. 2.3a) and phase chirps (Fig. 2.3b). The evolution of the normalized field ψ presents a Gamow part resulting as a superposition of exponential decays with quantized decay rates [14]:

$$\psi_n^G(x,z) = \sum_{n=0}^{N} \langle \mathfrak{f}_n^+ | \psi(x,0)\rangle \mathfrak{f}_n^-(x) e^{-i\kappa_0^2 pz} e^{-\frac{\Gamma_n}{2}z}. \tag{2.28}$$

Eq. (2.28) proves an intrinsical irreversibility of DSWs, where a backward propagation beyond the shock point is no physically possible because of the exponentially decaying evolution. This explains why the quantum representation of wave propagation theory in a RHS is called TAQM (here time is replaced by z). More details can be found in A.1 and in [14].

In the probabilistic interpretation of TAQM [17], the projection of Eq. (2.28) over $\sqrt{\Gamma_n}\mathfrak{f}_n^+$ gives the probability $p_n(z)$ of finding the system in a decaying GV

$$p_n(z) = \Gamma_n |\langle \mathfrak{f}_n^+ | \psi(x,0)\rangle|^2 e^{-\Gamma_n z}, \tag{2.29}$$

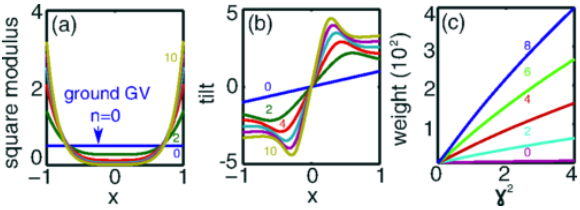

Figure 2.3: (a) $||\mathfrak{f}_n^-(x)||^2$ in Eq. (2.25) for increasing even order n; (b) corresponding phase chirps $\partial_x \mathrm{Arg}[\mathfrak{f}_n^-(x)]$; (c) weights $p_n(0)$ [Eq. (2.29)] of the GV expansion of a Gaussian wave packet.

which gives the $z-$dependent weight of the n-order GV. Initial weights $p_n(0)$ are reported in Fig. 2.3c as functions of γ^2. Since a Gaussian beam $\psi(x,0) = \varphi(x) = \exp(-x^2/2)/\sqrt[4]{\pi}$ is an even input, all the odd terms in Eq. (2.28) vanish due the $x-$parity. Figure 2.4a shows the numerical solution of Eq. (2.21). Yellow lines give the transverse intensity profile. We see that these are modeled by a superposition of exponential decays, where the plateau is given by the groundstate GV, and the peaks are given by higher order GVs. Simulations of weights $p_n(z)$ are in Figs. 2.4b,c. While dotted profiles are numerical results from Eq. (2.29), continuous lines result from the general projection definition $p_n(z) = \Gamma_n |\langle \mathfrak{f}_n^+ | \psi(x,z) \rangle|^2$, with $\psi(x,z)$ numerical solution of Eq. (2.21).

Anisotropic Dispersive Shock Waves in The Rigged Hilbert Space

Fixing z as the longitudinal and x, y as the transverse directions, we consider an initial beam which is even in the y direction, and odd along x. This initial condition causes a new phenomenon: the shock does develop an annular collapse, but around the zero-singularity it presents an abrupt intensity discontinuity. We theoretically analyze this anisotropic wave breaking. We model the beam propagation beyond the shock point by TAQM and uncover the mechanism of how such an abrupt intensity discontinuity is generated. We numerically simulate these results and find remarkable agreement with experiments and theoretical predictions [2].

By defining $I = |A|^2$ the intensity, $P_{MKS}(Z) = \int\int \mathrm{d}\boldsymbol{R}_\perp I(\boldsymbol{R})$ the power (MKS refers to the international system of units SI), $L_d = kW_0^2$ the diffraction length, and $\alpha = \frac{L_d}{L_{loss}} \sim 0$ (then $\partial_Z P_{MKS} \sim 0$) [119], and the response function

$$K(X,Y) = \tilde{K}(X)\tilde{K}(Y), \quad \tilde{K}(X) = \frac{e^{-\frac{|X|}{L_{nloc}}}}{2L_{nloc}}, \tag{2.30}$$

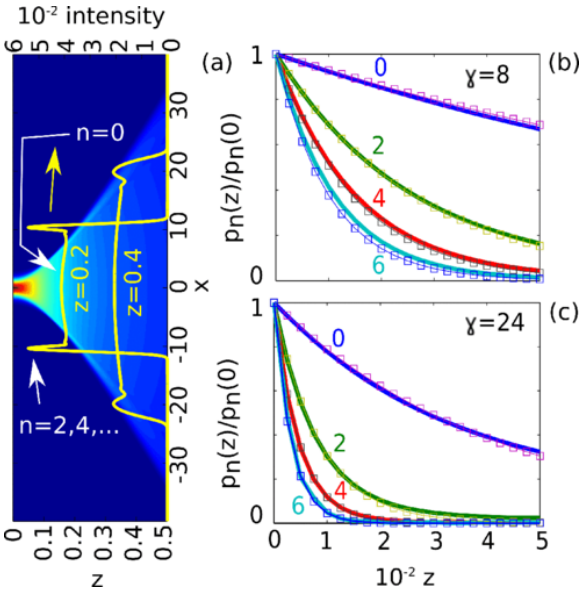

Figure 2.4: (a) Numerical solution of Eq. (2.21) with $p = 10^4$ and $\sigma^2 = 10$; (b) projection on GVs for increasing order n for $\alpha = 0.3$ and $\gamma = 8$; continuous lines are from Eq. (2.21), dots are from Eq. (2.29); (c) as in panel (b) for $\gamma = 24$.

we rescale Eq. (2.16) through the dimensionless variables $x = X/W_0$, $y = Y/W_0$ and $z = Z/L_d$, and obtain

$$\imath\partial_z\psi + \frac{1}{2}\nabla^2_{\boldsymbol{r}_\perp}\psi + \chi P K_0 * |\psi|^2\psi = 0, \tag{2.31}$$

where $\boldsymbol{r} = (\boldsymbol{r}_\perp, z) = (x, y, z)$, $\nabla^2_{\boldsymbol{r}_\perp} = \partial^2_x + \partial^2_y$, $\psi(\boldsymbol{r}) = \frac{W_0}{\sqrt{P_{MKS}}}A(\boldsymbol{R})$, $\chi = \frac{n_2}{|n_2|}$ and $P = \frac{P_{MKS}}{P_{REF}}$ with $P_{REF} = \frac{\lambda^2}{4\pi^2 n_0|n_2|}$ (REF stands for reference power). The asterisk $*$ in Eq. (2.31) stands for the convolution product, while $K_0(x, y) = \tilde{K}_0(x)\tilde{K}_0(y)$ with $\tilde{K}_0(x) = W_0\tilde{K}(X) = \frac{e^{-\frac{|x|}{\sigma}}}{2\sigma}$ and $\sigma = \frac{L_{nloc}}{W_0}$ the nonlocality degree.

In highly nonlocal approximation ($\sigma >> 1$), once fixed the initial conditions, $|\psi|^2$ mimics a delta function (or a narrow superposition of delta functions), and the nonlocal potential looses its I-dependence, becoming a simple function of the transverse coordinates [90, 115]:

$$\begin{aligned} K_0 * |\psi|^2 \simeq \kappa(\boldsymbol{r}_\perp) \simeq \kappa(\boldsymbol{0}) + \left(\partial_x\kappa|_{\boldsymbol{r}_\perp=\boldsymbol{0}}\right) x + \left(\partial_y\kappa|_{\boldsymbol{r}_\perp=\boldsymbol{0}}\right) y + \\ + \tfrac{1}{2}\left(\partial^2_x\kappa|_{\boldsymbol{r}_\perp=\boldsymbol{0}}\right) x^2 + \left(\partial_x\partial_y\kappa|_{\boldsymbol{r}_\perp=\boldsymbol{0}}\right) xy + \tfrac{1}{2}\left(\partial^2_y\kappa|_{\boldsymbol{r}_\perp=\boldsymbol{0}}\right) y^2, \end{aligned} \tag{2.32}$$

after a Taylor second-order expansion. This approximation maps the NLSE (2.31) into a linear Schrödinger equation $\imath\partial_z\psi(\boldsymbol{r}) = \hat{H}(\boldsymbol{p}_\perp, \boldsymbol{r}_\perp)\psi(\boldsymbol{r})$, with $\hat{H}(\boldsymbol{p}_\perp, \boldsymbol{r}_\perp) = \frac{1}{2}\hat{\boldsymbol{p}}_\perp^2 + \hat{V}(\boldsymbol{r}_\perp)$ the Hamiltonian, $\hat{\boldsymbol{p}}_\perp = (\hat{p}_x, \hat{p}_y) = (-\imath\partial_x, -\imath\partial_y)$ the transverse momentum and $\hat{V}(\boldsymbol{r}_\perp) = -\chi P\kappa(\boldsymbol{r}_\perp)\mathbb{1}$ the multiplicative potential ($\mathbb{1}$ is the identity operator). Let us consider the initial condition

$$\psi_{\text{ISO}}(\boldsymbol{r}_\perp) = \psi_2(x)\psi_2(y), \quad \psi_2(x) = \frac{1}{\sqrt[4]{\pi}} e^{-\frac{x^2}{2}}. \tag{2.33}$$

The shape of $\kappa(\boldsymbol{r}_\perp)$ depends on $\psi_{\text{ISO}}(\boldsymbol{r}_\perp)$. Indeed, since ψ_{ISO} is an even, separable function, all the first derivatives in Eq. (2.33) vanish and it results to be $\kappa(\boldsymbol{r}_\perp) = \kappa_0^2 - \frac{1}{2}\kappa_2^2 |\boldsymbol{r}_\perp|^2$, where $\kappa_0^2 = \frac{1}{4\sigma^2}$ and $\kappa_2^2 = \frac{1}{2\sqrt{\pi}\sigma^3}$.

In the defocusing case ($n_2 < 0$), the transversal profile of the solution of Eq. (2.31) with initial condition (2.33) is shown in Fig. 2.5(a). Fig. 2.5(b) exhibits the central part of the symmetric response function $K_0(x, y)$, while the longitudinal profile on x, z (same of y, z) is reported in Fig. 2.5(c). The corresponding Hamiltonian reads $\hat{H} = P\kappa_0^2 + \hat{H}_{\text{RHO}}(p_x, x) + \hat{H}_{\text{RHO}}(p_y, y)$, where

$$\hat{H}_{\text{RHO}}(p_x, x) = \frac{1}{2}\hat{p}_x^2 - \frac{\gamma^2}{2}\hat{x}^2 \tag{2.34}$$

is the one-dimensional RHOs Hamiltonian of frequency $\gamma = \sqrt{P}\kappa_2$. Once moved to $\phi(\boldsymbol{r}) = e^{\imath P\kappa_0^2}\psi(\boldsymbol{r})$, our Schrödinger equation becomes $\imath\partial_z\phi(\boldsymbol{r}) = \left[\hat{H}_{\text{RHO}}(p_x, x) + \hat{H}_{\text{RHO}}(p_y, y)\right]\phi(\boldsymbol{r})$, which is completely separable. In bra-ket notation

$$\begin{aligned} \imath\tfrac{\mathrm{d}}{\mathrm{d}z}|\phi(z)\rangle &= \hat{H}_{\text{ISO}}(\boldsymbol{p}_\perp, \boldsymbol{r}_\perp)|\phi(z)\rangle, \\ \hat{H}_{\text{ISO}}(\boldsymbol{p}_\perp, \boldsymbol{r}_\perp) &= \hat{H}_{\text{RHO}}(p_x, x) \otimes \mathbb{1}_y + \mathbb{1}_x \otimes \hat{H}_{\text{RHO}}(p_y, y), \\ |\phi(z)\rangle &= |\phi_2(z)\rangle_x \otimes |\phi_2(z)\rangle_y, \end{aligned} \tag{2.35}$$

with $\otimes$ the tensorial product, no more explicitly written hereafter. The solution of Eq. (2.35) lives in a tensorial product between two one-dimensional RHSs. Indeed, if we consider the evolution operator $\hat{U}(z) = e^{-\imath\hat{H}z}$ such that $|\phi(z)\rangle = \hat{U}(z)|\phi(0)\rangle$, for Eq. (2.35)
$|\phi(z)\rangle = e^{-\imath\hat{H}_{\text{RHO}}z}|\psi_2\rangle_x e^{-\imath\hat{H}_{\text{RHO}}z}|\psi_2\rangle_y$. The representation of $|\phi_2(z)\rangle_{x,y} = e^{-\imath\hat{H}_{\text{RHO}}z}|\psi_2\rangle_{x,y}$ in terms of GVs was already given in Eqs. (2.26-2.28). It is $|\phi_2(z)\rangle_{x,y} = |\phi_N^G(z)\rangle + |\phi_N^{BG}(z)\rangle$, with

$$|\phi_N^G(z)\rangle = \sum_{n=0}^{N} e^{-\frac{\gamma}{2}(2n+1)z}|\mathfrak{f}_n^-\rangle\langle\mathfrak{f}_n^+|\psi_2\rangle \tag{2.36}$$

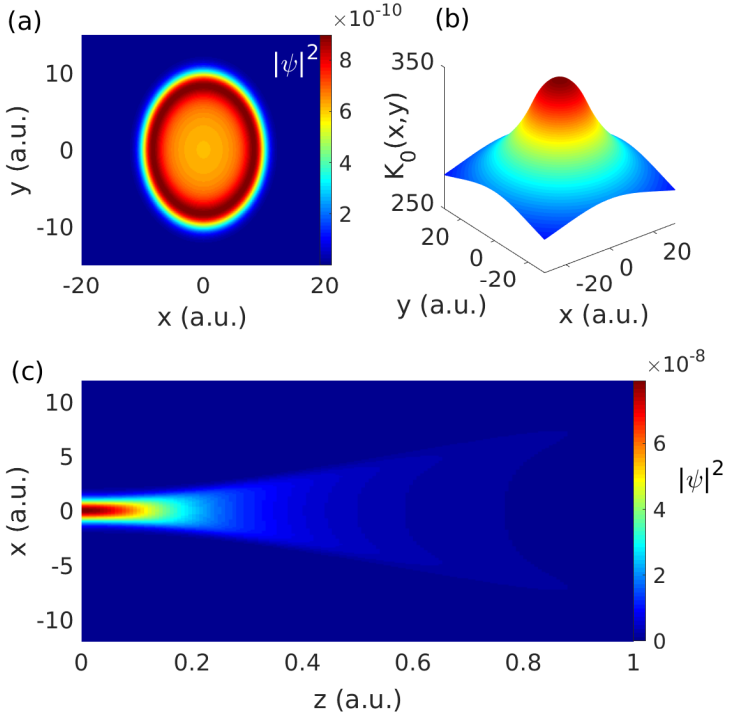

Figure 2.5: Solution of the defocusing NLSE (2.31) with initial condition (2.33), for $P = 4 \times 10^6$ and $\sigma = 120$, in arbitrary units: (a) shows the intensity transverse profile at $z = 0$, (b) exhibits the symmetric response function derived from Eq. (2.33), and (c) reports the intensity longitudinal outline, here on the plane (x, z), equal to one on the plane (y, z).

the decaying superposition of Gamow states $|\mathfrak{f}_n^-\rangle$, corresponding to the energy levels $E_n^{RHO} = \imath\frac{\gamma}{2}(2n+1)$, and $|\phi_N^{BG}(z)\rangle$ the background function, both belonging to the same one-dimensional RHS.

We model the initial asymmetric beam-shape as follows:

$$\psi_{\text{ANI}}(\boldsymbol{r}_\perp) = \psi_1(x)\psi_2(y), \quad \psi_1(x) = -\frac{\sqrt{2}}{\sqrt[4]{\pi}} x e^{-\frac{x^2}{2}}, \tag{2.37}$$

$\psi_2(y) = \frac{1}{\sqrt[4]{\pi}} e^{-\frac{y^2}{2}}$ as in Eq. (2.33). In this case, Eq. (2.32) is reduced to $\kappa(\boldsymbol{r}_\perp) = \kappa_0^2 + \frac{1}{2}\kappa_1^2 x^2 - \frac{1}{2}\kappa_2^2 y^2$, with $\kappa_0^2 = \frac{1}{4\sigma^2}$, $\kappa_1^2 = \frac{1}{4\sigma^4}$ and $\kappa_2^2 = \frac{1}{2\sqrt{\pi}\sigma^3}$.

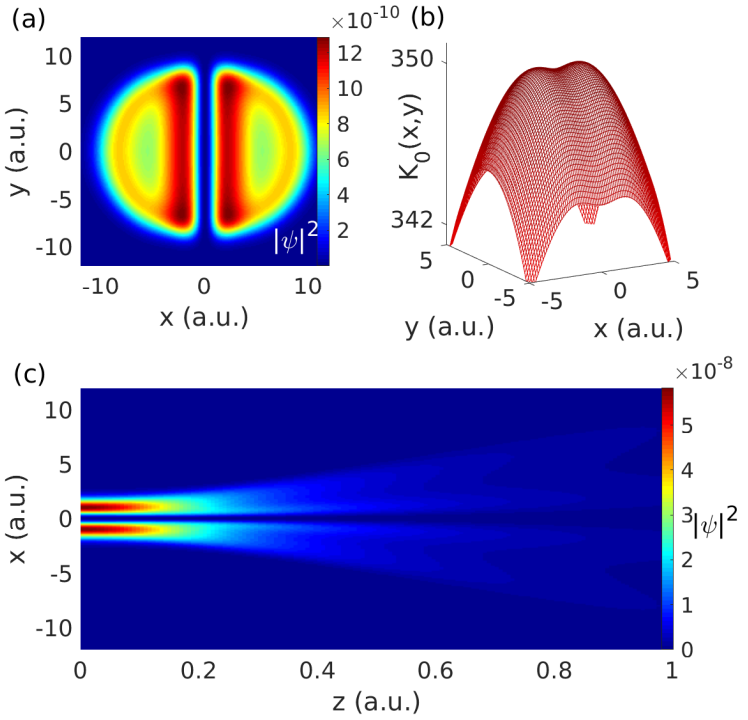

Figure 2.6: Solution of the defocusing NLSE (2.31) with initial condition (2.37), for $P = 4 \times 10^6$ and $\sigma = 120$, in arbitrary units: (a) shows the intensity transverse profile at $z = 0$, (b) exhibits the asymmetric response function derived from Eq. (2.33), and (c) reports the intensity longitudinal outline on the plane (x, z), with the zero-singularity.

The anisotropy appears evident: not only the initial condition presents a zero-singularity, but also the response function has two different behaviors along x, y directions. Numerical simulations are illustrated in Fig. 2.6. Fig. 2.6(a) shows the anisotropic DSWs [2], solution of the NLSE (2.31) with initial condition (2.33). Fig. 2.6(b) gives numerical proof of the response function anisotropy: the (x, y)-plane origin corresponds to a saddle point, with a locally increasing profile along $x > 0$, $y < 0$ and a locally decreasing outline along $x < 0$, $y > 0$. Fig. 2.6(c) reports the intensity zero-singularity in a neighborhood of $x = 0$ in propagation.

The presence of the saddle point in the response function has direct consequences through highly nonlocal approximation in mapping the NLSE in the quantum-like linear Schrödinger equation. From the expression of $\kappa(\boldsymbol{r}_\perp)$ above, for $\phi(\boldsymbol{r}) = e^{\imath P\kappa_0^2}\psi(\boldsymbol{r})$ we obtain

$$\begin{aligned} \imath\tfrac{\mathrm{d}}{\mathrm{d}z}|\phi(z)\rangle &= \hat{H}_{\mathrm{ANI}}(\boldsymbol{p}_\perp, \boldsymbol{r}_\perp)|\phi(z)\rangle, \\ \hat{H}_{\mathrm{ANI}}(\boldsymbol{p}_\perp, \boldsymbol{r}_\perp) &= \hat{H}_{\mathrm{HO}}(p_x, x)\mathbb{1}_y + \mathbb{1}_x\hat{H}_{\mathrm{RHO}}(p_y, y), \\ |\phi(z)\rangle &= |\phi_1(z)\rangle_x|\phi_2(z)\rangle_y, \end{aligned} \tag{2.38}$$

where $\hat{H}_{\mathrm{HO}}(p_x, x) = \frac{1}{2}\hat{p_x}^2 + \frac{\omega^2}{2}\hat{x}^2$ is the one-dimensional HO Hamiltonian with $\omega = \sqrt{P}\kappa_1$, and $\hat{H}_{\mathrm{RHO}}$ is the 1D-RHOs Hamiltonian in Eq. (2.34). The solution of Eq. (2.38) is the tensorial product of $|\phi_1(z)\rangle_x = \sum_{n=0}^{+\infty} e^{\imath\frac{\omega}{2}(2n+1)z}|\Psi_n^{HO}\rangle\langle\Psi_n^{HO}|\psi_1\rangle$, where $|\Psi_n^{HO}\rangle$ are $\hat{H}_{\mathrm{HO}}$-eigenstates corresponding to the energy levels $E_n^{HO} = \frac{\omega}{2}(2n+1)$ [14], and $|\phi_2(z)\rangle_y = |\phi_N^G(z)\rangle + |\phi_N^{BG}(z)\rangle$, explicitly written in Eq. (2.36).

Evidence of the presence of GVs is given in Fig. 2.7. By defining $\Gamma_n = \gamma(2n+1)$, we look for the first two quantized decay rates $\Gamma_{0,2}$ (the even Gaussian initial function lets achieve only even energy levels) in the longitudinal propagation in y-direction. Indeed, if one computes the intensity of the y-part, one finds $\langle\phi_2(z)|\phi_2(z)\rangle_y \overset{N>>0}{\simeq} \langle\phi_N^G(z)|\phi_N^G(z)\rangle = \sum_{n=0}^{N} e^{-\Gamma_n z}\left|\langle\hat{\mathfrak{f}}_n^+|\phi_2\rangle\right|^2$. Fig. 2.7(a) shows the theoretical section of the nonlinear sample where we seek decaying states. We fix $x = 2.29$, a little distant from the shock-gap, and report the corresponding intensity in y, z plane. The pink line is equivalent to $x = y = 2.29$. Fig. 2.7(b) exhibits $|\phi(x = 2.29, y = 2.29, z)|^2$, exponentially decaying. Two exponential fits demonstrate the GV occurrence: the fundamental Gamow state represents the plateau with decay rate $\Gamma_0 = 1.51$, whereas the first excited one interpolates the peak, with decay rate $\Gamma_0 = 1.51$. We stress that the rule $\frac{\Gamma_2}{\Gamma_0} = 5$ is respected.

This treatise demonstrates that the interplay of a trapping (HO) and an antitrapping (RHO) potential generates a novel kind of DSWs, with the contemporary presence of annular collapse singularities and a shock-gap enclosed by very intense light barriers. The outcoming dynamics is modeled through an advanced theoretical description in RHSs, by means of TAQM, proving its intrinsic irreversibility.

EXPERIMENTAL OBSERVATIONS IN THERMAL MEDIA

Shock waves described by Eq. (2.16) have been originally shown in an experiment from [66]. The sample is a cell of length 1mm filled with an aqueous solution of Rhodamine B (RhB), with a concentration of 0.6mM.

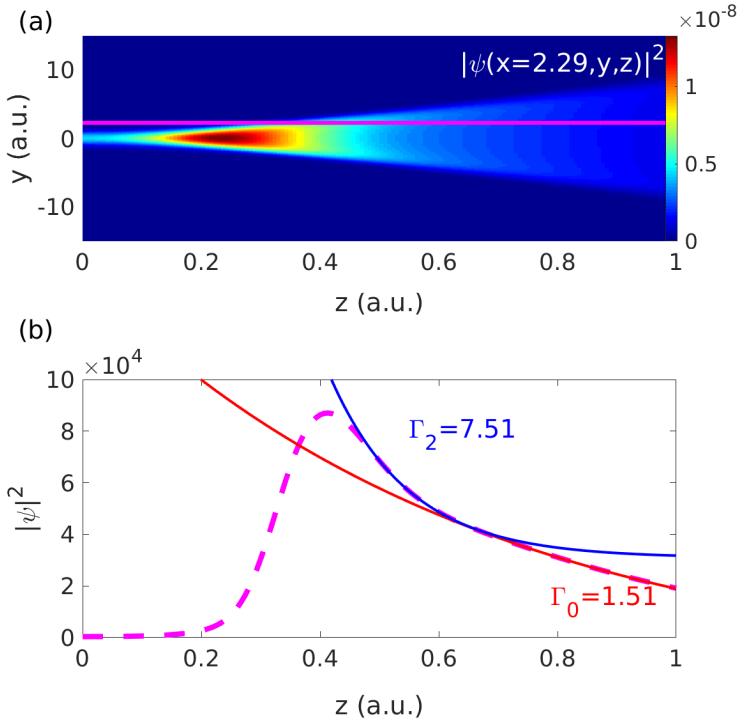

Figure 2.7: GVs signature. From Fig. 2.6, in the same conditions, (a) is the y, z profile at fixed $x = 2.29$. Intensity along the pink line, i.e., $|\phi(x = 2.29, y = 2.29, z)|^2$, is in (b), with the decaying part fitted with two exponential function: the fundamental GV, with decay rate Γ_0, and the first excited GV, with decay rate Γ_2.

Measurements of beam intensity profiles at different initial powers - the characteristic shock internal collapse is evident for the three highest power values - are in Fig. 2.8. A Gaussian CW-laser beam of intensity waist diameter $W_0 = 20\mu$m, at wavelength $\lambda = 532$nm, propagates in a material with linear refractive index $n_0 = 1.3$, defocusing Kerr coefficient $n_2 = -7 \times 10^{-7}\text{cm}^2\text{W}^{-1}$, loss length $L_{loss}^{-1} = 62\text{cm}^{-1}$. For water $D_T = 1.5 \times 10^{-7}\text{m}^2\text{s}^{-1}$, $\rho_0 = 10^3\text{kg m}^{-3}$, $c_p = 4 \times 10^3\text{J kg}^{-1}\text{K}^{-1}$, $\left|\frac{\partial n}{\partial T}\right|_0 = 10^{-4}\text{K}^{-1}$. The degree of nonlocality is estimated as $\sigma = 0.3$.

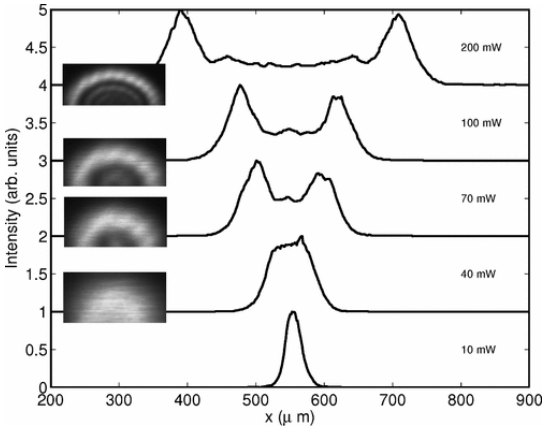

Figure 2.8: Experimental transverse intensity profiles of an initial Gaussian beam propagating in a thermal medium. Measurements are performed for varying input power $P = \pi W_0^2 I_0$. Insets show the 2D output patterns. Reprinted from [66].

The beam exhibits, beyond the shock point, the formation of undular bores moving outward with increasing power. The next subsections report different experiments exhibiting DSWs in nonlocal samples.

Rhodamine and Time Asymmetric Quantum Mechanics Interpretation

In this section we report two experiments in order to validate the presence of GVs in DSWs: a 2D propagation pattern to observe GVs decay rates Γ_n [16], and a 1D experiment to show that GVs describe also the M-shaped profile in the far field of a DSW in highly nonlocal approximation [75], in [74] identified for the first time as collapse singularity. These are validations of TAQM in describing DSW propagation.

The experimental setup is illustrated in Fig. 2.9A. Samples are prepared by dispersing 0.1mM of RhB in water. The solution is placed in a cuvette 1mm thick in the propagation direction. The measured defocusing Kerr coefficient is $|n_2| = 2 \times 10^{-12} \mathrm{m^2 W^{-1}}$ and the absorption length is $L_{loss} \simeq$ 1.6mm at the laser beam wavelength 532nm [69]. The CW-laser beam is focused through a lens into a sample. Light is collected by a spherical lens and a Charged Coupled Device (CCD) camera. A microscope is placed above the sample in order to capture top-view images of the laser beam along the propagation direction Z. The difference between the two experimental apparatus is the choice of the first lens (L1). In the

2D experiment [16], L1 is spherical with focal length 10cm, and a focus spot size of 10μm. The setup was placed having the beam propagating vertically through the sample, reducing thermal convection in the water. In the 1D experiment [75], it was used a cylindrical lens as L1, with focal length $f = 20$cm in order to mimic a nearly one-dimensional propagation. Being Z the propagation direction, the lens focuses the beam in the X direction. The input spot dimension is 1.0mm in the Y direction and 35μm in the X direction. These geometrical features make the one-dimensional approximation valid and allow us to compare experimental results with the theoretical one-dimensional model. The diffraction length in the X direction is $L_d = 3.0$mm. This time, the setup was placed horizontally.

Figures 2.9B,C report the observed laser beam propagation top-view, detected by a microscope through RhB fluorescence, and the numerical calculation from the NLSE, respectively. The beam displays the characteristic strongly defocusing and the M-shaped behavior, also evident in the transverse sections of the intensity in Figs. 2.9D,E. These are signatures of DSWs in nonlinear media at high power.

Decay rates in Fig. 2.10 are detected by slicing the intensity profile $I(X, Z)$ at $X \simeq 0.1$mm (yellow line in Fig. 2.9B) and fitting the intensity versus Z with two exponential functions. Different power levels exhibit very different dynamics. The presence of double exponential decays, that is, the superposition of the first two GVs, is more evident at high power. It was observed and calculated that double-exponential decay dynamics obey the quantized spectrum scaling $\Gamma_2/\Gamma_0 = 5$ at all investigated power levels, as shown in Fig. 2.10D. This demonstrates that we excited the fundamental state $\mathfrak{f}_0^-$ and the first excited state $\mathfrak{f}_2^-$ [16]. Odd states are not excited, as expected from Gaussian TEM_{00} $x-$parity. Each of the two rates has a square root dependence on P, signature of the underlying nonlinearity. This power dependence distinguishes RHOs dynamics from linear loss, due to absorption and scattering.

The RHOs eigenstates are quasi-eigenstates of the FT operator, which in optics represents the far field. Let us consider the RHOs Hamiltonian in the momentum basis ($\hat{p} \to \mathfrak{p}$ and $\hat{x} \to \imath\partial_{\mathfrak{p}}$)

$$\hat{H}_{RHO}(\mathfrak{p}, \imath\partial_{\mathfrak{p}}) = \frac{\mathfrak{p}^2}{2} + \frac{1}{2}\gamma^2\partial_{\mathfrak{p}}^2 = -\hat{H}_{RHO}(-\imath\partial_x, x). \tag{2.39}$$

Pure GVs are infeasible to describe a physical experiment, because one cannot neglect that GVs have an infinite support, i.e., the x-region where the eigenfunction is not null, is not finite. In order to account for the

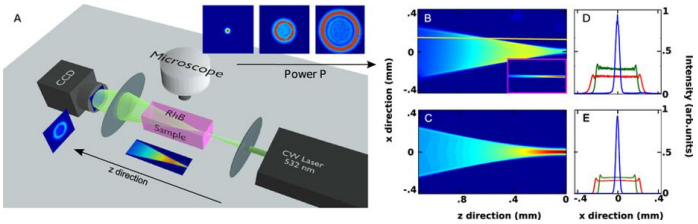

Figure 2.9: **A** Experimental setup. We collected the transmitted and fluorescence images of the laser beam propagating in RhB samples [16, 75]. Two types of launching lenses L1 were used: a cylindrical and a spherical, for the 1D and 2D experiments, respectively. The top fluorescence image of the propagating beam was collected by a microscope placed above the RhB samples. The second lens is spherical and was used to collect the transverse output profile. **B,C** Top-view intensity distribution as obtained from 2D experiment B and numerical simulations C. Respectively experimental **D** and numerical **E** sections of the images B and C taken at $z = 0.2$ (red), 0.6 (green) and 0.9mm (blue).

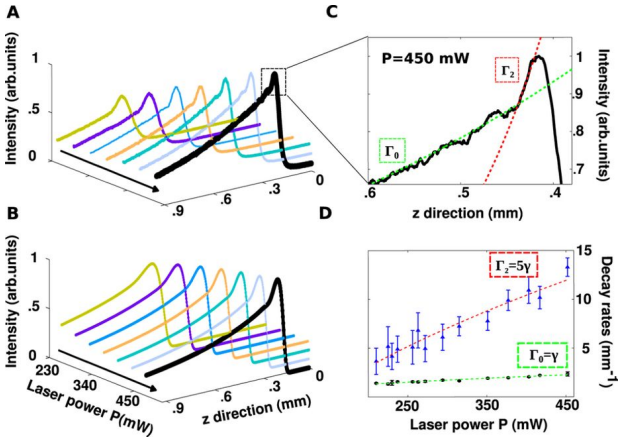

Figure 2.10: **A** Observed intensity decay at different laser powers, obtained by slicing along $X \simeq 0.1$mm the top-view intensity distribution the propagation direction (see the yellow line in Fig. 2.9B). **B** Numerically calculated decays in the conditions of panel A. **C** Peak region of the experimental curve at $P = 450$mW. The superposition of the first two exponential decays unveils the presence of two GVs, the fundamental state, $n = 0$ (slowly decaying) and the first excited state, $n = 2$ (fastly decaying). **D** Decay rates vs P for the fundamental state, Γ_0 (filled circles) and the excited state, Γ_2, (triangles).

spatial confinement of the experiment, the windowed GVs were introduced [75]:

$$\phi_G^W(x) = \sum_{n=0}^{N} \sqrt{\Gamma_n} \mathfrak{f}_n^- \langle \mathfrak{f}_n^+ | \psi(x,0) \rangle \mathrm{rect}_W(x), \tag{2.40}$$

where

$$\mathrm{rect}_W(x) = \begin{cases} 0 & \text{for} |x| \geq W \\ 1 & \text{for} |x| < W \end{cases}, \tag{2.41}$$

with W is the finite size of the physical system. During the evolution, the Gamow ground state has the lowest decay rate, i.e., $\gamma/2$. This allows us to consider, in the long term evolution, only the fundamental GV, and so only the FT $\mathcal{F}$ of the fundamental state of Eq. (2.40):

$$\begin{aligned} &\tilde{\psi}(k_x) = \mathcal{F}\left[\mathfrak{f}_0^{-,W}(x)\right] = \\ &= \left(\tfrac{1}{4} + \tfrac{\imath}{4}\right) e^{-\frac{\imath k_x^2}{2\gamma}} \frac{(-\imath\gamma\pi)^{1/4}}{W} \times \left\{ -\mathrm{Erf}\left[\frac{(\frac{1}{2} - \frac{\imath}{2})(k_x - W\gamma)}{\sqrt{\gamma}}\right] + \mathrm{Erf}\left[\frac{(\frac{1}{2} - \frac{\imath}{2})(k_x + W\gamma)}{\sqrt{\gamma}}\right] \right\}. \end{aligned} \tag{2.42}$$

Eq. (2.42) provides an analytical expression of the far field, which is compared below with the experiments. Indeed, Eq. (2.42) allows us to predict in closed form the typical M-shaped shock profile: it describes the internal undular bores and the correct scaling of the undulation period with respect to the power, i.e. the period T is predicted to scale with the square root of γ, and hence with the forth square root of the beam input power.

Figure 2.11 reports experimental results in RhB, through the previously described setup, and the comparison with the numerical results. Images of the beam in the far field (corresponding to the square modulus of the spatial intensity FT) for different input powers were collected and shown in Figs. 2.11a,b. For low power (not reported) the elliptical beam profile remains Gaussian along propagation. A different phenomenon occurs while increasing the power: the beam transverse section along X broadens and develops intensity peaks on its lateral edges. Essentially, it becomes M-shaped. These results are in remarkable agreement with Eq. (2.42), as shown in Figs. 2.11c,d.

Different positions in the Y direction correspond to different power levels. Any power level furnishes a different value of γ, being $\gamma = \sqrt{\frac{p}{\sqrt{\pi}\sigma^2}}$. The Gaussian beam profile in the Y direction, that is, $p \propto exp(-y^2)$, provides the link between Y, P and γ. This implies that,

observing a CCD image, intensity profiles at different Y correspond to different powers. Therefore, the expected exponential trend with respect to the power can be extracted from a single picture by looking at different Y positions. Figure 2.11e exhibits a fitting with two exponential decays in an intensity profile versus power. The extracted ratio of the related two decay rates is 5 and hence in agreement with the expected quantized theoretical values described in Sec. 2.2.2.

Undular bores of DSWs were analyzed and exhibited in Fig. 2.11f, while the field intensity undulation period T versus P is shown in Fig. 2.11g. In order to demonstrate univocally that $T \propto \sqrt[4]{P}$, inset in Fig. 2.11g reports the period T as function of $\sqrt[4]{P}$. The resulting linear behavior confirms the theoretical results.

Nonlinearity and Disorder in Thermal Media

Thermal media have been investigated also in their interplay with disorder. Theoretical studies demonstrated that, even if solitons are stable under a certain amount of randomness, the latter competes with nonlinearity, while nonlocality filters disorder-induced scattering effects and soliton random walk can be efficiently suppressed in highly nonlocal media [89, 91, 120]. DSWs are nonlinear coherent oscillations, and the phenomenon of light scattering affects their formation in significant way [69].

In this section we report experiments in two different optical systems that combines third-order nonlinearity (high-power laser beams) with nonlocality (thermal material response) and disorder (scattering particles). The first thermal medium is a dispersion of silica spheres of 1μm diameter in 0.1mM aqueous solution of RhB. The second one is a 1mm×1mm×8.5mm parallelepiped of silica aerogel. Despite observations of DSWs in disordered thermal media, a theoretical model that comprehends both nonlinearity, nonlocality and disorder has been developed only for solitons [89]. The existing theoretical model for DSWs is summarized below and neglects the nonlocality contribution. It approximates thermal nonlinearity to a local Kerr effect, and adds a random potential [69].

We start from Eq. (2.16) with $\Delta n[|A|^2] = n_2|A|^2 + \Delta n_R(X, Y, Z)$ and $L_{loss} \sim \infty$ (no loss). Through the same scaling of Sec. 2.2.1 and the one-transverse-dimension approximation $\partial_y \sim 0$ (experimentally generally given by a cylindrical lens), we obtain

$$\imath\epsilon\partial_z\psi + \frac{\epsilon^2}{2}\partial_x^2\psi - |\psi|^2\psi + U_R\psi = 0, \tag{2.43}$$

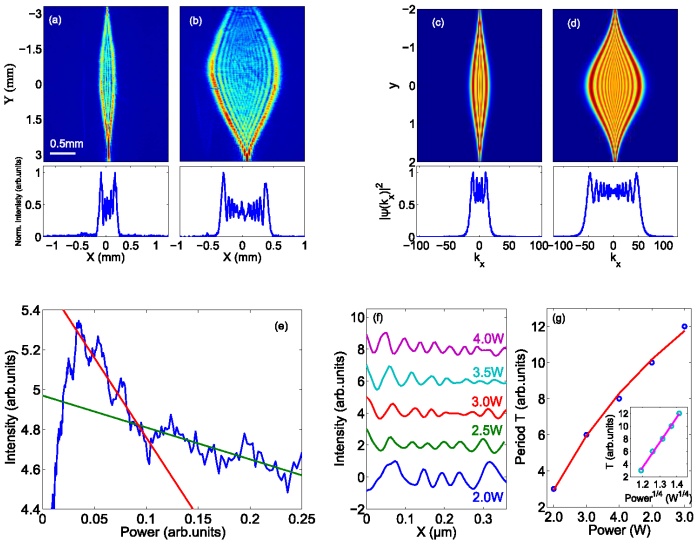

Figure 2.11: (a,b) Laser beam output intensity, detected by the CCD-camera, at laser powers $P = 2$W and 4W, respectively; the bottom panels show the normalized intensity profile along $Y = 0$, i.e., at the maximum width, resembling the M-shape. (c) Analytical solution obtained by Eq. (2.42) changing Gaussianly the power P in the y direction. (d) As in (c) but for higher powers; the bottom panels show the slice of panel (c) and (d) at $y = 0$, i.e., Eq. (2.42) square modulus for $W = 1.5$ and $\gamma \simeq 12$ and $\gamma \simeq 40$, respectively. (e) Log-scale normalized intensity as a function of power, as obtained by slicing along Y a region in panel (b). The slopes of the straight lines give the GV decay rates ($\gamma_1 = -8 \pm 0.4$ and $\gamma_2 = -1.6 \pm 0.1$). Their quantized ratio is 5.0 ± 0.4 as expected from theory [17]. (f) Intensity oscillations for different power values. (g) Measured oscillations period T as a function of power; continuous line is the fit function $T \propto \sqrt[4]{P}$, as expected by the theory; the inset shows the same curve of (g) with $P^{1/4}$ as abscissa axis. Reprinted from [75].

with $U_R(x,y,z) = \frac{\Delta n_R(X,Y,Z)}{n_2 I_0}$ taken as a random dielectric noise mainly acting on the phase [69]. In the hydrodynamic limit $\epsilon \sim 0$, the phase chirp behaves like a moving unitary mass particle [69]:

$$\frac{\mathrm{d}^2 x}{\mathrm{d}z^2} = -\frac{\mathrm{d}U}{\mathrm{d}x} + \eta_R, \tag{2.44}$$

with $U = \exp\left(-x^2/2\right)$ the deterministic potential for a Gaussiam TEM_{00} given by the nonlinearity, and $\eta_R = -\frac{\mathrm{d}U_R}{\mathrm{d}x}$ a Langevin force with Gaussian

distribution, such that $\langle \eta_R(z)\eta_R(z')\rangle = \eta^2\delta(z-z')$ and $\eta = \sqrt{\left\langle \left(\frac{dU_R}{dx}\right)^2 \right\rangle} \simeq \sqrt{\langle (\Delta n_R)^2\rangle}(|n_2|I_0)^{-1}$ the disorder strength. Brackets $\langle , \rangle$ denote the statistical average, and the dependence of η_R on x, y is neglected for stochastic independence and cylindrical symmetry, respectively, thus $\eta_R \simeq \eta_R(z)$.

Figure 2.12 shows trajectories $x(z)$ (Figs. 2.12a,b) and phase space (x, v) (Figs. 2.12c,d), where $v = \frac{dx}{dz}$, respectively without ($\eta = 0$) and with ($\eta = 0.1$) disorder, the latter obtained by a stochastic Runge-Kutta algorithm [121, 122]. In absence of disorder (Figs. 2.12a,c) the shock is signaled by the intersection of multiple trajectories $x(z)$ and, in the phase space, this corresponds to the induced wave breaking phenomenon, that is, the folding of the velocity profile into a multivalued function for increasing z. In presence of disorder, Figs. 2.12b,d, the particle-like dynamics tends to diffuse, as is evident from the related trajectories and phase space. Correspondingly, the propagation distance before the intersections is greater for the disordered case and the shock is delayed in the z direction.

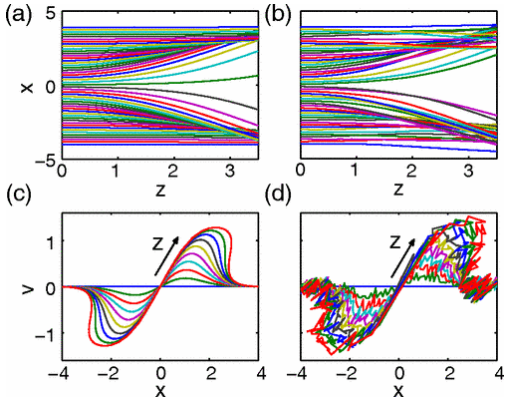

Figure 2.12: (a,b) Trajectories $x(z)$ and (b,d) phase space (x, v), respectively with disorder strength $\eta = 0$ and $\eta = 0.1$. z varies from $z = 0$ to $z = 3$. Reprinted from [69].

We report here the experiments in RhB with silica spheres dispersions [69]. In order to vary the degree of disorder, several silica concentrations were prepared, ranging from 0.005w/w to 0.03w/w, in units of weight of silica particles over suspension weight. The experimental setup is similar to that illustrated in Fig. 2.9A. The first lens focuses the beam on the input facet of the sample, reaching a beam waist diameter

$W_0 \simeq 10\mu$m. The aqueous solutions are put in 1mm×1cm×3cm glass cells with propagation along the 1mm vertical direction (parallel to gravity) to moderate the effect of heat convection. All measurements are performed after the temperature gradient has reached the stationary state and the particle suspensions are completely homogeneous. In [69], main loss mechanisms are absorption and scattering. The measured loss length (absorption plus scattering) varies in a range from 1.2mm to 1.6mm (highest value is for for pure dye solution). These values are obtained by fitting with exponential decay the beam intensity vs propagation distance Z. The fact that the loss length is always greater than the position of the shock point [69] allowed authors to neglect losses at a first approximation in their theory. In addition, they found that the scattering mean free path is of the order of millimeters for all the considered samples. In Fig. 2.13 images of the transmitted beam on the transverse plane for different input laser powers P and various concentrations c are shown. The number and the visibility of the DSW oscillations increase with P and decrease with c, evidence of DSWs enhancement by nonlinearity and inhibition by disorder.

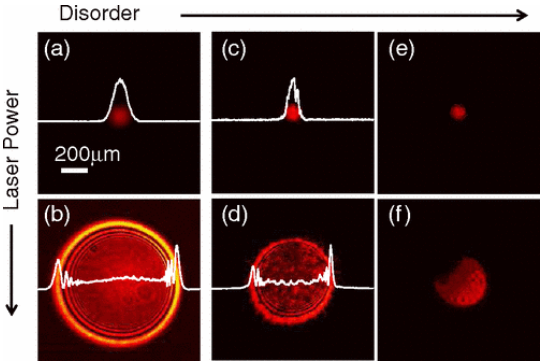

Figure 2.13: Transverse intensity patterns for different input power P and silica spheres concentration c: (a) $P = 5mW$, $c = 0$w/w, (b)$P = 400mW$, $c = 0$w/w, (c) $P = 5mW$, $c = 0.017$w/w, (d) $P = 400mW$, $c = 0.017$w/w, (e) $P = 5mW$, $c = 0.030$w/w, (f) $P = 400mW$, $c = 0.030$w/w. White 1D curves show the measured section of the intensity profiles vs X. Reprinted from [69].

Experimental observations have been also performed in silica aerogel [72]. The silica aerogel samples are prepared following a base-catalyzed sol-gel procedure [123], and in-depth details are given in [72]. It turns out that the sample used in the experiment has mass density $\rho = 0.215\text{g/cm}^3$ and refractive index $n_0 = 1.074$. Experimental setup is

very similar to the previous ones (Fig. 2.1a), except for the sample. In [72], authors vary the input beam waist diameter W_0, the input laser power P_{in}, and record the transmitted intensity distribution $I(X, Y, Z = 8.5\text{mm})$ by the CCD camera. Observations are shown in Fig. 2.14. Images in the second and third rows of Fig. 2.14 correspond to the same experimental conditions in term of incident laser power and beam size, but the incident laser beam impinges on different points. In correspondence of regions of the silica aerogel sample displaying low enough disorder (second row), a transition from scattering dominated regimes to nonlinear regimes is present: at moderate powers DSWs are not observed because of scattering losses, at high powers DSWs can be generated.

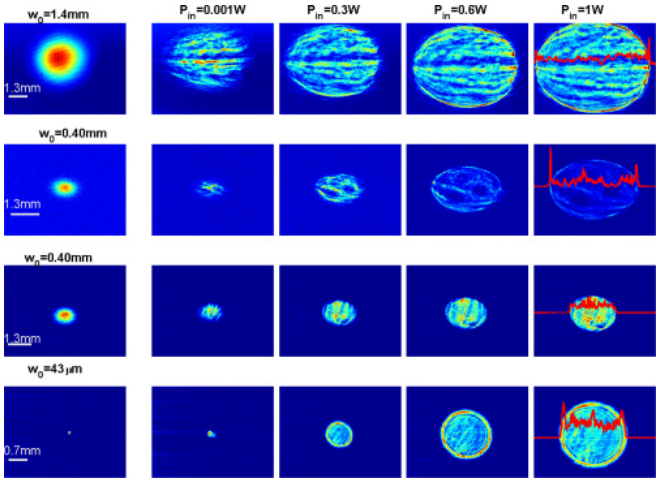

Figure 2.14: Far field intensity profiles at the output of the silica aerogel for P_{in} ranging from 1mW to 1W, and input beam waist diameter w_0 ranging from 43μm to 1.4mm. Images in the second and third rows correspond to the same incident laser power and beam size, but different positions of the incident laser beam. Reprinted from [72].

Dispersive Shock Waves in Biological Suspensions and Chemical Compounds

The study of optical effects in light propagation through chemical and biological solutions is a field of growing interest [73, 78, 93, 124–127], both from a linear and a nonlinear perspective. However, although observations of nonlinear optical phenomena in chemical and soft-matter systems can be found in a extensive literature [16, 66, 69, 71, 72, 75, 84, 93, 128–131], and new experiments in chemical media are useful only if the

material owns very specific properties, little is known about nonlinearity in biological fluids and the related literature is very recent [78, 126]. Biomaterials can be very interesting, because both chemical and biological compounds can be excellent tunable thermal media, and DSWs were already observed [66, 73, 78].

For sake of completeness, in this section we report two experiments. The first one (an a further one, reported in the next section) in M-Cresol/Nylon, a chemical solution that exhibits an isotropic giant self-defocusing nonlocal nonlinearity, tunable by varying the nylon concentration [73]. The second one in human red blood cell suspensions, where the concentration of Hemoglobin (Hb) and the input laser beam power make the nonlinearity change from self-focusing to nonlocal defocusing [78].

Figure 2.15 shows transverse profiles of output beam intensity after a propagation of 2mm in M-Cresol/Nylon. M-Cresol/Nylon is made up of an organic solvent (m-cresol) and a synthetic polymeric solute (nylon). When it is enlightened by a CW-laser beam, light absorption induces local temperature variations, which reduces the refractive index, that is, the material experiences a nonlinear thermo-optical effect. In particular, [93]'s authors measured the M-Cresol/Nylon nonlinear Kerr coefficient n_2 and found that, if for pure m-cresol it is $-9 \times 10^{-8}\text{cm}^2/\text{W}$, for a nylon mass concentration of 3.5% it is $-1.6 \times 10^{-5}\text{cm}^2/\text{W}$, higher than other thermal nonlinear materials where annular collapse singularities have been observed [8, 73]. Authors generated the DSWs in Fig. 2.15 by focusing the input beam (a CW-laser beam of wavelength 532nm) to $20 \pm 1\mu$m onto the surface of M-Cresol/Nylon solution of 3.5% nylon concentration. The input laser power was varied ranging from 2μW to 20mW and, when it reached 5mW, the wave-breaking occured.

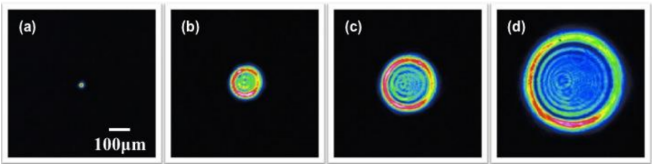

Figure 2.15: Output beam intensity transverse profiles, coming out from a 2mm long M-Cresol/Nylon solution. Input power varies: (a) $P_{in} = 2\mu$W, (b) $P_{in} = 5$mW, (c) $P_{in} = 10$mW, (d) $P_{in} = 20$mW. Reprinted from [73].

Figure 2.16 reports a part of the results obtained in lysed human red blood cells aged samples, where free RhB determines sign and nonlocality of the optical nonlinearity from self-focusing (and self-trapping) to strong thermal defocusing effects, regime in which DSWs occur [78]. Beyond the biological issues related to human red blood cells, holding uncountable

applications to life sciences and medicine, red blood cells refractive index tunability makes this medium be incredibly interesting also from a physical point of view [132–135]. In normal conditions, red blood cells are disc-shaped malleable cells, averagely with 8μm of diameter and 2μm of thickness, which have a spatially uniform refractive index because of the lack of nuclei and most organelles [133, 135]. To enable the passage through veins and narrow microcapillaries, red blood cells exhibit distinctive deformability. Since their optical properties depend on the shape and refractive index of cells, they can be used as tunable optofluidic microlenses [134].

The red blood cell refractive index is mainly determined by RhB, which is the largest part of the erythrocyte dry content by weight [132]. Fig. 2.16a shows the output beam waist diameter as a function of input power through the RhB solutions for four different concentrations, from 2.4 to 15.0 million cells per mL. Experiments in [78] are performed by using a linearly polarized CW-laser beam with a wavelength of 532nm focused through a lens of 125mm focal length into a 3cm long glass cuvette filled with the red blood cell suspensions. In particular, the focused beam has initial waist diameter $W_0 = 28\mu$m at the focal point, which was located at 1cm away from the input facet of the cuvette to avoid heating and surface effects [126]. Outputs from the sample were monitored with a CCD camera and a power detector, and are reported in Figs. 2.16b-e, at variance of RhB concentration and input power. DSWs occur at high power (Figs. 2.16c,e), more visible in high RhB concentration regime (Fig. 2.16c).

Anisotropic Shock Waves in M-Cresol/Nylon

Following experimental results in Fig. 2.15, we report evidences of two-dimensional optical DSWs with an anisotropic zero-singularity in M-Cresol/Nylon 3.5%-solution [2], theoretically treated in Sec. 2.2.3. Our experiments are performed with an asymmetric initial condition, designed through a phase mask, to attain an anisotropic light propagation. The setup is illustrated in Fig. 2.17(a). A laser beam with wavelength $\lambda = 532$nm passes through two lenses (L1 and L2) to collimate the light, and through a beam splitter (BS1), which divides the beam into two arms, one used for the nonlinear experiment, and the other for getting a reference beam for interference measurements. The beam outcoming from the first arm is transformed in our asymmetric input by a phase mask, and then is focused (via L3) onto the facet of a 2mm-long cuvette, which contains a M-Cresol/Nylon 3.5%-solution. The output is imaged (via L4 and BS2) onto a CCD camera.

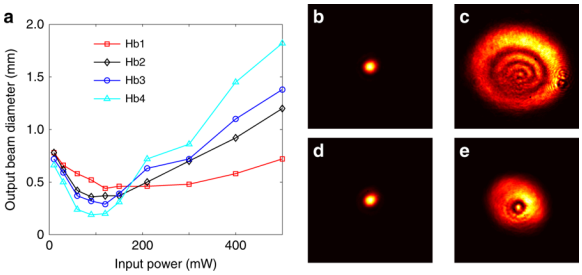

Figure 2.16: Output beam waist diameter for varying RhB concentration and input power. **a** Detected beam diameter as function of input power through the RhB solutions for four different concentrations (RhB1-RhB4): 2.4, 5.1, 8.6, and 15.0 million cells per mL. Nonlinear self-focusing of the beam occurs around 100mW for high concentrations of RhB, but it subsequently expands into thermal defocusing rings at high powers. **b-e** Output beam transverse intensity profiles for **b** self-trapped beam at high concentration and low power, **c** DSW at high concentration and high power, **d** self-trapped beam at low concentration and low power, **e** DSW at low concentration and high power. Reprinted from [78].

Figure 2.17(b) reports the input (intensity and phase patterns at initial power $P_{MKS} = 2$mW and waist diameter $W_0 = 15,8\mu$m) and the outputs at different initial powers. The input beam presents a phase discontinuity of π along $x = 0$. Here we observe the first realizations of what we define anisotropic DSWs: annular collapse singularities with an initial zero-singularity, which generates two barriers of light intensity around a gap in the middle of the beam. The analysis of the barriers, due to the HO component, and the corresponding shock-gap is also examined. Since $\hat{H}_{\rm HO}$ has potential $\hat{V}_{\rm HO}(x) = \frac{\omega^2}{2}\hat{x}^2$, we expect a shock-gap with the same behavior of the potential width $\Delta x \propto \frac{1}{\sqrt{\omega}} = \frac{2\sigma^2}{\sqrt{P}}$.

Figure 2.18 reports experimental measurements of the shock-gap at variance of initial power P_{MKS}. A theoretical fit with a function $\propto \frac{1}{\sqrt{P_{MKS}}}$ is drawn in the red line. The agreement between observations and numerical simulations confirms the theoretical statement.

The use of a thermal medium with a giant Kerr coefficient, the M-Cresol/Nylon 3.5%-solution, let us access an extremely-nonlinear highly-nonlocal regime and perform accurate experiments in absence of losses. These results not only confirm previous studies on the giant nonlinear response of M-Cresol/Nylon, but also disclose fundamental insights on propagation of DSWs with a singular initial intensity profile.

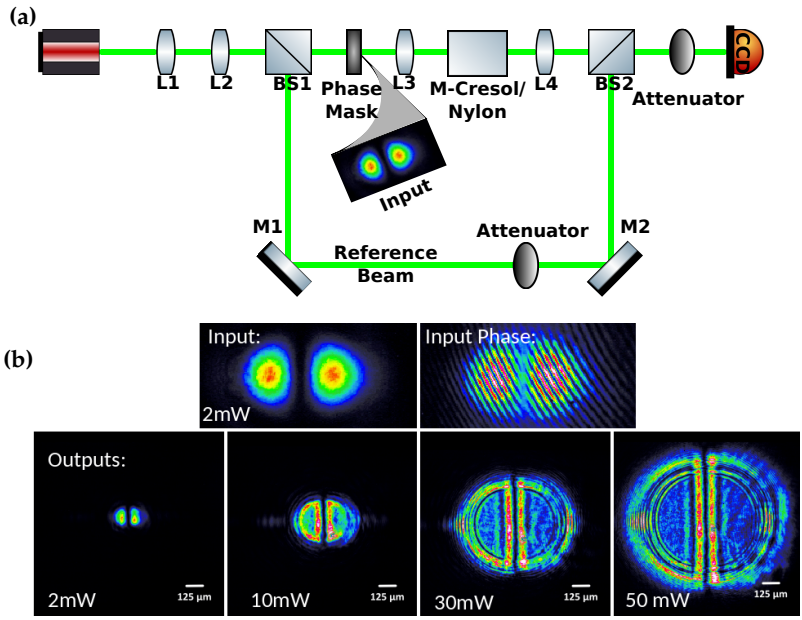

Figure 2.17: (a) Experimental setup. A $\lambda = 532$nm CW-laser beam is collimated through two lenses (L1 and L2). A beam splitter (BS1) divides the beam into two arms. the first is made asymmetric by a phase mask and propagates in a 2mm-long cuvette with M-Cresol/Nylon 3.5%-solution. The second is a reference beam for interference measurements. The output is imaged (via L4 and BS2) onto a CCD camera. (b) Input and outputs observed. The phase mask in (a) generates a π-discontinuity in the input phase, here reported with initial power $P_{MKS} = 2$mW and waist diameter $W_0 = 15,8\mu$m, together with the intensity profile. Several output at different initial power (from left-hand-side to right-hand-side: $P_{MKS} = 2$mW, $P_{MKS} = 10$mW, $P_{MKS} = 30$mW, $P_{MKS} = 50$mW) are shown. If at low power we cannot distinguish nonlinear effects from diffraction, the higher the power is, the stronger the nonlinear effects are. We observe the formation of anisotropic DSWs, with annular collapse singularity and the formation of two intense barriers in the beam center.

CONCLUSIONS

We reviewed the most widespread current theoretical models that describe nonlocal NLSE DSWs in spatial optical beam propagation. Moreover, we discussed their experimental observations.

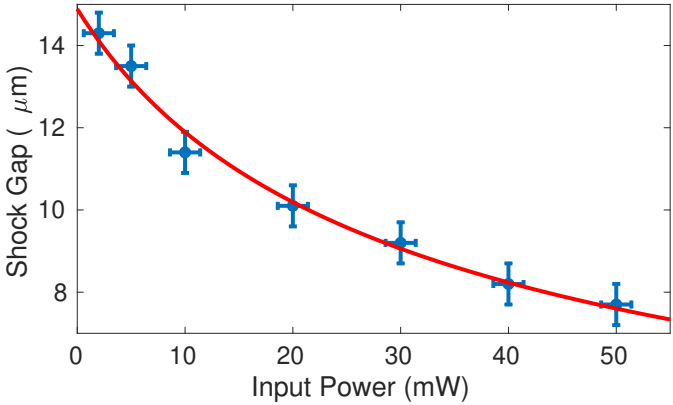

Figure 2.18: Observation of the shock-gap versus the initial power P_{MKS}. The red line shows the theoretical fit with a function $\propto \frac{1}{\sqrt{P_{MKS}}}$.

In Sec. 2.2 the derivation of nonlocal NLSE was detailed, and main features of wave breaking in thermal Kerr media were reported [66]. In order to exhibit the theoretical interpretations of these phenomena as intrinsically irreversible, TAQM approach was summarized [13, 74, 76].

Section 2.3 is a collection of experiments on DSW generation in thermal media, first about a quite rich literature on observations in Rhodamine [66], and their TAQM explaination [16, 17, 75]. As second instance, we analyzed the interaction between disorder and nonlinearity in Rhodamine with silica spheres [69] and in silica aerogel [72], where the randomness inhibits the DSWs occurrence. Moreover, we reviewed very recent works on generation of photonic wave breaking in chemical [73] and biological solutions [78], fields where DSWs are emerging as surprising tools, useful for sensing and control of extreme phenomena.

DSWs are complex nonlinear waves, and their complexity was here detailed in the highly nonlocal regime, which allows a simplified description. However, non-negligible nonlocality is limited to thermal media in spatial experiments, or non-instantaneous fibers, i.e., filled with specific gases, in temporal ones. In the much more widespread local case, such as common fibers or photorefractive crystals, other methods are necessary, like IST or finite-gap approximation. In what follows, we show how these sophisticated mathematical techniques foster the description of other extremely complex nonlinear waves, their related experimental observations, and also their control.

3 OPTICAL REALIZATION OF FERMI-PASTA-ULAM-TSINGOU RECURRENCE

INTRODUCTION

Nonlinear interaction in a multimodal system introduces coupling between its linear modes. When a reduced set of modes is initially excited, the energy exchange associated to this coupling provides the route to reach thermodynamic equilibrium. However, as discovered by Fermi in collaboration with Pasta, Ulam and Tsingou [136], the irreversible process towards thermalization can present local reversibility. Studying a chain of anharmonic oscillators with a single-mode initial condition, they found that the system fails to thermalize on small time scales and undergoes a dynamics characterized by the quasi-periodic appearance of specific states, a behavior known as Fermi-Pasta-Ulam-Tsingou Recurrence (FPUTR) [137–139].

An approach to understand the physical mechanism underlying the phenomenon rests on the quasi-integrability of the system [140–143]. This property implies the existence of a time scale for which the Fermi-Pasta-Ulam-Tsingou dynamics is essentially integrable. In fact, for integrable models, pure thermalization has never been reached since normal modes are phase-locked and not free to resonantly interact and spread energy over the entire spectrum [141]. Consistently, certain integrable systems support breathers; their phase space presents homoclinic orbits connecting unstable solutions, so that trajectories starting in proximity of these unstable points can return close to the original state.

The key role of integrability explains why the FPUTR has eluded in-depth experimental investigations. Specifically, while in numerical studies the thermalization time was too large to be initially identified, quite the opposite issue arises in experiments: in open systems involving several interacting modes recurrences to the initial state are not normally reported. In fact, due to the effect of intrinsic dissipation or input noise amplification [144], a natural process rarely is integrable and preserves multiple returns. Observations in quasi-Hamiltonian systems have so far been limited to one or two return cycles [145]. Evidences of the recurrence of states have been reported in deep water waves [145], surface gravity waves [146], magnetic rings [147], optical microresonators [148] and optical fibers [37, 149, 150]. In spite of these efforts, how the spe-

cific initial condition determines the properties of the recurrent behavior remains a fundamental point that has never found experimental validation. An important attempt in this direction has been reported very recently in loss-compensated optical fibers [37], where, however, the tailored amplification allows the system just to mimic the return cycles that would have its non-dissipative counterpart. In this setting, among the many recurrent behaviors expected varying the input state, only the two types with opposite symmetry has been observed and related to separate families of orbits in phase space [37]. The observation of the Fermi-Pasta-Ulam-Tsingou dynamics as predicted by exact solutions of an underlying integrable model remains an open challenge.

Here we observe the FPUTR in spatial NLO and provide evidence that the recurrent behavior is ruled by the exact solution of the Nonlinear Schrödinger Equation integrable dynamics. Specifically, we exploit a three-waves interferometric setup to finely tune amplitude and phase of the single-mode input excitation propagating in a photorefractive medium. The unstable mode manifests the Akhmediev breather profile and undergoes several growth and decay cycles whose partial-period and phase-shift are determined by the initial excitation in remarkable agreement with the analytic nonlinear Schrödinger theory. This allows us to retrieve the specific input state from the properties of the nonlinear stage of instability, the signature of the predictability of the underlying dynamics.

EXACT RECURRENCES IN THE NLSE

The integrable NLSE [Eq. (1.4)] is a universal model describing the propagation of a quasi-monochromatic field $\psi(x,z)$ in a weakly nonlinear medium [151]. Exact solutions of Eq. (1.4) corresponding to perturbations of the constant background wave have recently attracted considerable attention in hydrodynamics and optics [33, 152–157], in particular as they describe the dynamics of the MI and may be relevant in explaining the formation of extreme amplitude waves [RWs] [158–163]. On the other hand, the NLSE naturally arises as the continuous limit (infinite number of modes) for the dynamics of a chain of anharmonic oscillators coupled by a cubic nonlinearity, the so called β-Fermi-Pasta-Ulam-Tsingou model [164, 165]. In this framework, the problem of finding the time scale of the recurrence as a function of the specific input condition has been elusive up to recently. The analytic description of the recurrence for an initially-perturbed background field of finite length with a single unstable mode has been reported by *Grinevich and Santini* using the finite-gap approximation or matched asymptotic expansions [35, 36]. Theory

points out a variety of phase-shifted recurrences closely determined by the phase and amplitude of the input condition. In particular, considering the single-mode perturbed input field

$$\psi_0(x) = 1 + \varepsilon \left(c_1 e^{ikx} + c_2 e^{-ikx} \right), \tag{3.1}$$

with complex amplitudes c_1 and c_2 and $\varepsilon \ll 1$, we expect the recurrent growth of a coherent structure of the Akhmediev type (x-periodic) and its recurrent decay to the initial state. The first-appearance time or recurrence partial-period of this large-amplitude wave is predicted to as [35, 36]

$$Z_1 = \frac{1}{\sigma_k} \log \left(\frac{\sigma_k^2}{2\varepsilon|\alpha|} \right), \tag{3.2}$$

where $\sigma_k = k\sqrt{4-k^2}$ is the growth rate of the input unstable mode with wavevector k and $\alpha = c_1^* - c_2 \exp(2i\vartheta)$ with $\vartheta = \arccos(k/2)$. The multiple recurrence of the field to the initial condition corresponds to periodic orbits close to the homoclinic orbit described by the well-known Akhmediev breather exact solution of the NLSE [166]. In fact, in the m-th recurrent nonlinear stage of the dynamics ($m \geq 1$), the field is described by the Akhmediev breather, which, at its maximum, reads as

$$\psi(x, Z_m) = e^{i\xi_m} \frac{\cos(2\vartheta) + \sin(\vartheta)\cos[k(x - X_m)]}{1 - \sin(\vartheta)\cos[k(x - X_m)]} + O(\varepsilon), \tag{3.3}$$

where ξ_m, Z_m and X_m are parameters related to the input condition through the elementary functions [35, 36]

$$\begin{aligned} Z_m &= Z_1 + (m-1)\tfrac{2}{\sigma_k} \log \left(\tfrac{\sigma_k^2}{2\varepsilon\sqrt{|\alpha\beta|}} \right), \quad m \geq 1 \\ X_m &= \tfrac{\arg(\alpha) - \vartheta + \pi/2}{k} + (m-1)\tfrac{\arg(\alpha\beta)}{k}, \\ \xi_m &= 2Z_m + 2(2m-1)\vartheta, \end{aligned} \tag{3.4}$$

with $\beta = c_2^* - \exp(-2i\vartheta)c_1$. Although solution of the Akhmediev type have been observed and connected to recurrent behaviors in different settings [37, 145], experimental demonstration of Eq. (3.2), which forms the basis for the Fermi-Pasta-Ulam-Tsingou dynamics in a broad range of systems, is lacking. In other words, the way in which these exact recurrent solutions can have physical relevance is an open question.

PROPAGATION IN PHOTOREFRACTIVE MEDIA

The propagation equation of the complex optical field envelope $A(x, y, z)$ in a photorefractive crystal is a saturable NLSE, with a nonlinear term depending on intensity and time:

$$\imath\partial_z A + \frac{1}{2k}\nabla^2 A + \frac{k}{n_0}\delta n(I,t)A = 0, \tag{3.5}$$

with z the longitudinal coordinate, x, y the transverse coordinates, $\nabla^2 = \partial_x^2 + \partial_y^2$, and $n = n_0 + \delta n(I,t)$ the refractive index, weakly depending on the intensity $I = |A|^2$ ($\delta n(I) << n_0$). Time dependence is due to the nonlinear self-interaction, which increases, on average, with the exposure time up to a saturation value, on a slow timescale, typically seconds for peak intensities of a few $kWcm^{-2}$ [167]. In a centrosymmetric photorefractive crystal, at first approximation $\delta n = \frac{-\delta n_0}{\left(1+\frac{I}{I_S}\right)^2} f(t)$, with $f(t)$ the response function. δn_0 includes the electro-optic effect coefficient [167–169]. For weak intensities $I << I_S$, we obtain a Kerr-like regime with $\delta n = 2\delta n_0 \frac{I}{I_S} f(t)$, apart from a constant term. We consider the case $\partial_y A \sim 0$ (strong beam anisotropy), thus we look for solutions of the $(1+1)$-dimensional NLSE for the envelope $A \sim A(x, z)$:

$$\imath\partial_z A + \frac{1}{2k}\partial_x^2 A + 2\rho(t)|A|^2 A = 0, \tag{3.6}$$

with $\rho(t) = \frac{2\pi\delta n_0}{\lambda I_S} f(t)$. Introducing the change of variables $Z = \rho z$, $X = \sqrt{2k\rho}x$, the equation can be transformed into the dimensionless NLSE [Eq. (1.4)]. An analogous renormalization of the wave equation is widely adopted in nonlinear fiber optics, where the optical power of the input wave is exploited to mimic the spatial dynamics along the fiber [170]. Rigorously, since the normalization makes dispersive terms slowly varying along the propagation, the approach allows us to observe only an effective field evolution.

In the present case, the evolution in Z is studied at a fixed value of z (the crystal output) varying the exposure time t. In fact, experimental results obtained in similar photorefractive KTN crystals have verified that the average index change grows and saturates according to $f(t) = 1 - \exp(-t/\tau)$ [171]. The time dependence is well defined through the saturation time τ once the input beam intensity, applied voltage and temperature have been fixed. Using this relation with the measured $\tau \approx 100$ s, observations at the crystal output are rescaled as a function of the effective distance Z. The nonlinear response function $f(t)$ represents the main limitation of the technique in recostructing the

spatial dynamics from time-resolved measurements. Specifically, $f(t)$ is independent of the local intensity only in a first approximation, a fact that affects the accuracy of the obtained field evolution. When the intensity distribution presents large intensity variations or strong spatial inhomogeneities, intensity-dependent corrections to $f(t)$ should be taken into account to have a quantitative reconstruction along the evolution coordinate. These high-order terms are nonlocal in space and time; their main effect is that the time evolution of high-intensity regions slows down [167]. Therefore, in the present case, the method is particularly accurate up to a distance Z_1 (first-appearance time). Small longitudinal deformations appear at longer evolution scales [Figs. 3.2(a,b)] and the relative distance between the observed Akhmediev breather structures cannot be accurately evaluated. This fact explains the discrepancy with theory for the value of the recurrent period when measured through the Z-distance between returning intensity maxima. In particular, the recurrent Akhmediev breather seems to appear at an effective distance that is always shorter than expected according to theoretical predictions. Moreover, as the nonlinearity finally saturates in time, the field dynamics at large Z departs from that of the integrable model and evolution towards thermalization is observed.

SPATIAL OPTICAL SETTING

To investigate FPUTRs in optical dynamics, we consider the propagation of optical nonlinear waves in a photorefractive crystal. The wavectors of the optical field constitutes the linear modes which are coupled by nonlinear propagation. The transverse crystal size fixes the finite length of the input wave, a condition ensuring a countable set of Fourier modes and a finite recurrence period. Under specific conditions, the system can be described by the NLSE in the spatial domain, with the propagation direction acting as evolution coordinate [172].

The experimental geometry of our setup is shown in Fig. 3.1(a). A y-polarized optical beam at wavelength $\lambda = 532$nm from a continuous 30mW Nd:YAG laser source is split and recombined in the xz-plane to form a symmetric three-wave interferometer, with the two arms having opposite wavevectors and forming an angle θ with the 300μW central beam. The interference pattern is focused by a cylindrical lens down to a quasi-one-dimensional beam with waist diameter $\omega_0 = 15\mu$m along the y-direction and periodically-modulated along the x-direction [inset in Fig. 3.1(a)]. The copropagating waves are launched into an optical quality specimen of $2.1^{(x)}$x$1.9^{(y)}$x$2.5^{(z)}$mm Potassium-Lithium-Tantalate-Niobate $K_{0.964}Li_{0.036}Ta_{0.60}Nb_{0.40}O_3$ (KLTN) with Cu and V impurities. The

crystal exhibits a ferroelectric phase transition at the Curie temperature $T_C = 284$K. Nonlinear light dynamics are studied in the paraelectric phase at $T = T_C + 8$K, a condition ensuring a large nonlinear response and a negligible effect of small-scale disorder [173]. The time-dependent photorefractive response sets in when an external bias field E is applied along y (voltage $V = 500$V). To have the aforestated Kerr-like (cubic) nonlinearity from the photorefractive effect, the crystal is continuously pumped with an x-polarized 15mW laser beam at $\lambda = 633$nm. The pump does not interact with the principal beams propagating along the z-axis and only constitutes a reference intensity larger than the single-mode perturbed background wave. The spatial intensity distribution is measured at the crystal output as a function of the exposure time by means of an high-resolution imaging system composed by an objective lens ($NA = 0.5$) and a CCD camera at $15Hz$.

The three continuous, symmetrically interfering, laser sheets form a quasi-one-dimensional background wave with a coherent single-mode perturbation. Along the transverse x-direction, the relevant one for the dynamics under study, the optical field resulting from the symmetric interference of three mutually-coherent, linearly-polarized optical waves is $E = E_0 + E_1 e^{i\phi_1} e^{ikx} + E_2 e^{i\phi_2} e^{-ikx}$, with $k = 2\pi \tan(\theta)/\lambda$. The optical intensity normalized to the background I/I_0 ($I_0 = |E_0|^2$) can be expressed as $I/I_0 \equiv |\psi_0(x)|^2 = 1 + A\cos(kx + B)$, which directly maps the initial condition in Eq. (3.1) with $A = 2\varepsilon|\gamma|$, $B = \arg(\gamma)$ and $\gamma = c_1 + c_2^*$. With respect to the experimentally accessible parameters, the amplitude and phase of the perturbation read as $A = 2\sqrt{[I_1 + I_2 + 2\sqrt{I_1}\sqrt{I_2}\cos(\phi_1 + \phi_2)]/I_0}$ and $\tan(B) = (\sqrt{I_1}\sin\phi_1 - \sqrt{I_2}\sin\phi_2)/(\sqrt{I_1}\cos\phi_1 + \sqrt{I_2}\cos\phi_2)$. Therefore, the spatial frequency of the perturbation k can be varied acting on the geometrical angle θ in between the arms of the interferometer, whereas their optical power and phase delay $\phi \equiv \phi_1 + \phi_2 = \arg(c_1) + \arg(c_2)$ set, respectively, the amplitude and phase of the single-mode [Figs. 3.1(b,c)]. The fringe visibility is thus maximum for $\phi_1 + \phi_2 = 0$ and minimum for $\phi_1 + \phi_2 = \pi$. In the symmetric case $I_1 \simeq I_2$, we have $B \simeq (\phi_1 - \phi_2)/2$.

Since the propagation length cannot be varied in our setting and the intensity profile inside the crystal cannot be directly measured [174], nonlinear evolution of the input field is observed by the time the crystal is exposed to the copropagating light beams. The method relies on the nature of the photorefractive nonlinearity, that is noninstantaneous and accumulates in time as a photogenerated space-charge field builds up [167]. Since the process occurs on a slow time scale compared to wave propagation through the medium, this implies a nonlinear coefficient that depends parametrically on the exposure time. Due to the invariant prop-

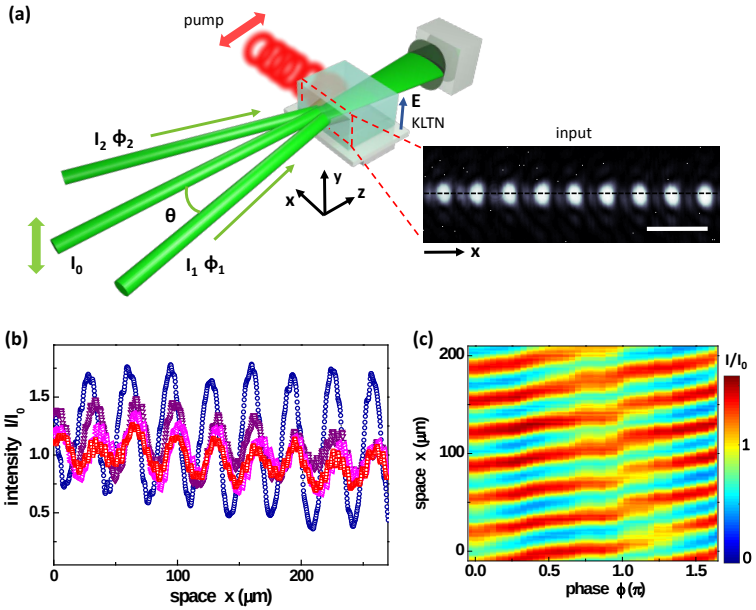

Figure 3.1: Experimental setup. (a) Sketch for the symmetric three-wave interferometric scheme used to generate a quasi-one-dimensional background wave with a single-mode perturbation that propagates in a pumped photorefractive KLTN crystal. The inset shows an example of the detected input intensity distribution (scale bar is 50μm). (b) Input intensity x-profiles normalized to the background for different amplitudes of the harmonic perturbation ($k = 0.019\mu\text{m}^{-1}$). (c) Phase control of the initial condition: intensity distribution varying the relative phase ϕ between the interfering waves.

erties of the wave equation, observations of the intensity distribution at the crystal output at different times correspond to beam propagation for increasing effective distances Z. This is equivalent to study the dynamics varying the strength of the nonlinearity through an external parameter, in close analogy with Fermi-Pasta-Ulam-Tsingou investigations in optical fibers where changes of the input optical power are exploited [149].

EXPERIMENTAL RESULTS

The spatial intensity distribution $I(x)/I_0$ detected as a function of the evolution coordinate Z is reported in Fig. 3.2(a) for $k = 0.019\mu\text{m}^{-1}$,

$A = 0.3$. We observe the input perturbation grow on the modulationally unstable background forming a train of large-amplitude localized waves, which decays back to an almost constant background and recurrently reappear from it. The set of linear modes undergoes several return cycles in which energy flows back and forth, passing from the zero and first mode (the initial perturbation) to a spectral distribution in which all the modes are excited, the signature of the Fermi-Pasta-Ulam-Tsingou dynamics [175]. At variance with classical and quantum beating, such as Rabi cycles in two-level quantum systems [176], here energy oscillations involve several modes and occur without any driving field. At each cycle, the whole field distribution is spatially shifted by an amount Δ, a phenomenon also referred to as broken symmetry of FPUTR [37, 145]. Although a similar phase-shift has been associated theoretically to the specific gain of the seeded wavevector [177] and the effect of dissipation [178], we show hereafter that it results from the sensitivity of the dynamics to the specific initial phase. This phase-shift, as well as the recurrence period detected through the first appearance distance Z_1 of the high-intensity pattern, strongly changes as the input perturbation is varied. For instance, in Fig. 3.2(b) we report the observed FPUTR for $k = 0.030\mu\text{m}^{-1}$ and $A = 0.5$, where no significant phase-shift occurs.

The recurrent behavior can be directly related to the excitation from the single-mode input perturbation of an orbit close to the Akhmediev breather [36]. As shown in Figs. 3.2(c,d), the periodic intensity profile detected along x when the amplified modes reach their first maximum is well fitted by the Akhmediev breather solution of the NLSE at its maximum [Eq. (3.3)]. Precisely, in fitting the data in Figs. 3.2(c,d), the coefficients ξ_m, k, ϑ and X_m are considered as bounded parameters. Consistently, we refer to these localized states as Akhmediev breathers. The finding of exact solutions indicates that our system remains close to the integrable regime on these effective distances, that is, it can be properly described by the NLSE.

We study the FPUTR by varying the single-mode input condition. Fixing the initial phase of the field through a careful maximization of fringe visibility, we first analyze the recurrence partial-period varying the amplitude of the perturbation A. Results in Fig. 3.3(a) show that the first appearance of the Akhmediev breather occurs at a distance that decrease as the single-mode amplitude becomes larger. An analogous behavior is observed for the recurrent breather (second appearance). In remarkable agreement with the analytic solution of the NLSE, the observed scaling follows Eq. (3.2), which predicts $Z_1 \propto \log(1/A)$. For modes k falling in proximity of the maximum gain, the recurrence period only weakly

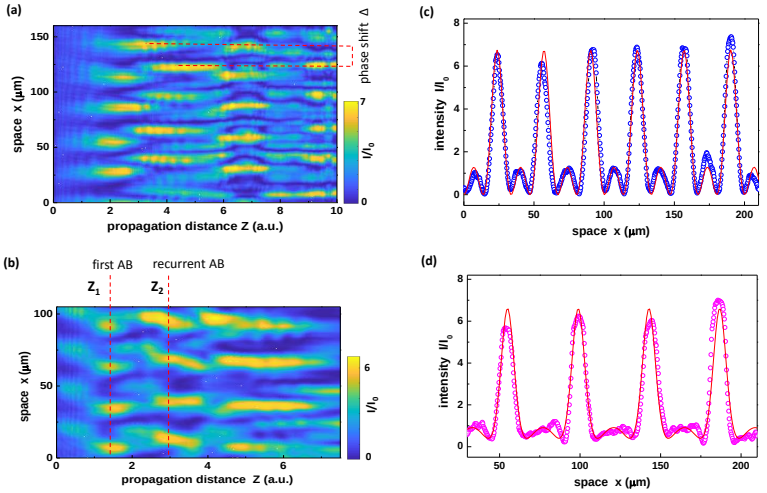

Figure 3.2: Observation of the FPUTR of Akhmediev breathers. (a-b) Evolution of the detected spatial intensity distributions for (a) $k = 0.019\mu\text{m}^{-1}$, $A = 0.3$ and (b) $k = 0.030\mu\text{m}^{-1}$, $A = 0.5$. Both observations show the appearance of a high-intensity pattern at a distance Z_1 (red dotted line), its return to the initial state and multiple recurrences with a spatial phase-shift that depends on the experimentally assigned input condition ($\Delta \approx 15\mu$m, 2μm in (a) and (b), respectively). (c-d) Intensity x-profile measured at the first appearance of the localized waves (circles) fitted with the Akhmediev breather profile at its maximum [red line, Eq. (3.3)] for (c) $k = 0.021\mu\text{m}^{-1}$ and (d) $k = 0.014\mu\text{m}^{-1}$.

depends on the input wavevector [Fig. 3.3(b)], a feature well captured by Eq. (3) through σ_k.

More importantly, the main effect on the recurrence is found to be related to the phase of the initial condition. To investigate its role, we balance the optical power in the interferometer arms ($I_1 \approx I_2$) and introduce a slight tilt in one of them, to have a perturbation with a phase that depends on the spatial point. The observed Fermi-Pasta-Ulam-Tsingou dynamics is reported in Fig. 3.3(c); the Akhmediev breather appears and recurs phase-shifted at a propagation distance that varies along the transverse coordinate.

As a function of the input phase delay, Z_1 presents an oscillation having a sharp maximum for $\phi \simeq -0.3\pi$ and a broad minimum for $\phi \simeq -0.9\pi, 0.35\pi$ [Fig. 3.3(d)]. This characteristic behavior, which reflects phase-dynamics in each return cycle, is in remarkable agreement with the NLSE theory and represents its main validation. In fact, in Eq. (3.2) the recurrent semi-period critically depends on $|\alpha|$, a quantity that oscillates

with the relative phase of the complex amplitudes c_1 and c_2 forming the initial perturbation. Specifically, in the case of symmetric perturbations ($I_1 \approx I_2$), theory predicts a sharp maximum in Z_1 for $\phi \simeq -2\vartheta$; from Fig. 3.3(d) we can thus obtain the theoretical parameter $\vartheta \simeq 0.15$, consistent with the one extracted from the Akhmediev breather profile. Moreover, a sharp transition is expected for the recurrent phase-shift as a function of the input phases [37]. In Fig. 3.3(e) we report the measured shift, which sharply passes from $\Delta \approx 0$ to $\Delta \approx 1/2k$ varying the phase delay, a behavior that well agrees with the theoretical condition $\cos(\phi) \gtrless \cos(2\vartheta)$. These effects indicate that the coherence of the field is maintained as energy is exchanged between different modes: phase-locking dominates the nonlinear stage of the unstable dynamics and thermalization slows down.

For an in-depth analysis, major information on theoretical fittings follows. For the measurements in Fig. 3.3(a) we consider $a\log(b/\varepsilon)$ as a fitting function, with a and b free parameters. In Fig. 3.3(b) we use $a\log(b(k\sqrt{K_{max}^2-k^2})^2)/k\sqrt{K_{max}^2-k^2}$, where a and b are free parameters and $K_{max} \approx 0.03\mu\text{m}^{-1}$ is the wavevector with maximum gain that we independently measure from spontaneous MI of the background wave. In Fig. 3.3(d) the detected Z_m is compared to $\log(a/\sqrt{c_1^2+c_2^2-2c_1c_2\cos(\phi+b)})$, being a, b, c_1 and c_2 bounded parameters. In this case, it is interesting to note that the fitting procedure returns $c_1 \simeq c_2$, that is, a balanced condition for the interferometer arms as experimentally settled. In Fig. 3.3(e) the fitting functions are $a + b/[\cos(\phi) - \cos(c)]$, as predicted for the symmetric case $|c_1| \approx |c_2|$.

The deterministic properties of the return cycle imply its predictability once the input condition is completely known, and viceversa. To investigate this integrable character in experimental conditions we retrieve the actual initial state from the features exhibited by the recurrent stage (inverse problem). We consider the Fermi-Pasta-Ulam-Tsingou dynamics reported in Fig. 3.4(a). The phase B of the input perturbation is obtained taking into account that the periodic transverse position X_1 at which the first Akhmediev breather has its maximum intensity strictly depends on ϕ, as well as the specific shift Δ characterizing the return cycle. In fact, according to Eq. (3.4), we have $X_1 = (\arg(\alpha) - \vartheta + \pi/2)/k$. At each recurrent cycle the breather solution is transversely shifted by $\Delta = \arg(\alpha\beta)/k$. Therefore, when $\vartheta \approx 0$, $\arg\beta \simeq k(\Delta - X_1) + \pi/2$ and the phase of the input excitation can be evaluated as

$$B = \arg(\gamma) \approx k(\Delta - X_1) - \vartheta, \tag{3.7}$$

where k and ϑ are extracted from the first Akhmediev breather profile. The amplitude of the single-mode follows from the observed Z_1 through

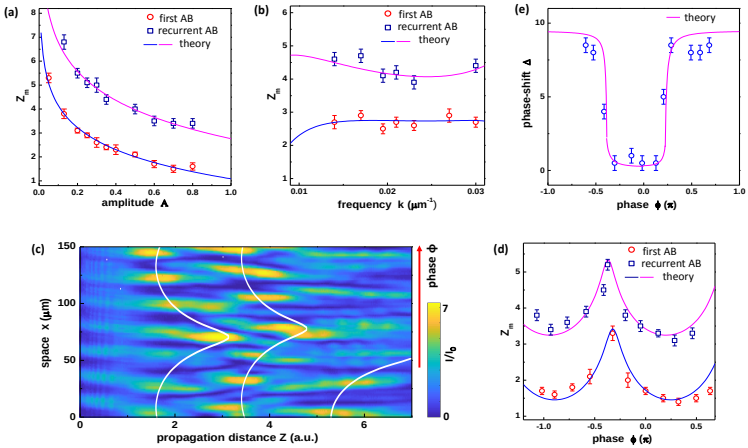

Figure 3.3: Properties of the recurrent behavior. Recurrence partial-period measured (dots) varying (a) the amplitude of the input excitation ($k = 0.023\mu\text{m}^{-1}$) and (b) the frequency of the input mode ($A = 0.3$). (c) Evolving intensity distribution detected for an input phase that varies along x ($k = 0.030\mu\text{m}^{-1}$). White lines interpolates local maxima and serve as guides. (d) Z_m as a function of the initial dephasing. Blue and magenta lines in (a-d) are fitting functions according with Eq. (3.2). (e) Recurrence phase-shift varying the input phase: measured sharp transitions (dots) and predicted behavior (line).

the scaling in Fig. 3.3(a). As shown in Figs. 3.4(b-d) for different initial dephasing, the field retrieved using this procedure agrees well with the experimental input condition that generates the recurrence: the non-equilibrium dynamics can be accurately traced on the basis of the underlying integrable model.

As for the following retrieval of the input perturbation, from the observed recurrences in Fig. 3.4(a,b) we measure, for example, $k = 0.021\mu\text{m}^{-1}$, $\Delta = 1 \pm 1\mu\text{m}$, $Z_1' = 2.6 \pm 0.1$, $\vartheta = 0.1$ which, for $X_1 = 208\mu\text{m}$, gives $B = -40.1 \pm 0.3$ and $A = 0.33 \pm 0.02$. For comparison, $B = -40.9 \pm 0.2$ and $A = 0.34 \pm 0.01$ are the values obtained fitting the experimental initial intensity.

The predictability of the Fermi-Pasta-Ulam-Tsingou dynamics is a general property of the system and does not depend on the specific input state. However, nonlinear evolution becomes more complex when several harmonics are initially excited. We observe that for two excited input modes recurrent high-intensity patterns still occur but their periodicity is lost and different states are experienced during propagation. Starting

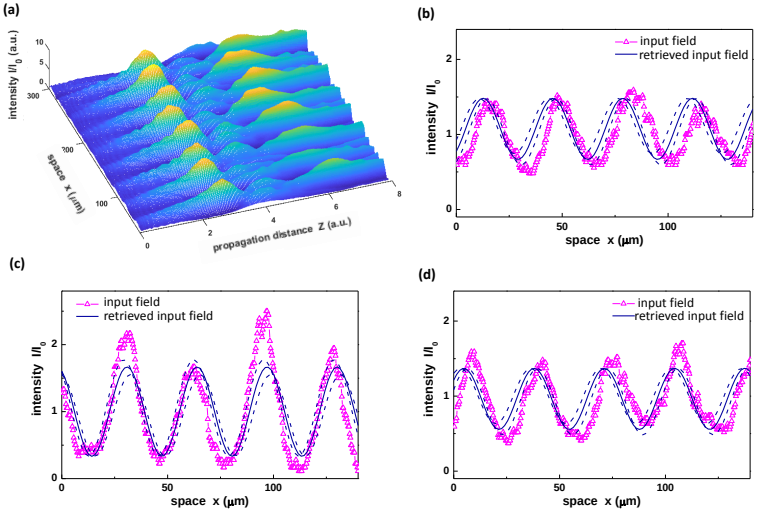

Figure 3.4: Inverse problem. (a) Experimental observation used to test the predictability of the input state from the recurrent dynamics ($k = 0.021\mu\text{m}^{-1}$). Measured (dots) and retrieved (line) input field for different initial phases: (b) $\phi \simeq \pi$, (c) $\phi \simeq 0$ and (d) $\phi \simeq 0.3\pi$. Dashed lines indicates the uncertainty of the retrieved condition.

with a superposition of a large number of modes, random noise or localized perturbations, wave turbulence sets in [110, 179]. In these complex regimes, disordered nonlinear interactions may play a crucial role with respect to exact solutions of the underlying model [180]. Finally, we note that the observed recurrence gradually disappears as the external pump is weakened, a finding that further corroborates integrability as the basis of the phenomenon. The continuous transition towards the non-integrable regime is reported in Fig. 3.5. Pseudo-recurrent breather structures persist as the nonlinearity approaches the saturable regime and the model departs from the canonical NLSE [181] [Figs. 3.5(a,b)], whereas no return to the initial state occurs in highly-saturated, non-integrable conditions [Fig. 3.5(c)]. Here, interacting spatial solitons form and evolve towards equilibrium compatibly with a soliton turbulence scenario [182].

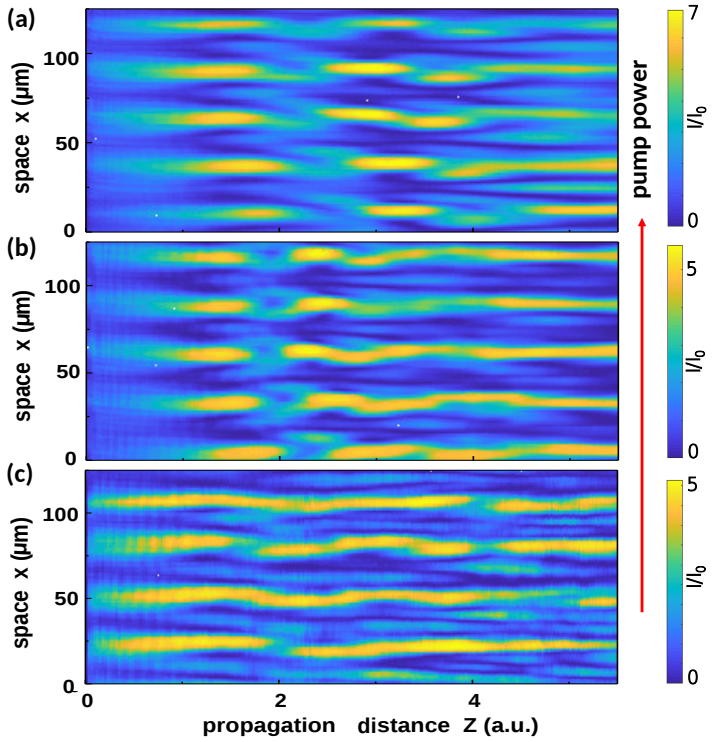

Figure 3.5: From the integrable to the non-integrable regime. Nonlinear evolution detected for $k = 0.021\mu m^{-1}$ and $A = 0.5$ varying the external pump power: (a) $P = 6$mW, (b)$P = 2$mW and (c) $P = 0.5$mW. The recurrent behavior in (a) is superseded by the appearance of spatial solitons (c) as the dynamics is far from integrability (highly-saturated conditions).

CONCLUSIONS

We have observed the FPUTR in nonlinear spatial optics providing an unprecedented experimental evidence of its underlying integrable dynamics. We reveal that the single-mode input field deterministically sets the properties of the recurrent behavior for several breathing cycles and in close agreement with the analytic NLSE theory. The dynamics is thus accurately predicted, a result that extends predictive approaches to unstable wave regimes and maps a strategy to achieve the control of localized large-amplitude waves in environmental conditions. The optical setting

we have introduced, in which the input condition can be in principle arbitrarily shaped, provides a general test-bed for investigating universal nonlinear phenomena. Our findings shed light on the foundations of the Fermi-Pasta-Ulam-Tsingou problem and represent a unique test for nonlinear wave theory.

4 TOPOLOGICAL CONTROL OF EXTREME WAVES

INTRODUCTION

As aforementioned, the NLSE [166] is a cornerstone of IST for detailing dispersive phenomena, as DSWs [48, 59, 67], RWs [159, 160, 183, 184] and shape invariant solitons [185–187]. DSWs regularize catastrophic discontinuities by mean of rapidly oscillations [13, 62, 66, 69, 188]. RWs are giant disturbances appearing and disappearing abruptly in a nearly constant background [154, 156, 157, 161, 163, 189–195]. Solitons are particle-like dispersion-free wave packets that can form complex interacting assemblies, ranging from crystals to gases [185, 186, 194, 196–198].

DSWs, RWs, and SG generation are related phenomena, and all appear in paradigmatic nonlinear evolutions, as the box problem for the focusing NLSE [110, 199–203]. However, for the box problem in the small-dispersion NLSE, IST becomes unfeasible. In this extreme regime, the problem can be tackled by the finite-gap approximation [200, 204]. It turns out that extreme waves are described in terms of one single mathematical entity, the Riemann theta function, and classified by a topological index, the genus g (see Fig. 4.1). In nonlinear wave theory, g represents the number of oscillating phases, and evolves during light propagation: "single phase" DSWs have $g = 1$, RWs have $g \sim 2$ and SGs have $g >> 2$. This creates a fascinating connection between extreme waves and topology. Indeed, the same genus g allows a topological classification of surfaces, to distinguish, for examples, a torus and sphere (Fig. 4.1). The question lies open if this elegant mathematical classification of extreme waves can inspire new applications. Can it modify the basic paradigm by which the asymptotic evolution of a wave is encoded in its initial shape, opening the way to controlling extreme waves, from lasers to earthquakes?

Here, inspired by the topological classification, we propose and demonstrate the use of topological indices to control the generation of extreme waves with varying genera g [201]. We consider the NLSE box problem where, according to recent theoretical results [200], light experiences various dynamic phases during propagation, distinguished by diverse genera. In particular, for high values of a nonlinearly-scaled propagation distance ζ, one has $g \sim \zeta$. By continuously varying ζ, we can change g and explore all the possible dynamic phases (see Fig. 4.1, where ζ is given in terms of the observation time t, detailed below). We experimentally

test this approach in photorefractive materials, giving evidence of an unprecedent control of nonlinear waves, which allows the first observation of the transition from focusing DSWs to RWs.

GENUS CHARACTERIZATION IN THE NLSE BOX PROBLEM

We consider the NLSE

$$\imath\epsilon\partial_\zeta\psi + \frac{\epsilon^2}{2}\partial_\xi^2\psi + |\psi|^2\psi = 0, \tag{4.1}$$

where $\psi = \psi(\xi,\zeta)$ is the normalized complex field envelope, ζ is the propagation coordinate, ξ is the transverse coordinate and $\epsilon > 0$ is the dispersion parameter. We take a rectangular barrier as initial condition

$$\psi(\xi,0) = \begin{cases} q & \text{for} |\xi| < l \\ 0 & \text{elsewhere} \end{cases}, \tag{4.2}$$

that is, a box of finite height $q > 0$, length $2l > 0$ and genus $g = 0$. In our work, we fix $q = l = 1$. Eq. (4.1) with (4.2) is known as the NLSE box problem, or the dam break problem, which exhibits some of the most interesting dynamic phases in nonlinear wave propagation [200, 205]. The initial evolution presents the formation of two wave trains counterpropagating that regularize the box discontinuities. These wave trains are single-phase DSWs ($g = 1$). Their two wavefronts superimpose in the central part of the box (see Fig. 4.1a) - occurring at $\zeta = \zeta_0 := \frac{l}{2\sqrt{2}q}$ - and generate a breather lattice of genus $g = 2$, a two-phase quasi-periodic wave resembling an ensemble of Akhmediev breathers [157, 159]. Since both $\xi-$ and $\zeta-$period increase with ζ, the oscillations at $\xi \simeq 0$ become locally approximated by Peregrine solitons [152, 159, 206, 207]. At long propagation distance $\zeta >> \zeta_0$, the wave train becomes multi-phase and generates a SG with $g \sim \zeta$.

In Figure 4.1a, we report the wave dynamics in physical units, as we make specific reference to our experimental realization of the NLSE box problem for spatial optical propagation in photorefractive media. In these materials, the optical nonlinearity is due to the time-dependent accumulation of free carriers that induces a time-varying low-frequency electric field. Through the electro-optical effect, the charge accumulation results into a time-varying nonlinearity, as shown in Sec. 3.3. The corresponding time-profile can be controlled by an external applied voltage and the intensity level [167–169]. These features enable to experimentally implement our topological control technique.

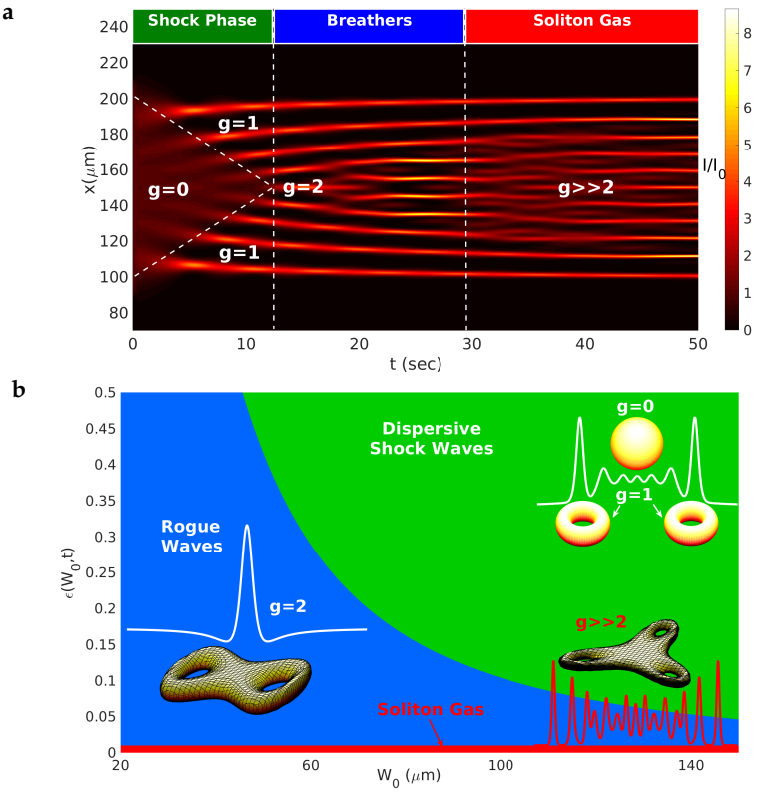

Figure 4.1: Topological classification of extreme waves. **a** Final states of the wave for a fixed initial waist diameter $W_0 = 100\mu m$ showing the generation of focusing dispersive shock waves ($g = 1$), RWs ($g \sim 2$) and a SG ($g >> 2$) after different time intervals in a photorefractive material. **b** Phase diagram reporting the final states in terms of the parameter ϵ and the initial beam waist diameter. Transitions occur by fixing waist diameter and varying ϵ or, equivalently, the observation time t. Different surfaces displayed in proximity of the various wave profiles, corresponding to the different regions in the phase diagram, outline the link between the topological classification of extreme waves in terms of the genus g and the topological classification of toroidal Riemann surfaces (for a sphere, $g = 0$, for a torus, $g = 1$, etc.).

In photorefractive media, Eq. (4.1) describes an optical beam with complex amplitude $A(z, x, t)$, intensity $I = |A|^2$, and initial condition

$$A(x,0) = \begin{cases} \sqrt{I_0} & \text{for} |x| \leq \frac{1}{2} W_0 \\ 0 & \text{elsewhere} \end{cases}, \tag{4.3}$$

through the transformation

$$\zeta = \frac{z}{\epsilon z_D}, \quad \xi = \frac{2x}{W_0}, \quad \psi = \frac{A}{\sqrt{I_0}}, \tag{4.4}$$

with W_0 the initial beam waist diameter along x-direction, $z_D = \frac{\pi n_0 W_0^2}{2\lambda}$ the diffraction length, $n = n_0 + \frac{2\delta n_0 I}{I_S} f(t)$ the refractive index, $\delta n_0 > 0$ the nonlinear coefficient, I_S the saturation intensity, I_0 the initial intensity. For photorefractive media

$$\epsilon = \frac{\lambda}{\pi W_0}\sqrt{\frac{I_S}{2n_0\delta n_0 I_0 f(t)}}, \tag{4.5}$$

namely, the dispersion is modulated by the time-dependent crystal response function $f(t) = 1 - \exp(-t/\tau)$, with the saturation time τ fixed by the input power and the applied voltage [10].

For a given propagation distance L (the length of the photorefractive crystal), the genus of the final state is determined by the detection time t, which determines ϵ, $\zeta = \frac{L}{\epsilon z_D}$, and g, correspondingly. The genus time-dependence is sketched in Fig. 4.1a. The output wave profile depends on its genus content, which varies with t.

Following the theoretical approach in [200], the two separatrix equations divide the evolution diagram in Fig. 4.1a in three different areas: the flat box plateau with genus $g = 0$, the lateral counterpropagating DSWs with genus $g = 1$, and the RWs after the DSW-collision point (corresponding to the separatrices intersection) with genus $g = 2$. The two separatrices (dashed lines in Fig. 4.1a) have equations

$$x = x_0 \pm \frac{W_0}{2t_0}(t - t_0) = x_0 \pm v(t - t_0), \tag{4.6}$$

with (t_0, x_0) the DSW-collision point, with $t_0 \simeq \frac{\tau I_s n_0 W_0^2}{64 I_0 \delta n_0 L^2}$ and x_0 given by the central position of the box. It turns out that the shock velocity is

$$v = \frac{W_0}{2t_0} = \frac{32\delta n_0 L^2}{I_s n_0 W_0^2 U_0 \tau} P, \tag{4.7}$$

proportional to the input power, as experimentally demonstrated below (Fig. 4.3b, other parameters are detailed below).

Eqs. (4.6) express the genus time-dependence for its first three values $g = 0, 1, 2$. It allows designing the waveshape, before the experiment, by associating a specific combination of the topological indices, and to predict the detection time corresponding to the target topology. In other words, by properly choosing the experimental conditions, we can manage

to predict the occurrence of a given extreme wave by using the expected genus g. According to Eq. (4.5), we use time t and initial waist diameter W_0 to vary ϵ. The accessible states are outlined in the phase diagram in Fig. 4.1b, in terms of ϵ and W_0. Choosing $W_0 = 100\mu m$ as in Fig. 4.1a, by varying t one switches from DSWs to RWs, and then to SGs.

We solve numerically Eq. (4.1) by a one-parameter-depending Beam Propagation Method (BPM) with a symmetrized split-step in the code core [208]. We use a high-order super-Gaussian initial condition

$$\psi(\xi, \zeta = 0) = q \exp\left\{-\frac{1}{2}\left(\frac{\xi}{l}\right)^{24}\right\}. \tag{4.8}$$

For each temporal value, Eq. (4.1) solutions have different dispersion parameter ϵ and final value of ζ, because from Eqs. (4.4) it reads $\zeta_{fin} = \frac{4L}{\epsilon(t)kW0^2}$, where L is the crystal length. In Figs. 4.2,4.4, we show the numerical results. The propagation in time considers $\psi(\xi, \zeta_{fin})$, which corresponds to detections at end of the crystal.

SUPERVISED TRANSITION FROM SHOCK TO ROGUE WAVES

The case $W_0 = 140\mu m$ is illustrated in Fig. 4.2 by numerical simulations (the corresponding experimental results are in Fig. 4.3). The two focusing DSWs and the SG are visible at the beginning and at the end of temporal evolution, respectively (see phase-diagram in Fig. 4.1b). As soon as an initial super-Gaussian wave (Fig. 4.2b) starts to propagate, two DSWs appear on the beam borders (Fig. 4.2c) and propagate towards the beam central part (Fig. 4.2d). When the DSWs superimpose, Akhmediev breathers are generated (Fig. 4.2e). From the analytical NLSE solutions for the focusing dam break problem [200], we see that Akhmediev breathers have ξ-period increasing with ζ. Moreover, one finds that $\partial_t \zeta > 0$, therefore the period in the x-direction must increase with time, and central peaks appear upon evolution. These peaks are well approximated by Peregrine solitons, for large t, as confirmed by Figs. 4.2f,g.

Figure 4.3 shows the experimental observation of the controlled dynamics simulated in Fig. 4.2. Figure 4.3a sketches the experimental setup. A y-polarized optical beam at wavelength $\lambda = 532$nm from a continuous 80mW Nd:YAG laser source is focused by a cylindrical lens down to a quasi-one-dimensional beam with waist diameter $U_0 = 15\mu$m along the y-direction. The initial box shape is obtained by a mask of tunable width, placed in proximity of the input face of the photorefractive crystal. A sketch of the optical system is shown in Fig. 4.3a. The beam is launched into an optical quality specimen of $2.1^{(x)} \times 1.9^{(y)} \times 2.5^{(z)} mm$ KLTN with

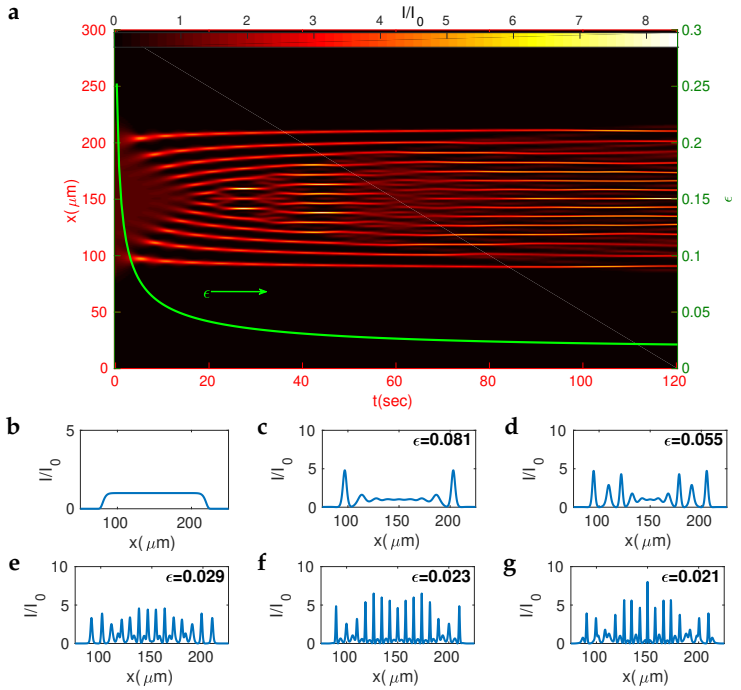

Figure 4.2: Controlling the extreme wave genus. **a** Numerical simulation of the control of the final state after a propagation distance $L = 2.5mm$ for an initial beam waist diameter $W_0 = 140\mu m$ ($I_0 = \frac{P}{U_0 W_0} = 0.38 \times 10^5 W/m^2$). Axis x represents the beam transverse direction, axis t the time of output detection. **b** Initial beam intensity: a super-Gaussian wave centered at $x = 150\mu m$ of height I_0 and width W_0. **c-d** Focusing dispersive shock waves occurrence: (**c**) represents the beam intensity at $t = 5s$, when the wave breaking has just occurred, so two lateral intense wave trains regularize the box discontinuity and start to travel towards the beam central part; (**d**) the beam intensity at $t = 11s$, which exhibits the two counterpropagating DSWs reaching the center $x = 150\mu m$. **e-g** Akhmediev breathers and Peregrine solitons generation: beam intensity at (**e**) $t = 49s$, (**f**) $t = 98s$, and (**g**) $t = 120s$, after the two dispersive shock waves superposition and the formation of Akhmediev breathers with period increasing with t. Since a Peregrine soliton is an Akhmediev breather with an infinite period, increasing t is tantamount to generating central intensity peaks, locally described by Peregrine solitons.

Cu and V impurities ($n_0 = 2.3$). The crystal exhibits a ferroelectric phase

transition at the Curie temperature $T_C = 284$K. Nonlinear light dynamics are studied in the paraelectric phase at $T = T_C + 8$K, a condition ensuring a large nonlinear response and a negligible effect of small-scale disorder [173]. The time-dependent photorefractive response sets in when an external bias field E is applied along y (voltage $V = 500$V). To have a so-called Kerr-like (cubic) nonlinearity from the photorefractive effect, the crystal is continuously pumped with an x-polarized 15mW laser beam at $\lambda = 633$nm. The pump does not interact with the principal beam propagating along the z axis and only constitutes the saturation intensity I_S. The spatial intensity distribution is measured at the crystal output as a function of the exposure time t by means of a high-resolution imaging system composed of an objective lens ($NA = 0.5$) and a CCD camera at 15Hz. In the present case, evolution is studied at a fixed value of z (the crystal output) by varying the exposure time t. In fact, the average index change grows and saturates according to a time dependence well defined by the saturation time $\tau \sim 100$s once the input beam intensity, applied voltage, and temperature have been fixed [see Secs. 3.3,3.5].

The observation for $W_0 = 140\mu m$ is reported in Fig. 4.3c. We observe an initial DSW phase that undergoes into a train of large amplitude waves. In this regime, we identify breather-like structure (Akhmediev breathers, inset in Fig. 4.3c) that evolves into a SG at large propagation time. The DSW phase is investigated varying the input power. We find a linear increasing behavior of the shock velocity when increasing the power (Fig. 4.3b), as predicted by Eq. (4.7). The shock velocity is proportional to the distance between the two counterpropagating DSWs at a fixed time. We measured the width Δx of the plateau at time $\bar{t} \sim 30s$. Referring to Eq. (4.7), we obtain the normalized velocity $\bar{v} = v/v_0$, with $v_0 = L/\bar{t}$.

PEREGRINE SOLITON EMERGENCE

Figure 4.4 illustrates the numerically determined dynamics at smaller values of the beam waist diameter ($W_0 = 10\mu m$), a regime in which the generation of single Peregrine solitons is evident. The intensity profile is reported in Fig. 4.4a. As shown in Fig. 4.1b, one needs to carefully choose W_0 for observing a RWs generation without the DSWs occurrence. For $W_0 = 10\mu m$, the super-Gaussian wave (Fig. 4.4b) generates a Peregrine soliton (Fig. 4.4c-e). The following dynamics shows the higher-order Peregrine soliton emergence (Figs. 4.4f,g), each order with a higher genus.

Figures 4.5a-g report the experimental results for the case $W_0 = 30\mu m$. Observations of the Peregrine-like soliton generation are shown, both in intensity (Figs. 4.5a-d) and in phase (Figs. 4.5e-g). For a small initial waist diameter, a localized wave, well described by the Peregrine soliton

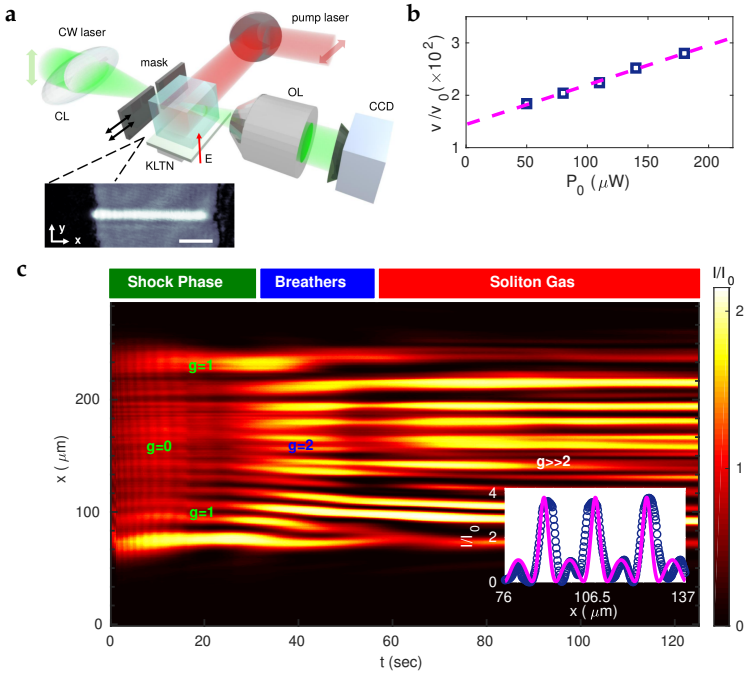

Figure 4.3: Experimental demonstration of the extreme wave genus control. **a** Experimental setup. A CW-laser beam is made a quasi-one-dimensional wave by a cylindrical lens (CL), then a tunable mask shapes it as a box. Light propagates in a pumped photorefractive KLTN crystal, it is collected by a microscope objective and the optical intensity is detected by a CCD camera. The inset shows an example of the detected input intensity distribution (scale bar is $50\mu m$). **b** Normalized shock velocity $[v_0 = L/\bar{t},\ L = 2.5mm,\ \bar{t} = (30 \pm 2)s]$, measured through the width of the oscillation tail at fixed time, versus input power. The blue squares are the experimental data, while the dashed pink line is the linear fit. **c** Experimental observation of optical intensity I/I_0 for an initial beam waist diameter $W_0 = 140\mu m$. Axis x represents the beam profile, transverse to propagation, collected by the CCD camera, while axis t is time of CCD detection. Output presents a first dispersive-shock-wave phase, a transition to a phase presenting Akhmediev breather structures and, at long times, a generation of a SG. The inset is an exemplary wave intensity profile detected at $t = 63s$ (dotted blue line), along with the theoretical Akhmediev breather profile.

(Figs. 4.5b,d), forms and recurs without a visible wave breaking. This dynamics is in close agreement with simulations in Figs. 4.4d-g, where

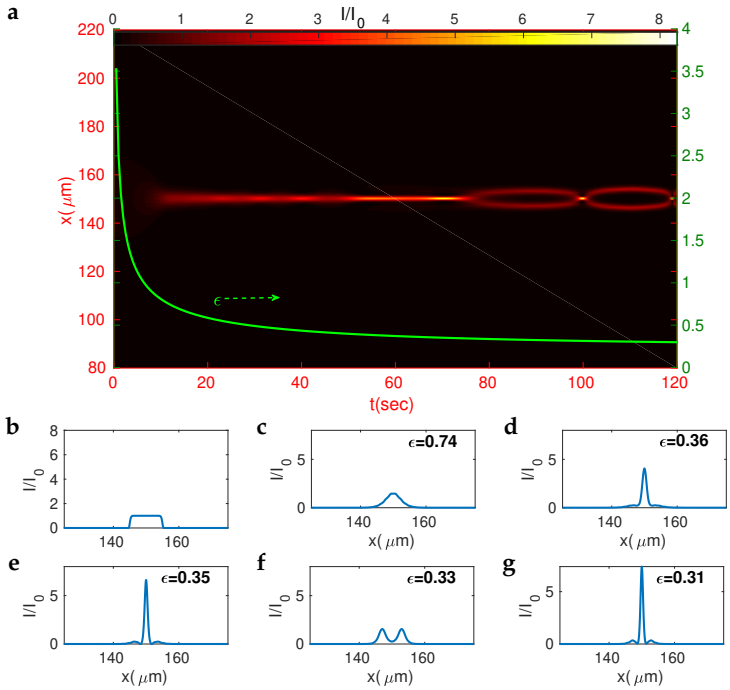

Figure 4.4: Simulation of the topological control for a small waist. **a** Numerical simulation of the control of the final state after a propagation distance $L = 2.5mm$ for an initial beam waist diameter $W_0 = 10\mu m$ ($I_0 = \frac{P}{U_0 W_0} = 5.33 \times 10^5 W/m^2$). Axis t expresses time of detection, while x is the beam transverse coordinate. **b** Initial beam intensity: a super-Gaussian wave centered at $x = 150\mu m$. **c-e** Peregrine soliton generation: beam intensity (**c**) at $t = 12s$, and (**d**) at $t = 64s$, during the formation of the Peregrine soliton, while (**e**) exhibits the Peregrine soliton profile at $t = 70s$. **f-g** Higher-order Peregrine soliton generation: beam intensity at (**f**) $t = 85s$, and (**g**) $t = 100s$, where the Peregrine soliton is alternately destroyed and reformed.

the Peregrine soliton is repeatedly destroyed and generated, each time at a higher order. Phase measurements are illustrated in Figs. 4.5e-g. Each Peregrine soliton has two phase signatures: a longitudinal smooth phase shift of 2π and a transversal rectangular phase shift profile, with height π and basis as wide as the Peregrine soliton width [206, 207]. Such signatures are here both experimentally demonstrated. From Fig. 4.5e, which shows interference pattern during the first Peregrine

soliton occurrence, we obtain the longitudinal phase shift behavior in Fig. 4.5g, by a cosinusoidal fitting along the central propagation outline. Fig. 4.5f reports the experimental transversal phase shift profile along x. A comparison with the measured interference fringes is also illustrated in the inset, which directly shows the phase jump (topological defect). Stressing the significance of these results is very important, because they are a proof of the topological control: the genus is determined by the input waist and time of detection. Indeed, the longitudinal phase shift represents the transition from genus 0 to genus 2, whereas the transversal Peregrine soliton phase shift outline unveils the value $g = 2$, equal to the number of phase jumps (first from 0 to π, then again from π to 0). This is summarized in Fig. 4.5h, which sketches numerical simulations of phase behavior at $W_0 = 10\mu m$, normalized in $[-\pi, \pi]$. Fig. 4.5h gives a picture of genera changes, Peregrine soliton occurrence and phase discontinuities. The genus is zero and the phase profile is flat until the first Peregrine soliton occurrences. After that, the phase value changes and the phase transverse profile presents two jumps of π.

MODULATION INSTABILITY AND LOSSES

We perform experiments - and validate them by numerical simulations - to prove that our results are genuinely caused by a NLSE box evolution, and they are not due to MI arising from noise in the central part of the box. Figure 4.6 reports the outcomes. MI generates transversal periodic waves; DSWs occur in strongly nonlinear regimes and present fast non-periodic oscillation. Figs. 4.6a-d show the different behaviors of such phenomena, occurring on two distinct spatial scales in our experiments. It turns out that MI from spontaneous noise affects light propagation only for very large beam waists, much larger than the ones previously analyzed, because the period of generated waves is comparable to the waist diameter corresponding to Fig. 4.6d. Fig. 4.6e illustrates the experimental gain related to Fig. 4.6a at $\bar{t} = (30 \pm 2)s$, computed through the expression [187]

$$G(k_x) = \frac{1}{L} \log \left[\frac{\hat{A}(k_x, z = L)}{\hat{A}(k_x, z = 0)} \right], \tag{4.9}$$

with $L = 2.5mm$ the propagation distance, $\hat{A}$ the FT of the field envelope and k_x the spatial momentum. A possible waist diameter threshold value, which separates the nonlinear and the MI dynamics, is also established by the the comparison of the spectral weights in Fig. 4.6f. Spectral weights are computed as maximum absolute values of $\hat{A}$ field for the DSW and

MI momenta, and they indicate a change of dominating effect around $W_0 \sim 150\mu m$. This is also proved numerically in Figs. 4.7a-e: above $W_0 \sim 150\mu m$ [Figs. 4.6a-d] MI alters significantly light propagation, while below, in Fig. 4.6e [corresponding to Fig. 4.2a, but with initial perturbative noise], we cannot appreciate any modification of nonlinear dynamics.

Another effect that could modify the nonlinear dynamics is the presence of loss, as shown in [206], where the dissipation significantly affects the local genus of the breather structure. Adding losses to Eq. (3.6), we obtain

$$\imath\partial_z A + \frac{1}{2k}\nabla^2 A + \frac{k}{n_0}\delta n(I)A = -\imath\frac{\alpha}{2}A. \tag{4.10}$$

The KLTN photorefractive crystal is transparent above $\lambda = 380nm$, and the copper doping introduces a small absorption from $\lambda = 550nm$ to $\lambda = 800nm$, where the value of the absorption coefficient α is approximately $\alpha = 2cm^{-1}$. It turns out that losses need a propagation length $L_{loss} = \alpha^{-1}$ to be effective for the pump laser beam ($\lambda = 633nm$), that is, one order of magnitude higher than the crystal length L, while the reference laser beam, generating the box, propagates without losses ($\lambda = 532nm$).

ROGUE WAVES AND SOLITON GASES STATISTICAL ANALYSIS

RWs are waves of unusually high intensity $|\psi_{RW}|^2$, whose Probability Density Function (PDF) does not decay exponentially (linearly on the semilogarithmic scale used in Figures 4.7f-i), but presents a tail at highest intensity values [192].

The statistical properties of the intensities illustrated in Figs. 4.7f,g confirm the occurrence of RWs in the small box regime, both with initial noise [Fig. 4.7f] and without [Fig. 4.7g]. The latter case is widely treated in this Chapter, where the emergence of Peregrine solitons is proved, and the agreement with analytical Peregrine soliton profile is demonstrated both in intensity and in phase outlines. The question regarding the deterministic nature of models generating Peregrine solitons, as the focusing NLSE with initial rectangular conditions, and so the fact that the Peregrine soliton emergence is wholly predictable and does not exhibit a statistical rarity, makes the debate on considering Peregrine solitons RW prototype still open. Another conventional criterion for RWs is $|\psi_{MAX}|^2 > 8|\psi_{BG}|^2$, with $|\psi_{MAX}|^2$ the intensity peak and $|\psi_{BG}|^2$ the background intensity [200]. Figs. 4.4,4.5 prove that the Peregrine solitons generated in simulations and experiments fulfill this requirement.

The same analysis can be done for the Akhmediev breathers generation, shown in Figs. 4.2,4.3, whose intensity PDF are reported in Figs. 4.7h,i.

Last point we want to discuss is about the formation of SGs in the long-term propagation reported in Figs. 1a, 4.2a,4.3c. Solitons are propagation-invariant waves with particle-like interactions. This means that, when many solitons form a disordered finite-density ensemble rather than a well-ordered modulated soliton lattice, they resemble a gas of particles. The definition of SG has required a huge effort from scientific community to be established. G. A. El *et al.* in 2005 derived the kinetic equations for SGs in physical systems described by integrable nonlinear wave equations [197].

About the box problem and its evolution in terms of genera, the leading theoretical paper is [200], and an introductory part of the related analysis is reported in the very first paragraphs. In [200], the authors associate the long-time asymptotic solution ψ with a "breather gas" and numerically observe the presence of higher-order RWs with maximum height $4 < |\psi_{MAX}| < 5$ in the regions with $g \geq 4$. Their numerical simulations suggest that the pattern of the $\xi - \zeta$ plane (splitting into the regions of different genera) persists as ζ increases, and therefore $g \sim \zeta$ asymptotically.

In 2018, A. A. Gelash *et al.* studied a statistically homogeneous SG with essential interaction between the solitons [194]. The model used by the authors is a focusing NLSE, and they generated ensembles of $N-$soliton solutions ($N \sim 100$) by using the Zakharov-Mikhailov variant of the dressing method. Through such a mathematical description, it was demonstrated that spontaneous noise-induced MI of a plane wave generates SGs [195].

In the KdVE theory, the thermodynamic type infinite-genus limit of finite-band potentials leads to the kinetic description of a SG [197]. Very recently, I. Redor *et al.* showed that it is possible to produce in a laboratory a SG described in statistical terms by integrable turbulence in hydrodynamics [198]. In optics, the focusing NLSE counterpart of this theory would include the breather gas description, yet to be developed, providing insights on NLSE turbulence, which is subject of active research [110].

CONCLUSIONS

The topological classification by the genus of the Riemann theta function opens a new route to experimentally control the generation of extreme waves. We demonstrated the topological control for the focusing box problem in optical propagation in photorefractive media. By using the time-dependent photorefractive nonlinearity, we were able to change the final state of the wave evolution in a predetermined way and explore all the possible dynamic phases. This enables the first observation of the transitions from shock to RWs. This also demonstrates that different extreme wave phenomena are deeply linked and that proper tuning of their topological content in the nonlinear evolution enables transformations from one state to another.

These results are general, and not limited to the photorefractive media.

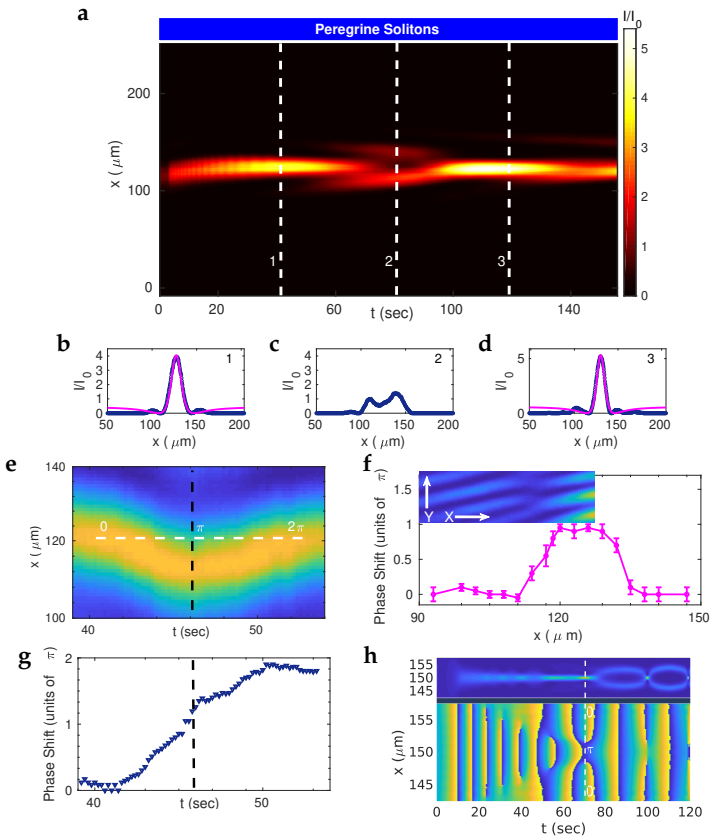

Figure 4.5: Experimental topological control for a small waist. **a** Observation of optical intensity I/I_0 for an initial beam waist diameter $W_0 = 30\mu m$. Axis t is time of output detection, x is the transverse direction. In this regime, we observe Peregrine-soliton-like structures formation (see Fig. 4.1b) [the colored scale goes from 0 (dark blue) to 5 (bright yellow)]. **c-d** Intensity outlines corresponding to numbered dashed lines in (**a**): the blue lines are experimental waveforms, the pink continuous lines are fitting functions according to the analytical Peregrine soliton profile. **e-h** Phase measurements (**e-g**) and simulations (**h**) of the Peregrine soliton. The detected interference pattern during the first Peregrine soliton generation is reported in (**e**), corresponding to (**b**). The jump from 0 to 2π along the white dashed line corresponds to the transition from $g = 0$ to $g = 2$. The black dashed line highlights the jump, shown in (**g**). The experimental transversal phase shift profile along x is reported in (**f**), showing the expected π shift corresponding to (**b**). Error bars represent standard deviation. The inset shows the corresponding area of the measured interference fringes on the transverse plane. Phase simulations at $W_0 = 10\mu m$ are reported in the bottom panel in (**h**) [the colored scale goes from $-\pi$ (bright yellow) to π (dark blue)(0 is green)]. Top panel sketches Fig. 4.4a, for at-a-glance correspondence between genera changes, Peregrine soliton occurrence and phase discontinuities.

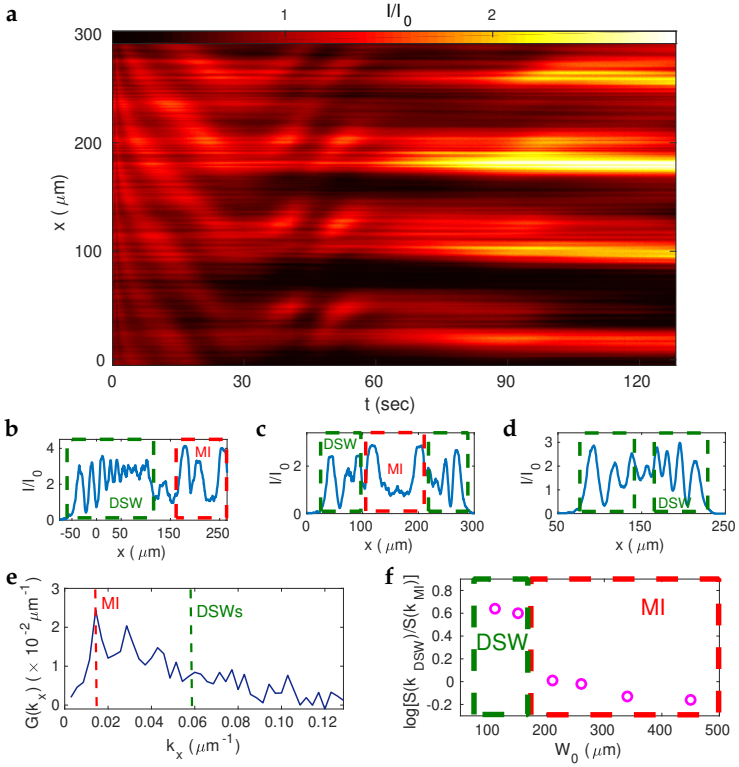

Figure 4.6: Experiments at large beam waists and modulation instability. **a** Observation of normalized optical intensity for an initial box-shaped beam propagation in KLTN photorefractive crystal, with a waist as large as the transverse crystal length (2.1mm). Axis t is time of output detection, x is the transverse direction. In this regime, MI dominates light propagation. **b-d** Observations of normalized optical intensity for initial box-shaped beams of waists (**b**) $W_0 = 450\mu m$, (**c**) $W_0 = 260\mu m$ and (**d**) $W_0 = 150\mu m$ at fixed time $\bar{t} = (30 \pm 2)s$. If MI from intrinsic noise generates periodic waves between the two DSWs in (**b**,**c**), with a period larger than the DSWs oscillation length, (**d**) represents a waist diameter threshold value, below which MI does not affect the dynamics. **e** Experimental gain [see Eq. (4.9)] for the initial infinite box-shaped beam versus spatial momentum, at time $\bar{t} = (30 \pm 2)s$. **f** Logarithm of the ratio between the two spectral weights, namely, the maximum absolute values of the FT of the optical field for the DSW and MI momenta. It highlights two beam waist intervals: the one below $150\mu m$, where MI does not affect light propagation, and the one above $150\mu m$, where MI dominates the dynamics.

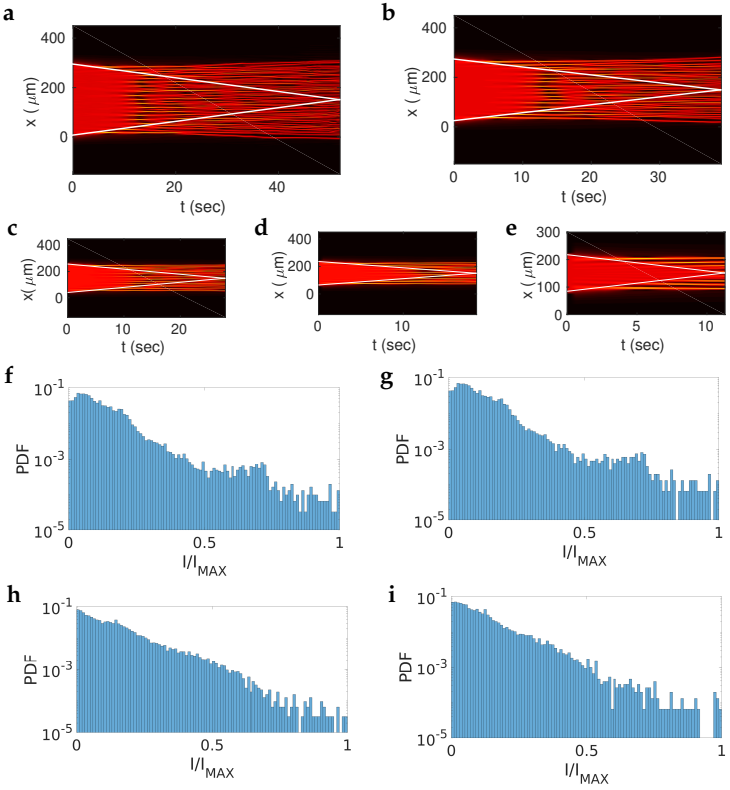

Figure 4.7: Modulation instability and rogue waves emergence. **a-e** Numerical simulations of the final states after a propagation distance $L = 2.5mm$ for beam waists (**a**) $W_0 = 300\mu m$, (**b**) $W_0 = 260\mu m$, (**c**) $W_0 = 220\mu m$, (**d**) $W_0 = 180\mu m$ and (**e**) $W_0 = 140\mu m$. Axis t expresses time of detection, while x is the beam transverse coordinate. The initial conditions are box-shaped beams with small-amplitude pertubations, implemented as Gaussian random noise. White lines represent the shock separatrices. MI generates periodic waves between the two DSWs in (**a-d**), but does not affect the dynamics in (**e**). **f-i** Probability density functions of the optical intensity I/I_{MAX} over a two-dimensional spatio-temporal computational window, centered at $x = 150\mu m$, for $t \in [0s, 60s]$, and I_{MAX} the peak intensity (semilogarithmic scale). Initial conditions are: (**a**,**b**) $W_0 = 20\mu m$ (small-waist regime) with and without random noise, respectively; (**c**,**d**) $W_0 = 100\mu m$ (large-waist regime) with and without random noise, respectively. All the configurations present a significant deviation from the exponential distribution, signature of presence of RWs.

Part III

COMPLEXITY IN QUANTUM NONLINEAR OPTICS

Outline of Part iii

This Part deals with the description of complex nonlinear regimes at a quantum level.

- Chapter 5 introduces the positive $\mathcal{P}$representation that maps the second quantized nonlinear Schrödinger equation to a system of stochastic differential equations.
- Chapter 6 studies the quantum effects on single solitons propagation. In particular, we study the quantum diffusion and its control.
- Chapter 7 describes quantum rogue waves. Specifically, it illustrates the effects of quantum noise on the quantum rogue wave generation.

Synopsis

Part ii presents our most important results on classical nonlinear waves in nonlinear optics, laying the groundwork for establishing one uniform theory of dispersive shock waves, and for controlling complex nonlinear regimes.

Here, we move to the study of quantum solutions of the nonlinear Schrödinger equation through a second quantized field theory of optical propagation in nonlinear dispersive media. The resulting equivalence between the quantum nonlinear Schrödinger equation and a system of two coupled stochastic nonlinear Schrödinger equations, obtained through space-space methods, allows numerical simulations of the quantum solitons and the quantum nonlinear box problem, with the analysis of quantum noise effect on recurrence.

We believe that this treatise can open the way to the design of new quantum sources and non-classical state generators for future quantum technologies, and also that the analysis of the evolution of quantum noise in nonlinear media can give incredible insights about all-optical reservoir computing.

5 QUANTUM THEORY OF NONLINEAR WAVES IN FIBERS

INTRODUCTION

Classical NLO studies the response of dielectric media to strong optical fields, sufficiently strong that the response is, as its name implies, nonlinear. This finds representation in the polarization, that is, the dipole moment per unit volume in the medium, which is not a linear function of the applied electric field. In Sec. 2.2, Eq. 2.3 shows that $\boldsymbol{P}(\boldsymbol{R},t) = \boldsymbol{P}^{(L)}(\boldsymbol{R},t) + \boldsymbol{P}^{(NL)}(\boldsymbol{R},t)$, with $\boldsymbol{P}^{(L)}(\boldsymbol{R},t) = \epsilon_0 \int_{-\infty}^{t} \mathrm{d}t_1 \tilde{\chi}^{(1)}(t-t_1)\boldsymbol{E}(\boldsymbol{R},t_1)$ and, for a third-order centrosymmetric medium, $\boldsymbol{P}^{(NL)}(\boldsymbol{R},t) = \epsilon_0 \int\int\int_{-\infty}^{t} \mathrm{d}t_1 \mathrm{d}t_2 \mathrm{d}t_3 \, \tilde{\chi}^{(3)}(t-t_1, t-t_2, t-t_3) \cdot \boldsymbol{E}^{\otimes 3}(\boldsymbol{R},t_1,t_2,t_3)$. A possible consequence of such a polarization nonlinear term, as previously deeply analyzed in nonlocal case (Sec. 2.2), is a no more constant refractive index, but depending on light intensity. Therefore, a beam with a non-uniform intensity profile can experience self-focusing or self-defocusing. However, when this behavior, here described by classical electromagnetic fields, is described by quantized fields, a number of new effects emerge [209–211].

Quantized fields are necessary, for example, if we want to model fields that originate from spontaneous emission [212]. Nevertheless, the quantization of electrodynamics in nonlinear dielectrics is not straightforward, and two approaches are possible: quantization from the macroscopic theory, that is, quantization of Maxwell's equations, and a microscopic treatise, that is, quantizing the entire matter-field system. In the first case the goal is to obtain a quantized theory where the Heisenberg equations of motion are the Maxwell's equations, so the medium properties are described by its polarizabilities. In the second approach, an effective Hamiltonian describes the behavior of the fields in the medium, i.e., the matter degrees of freedom are explicitly included in the theory [213]. Quantum electromagnetic field theory is a huge subject, here the discussion is limited to what is needed.

We report an exact quantum theory of pulses propagation in dispersive nonlinear fibers by a canonical quantization approach from Maxwell's equations [214]. The arena where the action takes place is a many-particle Hilbert space. Once obtained the Hamiltonian in the Schrödinger picture, we consider the related Von Neumann (or Quantum Liouville) Equation

(NE) for the density matrix in interaction picture. The quantum theoretical treatise is simplified by the choice of the positive-$\mathcal{P}$ representation to describe the propagated field [215], which leads to a Fokker-Planck Equation (FPE) with positive-semidefinite diffusion coefficients to be constructed over a space with twice the dimensions of the many-particle Hilbert space. Then an Itô stochastic differential equation system can be formulated in a nonclassical phase space. Specifically, we obtain a system of two coupled SNLSEs, with stochastic terms given by independent multiplicative white noises [213, 216]. The further numerical analysis can be performed by a stochastic Heun algorithm (equivalent to a Runge-Kutta of order 1.5) [217].

A parallel approach, instead of starting from first principles (i.e., the Maxwell's equations), quantizes directly the NLSE from its version describing propagation in fibers in Paraxial and Slowly Varying Envelope Approximation (P-SVEA). The result, that is, the QNLSE, is the Schrödinger equation corresponding to the same Hamiltonian that rules the SNLSEs system [218, 219].

Once given the theoretical foundations of light propagation in fibers at a quantum regime (i.e., at low photon number), the next Chapters will present three paradigmatic applications of such a treatise.

THE STOCHASTIC NONLINEAR SCHRÖDINGER EQUATION

Let us start again from the relation between the macroscopic interacting electric field and the induced polarization, now considering only the transverse components:

$$\boldsymbol{P}_T = \sum_n \boldsymbol{P}^{(n)} = \epsilon_0 \left[\chi^{(1)} \boldsymbol{E}_T + \boldsymbol{\chi}^{(2)} \cdot \boldsymbol{E}_T^{\otimes 2} + \boldsymbol{\chi}^{(3)} \cdot \boldsymbol{E}_T^{\otimes 3} + \dots \right], \tag{5.1}$$

with the frequency dependence omitted for the sake of simplicity. The classical electrical-field energy density for a dielectric is

$$H_E = \int_0^D \boldsymbol{E} \cdot \mathrm{d}\boldsymbol{D}, \text{with} \boldsymbol{D} = \epsilon \boldsymbol{E}_T + \sum_{n>1} \boldsymbol{P}^{(n)}, \tag{5.2}$$

from which, by integrating, one obtains the total energy

$$\begin{aligned} H &= \int_V \left[\tfrac{1}{2} \boldsymbol{E}_T \cdot (\epsilon \boldsymbol{E}_T) + \textstyle\sum_{n>1} \left(\frac{n}{n+1} \right) \boldsymbol{E}_T \cdot \boldsymbol{P}^{(n)} + \frac{1}{2\mu} \boldsymbol{B}^2 \right] \mathrm{d}\boldsymbol{x} \\ &= \int_V \left\{ \tfrac{1}{2\epsilon} \left[\boldsymbol{D}^2 - \left(\textstyle\sum_{n>1} \boldsymbol{P}^{(n)} \right)^2 \right] - \textstyle\sum_{n>1} \left(\frac{1}{n+1} \right) \boldsymbol{E}_T \cdot \boldsymbol{P}^{(n)} + \frac{1}{2\mu} \boldsymbol{B}^2 \right\} \mathrm{d}\boldsymbol{x}, \end{aligned} \tag{5.3}$$

where $\epsilon = \epsilon_0 \left(1 + \chi^{(1)}\right)$ is the frequency-dependent dielectric tensor (here reduced to a scalar for anisotropy), μ is the magnetic permeability and $\boldsymbol{B}$ is the magnetic induction field. The canonical quantization requires the knowledge of the momenta, not specified by previous arguments. Keeping in mind the free Maxwell's equations for the vector potential $\mathcal{A}$ (i.e., $\boldsymbol{B} = \nabla \times \mathcal{A}$), the Lagrangian density is [220]

$$L_0\left(\mathcal{A}, \dot{\mathcal{A}}\right) = \frac{\epsilon}{2}\boldsymbol{E}^2 - \frac{1}{2\mu}\boldsymbol{B}^2, \tag{5.4}$$

where $\dot{\mathcal{A}} = \frac{\mathrm{d}}{\mathrm{d}t}\mathcal{A}$ (the previous symbol ∂_t represents the partial temporal derivative, not the total one as this expressed by the dot). When we consider a non-trivial radiation-matter interaction, the field equation for $\mathcal{A}$ the Coulomb gauge transverse vector potential reads

$$\left(\nabla^2 - \frac{1}{c^2}\partial_t^2\right)\mathcal{A} = -\mu\dot{\boldsymbol{P}}_T, \tag{5.5}$$

and it is equivalent to the system of Euler-Lagrange equations

$$\frac{\partial L\left(\mathcal{A}, \dot{\mathcal{A}}\right)}{\partial \mathcal{A}_j} = \partial_t\left[\frac{\partial L\left(\mathcal{A}, \dot{\mathcal{A}}\right)}{\partial \dot{\mathcal{A}}_j}\right] \tag{5.6}$$

when the Lagrangian density is

$$L\left(\mathcal{A}, \dot{\mathcal{A}}\right) = U\left(\dot{\mathcal{A}}\right) - \frac{1}{2\mu}\sum_j \left(\partial_{x_j}\mathcal{A}\right)^2 \tag{5.7}$$

with (directly derived from last equations, once noted that $\boldsymbol{E}_T = -\dot{\mathcal{A}}$)

$$U\left(\dot{\mathcal{A}}\right) = \int_0^D \boldsymbol{D} \cdot \mathrm{d}\boldsymbol{E}_T = \boldsymbol{E}_T \cdot \boldsymbol{D} - H_E. \tag{5.8}$$

The resulting canonical momentum $\boldsymbol{\Pi}$ has components

$$\Pi_j = \frac{\partial L\left(\mathcal{A}, \dot{\mathcal{A}}\right)}{\partial \dot{\mathcal{A}}_j} = -D_j, \tag{5.9}$$

hence, $\boldsymbol{\Pi} = -\boldsymbol{D}$ and after a Legendre transformation, the resulting Hamiltonian corresponds to Eq. (5.3). We proceed in quantizing by promoting to operators $\hat{\mathcal{A}}$ and $\hat{\boldsymbol{D}}$ with commutation relations

$$\left[\hat{\boldsymbol{D}}_j(\boldsymbol{x}), \hat{\mathcal{A}}_k(\boldsymbol{x}')\right] = \imath\delta_{j,k}\delta(\boldsymbol{x} - \boldsymbol{x}'), \tag{5.10}$$

where $\delta_{j,k}$ is the Kronecker delta, and $\delta(\boldsymbol{x} - \boldsymbol{x}')$ is the Dirac delta function.

Classically, propagation in a third-order-nonlinear fiber for a complex envelope $A(z,T)$, where $\boldsymbol{E}_T = \Re\left\{A(z,T)e^{\imath[\beta(\omega_0)z-\omega_0 T]}\right\}\boldsymbol{E}_0$ and $\beta(\omega) = \frac{\omega}{c}\sqrt{\frac{\epsilon(\omega)}{\epsilon_0}} \simeq \frac{n(\omega)\omega}{c}$ (in case of negligible losses) is ruled by the equation

$$\partial_z A + \beta_1 \partial_T A + \frac{\imath\beta_2}{2}\partial_T^2 A - \imath\frac{\omega_0 n_2}{cA_{eff}}A|A|^2 = 0, \tag{5.11}$$

where $\beta_m = \partial_\omega^m \beta|_{\omega=\omega_0}$, n_2 is the nonlinear Kerr coefficient and A_{eff} is the effective mode area [31] ($A_{eff} = \pi W_0^2$ for a Gaussian distribution). Specifically, $\beta_1 = v_g^{-1}$, with v_g group velocity, and β_2 is the Group Velocity Dispersion (GVD). By defining the coordinates $s = z$ and $\tau = T - \beta_1 z$, one obtains the NLSE

$$\imath\partial_s A - \frac{\beta_2}{2}\partial_\tau^2 A + \frac{\omega_0 n_2}{cA_{eff}}A|A|^2 = 0. \tag{5.12}$$

The complex envelope A is such that $|A(s,\tau)|^2 = P$, with P the power. It turns out the following relation for total energy:

$$N_{ph}\hbar\omega_0 = \int |A(s,\tau)|^2 \mathrm{d}\tau, \tag{5.13}$$

where N_{ph} is the number of photons.

From all the previous arguments, in the corresponding quantum case, the suitable Hamiltonian can be chosen as the one ruling the usual model of linearly polarized waves in the lowest-order propagating transverse mode with a four-wave mixing (quartic nonlinearity) inside a volume V, including dispersion and neglecting terms $O\left(\hat{\boldsymbol{E}}_T^6\right)$ [214]:

$$\hat{H} = \sum_n \hbar\omega_n \hat{a}_n^\dagger \hat{a}_n - \frac{\epsilon_0 \boldsymbol{\chi}^{(3)}}{4\epsilon^4} \cdot \int_V \left[\hat{\boldsymbol{D}}(\boldsymbol{x})\right]^{\otimes 3} \cdot \hat{\boldsymbol{D}}(\boldsymbol{x})\mathrm{d}\boldsymbol{x}, \tag{5.14}$$

where $\hat{a}_n, \hat{a}_n^\dagger$ are the annihilation and creation operators, respectively, and the transverse electric displacement field expansion is

$$\hat{\boldsymbol{D}}(\boldsymbol{x}) = \imath\sum_n \sqrt{\frac{\epsilon\hbar v_g k_n}{2}}\hat{a}_n \boldsymbol{u}_n(\boldsymbol{r})e^{\imath k_n z} + h.c., \tag{5.15}$$

with $k_n = k_0 + n\Delta k$ the wave number corresponding to the frequency ω_n, $k_0 = \frac{\omega_0 n(\omega_0)}{c}$ the leading wave number, $\Delta k = \frac{2\pi}{L}$ the mode spacing, L the fiber length, $\boldsymbol{x} = (\boldsymbol{r}, z)$ with z the longitudinal coordinate, $\boldsymbol{u}_n(\boldsymbol{r})$ the normalized transverse mode $\left(\int_V |\boldsymbol{u}_n(\boldsymbol{r})|^2 \mathrm{d}\boldsymbol{x} = 1,\ L\int_V |\boldsymbol{u}_n(\boldsymbol{r})|^4 \mathrm{d}\boldsymbol{x} = A_{eff}^{-1}\right)$ related to the longitudinal-mode operator $\hat{a}_n$. This periodic mode spacing imposes periodic boundaries, later taken to infinity. We treat only a finite

frequency range, with $\chi^{(3)}(\omega) \simeq \chi^{(3)}(\omega_0)$. Many more details can be found in [213].

In summary, we are discretizing the longitudinal spatial dependence of our problem, building a one-dimensional lattice: we divide the fiber in $2N+1$ cells of length $\Delta z = \frac{L}{2N+1}$, arranged from $l = -N$ to $l = N$. In order to take into account the linear dispersion, we expand ω_n to the second order

$$\omega_n = \omega(k_0 + n\Delta k) \simeq \omega_0 + \Delta\omega + n v_g \Delta k - \frac{v_g^3 \beta_2 (n\Delta k)^2}{2} \tag{5.16}$$

and define the local discrete operators

$$\hat{\alpha}_l = (2N+1)^{-1/2} \sum_{n=-N}^{n=N} e^{\frac{2\pi i n l}{2N+1}} \hat{a}_n, \tag{5.17}$$

such that $\left[\hat{\alpha}_l, \hat{\alpha}_{l'}^*\right] = \delta_{l,l'}$, $\left[\hat{\alpha}_l, \hat{\alpha}_{l'}\right] = \left[\hat{\alpha}_l^*, \hat{\alpha}_{l'}^*\right] = 0$. Through an inverse FT and the Rotating Wave Approximation (RWA) (terms in the Hamiltonian which oscillate rapidly are neglected), we can move to the interaction picture, because the Hamiltonian in Eq. (5.14) now reads [214]

$$\begin{aligned} \hat{H} &= \hat{H}_0 + \hat{H}_I, \\ \hat{H}_0 &= \hbar\omega_0 \textstyle\sum_l \hat{\alpha}_l^\dagger \hat{\alpha}_l, \\ \hat{H}_I &= \hbar \left(\textstyle\sum_{l,l'} \omega_{ll'} \hat{\alpha}_l^\dagger \hat{\alpha}_{l'} - \chi_\alpha \sum_l \hat{\alpha}_l^\dagger \hat{\alpha}_l^\dagger \hat{\alpha}_l \hat{\alpha}_l \right), \end{aligned} \tag{5.18}$$

where

$$\begin{aligned} \omega_{ll'} &= \textstyle\sum_n \frac{n v_g \Delta k - \frac{1}{2}(n\Delta k)^2 v_g^3 \beta_2}{2N+1} e^{\frac{2\pi i n (l-l')}{2N+1}} + \Delta\omega \delta_{l,l'}, \\ \chi_\alpha &= \frac{3\hbar (v_g k_0)^2}{8\epsilon^2 \Delta V} \epsilon_2, \\ \Delta V &= \frac{L A_{eff}}{2N+1}. \end{aligned} \tag{5.19}$$

χ_α is the effective nonlinearity, and ΔV is the effective quantization volume per local operator. Similarly to Eq. (2.7), we define $\epsilon_2 = \epsilon_0 L A_{eff} \langle \boldsymbol{\chi}^{(3)} \cdot \int_V [\boldsymbol{u}_n(\boldsymbol{r})]^{\otimes 3} \cdot \boldsymbol{u}_n(\boldsymbol{r}) d\boldsymbol{x} \rangle$ with the transverse-mode functions $\boldsymbol{u}_n(\boldsymbol{r})$ assumed identical for all the relevant wavelengths.

In the interaction picture, the NE for the density operator $\hat{\rho}(t)$ reads

$$\imath\hbar \frac{\mathrm{d}}{\mathrm{d}t} \hat{\rho}(t) = \left[\hat{H}_I, \hat{\rho}(t)\right]. \tag{5.20}$$

By using coherent-state representation, we can write $\hat{\rho}(t)$in terms of a non-diagonal projection operator on multimodal coherent states, namely,

$$\begin{aligned} |\alpha_n\rangle &= e^{-\frac{|\alpha_n|^2}{2}} \textstyle\sum_{k=0}^{+\infty} \frac{\alpha_n^k}{\sqrt{k!}} |k\rangle, \\ |\boldsymbol{\alpha}\rangle &= |\alpha_{-N}\rangle \otimes |\alpha_{-N+1}\rangle \otimes \cdots \otimes |\alpha_{N-1}\rangle \otimes |\alpha_N\rangle, \\ \hat{\Lambda}(\boldsymbol{\alpha}, \boldsymbol{\beta}) &= \frac{|\boldsymbol{\alpha}\rangle \langle \boldsymbol{\beta}^*|}{\langle \boldsymbol{\beta}^* | \boldsymbol{\alpha} \rangle}. \end{aligned} \tag{5.21}$$

We use the Drummond-Gardiner positive-$\mathcal{P}$ representation [213–216] and express the density operator as

$$\hat{\rho}(t) = \int_{\mathbb{R}^{4(2N+1)}} \mathrm{d}\mu(\boldsymbol{\alpha},\boldsymbol{\beta})\mathcal{P}(\boldsymbol{\alpha},\boldsymbol{\beta})\hat{\Lambda}(\boldsymbol{\alpha},\boldsymbol{\beta}), \tag{5.22}$$

with $\mathrm{d}\mu(\boldsymbol{\alpha},\boldsymbol{\beta}) = \mathrm{d}^2\alpha_{-N}\ldots\mathrm{d}^2\alpha_N\mathrm{d}^2\beta_{-N}\ldots\mathrm{d}^2\beta_N$. It turns out that the NE becomes

$$\imath\hbar\int_{\mathbb{R}^{4(2N+1)}} \mathrm{d}\mu(\boldsymbol{\alpha},\boldsymbol{\beta})\frac{\mathrm{d}}{\mathrm{d}t}\mathcal{P}(\boldsymbol{\alpha},\boldsymbol{\beta})\hat{\Lambda}(\boldsymbol{\alpha},\boldsymbol{\beta}) = \int_{\mathbb{R}^{4(2N+1)}} \mathrm{d}\mu(\boldsymbol{\alpha},\boldsymbol{\beta})\mathcal{P}(\boldsymbol{\alpha},\boldsymbol{\beta})\left[\hat{H}_I,\hat{\Lambda}(\boldsymbol{\alpha},\boldsymbol{\beta})\right]. \tag{5.23}$$

Through correspondence rules [216]

$$\begin{aligned}
\hat{\alpha}_l\hat{\Lambda}(\boldsymbol{\alpha},\boldsymbol{\beta}) &= \alpha_l\hat{\Lambda}(\boldsymbol{\alpha},\boldsymbol{\beta}),\\
\hat{\alpha}_l^\dagger\hat{\Lambda}(\boldsymbol{\alpha},\boldsymbol{\beta}) &= \left(\beta_l + \tfrac{\partial}{\partial\alpha_l}\right)\hat{\Lambda}(\boldsymbol{\alpha},\boldsymbol{\beta}),\\
\hat{\Lambda}(\boldsymbol{\alpha},\boldsymbol{\beta})\hat{\alpha}_l^\dagger &= \beta_l\hat{\Lambda}(\boldsymbol{\alpha},\boldsymbol{\beta}),\\
\hat{\Lambda}(\boldsymbol{\alpha},\boldsymbol{\beta})\hat{\alpha}_l &= \left(\alpha_l + \tfrac{\partial}{\partial\beta_l}\right)\hat{\Lambda}(\boldsymbol{\alpha},\boldsymbol{\beta}),
\end{aligned} \tag{5.24}$$

we obtain the FPE

$$\begin{aligned}
\tfrac{\mathrm{d}\mathcal{P}(\underline{\alpha},\underline{\beta})}{\mathrm{d}t} = \imath\sum_l\Big[&\tfrac{\partial}{\partial\alpha_l}\left(\textstyle\sum_{l'}\omega_{ll'}\alpha_{l'} - 2\chi_\alpha\alpha_l^2\beta_l\right) + \chi_\alpha\tfrac{\partial^2}{\partial\alpha_l^2}\alpha_l^2 +\\
&-\tfrac{\partial}{\partial\beta_l}\left(\textstyle\sum_{l'}\omega_{ll'}\beta_{l'} - 2\chi_\alpha\alpha_l\beta_l^2\right) - \chi_\alpha\tfrac{\partial^2}{\partial\beta_l^2}\beta_l^2\Big]\,\mathcal{P}(\underline{\alpha},\underline{\beta}).
\end{aligned} \tag{5.25}$$

The coupled Itô Stochastic Partial Differential Equations (SPDEs) derived from Eq. (5.25) are [214, 216]

$$\begin{aligned}
\partial_t\alpha_l &= -\imath\left(\textstyle\sum_{l'}\omega_{ll'}\alpha_{l'} - 2\chi_\alpha\alpha_l^2\beta_l\right) + \sqrt{2\imath\chi_\alpha}\alpha_l\xi_l(t),\\
\partial_t\beta_l &= \imath\left(\textstyle\sum_{l'}\omega_{ll'}\beta_{l'} - 2\chi_\alpha\alpha_l\beta_l^2\right) + \sqrt{-2\imath\chi_\alpha}\beta_l\eta_l(t),
\end{aligned} \tag{5.26}$$

with $\xi_l(t),\eta_l(t)$ Gaussian white noises $\langle\xi_l(t)\xi_{l'}(t')\rangle = \langle\eta_l(t)\eta_{l'}(t')\rangle = \delta_{l,l'}\delta(t-t')$, $\langle\xi_l(t)\eta_{l'}(t')\rangle = 0$.

The final step is to move towards a continuous phase space, to attain a system of two coupled NLSEs. In the limit $\Delta z\to 0$, we define $z := l\Delta z$, and attain

$$\begin{aligned}
\phi(z,t) &= \lim_{\Delta z\to 0}\alpha_l(t)\sqrt{\tfrac{v_g}{\Delta z}},\\
\psi(z,t) &= \lim_{\Delta z\to 0}\beta_l(t)\sqrt{\tfrac{v_g}{\Delta z}}.
\end{aligned} \tag{5.27}$$

From Eqs. (5.26), the main steps of the calculations are

$$\begin{aligned}\lim_{\Delta z\to 0}\sqrt{\tfrac{v_g}{\Delta z}}\textstyle\sum_{l'}\omega_{ll'}\alpha_{l'} &= \left(\tfrac{v_g^3\beta_2}{2}\partial_z^2-\imath v_g\partial_z+\Delta\omega\right)\phi(z,t),\\ \lim_{\Delta z\to 0}\sqrt{\tfrac{v_g}{\Delta z}}\chi_\alpha\alpha_l^2\beta_l &= \tfrac{\chi_\Phi v_g}{2}\phi^2(z,t)\psi(z,t),\\ \lim_{\Delta z\to 0}\sqrt{\tfrac{v_g}{\Delta z}}\sqrt{2\imath\chi_\alpha}\alpha_l\xi_l(t) &= v_g\sqrt{\imath\chi_\Phi}\phi(z,t)\xi(z,t),\end{aligned} \tag{5.28}$$

where $\chi_\Phi=\lim_{\Delta z\to 0}\frac{2\Delta z}{v_g^2}\chi_\alpha=\frac{3\hbar\omega_0^2\epsilon_2}{4\epsilon\epsilon_0c^2A_{eff}}$, and $\xi(z,t)=\lim_{\Delta z\to 0}\frac{\xi_l(t)}{\sqrt{\Delta z}}$. We move to the travelling-frame coordinates $s=v_gt$, $\tau=t-\beta_1z$, with noise $\xi(s,\tau)=\xi(z,t)$ and $\Delta\omega\simeq 0$, and obtain the two coupled SNLSEs

$$\begin{aligned}\imath\partial_s\phi &= \tfrac{\beta_2}{2}\partial_\tau^2\phi-\chi_\Phi\phi^2\psi+\imath\sqrt{\imath\chi_\Phi}\phi\xi,\\ \imath\partial_s\psi &= -\tfrac{\beta_2}{2}\partial_\tau^2\psi+\chi_\Phi\phi\psi^2+\imath\sqrt{-\imath\chi_\Phi}\psi\eta,\end{aligned} \tag{5.29}$$

with white noise correlations $\langle\xi(s,\tau)\xi(s',\tau')\rangle=\langle\eta(s,\tau)\eta(s',\tau')\rangle=\delta(s-s')\delta(\tau-\tau')$, and $\langle\xi(s,\tau)\eta(s',\tau')\rangle=0$. These equations are the quantum counterpart of Eq. (5.12). The system can be numerically solved through a stochastic Heun algorithm with initial condition $\phi(0,\tau)=\psi^*(0,\tau)$. The quantum nature of the computation is evident in the stochastic terms of the SPDEs. Indeed, we need to average the simulations results in order to obtain the propagated quantum nonlinear wave into the fiber. None classical, deterministic numerical code needs such a probabilistic analysis.

THE QUANTUM NONLINEAR SCHRÖDINGER EQUATION

From Eq. (5.12) and the transformation $t=-\frac{\beta_1^2}{\beta_2}s$, $x=\frac{\sqrt{2}\beta_1}{\beta_2}\tau$, $u(x,t)=\frac{A(s,\tau)}{A_0}$ with $A_0=\sqrt{\frac{\sqrt{2}\beta_1\hbar\omega_0}{|\beta_2|}}$, $\chi=\frac{\beta_2}{|\beta_2|}$ and $c_0=\frac{\omega_0n_2|\beta_2|A_0^2}{2c\beta_1^2A_{eff}}$, the normalized NLSE reads

$$\imath\partial_tu=-\partial_x^2u+2\chi c_0|u|u^2. \tag{5.30}$$

We can use the same coordinates to get normalized Eqs. (5.29)

$$\begin{aligned}\imath\partial_tu &= -\partial_x^2u+\chi c_0u^2v-\imath\chi\sqrt{\imath c_0}u\sigma,\\ \imath\partial_tv &= \partial_x^2v-\chi c_0uv^2-\imath\chi\sqrt{-\imath c_0}v\nu,\end{aligned} \tag{5.31}$$

with $u(x,t)=\frac{\phi(s,\tau)}{\phi_0}$, $v(x,t)=\frac{\psi(s,\tau)}{\phi_0}$, $\phi_0=\sqrt{\frac{\sqrt{2}\beta_1}{|\beta_2|}}$, $c_0=\frac{\sqrt{2}\chi_\Phi}{\beta_1}$, $\chi=\frac{\beta_2}{|\beta_2|}$, $\sigma(x,t)=\frac{\xi(s,\tau)}{\xi_0}$, $\nu(x,t)=\frac{\eta(s,\tau)}{\xi_0}$, $\xi_0=\frac{\sqrt{\sqrt{2}\beta_1^3}}{|\beta_2|}$, $\langle\sigma(x,t)\sigma(x',t')\rangle=\langle\nu(x,t)\nu(x',t')\rangle=\delta(x-x')\delta(t-t')$ and $\langle\sigma(x,t)\nu(x',t')\rangle=0$.

The QNLSE [218, 219, 221, 222] can be obtained directly quantizing Eq. (5.30), and it reads

$$\imath\partial_t\hat{\Phi} = -\partial_x^2\hat{\Phi} + 2\chi c_0\hat{\Phi}^\dagger\hat{\Phi}\hat{\Phi}, \tag{5.32}$$

where $\Phi(x,t)$ and $\hat{\Phi}^\dagger(x,t)$ are the Fourier trasform of the annihilation and the creation operators at position x and time t, respectively, namely, $\hat{\Phi}(x,t) = \int \frac{dk}{\sqrt{2\pi}}\hat{a}(k,t)e^{\imath kx}$, with commutation rules

$$\left[\hat{a}(k,t),\hat{a}^\dagger(k',t)\right] = \delta(k-k'), \quad \left[\hat{a}(k,t),\hat{a}(k',t)\right] = \left[\hat{a}^\dagger(k,t),\hat{a}^\dagger(k',t)\right] = 0, \tag{5.33}$$

from which we derive

$$\left[\hat{\Phi}(x,t),\hat{\Phi}^\dagger(x',t)\right] = \delta(x-x'), \quad \left[\hat{\Phi}(x,t),\hat{\Phi}(x',t)\right] = \left[\hat{\Phi}^\dagger(x,t),\hat{\Phi}^\dagger(x',t)\right] = 0. \tag{5.34}$$

The QNLSE Hamiltonian is [219]

$$\hat{H} = \hbar\left[\int \mathrm{d}x\left(\hat{\Phi}_x^\dagger\hat{\Phi} + \chi c_0\hat{\Phi}^\dagger\hat{\Phi}^\dagger\hat{\Phi}\hat{\Phi}\right)\right], \tag{5.35}$$

corresponding, in the Fourier space, to

$$\begin{aligned}\hat{H} \quad = \quad & \hbar\left[\int \mathrm{d}k\hat{a}^\dagger(k,t)\hat{a}(k,t)k^2 + \right. \\ & \left. + \chi c_0\int \mathrm{d}k\mathrm{d}k_1\mathrm{d}k_2\hat{a}^\dagger(k,t)\hat{a}^\dagger(k_1,t)\hat{a}(k_2,t)\hat{a}(k+k_1-k_2,t)\right].\end{aligned} \tag{5.36}$$

It is possible to prove that Eq. (5.32) can be derived from Eqs. (5.26) by defining $\hat{\Phi}(z,t) = \sqrt{\frac{v_g}{L}}\sum_n \hat{a}_n(t)e^{i(k_n-k_0)z}$ [214]. At the same time, from Eq. (5.32) we can derive Eqs. (5.31) following the scheme sketched in Fig. 5.1. This definitively demonstrates the the two approaches, the first one starting from the quantization of Maxwell's equations and attaining SNLSEs [214], and the second one quantizing directly the NLSE, getting the QNLSE [218, 219], are equivalent.

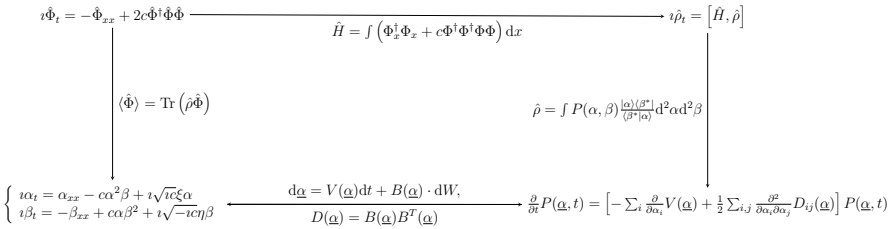

Figure 5.1: Pictorial sketch of the positive-$\mathcal{P}$ representation method to obtain the SNLSEs from the QNLSE.

CONCLUSIONS

Classical NLO can tell many things about complexity, much more than what is commonly known, also about topics regarded as genuinely quantum, such as entanglement, or photon teleportation [223–226]. Nevertheless, introducing quantized optical fields is not only necessary [212], but it also is something that enriches complexity science. Here we saw just a little part about what phase-space methods - as the positive-$\mathcal{P}$ representation - can describe. The starting point of our treatise is semiclassical, through superpositions of coherent states. In a truly quantum regime, choosing an initial condition as $\phi(0,\tau) = \psi^*(0,\tau)$ for Eqs. (5.29) is not enough, but we have to choose a certain statistical distribution of initial data.

We clearly are many steps far away from this, but an *all-optical nonlinear computer*, working at low-photon number with quantum nonlinear waves, is more reachable than what we think. The next Chapters of this Part present three paradigmatic models of quantum nonlinear waves. In the next part, instead, finally the random optical machine is introduced. This machine takes advantage of the disorder to perform reservoir computing. What if the randomness is directly given by the quantum nature of the source, and not by the medium? In what follows, a tentative answer is given.

6 QUANTUM CONTROL OF QUANTUM SOLITONS

INTRODUCTION

Strategies for large-scale control are fundamental for the success of quantum technologies. Controlling a quantum system means routing the evolution towards a desired state without collapse or excitation to spurious states. Effective control allows engineering molecular scale transformations, or novel form of matter [227]. In addition, controllability is unavoidable for universal quantum computing, quantum simulations and quantum annealing [228]. For these reasons, various strategies for quantum control have been developed, like shortcuts to adiabaticity [229–231], quantum feedback control [232], and quantum optimal control [233–235].

Recent years have witnessed a fast development of new methodologies, with applications spanning many quantum architectures and protocols, from few- to many-body theories [236–245], from open to closed systems [233, 235, 246–248]. Moreover, these novel approaches may foster the exploration of fundamental limits of manipulation of quantum matter and of the complexity of optimization protocols [249–252].

A potentially important and strategic field of application of quantum control is quantum NLO, where broadband generation of entangled and highly non-classical states was reported [253–255]. Proper control of a nonlinear field evolution with four-wave mixing nonlinearity allows the generation of multi-photon entangled quantum states, suitable for optical quantum information [256, 257]. Controlling quantized pulses propagating in an optical fiber is a crucial challenge and needs to step forward for large-scale quantum technologies [258].

Can the quantum control strategies contrast quantum effects on solitons propagation at low-photons regime? In this Chapter, we study the control of quantum dynamics of solitons, showing that the soliton quantum diffusion can be compensated by a proper time-dependent term in the Hamiltonian; this enables to moderate the soliton quantum spreading and to preserve information. We adopt the phase-space positive-$\mathcal{P}$ representation [259], and we combine SPDEs and Chopped Random-Basis (CRAB) quantum optimal control [260]. Our control strategy can be experimentally implemented by dispersion compensation techniques [261].

Quantum solitons are the quantum counterpart of the self-localized propagation-invariant classical solutions of a specific class of integrable equations, which includes the NLSE [218, 219]. We already saw that classical solitons are very well studied. Moreover, the use of solitons and the so-called nonlinear FT for optical transmission systems has recently gained considerable attention [262–265]. However, quantum solitons have a much richer dynamics with respect to their classical counterpart [266–271]. When the number of quanta goes to infinity, quantum solitons tend to classical solitons; conversely the fully quantum regime may provide many new solutions for quantum computing and cryptography in optics, polaritonics and BEC [245, 272]. Experimentally, quantum solitons in nonlinear optical fibers are known and studied as well. They are very suitable for observation of squeezing and for quantum nondemolition measurements [221, 273–275].

We believe that the control of quantum solitons opens new perspectives for quantum processors and quantum simulations. Moreover, quantum self-localization may be also employed to encode and transmit information [276, 277], a key-point in the curvy route towards the all-optical computation.

QUANTUM SOLITONS PROPAGATION

In order to model the propagation of an optical quantum soliton in a fiber, we adopt Eq. (5.32). If we consider the Fock basis, then we can express every state as follows

$$|\psi\rangle = \sum_n \frac{a_n}{\sqrt{n!}} \int \mathrm{d}\mathbf{x} f_n(\mathbf{x}, t) \hat{\Phi}^\dagger(x_1) ... \hat{\Phi}^\dagger(x_n) |0\rangle, \tag{6.1}$$

with $\sum_n |a_n|^2 = 1$ and $\int \mathrm{d}x_1 ... \mathrm{d}x_n |f_n(x_1, ..., x_n, t)|^2 = 1$.
Through Eq. (5.32), Eq. (6.1) gives

$$\imath \frac{\mathrm{d}}{\mathrm{d}t} f_n = \left[-\sum_{j=1}^{n} \frac{\partial^2}{\partial x_j^2} + 2\chi c_0 \sum_{1 \le i < j \le n} \delta(x_j - x_i) \right] f_n, \tag{6.2}$$

which is exactly solved by the Bethe-ansatz with Kerr interactions [218, 219]

$$f_n(x_1, ..., x_n, t) = e^{-\imath E_n t} \sum_{|Q|} A_Q e^{\imath \sum_{j=i}^{n} k_{Q(j)} x_j}, \tag{6.3}$$

where $x_1 \le ... \le x_n$ and $E_n = \sum_{j=i}^{n} k_j^2$. We are interested in the exact solution that, in the many-particle limit, has expectation average of

the field $\psi_s(x,t) = \langle\hat{\Phi}\rangle$, with $\psi_s(x,t)$ the fundamental classical soliton, solution of the NLSE (5.30). We consider an attractive interaction $\chi < 0$ and $c_0 > 0$.

Under this hypothesis [219]

$$\begin{aligned} k_j &= p + \imath\tfrac{\chi c_0}{2}(n-2j+1), \\ f_{n,p}(x_1,...,x_n,t) &= e^{\imath E(n,p)t} f_{n,p}(x_1,...,x_n), \\ f_{n,p}(x_1,...,x_n) &= \mathcal{N}_n e^{\imath p\sum_{j=1}^n x_j + \frac{\chi c_0}{2}\sum_{1\le i<j\le n}|x_j-x_i|}, \\ \mathcal{N}_n &= \frac{\sqrt{(n-1)!}}{\sqrt{2\pi}}|\chi c_0|^{\frac{n-1}{2}}, \\ E(n,p) &= np^2 - \tfrac{|\chi c_0|^2}{12}n(n^2-1). \end{aligned} \tag{6.4}$$

A quantum soliton is a superposition of eigenstates of the Hamiltonian (5.35), whose eigenstates are $|n,p\rangle = \frac{1}{\sqrt{n!}}\int \mathrm{d}\mathbf{x} f_{np}(\mathbf{x})\hat{\Phi}^\dagger(x_1)...\hat{\Phi}^\dagger(x_n)|0\rangle$. The states $|n,p\rangle$ are also eigenstates of the number operator $\hat{N} = \int \mathrm{d}x\hat{\Phi}^\dagger(x)\hat{\Phi}(x)$ and of the momentum $\hat{P} = -\imath\frac{\hbar}{2}\int \mathrm{d}x\left[\hat{\Phi}^\dagger(x)\partial_x\hat{\Phi}(x) - \partial_x\hat{\Phi}^\dagger(x)\hat{\Phi}_x(x)\right]$, with eigenvalues n and $\hbar np$, respectively. The quantum soliton is defined as the state that has a field expectation value corresponding to the classical soliton and, at $t=0$, it is given by

$$|\psi_s\rangle|_{t=0} = \int \mathrm{d}p g(p)|\alpha,p\rangle, \tag{6.5}$$

with $|\alpha,p\rangle = \sum_n \frac{\alpha_0^n}{\sqrt{n!}}e^{-\frac{|\alpha_0|^2}{2}}|n,p\rangle$ the coherent state with total momentum $\hbar|\alpha_0|^2 p$, and $g(p) = \frac{e^{-\frac{p^2}{2\Delta p^2}}}{\sqrt{\sqrt{\pi}\Delta p}}$ a Gaussian distribution of the momenta. By this definition of quantum soliton, the optical field expectation value is [278]

$$\psi_s(x) := \langle\psi_s|\hat{\Phi}(x,0)|\psi_s\rangle| \simeq \tfrac{n_0}{2}\sqrt{|\chi c_0|}\mathrm{sech}\left(\tfrac{|\chi c_0|n_0}{2}x\right)e^{-(\Delta p x)^2}, \tag{6.6}$$

where $n_0 = |\alpha_0|^2 = \langle\hat{N}\rangle$ is the photon number, and the many-particle limit $\Delta p \overset{n_0\to+\infty}{\longrightarrow} 0$ guarantees that $\psi_s(x)$ tends towards the fundamental classical soliton. It turns out that the QNLSE soliton solutions is $|\psi_s\rangle = \int \mathrm{d}p g(p)|\alpha,p,t\rangle$, with $|\alpha,p,t\rangle = e^{\imath E(n,p)t}|\alpha,p\rangle$. By adopting the positive-$\mathcal{P}$ representation [259, 279, 280], we can study the evolution of the quantum soliton, as sketched in Fig. 5.1.

It is important to remark that the explicit expression in Eq. (6.6) is valid only in the semiclassical regime $\Delta p << n_0 c_0$ and $n_0 >> 1$ [278]. Indeed, in the many-body limit (and only in this case), the momenta distribution $g(p)$ approaches the Dirac delta function, and the soliton tends towards a coherent state, i.e., a nearly classical state. Considering the opposite

relations, which characterize the quantum regime, once fixed the photon number, we can state that the larger the pulse is, the more quantum the soliton is.

QUANTUM SOLITONS CONTROL

We analyze the different behaviors - at diverse regimes - of quantum solitons by solving numerically the SPDEs (5.31), through a stochastic Heun algorithm [217]. The photon number n_0 affects the strength of the quantum noise, which disappears in the classical limit $n_0 \to \infty$. To see this, let us normalize $\psi_s(x)$, now such that $\int \mathrm{d}x|\psi_s(x)|^2 \simeq n_0$ at high photon number, and define

$$\tilde{\psi}_s(\tilde{x}) = \frac{\psi_s(x)}{\sqrt{|c_0|n_0}} = \frac{1}{2}\mathrm{sech}\left(\frac{1}{2}\tilde{x}\right) e^{-\left(\frac{\Delta\tilde{p}}{n_0}\tilde{x}\right)^2} \tag{6.7}$$

with $\tilde{x} = |c_0|n_0 x$ and $\Delta\tilde{p} = \frac{\Delta p}{|c_0|}$. The result is $\int \mathrm{d}\tilde{x}|\tilde{\psi}_s(\tilde{x})|^2 = 1$, and, by choosing also $\tilde{t} = -\chi c_0^2 n_0^2 t$, $\tilde{u}(\tilde{x},\tilde{t}) = \frac{u(x,t)}{\sqrt{|c_0|n_0}}$, $\tilde{v}(\tilde{x},\tilde{t}) = \frac{v(x,t)}{\sqrt{|c_0|n_0}}$, $\tilde{\sigma}(\tilde{x},\tilde{t}) = \frac{\sigma(x,t)}{(|c_0|n_0)^{\frac{3}{2}}}$ and $\tilde{\nu}(\tilde{x},\tilde{t}) = \frac{\nu(x,t)}{(|c_0|n_0)^{\frac{3}{2}}}$, Eqs (5.31) are transformed into

$$\begin{aligned}
\partial_{\tilde{t}}\tilde{u} &= -\imath\chi\partial_{\tilde{x}}^2\tilde{u} + \imath\mathrm{sgn}(c_0)\tilde{u}^2\tilde{v} + \sqrt{\frac{\imath\mathrm{sgn}(c_0)}{n_0}}\tilde{u}\tilde{\sigma}, \\
\partial_{\tilde{t}}\tilde{v} &= \imath\chi\partial_{\tilde{x}}^2\tilde{v} - \imath\mathrm{sgn}(c_0)\tilde{u}\tilde{v}^2 + \sqrt{\frac{-\imath\mathrm{sgn}(c_0)}{n_0}}\tilde{v}\tilde{\nu},
\end{aligned} \tag{6.8}$$

with $\mathrm{sgn}(c_0) = \frac{c_0}{|c_0|}$. Eqs. (6.8) show that quantum noise affects the propagation as strongly as $\frac{1}{\sqrt{n_0}}$ is high, no matter which initial condition one chooses (these equations are generally derived by QNLSE).

On the other hand, the momentum spread Δp is a quantum soliton feature. For a fixed n_0, $|\psi_s\rangle$ is a superpositions of Hamiltonian eigenstates with different photon number and, more important, different momentum [218, 219, 278]. It has optical field mean value corresponding to a propagation-invariant soliton if and only if $\Delta p \ll n_0|c_0|$. In Fig. 6.1 we show simulations of soliton evolution for various n_0 once fixed $\Delta\tilde{p} = 100$. In Fig. 6.1a, $n_0 = 10^6$ and we observe an invariant propagation, namely, the nearly classical regime; Fig. 6.1b shows the quantum spreading in the low-photon number regime $n_0 = 200$.

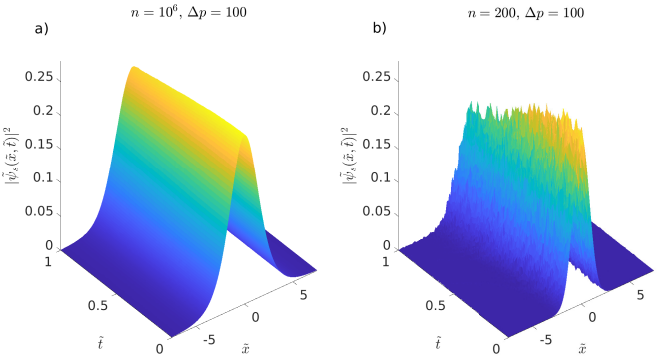

Figure 6.1: **Classical Vs Quantum Solitons.** (a) Nearly classical soliton evolution for $n_0 = 10^6$, $\Delta\tilde{p} = 100$; (b) quantum regime for $n_0 = 200$, $\Delta\tilde{p} = 100$.

Quantum Control of Diffusion

The quantum diffusion of the soliton may be characterized by the mean position operator

$$\hat{\bar{X}} = \left[\int x\hat{\Phi}^\dagger(x)\hat{\Phi}(x)\mathrm{d}x\right]\hat{N}^{-1}, \tag{6.9}$$

with $\left[\hat{\bar{X}},\hat{P}\right] = \imath\hbar$, and $\langle\Delta\bar{X}\rangle \simeq \sqrt{\frac{1}{(2n_0\Delta p)^2} + (2t\Delta p)^2}$, which gives the dynamics of the spreading [278]. This causes also a time-dependent modification of the Heisenberg principle. As $\langle\Delta P\rangle \simeq \hbar n_o \Delta p$, it turns out that $\langle\Delta\bar{X}\rangle\langle\Delta P\rangle \simeq \frac{\hbar}{2}\sqrt{1+\left[4tn_0(\Delta p)^2\right]^2} \simeq \frac{\hbar}{2}\left\{1+2\left[2tn_0(\Delta p)^2\right]^2\right\}$, similar to other cases in which quantum effects on classical optical propagation have been studied [6].

Our goal is to show that the soliton diffusion, which has a purely quantum origin, may be compensated by the quantum control techniques. We use a time-dependent kinetic energy, with a control function $\Gamma(t)$

$$\hat{H}[\Gamma](t) = \int \mathrm{d}x\left[\Gamma(t)\hat{\Phi}^\dagger{}_x\hat{\Phi}_x + \chi c_0\hat{\Phi}^\dagger\hat{\Phi}^\dagger\hat{\Phi}\hat{\Phi}\right] \tag{6.10}$$

to demonstrate that we can control the evolved state at a given instant $t = T$. We define the *infidelity* at the final target state $|\phi(T)\rangle$, given the initial soliton state $|\psi_s\rangle$, as

$$\mathcal{I}(|\phi(T)\rangle) = 1 - |\langle\phi(T)|\psi_s\rangle|^2. \tag{6.11}$$

We apply a square-wave periodic-modulation of the $\Gamma(t)$ function with frequency f

$$\Gamma(t) = \text{sgn}\left[\cos(2\pi f t)\right] \tag{6.12}$$

in order to have $\Gamma(0) = \Gamma(T) = 1$, so the same Hamiltonian at the initial and final instant. We solve the resulting SPDEs at varying f. In Figure 6.2a, we show the calculated infidelity (averaged over $N_R = 10$ realizations of quantum noise): for different photon numbers, one can identify different optimal frequencies corresponding to minimal infidelity. Figure 6.2b shows an example of the resulting quantum dynamics at optimal frequency for $n_0 = 200$. In this case, one can see that the infidelity goes from 0.236 to 0.007, reaching its minimum at $f = 1.421$.

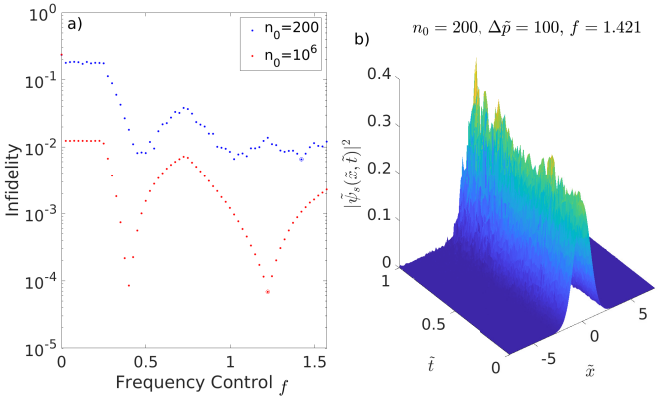

Figure 6.2: **Inibition of Quantum Diffusion by quantum control.** (a) Infidelity in Eq. (6.11) for $c_0^2 n_0^2 T = 1$ and $\Delta\tilde{p} = 100$, averaged over $N_R = 10$ realizations, and for various photon numbers; (b) controlled quantum evolution for $n_0 = 200$, $\Delta\tilde{p} = 100$, at optimal frequency $f = 1.421$.

Our control results improve when adopting the CRAB approach. In this case, the function $\Gamma(t)$ is written as

$$\Gamma(t) = 1 + \lambda^{-1}(t) \sum_{n=1}^{N_C} \left[A_n \sin(\omega_n t) + B_n \cos(\omega_n t)\right], \tag{6.13}$$

where $n = 1, 2, ..., N_C$ and $\omega_n = \frac{2\pi n(1+r_k)}{T}$; $r_k \in [0;1]$ is a random number and T is the total time evolution. Furthermore, $\lambda^{-1}(t) = (t/T)^2 - (t/T)$ is chosen in order to satisfy the constraint $\Gamma(0) = \Gamma(T) = 0$ [242]. With

reference to $\mathcal{I}$, in Fig. 6.3a we see the two-dimensional surface of the cost function versus the parameters A and B for the single frequency case ($N_C = 1$). The minimum of the infidelity as a function of (A, B) is 0.130 (while its maximum is 0.219). Figs. 6.3b,c report the optimal $\Gamma(t)$ and the optimized dynamics, respectively.

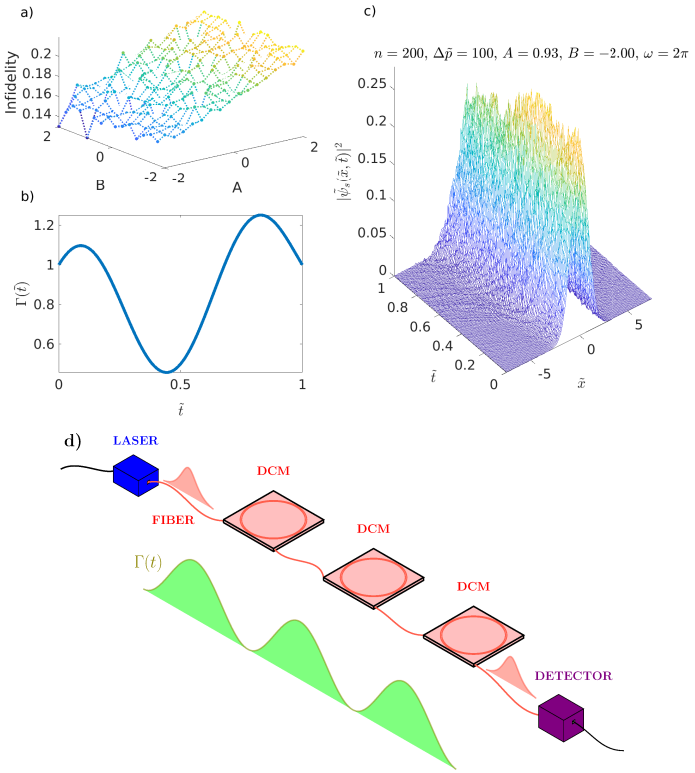

Figure 6.3: **CRAB Control of a quantum soliton.** (a) Infidelity versus A and B for $n_0 = 200$, $\Delta\tilde{p} = 100$, $n_0 T = 1$ and $\omega = 2\pi$, averaged over $N_R = 10$ realizations; (b) optimal control function, obtained by setting $A = 0.93$ and $B = -2.00$, for $\omega = 2\pi$; (c) dynamics of soliton with $n_0 = 200$ and $\Delta\tilde{p} = 100$ at optimal control; (d) experimental setup for quantum control of solitons by dispersion-management [261]. By tuning the fiber dispersion through a series of dispersion-compensation modules (DCMs), one obtains a prescribed Γ function.

Experimental Realization by Soliton-Dispersion Management

The time-dependent kinetic term in Eq. (6.10) is experimentally realizable by a technique called "dispersion-management" [261]. Fig. 6.3d shows a sketch of a chain of optical fibers with different dispersion properties, tunable, e.g., by stress and temperature. This setup allows one to engineer the Γ function to control the quantum solitons. Similarly, one can modulate the nonlinear terms weighted by c [258]. For example, in a common silica fiber with parameters

$$A_{eff} = 10^{-12} m^2,\ |\beta_2| = 10^{-25} s^2 m^{-1},$$
$$\beta_1 = 0.5 \times 10^{-8} s m^{-1}, n_2 = 2 \times 10^{-20} m^2 W^{-1}$$
$$\text{and} \lambda = 800 nm,$$

we find that the spatial scale of the control is of the order of $100 km$ for the simulations reported above [258].

CONCLUSIONS

We have investigated the quantum control of optical solitons, and have shown that a proper tailoring of the time-dependent Hamiltonian allows us to counteract quantum spreading and to sustain a propagation-invariant evolution even at low photon number. An ideal control function hence optimizes quantum nonlinear effects, because the photons interact over longer distances when the quantum diffusion is compensated. Many-body quantum control, via CRAB, turns out to be effective also for second-quantized nonlinear waves. Moreover, we have shown that quantum optimal control of quantum solitons is experimentally realizable by soliton-dispersion management [261].

In order to clarify the technique we used, we briefly compare our optimal quantum control of quantum solitons with the well known and developed quantum control of Bose Einstein condensates. Let us consider [281]: in that work, each atom of the condensate is prepared in the ground state of separate wells of an external optical double-well potential. The symmetrized initial state is the superposition of two wave functions, the first one localized in the left well and the second one localized in the right well. To control this atomic system, authors change the potential by lowering the right well with respect to the left one. Atoms initially in the right well remains in the ground state, while atoms initially in the left well evolves into the first excited state. The operation of changing the shape of the optical potential, is performed by rotating the polarization of the optical beam: experimentally, they follow a classical procedure to realize a quantum prescription. The same phenomenon occurs in our case: we have a purely quantum effect, that is, the soliton spreading, and we control its action by optimal quantum control, namely, through a genuinely quantum prescription, but using a classical procedure, the dispersion management [261]. This means that we can easily implement a quantum prescription experimentally.

We believe that our approach to quantum control may be extended to many different nonlinear optical processes, opening the way to genuine quantum design of optical soliton devices as quantum sources and non-classical state generators for future quantum technologies.

7 QUANTUM NONLINEAR BOX PROBLEM

INTRODUCTION

Light propagation at low intensity can experience quantum noise effects; the lower the photon number is, the stronger the modifications between classical and quantum optical evolutions are. In nonlinear media, optical beam profiles can reproduce water wave propagation, and several examples of such analogies are reported in literature [282, 283]. In particular, a laser beam propagating in a third-order nonlinear crystal with an initial rectangular shape mimics the focusing dam break flow and generates Peregrine-like RWs [7, 200].

The mechanism hidden behind this argument is examined in Chapter 4, and it is here summarized. Starting from the small-dispersion NLSE in Eq. 4.1 with initial condition 4.2, we define the NLSE box problem, or the dam break problem [200, 205]. The initial evolution presents the formation of two single-phase, counterpropagating DSWs, which regularize the box discontinuities. Their two wavefronts superimpose in the central part of the box (see Fig. 4.1a) and generate a two-phase quasi-periodic wave locally approximated by a Peregrine soliton [152, 159, 206, 207]. However, quantum noise contribution to this Peregrine solitons generation has not been investigated yet.

We report relevant quantum effects on the emergence of optical RWs in focusing third-order-nonlinear media for super-Gaussian beams and show the way the quantum noise modifies both the intensity of the maximum peak and the time of its occurrence. We also show that uncertainties have increasing global behavior when decreasing the number of photons. Our results cast light on the RW generation at quantum regimes.

QUANTUM EFFECTS ON ROGUE WAVES GENERATION

To analyze the modifications to the RWs emergence in the optical dam break problem at low intensity, namely, to work on the quantum nonlinear box problem, we use the same strategy of Chapter 6 for the study of the quantum solitons evolution. We consider a quantum state $|\psi_b\rangle$ such that

$$\langle\psi_b|\hat{\Psi}|\psi_b\rangle \simeq \psi_b(x) := \begin{cases} \sqrt{|c_0|}n_0 & \text{if} \quad |x| \leq \frac{1}{2|c_0|n_0} \\ 0 & \text{if} \quad |x| > \frac{1}{2|c_0|n_0} \end{cases}, \tag{7.1}$$

hence $\int \mathrm{d}x|\psi_b(x)|^2 = n_0$, as for Eq. (6.6) at high photon number.

Again, similarly to the previous Chapter, we normalize as follows:

$$\tilde{\psi}_b(\tilde{x}) = \frac{\psi_b(x)}{\sqrt{|c_0|n_0}} = \begin{cases} 1 & \text{if} \quad |\tilde{x}| \leq \frac{1}{2} \\ 0 & \text{if} \quad |\tilde{x}| > \frac{1}{2} \end{cases}, \tag{7.2}$$

with $\tilde{x} = |c_0|n_0 x$, $\tilde{t} = -\chi c_0^2 n_0^2 t$, $\tilde{u}(\tilde{x},\tilde{t}) = \frac{u(x,t)}{\sqrt{|c_0|n_0}}$, $\tilde{v}(\tilde{x},\tilde{t}) = \frac{v(x,t)}{\sqrt{|c_0|n_0}}$, $\tilde{\sigma}(\tilde{x},\tilde{t}) = \frac{\sigma(x,t)}{(|c_0|n_0)^{\frac{3}{2}}}$ and $\tilde{v}(\tilde{x},\tilde{t}) = \frac{\nu(x,t)}{(|c_0|n_0)^{\frac{3}{2}}}$. Therefore, $\int \mathrm{d}\tilde{x}|\tilde{\psi}_s(\tilde{x})|^2 = 1$ and the evolution is ruled by the SNLSEs (6.8).

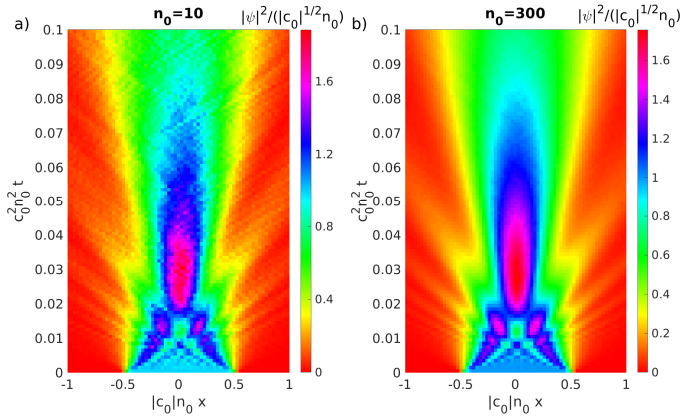

Figure 7.1: Intensity profiles of a rectangular-shaped beam propagating in a third-order nonlinear medium. (a) Quantum nonlinear box problem numerical solution at low photon number $n_0 = 10$; (b) Quantum nonlinear box problem numerical solution at high photon number $n_0 = 300$. Every simulation is averaged on $N_R = 16$ realizations.

We numerically simulate the box propagation, using as initial condition a normalized super-Gaussian function $e^{-\frac{1}{2}(2x)^{24}}$, for the same reasons explained in Chapter 4, namely, to avoid numerical errors due to the box discontinuities. Figure 7.1 reports simulations at different photon numbers. Figure 7.1(a) shows the box propagation at a quantum level ($n_0 = 10$), while in Fig. 7.1(b) the box evolution resembles the Peregrine soliton generation in Fig. 4.4, which confirms its classical behavior ($n_0 = 300$).

We study the quantum noise effects on the Peregrine soliton generation, and outcomes are illustrated in Fig. 7.2. By analyzing the Peregrine soliton peak intensity position, and its own value, varying n_0, we can highlight

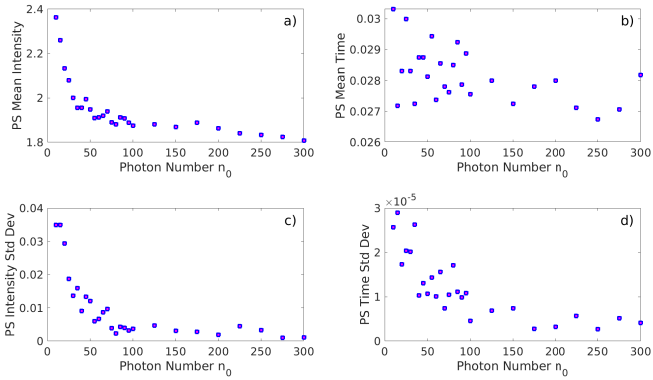

Figure 7.2: Quantum noise effects on Peregrine soliton, varying n_0. (a) Peak intensity mean value; (b) averaged time of Peregrine soliton occurrence; (c) Peak intensity standard deviation; (d) standard deviation of Peregrine soliton temporal occurrence. Every simulation is averaged on $N_R = 16$ realizations.

the different behaviors at low and high photon numbers regimes. Figures 7.2(a,c) prove that the quantum regime enhances both the intensity per photon number and its standard deviation. Figures 7.2(b,d) shows the time of Peregrine soliton occurrence has not a monotonic behavior that is as well-defined as peak intensity profile: its mean value is affected by numerical fluctuation at every photon number regime. The peak intensity standard deviation, instead, does not monotonically decrease, but however owns a decreasing global behavior.

CONCLUSIONS

We showed that third-order nonlinear waves at the quantum level can be numerically studied through SNLSEs, solved by a stochastic Heun algorithm. Moreover, we proved that this analysis can also be applied to the quantum nonlinear box problem, the quantum optical analog of the hydrodynamical dam break problem.

Our results unveil a new direction in the realization of all-optical nonlinear devices. Since in Chapter 4 we showed how a box-shaped beam can access very complex nonlinear dynamics, and its propagation can be supervised, or controlled, this study represents for an invaluable starting point for our future intent, as we illustrate at the end of this thesis, aiming at new routes for computation.

Part IV

COMPLEXITY IN CLASSICAL AND QUANTUM COMPUTATION

Outline of Part iv

This Part reports the first investigations on the use of waves in computing.

- Chapter 8 is a general introduction to quantum and classical computing, with emphasis on annealer devices, as Ising machines and D-waves.
- Chapter 9 describes a simple, large-scale Ising machine, which has been developed during this thesis.
- Chapter 10 is a general introduction to machine learning models and a demonstration of the use of artificial neural networks for designing topological devices.
- Chapter 11 describes random neural networks and their implementation by disordered media. In particular, the design of quantum gates is outlined.

Synopsis

Parts ii and iii present our results on optical nonlinear waves, both at a classical and at a quantum regime. The complexity of light propagation in nonlinear media is there examined from all the main points of view: extreme phenomena, recurrence, control, modulation instability, etc.

Here, we introduce our study towards the realization of an all-optical computer, able to do computation by implementing machine learning algorithms. After an overview of computational complexity and machine learning techniques (with application to topological lasers), the first all-optical realization of the Ising machine and the theoretical foundations of the random optical machine are illustrated. Applications to quantum gates are designed as well.

Can nonlinear waves do computation? We believe that the random optical machine draws the route for an affirmative answer to this question, and the reasons for our claim are here reported.

8

COMPUTATIONAL COMPLEXITY AND QUANTUM ANNEALING

INTRODUCTION

Many problems of interest are optimization problems, in which each feasible solution has an associated value, and we wish to find a feasible solution with the best value. However, complexity can arise one step before, not when we are considering optimization problems, but when we are dealing with decision problems, in which just the choice between the two simple answers “yes” or “no” (or, more formally, 1 or 0) can be harder than we think.

We usually can cast a given optimization problem as a related decision problem by imposing a bound on the value to be optimized. For example, for the optimization problem “shortest-path", where the algorithm has to find the shortest way to connect all the nodes of a graph, the related decision problem could be called “path", in which the algorithm has to state only if a possible way to connect all the nodes in at most k edges exists. If it does, “shortest-path" finds the minimal k. On the other hand, if we are able to solve “shortest-path", we can design the minimal value of k for which “path" returns “yes". From this example, we can see the relation between optimization and decision problems works in our favor when we try to show that the optimization problem is “hard”: if an optimization problem is easy, its related decision problem is easy as well, if a decision problem is hard, its related optimization problem is also hard. In computational complexity science, the word “hard" has a very specific meaning.

Generally, we think that most of the problems are solvable in a polynomial time, but the truth is the opposite. Not only most of the problems are not solvable in a polynomial time, being intractable, or hard, but they are not solvable at all. There are lots of problems that cannot be solved by any computer, such as Turing’s famous “Halting Problem”, no matter how much time is provided. This can be demonstrating by thinking about the cardinality of the set containing all the possible programs and the set containing all the possible decision problems. A program is a finite string of 0 or 1, that is, a binary number, isomorphic to a natural number. Therefore, we represent the programs set as $\mathbb{N}$. A decision problem is a function that to every program (i.e., to every natural number) associate

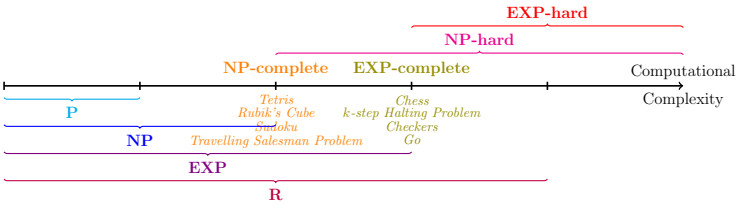

Figure 8.1: Schematic of the decision problems computational complexity.

"yes" or "no" (i.e., 1 or 0), so it is a function $f : \mathbb{N} \to \{0, 1\}$. How many are these functions? They are as many as the numbers in $\mathbb{R}$ [284]. Hence, we represent the decision programs set as $\mathbb{R}$. It turns out that we have $\mathbb{R} - \mathbb{N}$ unsolvable problems.

Speaking about solvable - or computable - decision problems, we can classify them with respect to time we need to solve them. Figure 8.1 draws the list of the corresponding sets on an increasing computational complexity:

P= { problems solvable at most in polynomial time $O(n^c)$ },

NP= { problems solvable in polynomial time via a "lucky" (i.e., nondeterministic) algorithm }
= { problems with solutions that can be checked in polynomial time },

EXP= { problems solvable at most in exponential time $O\left(2^{n^c}\right)$ },

R= { problems solvable in finite time }, here R stands for "recursive" [285].

About the set difference NP−P, the so-called P≠NP question has been one of the deepest, most perplexing open research problems in theoretical computer science since it was first posed in 1971. The list above the line in Fig. 8.1 illustrates

NP-Hard= { problems as hard at least as every problem in NP },

NP-Complete=NP∩NP-Hard,

EXP-Hard= { problems as hard at least as every problem in NP },

EXP-Complete=EXP∩EXP-Hard.

The above classification becomes very useful after having defined the *algorithm reduction*. Let us consider a decision problem A that we would like to solve in polynomial time. We call the input to a particular problem an *instance* of that problem. Now suppose that there is a different decision problem B that we already know how to solve in polynomial time, and suppose that we have a procedure that transforms any instance a of A into some instance b of B with the following characteristics:

1. the transformation takes polynomial time,
2. the answer for a is "yes" if and only if the answer for b is also "yes".

The final result is that we have converted A in B, and solving B solves A as well. Therefore $B \in \text{P} \Rightarrow A \in \text{P}$. Reduction can be used also for proving NP-completeness. The proof methodology is similar: we reduce A to B, we demonstrate that $A \in$NP-Complete, and we have for granted that $B \in$NP-Complete.

The algorithm reduction is a powerful tool. As the multiscale method allows us to derive model equations (see Chap. 1), the *multicall reductions* (series of reductions) allows us to establish models of computation that, once solved, give us the solutions of entire classes of problems. Some of these models of computation are represented by the minimization of the Ising Hamiltonian for different couplings [9], briefly illustrated in what follows.

ISING MODELS

The Ising model, in its one-dimensional version, was proposed in 1925 by Ernst Ising in his Ph. D. thesis. He wanted to describe the thermodynamic properties of magnetic systems from a microscopic point of view, but in the case he considered, Ising found that the system does not exhibit any phase transition for positive temperature $T > 0$, thus he concluded that the whole model was not useful. The history of physics showed that his conclusion was incorrect. Indeed, his model has been later studied again in many different configurations, and lots of important properties have been discovered.

Ising model has been one of the most heavily studied in statistical mechanics and it is often used as a testing ground when new theories or methods are developed. The d-dimensional Ising model is defined as follows: let us consider a d-dimensional lattice with N sites, each labelled by an index $j = 1, \ldots, N$; in general the lattice is supposed to

be hypercubic, but this is not necessary [1]; the degrees of freedom of the model are discrete variables $\sigma_j \in \{-1, 1\}$, defined on each site, thus the number of the possible configurations of the system is 2^N. In the original intent of the Ising model, the lattice represents the atomic configuration of a metal, and the variables σ_j are the spin components along the vertical axis. The study of this model should determine if and how all these spins can align in a way that the system has a spontaneous net magnetization, and it corresponds to minimazing the Hamiltonian

$$H = -\sum_{jh} J_{jh}\sigma_j\sigma_h, \tag{8.1}$$

with J_{jh} coupling constants.

An extremely important characteristic of the Ising model is that it does not only apply to magnetic systems, but to many others. Beyond fluids, binary alloys, and others [286, 287], it can be applied also to ANNs [288, 289]. In this case, every site of the lattice represents a neuron and the interaction bonds are synapses. When neurons are transmitting an electric pulse $\sigma_j = 1$, when they are not $\sigma_j = -1$.

Since when it was formulated for the first time, Ising model has been analyzed, generalized, and computerized, but rarely solved. The scientific community got exact solutions for two-dimensional systems, but have never been able to make the leap out of the plane. There is a good reason hidden behind this problem: the three-dimensional Ising model is NP-Complete. The complexity result was definitively announced in 2000 [290], but previous works showed that all versions of the Ising model are computationally intractable when the setting is three-dimensional [291].

The search for the ground state of the Hamiltonian (8.1) is feasible in models with J_{jh} a positive constant $\forall j, h$, where the configuration with all the spins aligned (either $\sigma_j = 1$ or $\sigma_j = -1\ \forall j$) decreases the total energy. If the coupling constants are a mix of positive and negative numbers - as they are for spin glasses - finding the ground state is a hard problem, and computational complexity comes in. At this point, it is natural to suspect intimate connections between the Ising model and all the other NP-Complete problems. Indeed, there exists a polynomial time mapping the Ising model to any other element of the NP-Complete set [292]: the Ising Hamiltonian minimization is a model of computation, and solving it means solving the entire class of NP-Complete problem. In [292] it is described how "all of the famous NP problems" [293, 294] can be written

1 in two dimensions, for example, we can consider triangular or "honeycomb" lattices, while in three dimensions we can have body-centered or face-centered cubic lattices; what distinguishes one lattice from another is the number of the nearest neighbours of a site z.

down as an Ising model with specific coupling constants, and with a polynomial number of spins which scales no faster than N^3.

Analogies between the statistical physics of Ising spin glasses and NP problems have been also used to construct simulated annealing algorithms [295, 296]. These connections have suggested a physical understanding of the emergence of hardness in these problems via a complex energy landscape with many local minima [297]. As consequence, recently an increasing interest in the possibility of using adiabatic quantum optimization to solve NP-Complete and NP-Hard problems has been spreading out. These and other topics are introduced in the next section.

QUANTUM ANNEALING AND D-WAVE SYSTEMS

As we have already showed in Chapter 6, many techniques of quantum control work by changing a continuous parameter into the Hamiltonian: they force the evolution towards a target state, without exciting new spurious states. Relevant examples of these methods are quantum shortcuts to adiabaticity [229, 298], quantum feedback control [232] and quantum optimal control [242, 299]. In shortcuts to adiabaticity, a quantum adiabatic process [2] is substituted by an alternative faster evolution which reproduces the same final state in shorter time. In other words, a slowly-varying time-dependent Hamiltonian $\hat{H}_0(t)$ is associated to another Hamiltonian $\hat{H}_1(t)$ that exactly carries the instantaneous eigenstates of $\hat{H}_0(t)$, namely, without transitions between them. In this context, [231]'s Authors establish an important bridge between the latter technique and the IST [79], by associating the KdVE Lax pair $\hat{L}(t), \hat{M}(t)$ to the Lewis-Riesenfeld dynamical invariant and the Hamiltonian, respectively. This suggests that the link between shortcuts to adiabaticity and nonlinear waves is deep and well-defined.

In this Section, another deep link is going to be illustrated: the connection between quantum annealing and computation of NP-Complete problems. Let us suppose that we have a quantum Hamiltonian $\hat{H}_1$, whose ground state encodes the solution to a problem of interest. At the same time, we have another Hamiltonian $\hat{H}_0$, whose ground state is easy to find/prepare, and that $\hat{H}_0$ and $\hat{H}_1$ do not commute. If we prepare a quantum system to be in the ground state of $\hat{H}_0$, and then adiabatically change the Hamiltonian for a time T, considering a new Hamiltonian

$$\hat{H}(t) = \left(1 - \frac{t}{T}\right)\hat{H}_0 + \frac{t}{T}\hat{H}_1, \tag{8.2}$$

2 as defined in 1928 by Born and Fock in the adiabatic theorem: "a physical system remains in its instantaneous eigenstate if a given perturbation is acting on it slowly enough and if there is a gap between the eigenvalue and the rest of the Hamiltonian's spectrum".

with T large enough, then the quantum system remains in the ground state, by the adiabatic theorem of QM. At time T, measuring the quantum state evolved by the Hamiltonian (8.2) has to return the ground state of $\hat{H}_1$ [300, 301].

Summaring, quantum annealing can be seen as a generic algorithm that uses QM fluctuations to search for the solution of an optimization problem. However, scientists are still debating about whether or not these algorithms can solve optimization problems faster than classical algorithms [302–304]. In fact, if the problem has size N, one typically finds

$$T = O\left[\exp\left(\alpha N^{\beta}\right)\right], \tag{8.3}$$

with α, β positive real numbers. This is a consequence of the requirement that exponentially small energy gaps between the ground state of $H(t)$ and the first excited state, at some intermediate time, do not lead to Landau–Zener transitions into excited states [304].

While it is unlikely that NP-Complete problems can be solved in polynomial time by quantum annealing algorithms, the coefficients α, β may be smaller than known classical algorithms, so there is still a possibility that quantum annealing is more efficient on some classes of optimization problems.

In 2011, D-Wave Inc. released their first quantum computer, working through quantum annealing. The first commercially produced D-Wave processor was a programmable, superconducting integrated circuit with up to 128 pair-wise coupled superconducting flux qubits. The 128-qubit processor was superseded by a 512-qubit processor in 2013. The processor is designed to implement a special-purpose quantum annealing. Therefore, it does not operate as a universal gate-model quantum computer.

Many researchers are highly sceptical about what D-Wave claims. The remaining contention lies in how useful the D-Wave machine is, and some researchers still question whether D-Wave's approach will yield a significant computation increase. A non-negligible group of researchers, also, pointed out that the D-Wave machine might not be a quantum computer, but instead operates in a complex but classical way.

CONCLUSIONS

Solving NP-complete problems is a current scientific challenge, an the engineering of a new type of computer, able to overcome such a challenge, could be the starting point of a new computational era, which might significantly change our every-day lives. Ising machine, as a model of computation, remains a paradigm that, once solved, can open the way to the design of new devices. D-wave, through quantum annealing, built a quantum computer that, in its last version, handles 2048 qubits, without the hypothesis of the universality.

In the next Chapter, we show how, with a simple (and cheap) Spatial Light Modulator (SLM), we built a (classical) all-optical Ising machine, able to find the ground state of the Ising Hamiltonian in the all-to-all spin interaction and Mattis models.

9 ALL-OPTICAL ISING MACHINE FIRST REALIZATION

INTRODUCTION

A large number of internal states characterizes complex systems from biology to social science. The fact that the number of these states grows exponentially with the system size hampers large-scale computational possibilities. Complex optimization problems involving these models are in many cases classified as NP-hard (intractable) and cannot be tackled efficiently by standard computing architectures. In Chapter 8, we show how a broad class of such computationally intractable problems maps to the search of the ground state of a classical system of interacting spins: the minimization of an Ising Hamiltonian with specific spin couplings [291, 292, 305].

Growing research interest is emerging towards physical and artificial systems that evolve according to an Ising Hamiltonian and enable to find the optimal combinatorial solution by the ground state observed in the experiment. Quantum and classical Ising systems have been realized by trapped atoms [306, 307], single photons [308], superconducting circuits [309], electromechanical modes [310], nanomagnets [311] and polariton condensates [312]. In optics, spin-glass dynamics have been observed in random lasers [313, 314], multimodal cavities [315, 316] , coupled laser lattices [317], beam filamentation [318] and nonlinear waves propagation in disordered media [319]. In these photonic systems, one has easy access to thousands of optical spins, but controlling their interaction is challenging.

Novel photonic platforms with numerous and easily accessible spin variables are particularly relevant for computation. Optical computing machines offer high-speed and scalability with respect to conventional hardware. Various authors reported coherent Ising machines based on time-multiplexed optical parametric oscillators finding approximate solutions to optimization problems with several nodes [320–324]. Others proposed nanophotonic circuits to implement any small-scale spin systems directly on a programmable chip [325–327]. Matrix operations can also be performed by spatially shaped optical fields, without engineered wave-mixing devices [328, 329], by exploiting randomly reflected waves [330] or disordered biological samples [1]. However, using spatial

optical modulation to solve Ising spin dynamics has remained unexplored.

In this Chapter, we propose and experimentally demonstrate the use of spatial light modulation for calculating the ground state of an Ising Hamiltonian. The phase matrix on a SLM acts as a lattice of spins whose interaction is ruled by the constrained optical intensity in the far-field. Feedback from the detection plane allows the spatial phase distribution to evolve towards the minimum of the selected spin model. We find ferromagnetic-like ground states in agreement with mean-field predictions. Our spatial Ising machine hosts thousands of parallelly-processed spins, and represents a scalable and efficient approach for photonic computing.

THE SPATIAL PHOTONIC ISING MACHINE

We implement a spatial photonic Ising machine by using the phases in separated spatial points of the optical wavefront. A binary phase modulated beam encodes binary spins with configurable interactions [Fig. 9.1(a)]. A spin variable $\sigma_j = \exp(\imath\phi_j) = \pm 1$ corresponds to a spatial point of the optical field with phase $\phi_j \in \{0, \pi\}$. As illustrated in Figs. 9.1(b,c), a SLM acting as a reprogrammable matrix of pixels imprints binary phase values on the coherent wavefront.

Setting the SLM in the Fourier space of the electric field $\tilde{E}(k)$ ("tilde" denotes Fourier transform in this Chapter), we have

$$\tilde{E}(k) = \sum_j \xi_j \sigma_j \tilde{\delta}_W(k - k_j), \tag{9.1}$$

where ξ_j indicates the field amplitude incoming on each pixel. In Eq. (9.1) we make reference - without loosing generality - to a one dimensional spin configuration to simplify the notation. The normalized rectangular function $\tilde{\delta}_W$ models the pixel of finite size $2W$ [Fig. 9.1(c)], so that $k_j = 2Wj$, with $j = 1, ..., n$. The resulting far-field intensity after free-space propagation is

$$I(x) = |E(x)|^2 = \sum_{jh} \xi_j \xi_h \sigma_j \sigma_h \delta_W^2(x) e^{2\imath W(h-j)x}, \tag{9.2}$$

with $\delta_W(x) = \sin(Wx)/(Wx)$ the inverse Fourier transform of $\tilde{\delta}_W(k)$. Spin-spin interaction can be induced by acting on the intensity on the detection plane. We constrain $I(x)$ by a measurement and feedback method to couple the phases on the SLM plane. Minimizing $\|I_T(x) - I(x)\|$ for an arbitrary target intensity image $I_T(x)$ thus corresponds to minimizing a Hamiltonian H. After normalization $\int [I_T(x)]^2 \mathrm{d}x \simeq \int [I(x)]^2 \mathrm{d}x$, and the

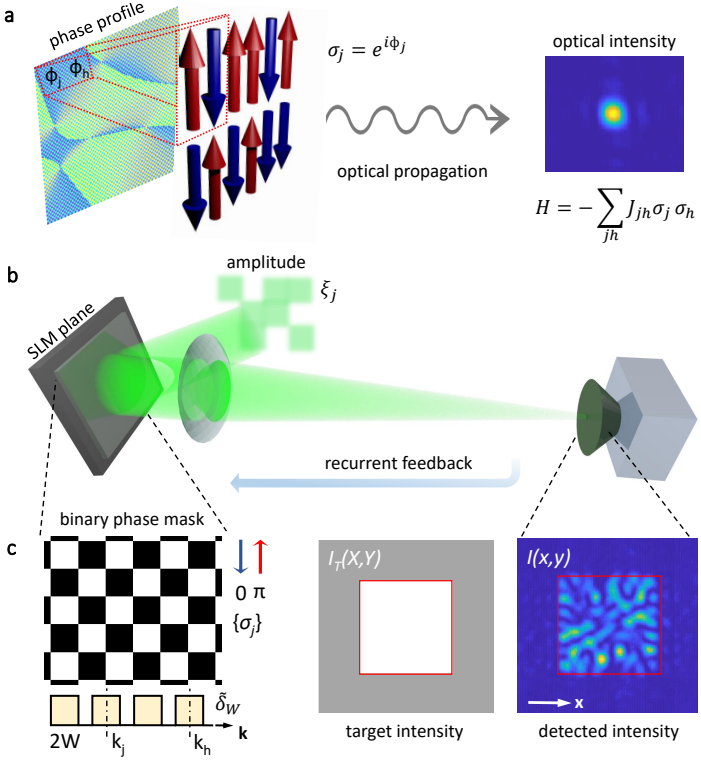

Figure 9.1: Ising machine by spatial light modulation. (a) The wave phase in different spatial points gives the spins evolving through optical propagation. (b) Experimental setup: an amplitude-modulated laser beam is phase modulated by a reflective SLM and detected by a CCD camera in the far-field. (c) A discrete phase mask with binary values $\phi_j = 0, \pi$ in the Fourier plane mimics Ising spins $\sigma_j = \pm 1$. Spin interaction is encoded in the input intensity distribution and occurs through recurrent feedback from the detection plane [Eq. (9.3)]. Inset is an example of the detected intensity when the binary hologram is tailored to generate a squared intensity target I_T.

function H takes the form of the Ising Hamiltonian in Eq. (8.1), with spin interactions given by

$$J_{jh} = 2\xi_j\xi_h \int I_T(x)\delta_W^2(x)e^{2\imath W(h-j)x}\mathrm{d}x. \tag{9.3}$$

When the effect of the SLM pixel size can be neglected, $\delta_W(x) \sim 1$, and the couplings reduce to

$$J_{jh} = 2\pi\xi_j\xi_h\tilde{I}_T[2W(j-h)], \tag{9.4}$$

which indicates that the interaction matrix is set by the input amplitude modulation along with the Fourier transform of the far-field target image. The interaction passes from short- to long-range by changing the spatial profile of I_T. In particular, in the case of a point-like target image, the spins are all-to-all interacting ($J_{jh} = \text{const}$) for an input wave with constant amplitude. Using a programmable (quenched) amplitude mask on the input beam the couplings can be varied according to $J_{jh} \propto \xi_j\xi_h$, which allows us to implement the entire class of spin-glass models, known as Mattis models [331, 332], where the pairwise interaction can be expressed as product of two independent variables. Figure 9.1(c) shows the principle of operation of our Ising machine. A spin configuration $\{\sigma_j\}$ is generated upon an amplitude-modulated wavefront using binary phases on the SLM and the corresponding intensity distribution $I(x)$ is measured in the far-field. The detected image is compared with the target $I_T(x)$, which, according to Eq. (9.4), fixes the interaction together with the specific input modulation, and the information is feedback to the SLM plane. At each time step, the system is made to evolve towards minimization of the cost function $f = ||I_T(x) - I(x)||$, which corresponds to looking for the Ising ground state.

The experimental implementation of this optical machine follows the setting shown in Fig. 9.1(b). Light from a CW-laser source with wavelength $\lambda = 532$nm is expanded, eventually modulated in amplitude, and made to impinge on a twisted nematic liquid crystal reflective modulator (Holoeye LC-R 720, 1280×768 pixels, pixel pitch $20 \times 20\mu$m) whose active area is selected by a rectangular aperture to host $N = L \times L$ spins (pixels). The SLM is set into a phase-modulation mode with less than 10% residual intensity modulation by a combination of incident and analyzed polarizations. Phase-modulated light is spatially filtered (3mW power) and then focused by a lens (f= 500mm) on a CCD camera. The intensity is measured on $M = 18 \times 18$ spatial modes obtained grouping 16×16 camera pixels to average over speckles arising from spatial phase fluctuations in the far-field plane.

ALL-TO-ALL SPIN INTERACTIONS

We first demonstrate the spatial Ising machine for $N = 4 \times 10^4$ spins with all-to-all couplings ($J_{jh} = \text{const}$), which corresponds to a number of spin-spin connections orders of magnitude larger than those realized

in time-multiplexed platforms [321, 322]. In this case, $\xi_j = \xi_h = \xi_0$ and the target corresponds to intensity focused only in a single spatial mode, that is, a bright localized spot [Fig. 9.2(a)]. The binary phases on the SLM are initialized by a random distribution, which gives a weak and broad speckle pattern in the detection plane. By a Monte Carlo-like method, at each iteration we randomly flip a small cluster of spins and measure the corresponding far-field intensity, retaining the change only if its difference with the target image decreases [333]. Unlike other photonic Ising machines [334], no information about the target Hamiltonian is used to affect electronically the spin evolution. To prevent trapping into local minima induced by the algorithm, we select clusters with a gradually increasing size. To follow the system evolution, we consider as physical observables the energy H and the magnetization $m = \langle \sigma_j \rangle$ of each configuration. As shown in Fig. 9.2(b) for different realizations, we observe a monotonic growth of $|m|$, which saturates to a large value after approximatively 10^3 iterations. The Hamiltonian monotonically decreases toward a plateau, thus indicating the onset of a low-energy ferromagnetic-like state. The actual temperature T of these spin configurations is determined by the random phase fluctuations in the Fourier plane, which results from the intrinsic noise characterizing each operation in the experimental setup. Sources of noise come from the quantization on the CCD discrete modes of the detected intensity as well as from the imperfect spatial phase modulation [335].

To test the solution found by our machine, we use a different and complementary approach based on phase retrieval. The aim is to evaluate the energy statistical distribution function (PDF) of all those $\{\sigma_j\}$ that satisfy the far-field constraint and compare with the low-energy solutions found by the machine. The method allows distinguishing the errors related to the feedback algorithm to those associated with the optical setup. We use a Quantized Phase-Retrieval (QPR) algorithm [336] to numerically generate binary phase distributions from the target image I_T and we measure the far-field intensity I. Among the many possible states that we determine by the QPR, which are associated with different phase patterns in the target plane, the solution of the machine is determined by minimizing the cost function f. Figures 9.2(c,d) show the results from 16 sets of measurements, each with 100 phase-retrieved spin configurations. We observe that the identified solutions populate the tail of the energy distribution [Fig. 9.2(c)] and have maximum magnetization [Fig. 9.2(d)]. This indicates that ground states of the Ising Hamiltonian are successfully found. In particular, the machine gives with 87% probability the correct minimum solution, that is, a spin configuration lying in the 5% of those with the lowest energy. This ground state probability quantifies the

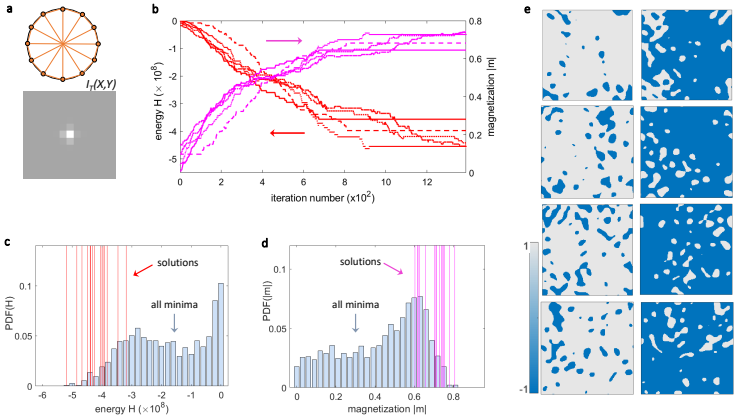

Figure 9.2: Optically solving the Ising Hamiltonian with all-to-all spin interactions. (a) An unweighted Möbius-Ladder graph with fully-connected vertices (results refer to $N = 4 \times 10^4$ vertices) along with the employed target intensity I_T. (b) Measured evolution of the system energy H ($J_{jh} = 1$) and magnetization $|m|$ for different initial random spin matrices. (c-d) Observed probability distribution function for the (c) energy and (d) magnetization of spin configurations satisfying the interaction constrain I_T (see text); red and magenta lines indicate H and $|m|$ of the identified ground state solutions, respectively. (e) A set of ground state spin configurations: small-size ferromagnetic clusters with opposite magnetization are visible.

correspondence between the cost-function minima and spin states with lower energy, and is independent of the way the ground state has been found.

To quantify the physical state resulting from the optical computation, we analyze the spin configurations. Figure 9.2(e) shows the typical ground states retrieved by the optical machine. We observe ferromagnetic domains of various size embedded in a phase with opposite magnetization. Spin states with $m < 0$ and $m > 0$ appear with almost equal probability, as expected from spontaneous symmetry breaking in the absence of external magnetic fields. From the set of $\{\sigma_j\}$ we can estimate the actual temperature according to the mean-field solution of Eq. (5.35), which describes the case with all-to-all interacting spins [332, 337]. Considering the equation of state $m = \tanh[(T_c/T)m]$, from the observed mean magnetization we obtain $T/T_c = 0.80 \pm 0.03$. We also analyze the measured spin spatial autocorrelation according to $g(r) = \exp(-r/\xi)$, where the autocorrelation length ξ gives an estimation of the mean

domain size. In the mean-field approach, ξ diverges at the critical temperature as $\xi = R_* (1 - T/T_c)^{-\beta}$, where the critical exponent $\beta = 1/2$ and R_* is the minimum cluster length. In this case, the resulting temperature is $T/T_c = 0.83 \pm 0.02$. Therefore, the observed ground states have magnetizations and domain configurations consistent with a mean-field Ising model at fixed temperature.

One of the main features of our spatial photonic setting is the extremely large number of spins that can be simulated. Varying the active area on the SLM (the transverse size of the spatially modulated laser beam), we investigate how the machine operation depends on the system size L. Figure 9.3(a) shows the magnetization and the fidelity (probability of finding the Ising ground state) of the observed ground state varying the number of spin from $N = 74 \times 74$ to $N = 274 \times 274$ and leaving unchanged their interaction. At variance with other photonic settings [321], we find that the performance of our Ising machine does not sensibly depend on the number of spins [inset in Fig. 9.3(a)]. For large sizes N, a minor decrease of the magnetization and fidelity is observed, and due to the lower spatial resolution in the detection plane. At low spin number, we observe a linear decrease of $|m|$ as N is reduced. We ascribe this behavior to finite-size effects. The observed spin autocorrelation function strongly varies with the number of spins, and a well-defined single decay only emerges at large N [Fig. 9.3(b)]. For configurations with few spins, we find that the measured correlation length grows linearly with the configuration size [Fig. 9.3(c)], in close agreement with finite-size scaling arguments, which predicts a mean-field behavior $\xi \propto L$ [338]. For large L the size of ferroelectric domains becomes independent of the system scale. The photonic machine thus points out a fundamental phenomenon of spin models [339].

MATTIS MODEL

We investigate other Ising models, by tailoring the spin couplings. As suggested by Eq. (9.4), Mattis spin-glasses can be realized varying the input amplitudes ξ_i and keeping a point-like target image ($\tilde{I}_T[2W(i - j)] \simeq$ const).

For these experiments, the SLM is split into two independent parts [340]. A portion of the SLM is used for amplitude modulation to generate controlled ξ_i distributions, that are imaged pixel by pixel on the second portion, where binary phase modulation and spin dynamics occur. We implement coupling matrices $J_{jh} \propto \xi_j \xi_h$ made of large random blocks with strongly ($\xi_j = \xi_0$) and weakly ($\xi_j = 0$) interacting spins [Fig. 9.4(a)]. Following the theoretical solution of the Mattis model [332], the expected

spin ground state is identical to the interaction configuration ξ_j, or to its reversal, except for the weakly interacting regions where spins are randomly oriented. Therefore, in our photonic simulation, we quantify the fidelity of the measured inhomogeneous ferromagnetic ground state by the spatial correlation $C = \sum_j \sigma_j \xi_j / \xi_0$. $C = \pm 1$ for the ideal Mattis model in the lowest energy state. Figure 9.4(b) shows that the measured ground states are strongly correlated or anticorrelated with the interaction matrix, as expected. Since in the Mattis models a minimal amount of noise introduces frustration [332], the differences between the machine solutions and the ideal ones are due to the non-zero effective temperature of the system.

CONCLUSIONS

We have demonstrated that spatial light modulation can be exploited to find the ground state of Ising Hamiltonians. By using binary phases on the wavefront of an amplitude modulated laser beam, a detection and feedback method, we optically calculate the low-energy ferromagnetic spin configuration. The ground states display finite-size scaling effects and mean-field properties at a fixed temperature. This finding opens the way to photonic simulations of phase-transition phenomena. The platform naturally hosts tens of thousands of spins (not limited to binary spins, when adopting multilevel phase modulations) and is scalable to larger sizes. The speed of our machine is limited only by the SLM response, camera rate, and data processing. The iteration time can be potentially reduced to few milliseconds with the most recent technologies [341]. Moreover, a recent theoretical proposal in the time domain [327] suggests a possible direction for further reducing the steps performed digitally by wave-mixing devices. The use of temporally modulated light pulses in addition to spatial modulation may also allow implementing three-dimensional spin systems with controllable interaction, even including the quantum optical regimes in which the coherent laser source is replaced by non-classical light. Similar large-scale simulators may also be conceived with quantum wavepackets as in ultracold gases, and Bose-Einstein condensates, by proper control and preparation of the initial states.

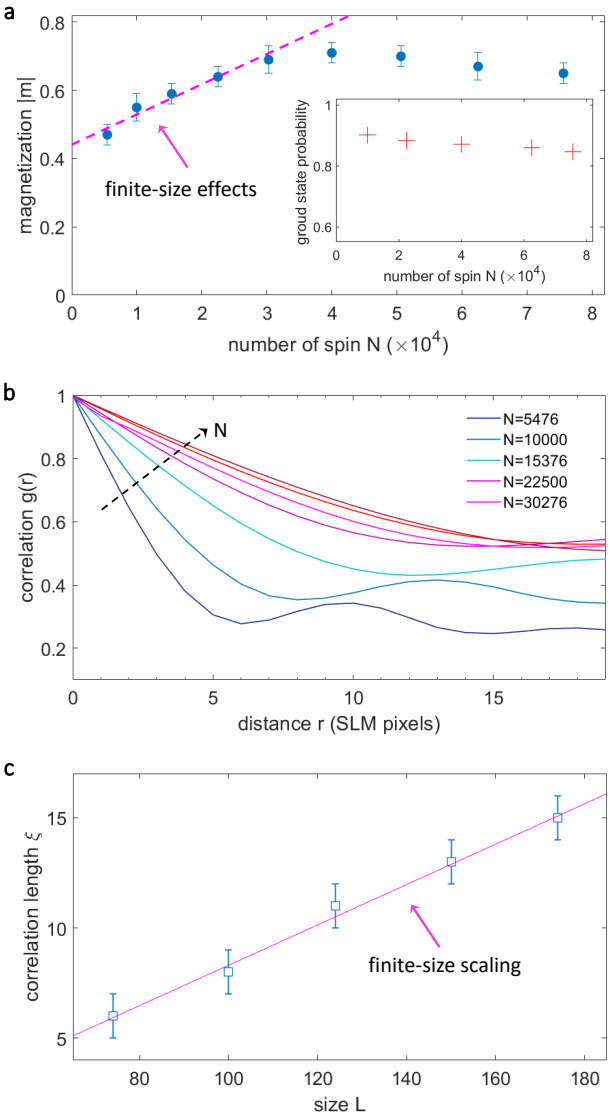

Figure 9.3: Scaling properties of the ferromagnetic ground state. (a) Observed magnetization varying the spin number (the dotted line is a linear trend serving as a guide). The inset shows the scaling of the machine performance. (b) Spatial spin autocorrelation functions (distance in pixel units) for different N. (c) Corresponding autocorrelation length as a function of the system size L (dots) and linear fitting behavior (line).

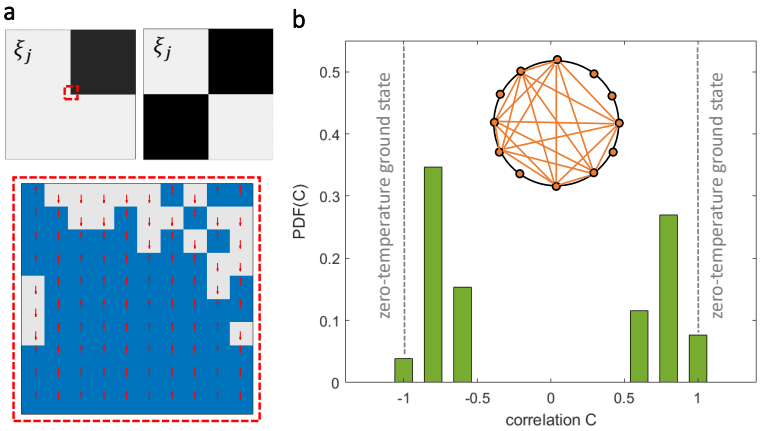

Figure 9.4: Programming the spin interaction by amplitude modulation. (a) Examples of coupling configurations ($N = 10^4$, top panels) made of random blocks in which the interaction assumes two positive values ($\xi_j = 0, \xi_0 > 0$). The corresponding spin ground state observed in the red box region is shown in the bottom panel. (b) Measured probability distribution of the correlation C between the ground state and the couplings for the Mattis models. The inset shows a corresponding Möbius-Ladder graph with connected and unconnected nodes.

10 MACHINE LEARNING AND APPLICATIONS TO OPTICS

INTRODUCTION

Early research on ML adopted an informal approach to evaluation. Papers typically reported runs of learning methods on a small set of training cases or problems, the outputs of these runs, and arguments for why the latter were reasonable or desirable results. In 1988, *Kibler and Langley* [342] laid out a framework for an experimental science of ML. Many authors adopted this perspective and, within a few years, the vast majority of articles reported experimental results about performance improvement on well-defined tasks.

The early movement in ML was also characterized by an emphasis on symbolic representations of learned knowledge, such as production rules, decision trees, and logical formulae. This bias was understandable, since ML was an outgrowth of symbolic Artificial Intelligence (AI) and cognitive science, with most of these researchers being concerned with automatically constructing expert systems or modeling human acquisition of knowledge structures. However, the growing interest on performance improvement definitively changed the definition of this field. In 1980s, ML was still viewed as a branch of AI. By 2000, many researchers committed to ML treated it as a separate field with few links to its parent discipline. This shift occurred partly because it was far easier to carry out experiments in classification and regression domains, and partly because of the commercial success of many data-mining applications. The growing use of statistical and pattern-recognition approaches, which improved performance, pushed away ML from AI.

Recently, ML [343–345] has been proposed as an encompassing technology for dealing with greatly differing problems through an unified approach. ML techniques have shown a remarkable growth in sophistication and application scope in multiple fields [346–348]. Moreover, ML offers exciting perspectives in photonics. It is applied in two main classes of problems:

1. classification for categorizing information,
2. regression to predict continuous values,

and, depending on the nature of the problem, there are different ML approaches, based on the type and volume of the data, here listed.

Supervised learning.

Supervised learning typically begins with an established set of data and a certain understanding of how that data is classified. It is intended to find patterns in data that can be applied to an analytics process. This data has labeled features that define the meaning of the data itself. When the label is continuous, it is a regression; when the data comes from a discrete set of values, it is known as classification. The algorithms are trained using preprocessed examples, and the performance of the algorithms is evaluated with test data.

Unsupervised learning.

Unsupervised learning is best suited when the problem requires a massive amount of data that is unlabeled. Understanding the meaning behind this data requires algorithms that are able to classify the information based on patterns or clusters. Then, the supervised learning conducts an iterative process of analyzing data. In essence, either this process is used to add labels to the data so that it becomes supervised, or it is used to determine outcomes from huge amounts of data more quickly than a supervised learning approach.

Reinforcement learning.

Reinforcement learning is a behavioral learning model. The algorithm receives feedback from the analysis of the data, so the user is guided to the best outcome. Reinforcement learning differs from other types of supervised learning because the system is not trained with the sample data set. Rather, the system learns through trial and error. Therefore, a sequence of successful decisions will result in the process being "reinforced", because it best solves the problem at hand.

ANNs and Deep Learning.

Deep learning is a specific method of ML that incorporates ANNs in successive layers, in order to learn from data in an iterative manner. Deep learning is especially useful when one is trying to learn patterns from unstructured data. Complex ANNs are designed to emulate how the human brain works, so computers can be trained to deal with abstractions and problems that are poorly defined.

An ANN consists of three or more layers: an input layer, one or many hidden layers, and an output layer. Data is ingested through the input layer. Then the data is modified in the hidden layers and the output layer, based on the weights applied to these nodes. Figures 10.1a,b show examples of regressive ANNs. A regressive ANN is a configuration of computational layers such that a specific set of input nodes $\underline{I}$ is connected to a single output node, through a configurable set of N_h hidden layers, each containing n_i nodes h_{ij}, where $i = 1, ...N_h$ and $j = 1, ...n_i$. A generic node $k+1, j$, shown in Figs. 10.1c, receiving as inputs h_{ki}, with $i = 1, ..., n_k$, yields on output $h_{k+1j} = g\left(\sum_l w_{k+1jkl} h_{kl} + b_{k+1j}\right)$, with $g(x)$ being a nonlinear activation function, w_{k+1jkl} the weight of h_{kl} on h_{k+1j}, and b_{k+1j} a bias term. The typical ANN may consist of thousands or even millions of simple processing nodes that are densely interconnected. The term deep learning is used when there are multiple hidden layers within an ANN. Using an iterative approach, an ANN continuously adjusts and makes inferences until a specific stopping point is reached. Deep learning is a ML technique that uses hierarchical ANNs to learn from a combination of unsupervised and supervised algorithms, and it is often called a sub-discipline of ML.

SOLVING THE INVERSE PROBLEM IN TOPOLOGICAL LASERS

The rapidly growing interest in topological photonics [349, 350] is leading to the design of complex structures for the many applications of optical topological insulators [351]. One leading goal of topological photonics is photon transport protected from unwanted random scattering. This is achieved by realizing analogues of the quantum Hall effect [352–354] through magnetic-like Hamiltonians in photonic systems [355]. In the optical domain, topological insulators [356] have been implemented in modulated honeycomb lattices [355], in arrays of coupled optical ring resonators [357] and optical quantum walks [358]. Geometry-independent topological structures have been proposed to obtain nonreciprocal single mode lasing [359–362] as well as systems with balanced gain and loss for parity-time symmetric structures with topological order [363, 364]. Emulations of four-dimensional physics have also been reported [365, 366]. By using one-dimensional Harper modulations, it is possible to simulate two-dimensional topological systems. Similarly, by two-dimensional topological systems, one can simulate four-dimensional ones, as recently investigated in [365, 366].

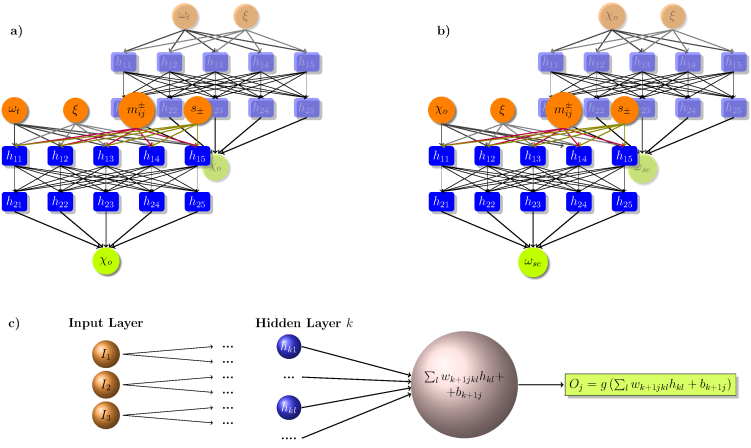

Figure 10.1: Architecture of fully-connected feed-forward ANNs. Orange and green circles are the input and output units, respectively. Blue ones represent the nodes of the hidden layers. Interconnections among the units are given by arrows. The networks in the background are specific to the unfolded problem; in the foreground we show the networks with extra mode and trend inputs. a) Inverse problem network. b) Direct problem network. c) Single unit scheme. The node performs a linear combination of its inputs followed by a nonlinear activation function.

One challenge in this field is to find an effective methodology for the inverse problem in which the target optical properties result from topological characteristics. Although various computational techniques are available, these require specific implementations, tailored to the task at hand. In this Chapter, we employ ML regression for solving the inverse problem in topological photonics. We apply advanced ML techniques to design photonic topological insulators, enabling innovative applications through custom tailoring of desired optical parameters. In our approach, we introduce a twist in order to ensure that only physically possible solutions are found. This twist is based on a self-consistent cycle, in which a tentative solution, obtained from the inverse problem ANN, is run through the direct problem ANN in order to ensure that the solution obtained is indeed viable. This has the added benefit of checking that multivalued degeneracy has been effectively removed.

The Photonic Topological Insulator

We consider one of the simplest structures that support non-trivial topological properties. In one-dimensional (1D) systems, synthetic magnetic fields occur by lattice modulation [367] of the optical structure. In the Aubry-Andre-Harper (AAH) model [368, 369], identical sites - resonators, two-level atoms, waveguides, etc. - are centered at positions $z_n = d_o\left(n + \eta\delta_n^H\right)$, with n an integer label, d_o the primary lattice period, η the modulation strength and $\delta_n^H = \cos(2\pi\beta n + \phi)$ the Harper modulation [369]. The parameter β is the frequency of the Harper modulation. Together, β and the phase shift ϕ furnish the topological properties by a "two-dimensional ancestor" mapping [370]. The 2D ancestor is characterized by the dependence of the dielectric function on the coordinate z and on the parameter ϕ, which acts as a periodic artificial coordinate. Hence, the phase ϕ can be treated as a wave vector in a fictitious auxiliary direction [370]. For $\beta = p/q$, with $p > 0$ and $q > 0$ integers, the lattice displays two commensurate periods with q sites z_n in the unit-cell. Properly chosen parameters give rise to nontrivial topological phases with protected states at the border of the structure. These "edge-states" are hallmarks of topological insulators. The phase ϕ tunes edge-state eigenfrequency in the photonic band-gaps.

Our photonic topological insulator is an array of layers A of normalized thickness $\xi = L_A/d_o$ (characteristic size ratio), centered in z_n, in an homogeneous bulk of material B. This kind of structure can be effectively modeled by the transfer matrix technique [364, 371], as reported in Fig. 10.2a. In this figure A_0 and A_n are the initial and final amplitudes of the right-travelling waves; while B_0 and B_n are their equivalent for the left-travelling wave amplitudes.

Given the stepped and periodic dielectric function of period $D = qd_o$:

$$\varepsilon_\phi(z) = \begin{cases} \varepsilon_A, \text{if} z_n - L_A/2 \leq z \leq z_n + L_A/2 \\ \varepsilon_B, \text{if} z_n + L_A/2 \leq z \leq z_{n+1} - L_A/2 \end{cases}$$

in each layer the electric field can be represented as the superposition of a left- and a right-traveling wave. Applying the boundary conditions, the matrices

$$M_{\alpha\gamma} = \frac{q_\gamma + q_\alpha}{2q_\gamma}\begin{pmatrix} 1 & r_{\alpha\gamma} \\ r_{\alpha\gamma} & 1 \end{pmatrix}$$

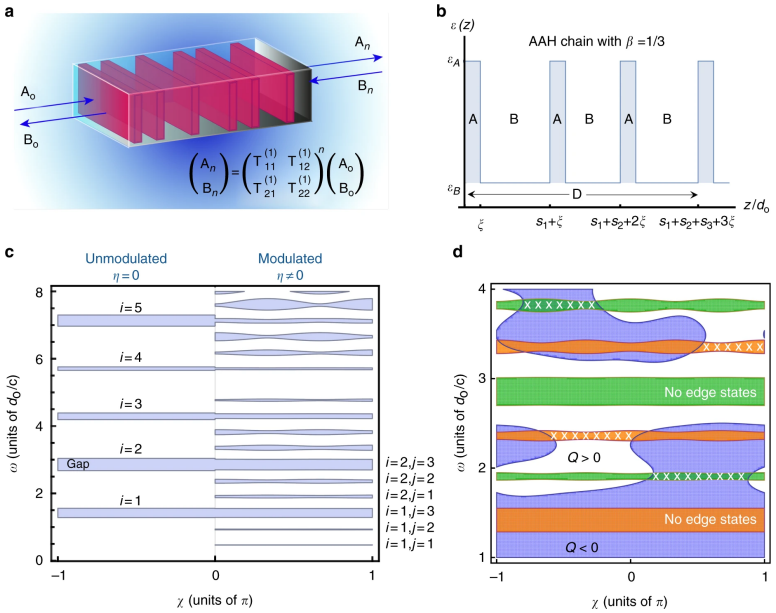

Figure 10.2: a) Scheme of the topological optical structure. b) Dielectric function profile for an AAH chain with $\beta = 1/3$, with $s_i = [z_{i+1} - z_i - L_A]/d_o$. c) Band diagram with $\chi = \phi + \pi(2\beta - 1)/2$. For $|\chi/\pi| > 1$ one can identify the gaps of the unmodulated structure (blue regions). The range $|\chi/\pi| < 1$ shows the gaps with Harper modulation: each gap of the unmodulated structures ($|\chi/\pi| > 1$) splits into q bands. d) Orange and green regions correspond to gaps. White areas indicate the regions where $Q(\omega, \chi, \xi) > 0$, blue the regions where $Q(\omega, \chi, \xi) < 0$. Edge states are possible only in the regions with crosses in orange and green gaps.

with $\alpha, \gamma = A \text{or} B$, and $r_{\alpha\gamma} = \frac{q_\gamma - q_\alpha}{q_\gamma + q_\alpha}$, describe the light propagation through the interfaces, having introduced $q_\alpha = (\omega/c)\sqrt{\epsilon_\alpha}$, while the propagation within each layer A and B is given by:

$$T_A = \begin{pmatrix} e^{iq_A d_o \xi} & 0 \\ 0 & e^{-iq_A d_o \xi} \end{pmatrix}, T_{B_n} = \begin{pmatrix} e^{iq_B d_o s_n} & 0 \\ 0 & e^{-iq_B d_o s_n} \end{pmatrix}$$

where $s_n = [z_{n+1} - z_n - L_A]/d_o$ are the normalized thicknesses of the B layers.

From these we obtain the transfer matrix for the single period $T^{(1)}(\omega)$, the matrix connecting the fields in the left side of the elementary cell to the ones in the right side:

$$T^{(1)} = \prod_{i=0}^{q-1} T_{B(q-i)} M$$

with $M = M_{AB} T_A M_{BA}$. The quantity $\rho = -\frac{1}{2} Tr T^{(1)}(\omega, \phi, \xi)$ allows one to locate bulk bands in the regions where $\rho^2 \leqslant 1$, and gaps where $\rho^2 > 1$. Alternatively, the amplitude $|r_\infty(\omega, \phi, \xi)|^2$ of the reflection coefficient of the structure [370]

$$r_\infty(\omega, \phi, \xi) = \frac{e^{ik(\omega)D} - T_{11}^{(1)}(\omega, \phi, \xi)}{T_{12}^{(1)}(\omega, \phi, \xi)}, \tag{10.1}$$

where $e^{ik(\omega)D}$ is an eigenvalue of the matrix $T^{(1)}(\omega, \phi, \xi)$, can also be used to locate the gaps of the system.

Figure 10.2a shows the final wave amplitudes A_n, B_n by the n-fold repeated action of $T^{(1)}(\omega, \phi, \xi)$ on A_0, B_0. The dielectric constant profile - for the case $\beta = 1/3$ - is schematically illustrated in Fig. 10.2b.

For $\eta = 0$, we have a periodic unmodulated structure with frequency bandgaps labeled by an integer i, with frequency $\tilde{\omega}_0 = \omega_0 d_0 / c = \pi / (\sqrt{\varepsilon_A} + (1 - \xi)\sqrt{\varepsilon_B})$. For $\eta \neq 0$, each gap of the unmodulated structure splits into q gaps, each one labelled by indices (i, j) $(j = 1, ..., q)$ [372]. This splitting is shown in Fig. 10.2c for $\beta = 1/3$ with respect to the variable $\chi = \phi + \pi(2\beta - 1)/2$.

To determine the existence of the edge states, one needs to specify the boundary conditions on each edge of the structure. For the left edge this condition is given by:

$$0 = (q_b + q_a) A_1 + (q_b - q_a) B_1$$

where A_1 and B_1 are the amplitudes of the right and left-travelling waves in the first layer of the structure. This condition can be reformulated as

$$det(b_1, a_1) = 0$$

with $b_1 = ((q_a - q_b), (q_a + q_b))^T$ and $a_1 = (A_1, B_1)^T$, and, together with the eigenvalues $\lambda_\pm$ and eigenvectors $v_\pm = (T_{12}^{(1)}, \lambda_\pm - T_{11}^{(1)})$ of the transfer matrix $T^{(1)}$, it is possible to determine existence and dispersion of edge states.

Following [373, 374], it can be, in fact, shown that a proportionality relation exists between the boundary vector b_1 and the eigenvectors $v_\pm$ of

the transfer matrix. So the condition for the existence of the edge states is given by $det(b_1, v_\pm) = 0$, in a gap where $|\lambda_\pm| < 1$. This entails searching for the zeros of the function $F_{l,\pm} = (q_A - q_B)(\lambda_\pm - T_{11}^{(1)}) - T_{12}^{(1)}(q_A + q_B)$.

Specifically, the real part of $F_{l,\pm} = 0$ yields the function $Q(\omega, \phi, \xi) = Re\{T_{12}^{(1)}(q_A + q_B) - (q_A - q_B)(T_{22}^{(1)} - T_{11}^{(1)})/2\}$ and, as shown in Fig. 10.2c, this implies that edge states exist only in the gaps where $|\rho| > 1$ and $Q(\omega, \phi, \xi) \cdot \rho > 0$. At the same time, edge states cannot exist in gaps where $Q(\omega, \phi, \xi)$ does not change sign. Moreover, due to a bulk-boundary correspondence [375], the number of these edge modes is equal to the modulus of the associated topological invariant $|\nu_{ij}|$, given by the winding number of the reflection coefficient:

$$\nu_{ij} = \frac{1}{2\pi i} \int_{-\pi}^{\pi} d\chi \frac{\partial ln(r_\infty(\omega, \chi))}{\partial \chi}, \tag{10.2}$$

i.e., the extra phase (divided by 2π) of $r_\infty(\omega, \chi)$ when χ varies in the range $(-\pi, \pi)$, with ω in the stop band [376].

By relying on the transfer matrix method, our approach can be applied to a general class of problems and thus makes it suitable for a wide range of systems beyond our baseline AAH model. Specifically, it can be extended to many physical systems whose behavior is described by a gapped unitary operator, e.g photonic Floquet topological insulators [355, 377] and photonic topological quantum walks [378]. Analogously to the AAH model, the edge states of these systems can be defined with an equivalent $F_{l,\pm}(\omega, p_1, ..p_n)$ function, where $(p_1, ..p_n)$ are relevant parameters describing the structure. The imaginary component of $F_{l,\pm}(\omega, p_1, ..p_n) = 0$ furnishes the dispersion relations of the edge modes and hence the training dataset of our ML inverse problem.

Implementation of Supervised Machine Learning Regression

As illustrated in Fig. 10.2d, enforcing boundary conditions at the left edge [373, 374], and defining the function $Q(\omega, \phi, \xi)$, enables one to establish the presence of edge states corresponding to poles ω_t of the reflection coefficient. However, the function $\omega_t = \omega(\chi, \xi)$ cannot be analytically inverted to express the geometrical parameters χ and ξ in terms of the variable ω_t. Exploiting ML techniques, we solve this inverse problem and design topological insulators with target edge modes.

The inverse problem in ANN theory - and therefore in ML - is widely discussed in numerical modelling, engineering and other fields [379–383]. Regression in ML optimizes an ANN so that a given vector input ($\mathbb{R}^n$) results in a scalar ($\mathbb{R}$) output, emulating the behaviour of the training

data. For our purposes, we use a regressive ANNs approach, with $g(x) = \tanh(x)$ the activation function, as common, accepted practice.

Optimization of the ANN is performed by minimizing a cost function by a gradient descent method that updates weights and biases. In the initial state, weights w_{ijkl} are selected from a truncated normal and biases are set to zero. Training applies this procedure to a data-set randomly split into two separate classes: (i) an actual training set and (ii) a validation set. The network is iteratively updated until the error on the validating data-set converges to a given rate.

The inverse topological problem at hand is to obtain the desired optical behaviour: a target edge-state at frequency ω_t, which is an input to the design (Fig. 10.1a). ML techniques achieve this result by modeling the multidimensional nonlinear relationships among all the structure parameters ω_t, χ, β, ϵ_A, ϵ_B and ξ. In our specific case, the data-set fixes ϵ_A, ϵ_B, β at the values $\epsilon_A = 9$, $\epsilon_B = 4$ and $\beta = 1/3$.

First we generate a data-set to train our ANNs by numerically computing the complex roots of $T_{12}^{(1)}(\omega, \chi, \xi)$, covering the region of interest for parameters χ and ξ. The real part of these roots, shown in Fig 10.3a, represents the edge states dispersion. Interestingly, the same data-set can be used both for the inverse and direct ANN training phase, by suitably selecting the features and target fields. The inverse problem ANN (Fig. 10.1a) targets a value $\chi = \chi_o$, a topological parameter on the basis of features including ω_t. For a direct problem (Fig. 10.1b), the mode frequency ω_t would be the target of a network whose features include the topological parameters (χ, ξ).

The data-set contains various branches, since there exists an edge state for each band gap (i, j) with $j \neq 3$, as results by Eq. (10.2). Due to the folding of the Brillouin zones, the edge state frequency $\omega(\chi, \xi)$ is then a multi-mode function, which we unfold by introducing a label $m_{ij}^{\pm}$ for each mode; here $i = 1, ...\infty$ and $j = 1, ...q$, while the sign $\pm$ indicates modes in the positive/negative χ domain. In Fig. 10.3a, data points with different i, j values are identified with different colors and, solving the inverse problem is a matter of determining when these surfaces intercept a specific target value of the ω axis. Three outcomes are possible: a single value for χ and ξ when a monotonic mode surface is intercepted, no solution for values of ω laying between surfaces, and multiple solutions in other cases. This implies that the feature set (χ, ξ, $m_{ij}^{\pm}$) is insufficient. To tackle this problem, we take into account the trend $s_{\pm} = \text{sgn}\,(d\omega_t/d\chi)$ as an additional variable. The ANNs with this enlarged feature set are illustrated in Figs. 10.1a,b.

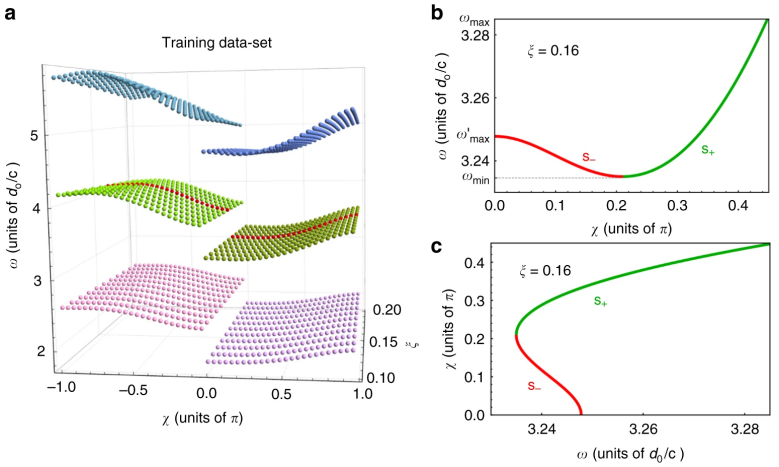

Figure 10.3: a) The training dataset. Points are the real component (mode frequencies) of the complex roots of the function $T_{12}^{(1)}(\omega, \chi, \xi)$. b) Edge state dispersion for a specific mode and ξ value, exhibiting a positive s_+ (green) and negative s_- (red) trend. c) Multivalued relationship of features and targets for the same edge mode dispersion. The $s_\pm$ labels are used for training the inverse model.

In the terminology used in ML, the mode indices $m_{ij}^{\pm}$ and trend labels $s_\pm$ are *categorical features* and lead to two possible courses of action for the actual implementation of the ANNs used in our problem. One in which a single ANN is constructed in a hybrid feature space with both continuous variables (real valued ξ's and χ's) and categorical features, as illustrated in Fig. 10.1b. Another course is to adopt multiple independent ANNs, one ANN for each mode and each trend.

The single ANN approach is hindered by the presence of discontinuities in the features domain: with respect to the ω variable they are a consequence of the fact that edge states fall within the bulk energy gaps; with respect to the χ variable these arise from considering only the left-edge states. Fig. 10.3a clarifies this aspect. Due to these discontinuities we have chosen to use multiple independent ANNs. Moreover, when considering the solution provided by the inverse ANNs, we identify a specific problem in the use of ML as they may furnish solutions that are not physical. An example of this issue is given in Fig. 10.3b, where - for a fixed band and a fixed ξ - the curve representing ω as a function of χ is shown together with its inverse (Fig. 10.3c). Inverting the function $\omega(\chi)$, we consider an interval of values for ω spanning from its minimum ω_{min}

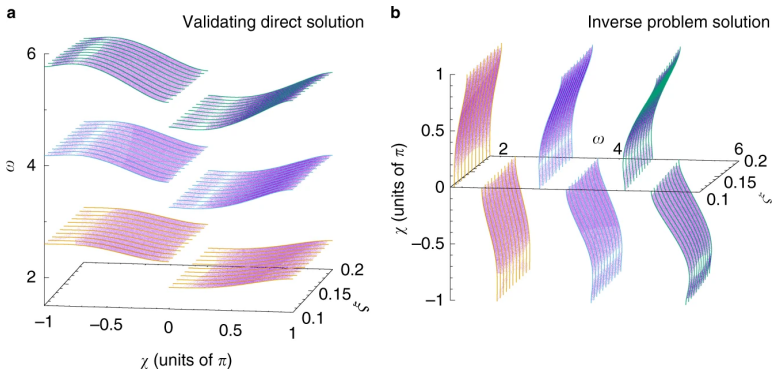

Figure 10.4: Reconstruction of edge states dispersion by ANN models. a) Direct problem solution as reproduce by our self-consistent cycle. b) Inverse problem solution. ω is in units of d_0/c.

to the maximum ω_{max}, but for the two branches of the inverse function $\chi(\omega)$ - identified by colors in Fig. 10.3c - the range of ω is different. For example, for the red branch the maximal value of ω is $\omega'_{max} < \omega_{max}$. When the target frequency is outside this range, the ANN produces an output outside the physically acceptable range for χ. The inverse ANN can furnish spurious non-physical solutions.

Our approach tackles this issue by a two-step self-consistent cycle: (i) in the first stage, a desired input ω_t forms part of the feature set $(\omega_t, m_{ij}^{\pm}, s_{\pm})$ resulting in the output χ_o of the inverse ANN; this set is used as input $(\chi_o, m_{ij}^{\pm}, s_{\pm})$ to a direct problem network; (ii) in the second stage, the target of this direct network ω_{sc} is compared with the input value ω_t and χ_o is retained as a solution of the inverse model if $|\omega_{sc} - \omega_t| < \delta$ with δ a user-defined small positive quantity. The value of δ affects the model accuracy. A reasonable choice can be $\delta \sim E_j^{max}$ (with j=I,D), i.e., the maximum value of the squared error functions for the inverse (I) and the direct (D) networks.

In details, let us consider as target a smooth, non monotic function $\omega_t(\chi)$. Without loss of generality, $\omega_t(\chi)$ may have two regions of monoticity: it decreases from $\omega_t = \omega'_{max}$ to $\omega_t = \omega_{min}$ for $\chi \in (0, \chi_1)$, and increases from $\omega_t = \omega_{min}$ to $\omega_t = \omega_{max}$ for $\chi \in (\chi_1, 1)$, with $\omega_{min} < \omega'_{max} < \omega_{max}$, $0 < \chi_1 < 1$. When we use an inverse ANN to compute $\chi_o(\omega_t)$, ML is engineered in a way such that it generalizes the solutions and associates to every $\omega_t \in [\omega_{min}, \omega_{max}]$ a value $\chi_o \in [0, 1]$ for each branch, producing new, unphysical values for $\omega_t \in (\omega'_{max}, \omega_{max}]$.

These values must be eliminated. To avoid the solution generalization, we test the self-consistency by the procedure sketched in Fig. 10.5. After the training stage, implemented through numerically computed data (ω, χ, ξ), we use an inverse ANN with input (ω_t, ξ) to attain an output χ_o. In order to have the unfolding and determine in advance the slope of $\omega_t(\chi)$ in its different branches, we add the mode index $m_{ij}^{\pm}$ and the trend $s_{\pm}$ as inputs. To clarify the idea, let us fix the normalized thickness ξ and the mode index $m_{ij}^{\pm}$: we have two correspondences, i.e., on one hand

$$(\omega_t, s_-) \longrightarrow (\chi_o, s_-), \tag{10.3}$$

on the other hand

$$(\omega_t, s_+) \longrightarrow (\chi_o, s_+). \tag{10.4}$$

While Eq. (10.4) associates $\omega_t \in [\omega_{min}, \omega_{max}]$ to $\chi_o \in [\chi_1, 1]$, Eq. (10.3) should associate just $\omega_t \in [\omega_{min}, \omega'_{max}]$ to $\chi_o \in [0, \chi_1]$, but ML produces extra values. Hence, how may we be sure that χ_o corresponds to a physical solution, i.e., χ_o does not belong to a forbidden region? We need to test the validity of our result by a direct ANN that takes the previous values $(\chi_o, \xi, m_{ij}^{\pm}, s_{\pm})$ as input and gives back a self-consistent output ω_{sc}. In order to complete our cycle, we need to compare the resulting value ω_{sc} with the input ω_t by the choice of a tolerance δ, which affects the model accuracy. Finally, if $|\omega_{sc} - \omega_t| < \delta$, then χ_o is accepted as solution of the inverse model, otherwise it is discarded.

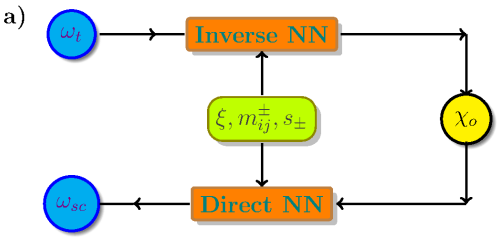

Figure 10.5: Scheme of the self-consistent procedure for the ML inverse problem solution.

The training dataset is generated with eleven sets of ξ ranging from 0.10 to 0.20 in steps of 0.01 and for each set χ spans $-\pi$ to π with 997 equally spaced values. Results based on using an array of ANNs each composed of 5 hidden layer of 131 nodes are shown in Fig. 10.4 together

with its training set (colored lines). The model is developed using 80% of the dataset randomly chosen the rest being used for validation and comprising of 250,000 steps. Training each model takes about 8 minutes on our hardware using a single Nvidia GP-GPU Tesla K20c. The purple dots in Fig. 10.4 are based on 100 values of ξ while exploring the ω domain with a resolution of 10^{-5}. Each array element is trained for a specific value of the categorical features and pertains to either the positive or the negative χ domain.

The results of applying the direct and inverse ANNs, portrayed in Figs. 10.4a,b, respectively, show that the proposed method gives accurate solutions matching the original data in the whole range of interest. Figure 10.4 clearly shows that our ML strategy solves the inverse topological design problem.

To implement the ML algorithm we use TF. TF is Google's versatile open-source multiplatform dataflow library capable of efficiently performing ML tasks such as implementing ANNs. Multidimensional data arrays, referred to as "tensors" are executed on the basis of stateful dataflow graphs, hence the name TF. For our final code implementation, TF version 1.3 with python Application Program Interface (API) bindings is used.

The nature of our problem is such that there is a discontinuity in $\xi = 0$ which cannot be correctly handled by a single ANN bridging this point; this is relevant to both the inverse and direct cases. Breaking up the data-set into two parts to be used for two separate ANNs is the simplest solution to this problem.

Another interesting aspect is related to the fact that the feature set in our inverse and direct ANNs contain both continuous and discrete variables. The discrete variables can either be treated as such or handled by constructing multiple ANNs each relative to a specific value of the discrete variable. The trend variable which has two possible values is one such case as is the mode number. In our code we have implemented a flexible system which allows one to decide which discrete variables are to be included in each ANN, the others being broken up into arrays of ANNs one for each value of the variable. Once the bookkeeping issues have been tackled,this generalized approach allows one to tailor the problem to the given data-set.

CONCLUSIONS

The inverse problem in topological design is solved by a supervised ML regression technique. We employ a self-consistent procedure to rule out unphysical solutions enabling tailored engineering of protected edge-states. We successfully tackle multivalued functions introducing categorical features, as the trend, which tags training data according to their gradient's sign. Discontinuous domains are effectively treated by adopting multiple independent ANNs each one specific to its domain. Our general method can be extensively applied - well beyond the example considered in this work - and may also be exploited for other physical systems in topological science, as polaritonics [384, 385], quantum technologies and ultra-cold atoms [386, 387]. The method is scalable to very complex structures involving hundreds of topological devices, as those recently considered for large scale synchronization [388], and frequency comb generation [389], eventually including non-hermitian systems [390, 391]. Further applications include 2D and 3D topological systems [359] and quantum sources and simulations [365, 366].

11 RANDOM NEURAL NETWORKS IN DISORDERED MEDIA

INTRODUCTION

In the long path for designing all-optical machines, able to do computation, Chapter 9 and this Chapter, together, show our main results on the engineering of photonic computers. In Chapter 9, the realization of a scalable Ising machine is illustrated, and its relevance towards the fulfilment of our aspiration of building all-optical machines able to solve NP-Complete problems drives us to do many other attempts. The theoretical design of a random optical machine, where light transmission in random media turns out to act as an ANN architecture, performing untrained ML, is undeniably an important achievement in that direction, and it is here illustrated, together with applications to quantum gates implementation.

Random media with tailored optical properties are attracting for applications in many areas, such as imaging, biophysics, energy, nanomedicine, spectroscopy, cryptography, and telecommunications [1, 392–396]. The transmission of light in the presence of diffusion and multiple scattering can be effectively controlled by manipulating its wavelength, polarization, and spatiotemporal dynamics [397–400]. This rich behavior is enabled by a large multitude of optical modes that can interact during propagation [401, 402].

A key paradigm for describing this modes interaction is the transmission matrix, the tensorial link between the input and the output signals, completely measurable even in case of nonlinearity [403, 404]. The transmission matrix has specific statistical properties, such as the existence of lossless channels, that can be used to transmit information, and are determined by the disorder distribution. Lossless channels may be modulated and the transmission matrix tuned accordingly. Typically, this approach is based on iterative algorithms that modify the state of the light at the input of the random material, until a predetermined figure of merit is obtained at the output.

This approach can be implemented very efficiently [405–409]. The trait of this technique is that it treats the random material as a black box, in which light is efficiently coupled to and transported by transmission channels created by long-range intensity correlations, as a result of

interference effects [410, 411]. In essence, the random medium acts as an untrained ANN with a large number of weights, each one optimized iteratively by tuning input and readout.

It turns out, by electromagnetic perturbation theory, that weakly tampering the medium with external factors, such as changing enviroment temperature or adding chemical agents, alters the transmission matrix, which at the new steady state is given by the product between the previous matrix and a further one. So forth, the higher the number of perturbations is, the longer the product between transmission matrices is.

In standard ML, one trains the parameters (*weights*) of an ANN to fit a given function linking input and outputs. In reservoir computing [412, 413], due to the increasing computational effort to train a large number of weights, one internal part of the network is left untrained ("the reservoir") and the weights are optimized only at input and readout. If each transmission matrix represents a ANN hidden layer, we are moving from an extreme learning machine (unperturbed system) to untrained deep learning (many perturbations). In any case, we obtain a random optical machine working through reservoir computing, as demonstrated in what follows.

TRANSMISSION THROUGH DISORDERED MEDIA

We first review the Green function formalism [404, 409, 414], which shows the way light propagation in a complex medium is mapped to an ANN model.

We follow [409], and adopt the Dirac notation formalism, which is handy for classical vectorial waves. This notation is detailed in the book by Economou [414]. The field scattered by a random medium is $|\mathbf{E}\rangle = \mathbf{K}|\mathbf{E}^{\text{in}}\rangle$, where $|\mathbf{E}^{\text{in}}\rangle$ is the incident field, $\mathbf{K} = \mathbb{1} - \mathbf{G}\mathbf{e}_s$ is a generalized propagator [415], $\mathbb{1}$ is the identity operator, and the Green function $\mathbf{G}$ is such that

$$(\boldsymbol{\mathcal{D}} + \mathbf{e})\,\mathbf{G} = \mathbb{1}. \tag{11.1}$$

In Eq. ((11.1)), $\boldsymbol{\mathcal{D}}(\mathbf{r}) = -\nabla \times \nabla \times$, and $\mathbf{e} = \mathbf{e}_b + \mathbf{e}_s$ is the operator given in terms of the position representation

$$\langle \mathbf{r}|\mathbf{e}|\mathbf{r}'\rangle = k_0^2 \varepsilon(\mathbf{r})\delta(\mathbf{r} - \mathbf{r}'), \tag{11.2}$$

associated to the relative permittivity $\varepsilon(\mathbf{r}) = \varepsilon_b(\mathbf{r}) + \varepsilon_s(\mathbf{r})$, with $\varepsilon_b(\mathbf{r}) = 1$ the permittivity of the homogenous background medium and $1 + \varepsilon_s(\mathbf{r})$ the relative permittivity of the scattering medium.

In the position representation $\mathbf{r}$, the propagator reads

$$\langle \mathbf{r}|\mathbf{K}|\mathbf{r}'\rangle = \delta(\mathbf{r} - \mathbf{r}') - k_0^2 \varepsilon(\mathbf{r}')\langle \mathbf{r}|\mathbf{G}|\mathbf{r}'\rangle, \tag{11.3}$$

and its matrix elements are

$$k_{mn} = \langle m|\mathbf{K}|n\rangle, \tag{11.4}$$

where $|n\rangle$ corresponds to input/output eigenmodes, or "channels" (as detailed in [409]), with $n = 1, ..., N$.

Given the input field $|\mathbf{E}^{\text{in}}\rangle$, one can choose a basis representation such that the input is represented by a vector $(E_n^{\text{in}})_{n=1,...,N}$. Since, in our random optical machine, we design the input by a SLM set in the Fourier input plane, we choose to represent each n as a different plane wave corresponding to each segment in the SLM. The SLM pixels are grouped in a number N of segments and, as also detailed below, the SLM and the related Fourier-transforming optics act as an optical convolutional ANN layer. As the total field in the presence of the scatterer is $|\mathbf{E}\rangle = \mathbf{K}|\mathbf{E}^{\text{in}}\rangle$, one can represent the trasmission through the system by the matrix elements k_{mn} such that, letting $E_n = \langle n|\mathbf{E}\rangle$. One obtains

$$E_m = \sum_{n=1}^{N} k_{mn} E_n^{\text{in}}. \tag{11.5}$$

Equation ((11.5)) can be represented as in Fig. 11.1a: to the input mode with amplitude E_n^{in} is associated the input node n, for the output node with amplitude E_m we have the output node m, and the link is weighted by the coefficient k_{mn}. A schematic representation of the overall network is in Fig. 11.1b, with $\mathbf{x}$ denoting the input vector with components $x_n = E_n^{\text{in}}$ and $n = 1, 2, ..., N$, while $\mathbf{y}$ is the output vector, with components $y_n = E_n$ and $n = 1, 2, ..., N$.

EFFECT OF PERTURBATIONS

In the presence of the perturbation, the perturbed propagator is

$$\mathbf{K}' = \mathbb{1} - \mathbf{G}'\mathbf{e}', \tag{11.6}$$

with $\mathbf{G}'$ the perturbed Green's function such that

$$\left(\boldsymbol{\mathcal{D}} + \mathbf{e}_b + \mathbf{e}_s + \mathbf{e}'\right)\mathbf{G}' = \mathbb{1}, \tag{11.7}$$

and $\mathbf{e}'$ is the operator associated to the perturbed permittivity $\Delta\varepsilon(\mathbf{r})$, where $\varepsilon(\mathbf{r}) = \varepsilon_b(\mathbf{r}) + \varepsilon_s(\mathbf{r}) + \Delta\varepsilon(\mathbf{r})$ is the total relative permittivity.

The field in the presence of perturbation $|\mathbf{E}'\rangle$ can be then expressed in terms of the state without perturbation $|\mathbf{E}\rangle$ and the input state $|\mathbf{E}^{\text{in}}\rangle$ as operator multiplication

$$|\mathbf{E}'\rangle = \mathbf{K}'|\mathbf{E}\rangle = \mathbf{K}'\mathbf{K}|\mathbf{E}^{\text{in}}\rangle. \tag{11.8}$$

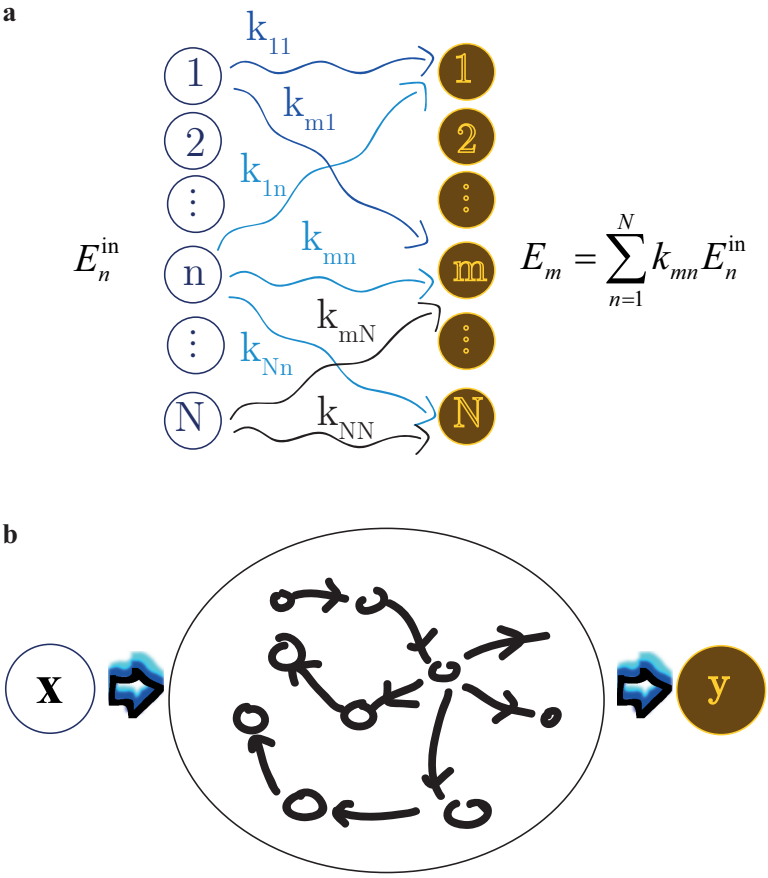

Figure 11.1: Representing light propagation in a random medium as a layer of an ANN with random coefficients. (a) Dense layer representing Eq. 11.5. (b) Representation of the random layer.

Correspondingly, the transmission matrix elements k^{P}_{mn} in the presence of the nonlinear perturbation are written as results of a matrix multiplication

$$k^{(\text{P})}_{mn} = \sum_{q=1}^{N} k'_{mq} k_{qn}. \tag{11.9}$$

To simplify the notation, we omit in the following the sum over repeated indices, and Eq. ((11.9)) reads

$$k_{mn}^{(\mathrm{P})} = k'_{mq} k_{qn}. \tag{11.10}$$

In addition, we introduce a tensorial notation by using a three index tensor k_{mnq}, such that

$$k_{mn1} = k_{mn}, \tag{11.11}$$

$$k_{mn2} = k_{mn}^{(P)} \tag{11.12}$$

. This notation is useful when one has many layers, and each layer corresponds to a different value of the third index q. In this notation, Eq. ((11.9)) reads

$$k_{mn2} = k'_{mq} k_{qn1}. \tag{11.13}$$

By using (11.6), the element of the rotation matrix k'_{mq} is written as

$$k'_{mq} = \delta_{mq} + w_{mq}, \tag{11.14}$$

with δ_{mq} the Kronecker symbol and the perturbation elements

$$w_{mq} = -\langle m|\mathbf{G}'\mathbf{e}'|q\rangle. \tag{11.15}$$

The element of the perturbed matrix can then be written as

$$k_{mn2} = k_{mn1} + w_{mq} k_{qn1} = k_{mn1} + w_{m1} k_{1n1} + ... + w_{mN} k_{Nn1}. \tag{11.16}$$

Eq. (11.16) is graphically represented in Fig. 11.2, and can be interpreted as follows: in the absence of perturbation, light is channelled - with amplitude k_{mn} - from the channel n to the channel m (see Fig. 11.2a). In the presence of the perturbation, further contributions arise from other channels. For example, the light channeled from n to 1 with amplitude k_{1n} also contributes to the signal in the channel m with amplitude w_{1m} (see Fig. 11.2b). This may be described by stating that any perturbation adds further channels for light by scattering from one unperturbed channel to another or, in terms of ANNs, this corresponds to a new layer whose weights w_{mn} are proportional to the strength of the perturbation. This is sketched in Fig. 11.3: in the presence of the perturbation, the input signal $\mathbf{x}$ activates an hidden layer with state vector $\mathbf{h}^{(1)}$ and elements h_{m1}, such that

$$h_{m1} = k_{mn1} x_n, \tag{11.17}$$

and the hidden layer activates the output layer as

$$y_m = k'_{mq} h_{q1} = k'_{mq} k_{qn1} x_n = k_{mn2} x_n. \tag{11.18}$$

This analysis shows how to implement ANNs by the mean of random (or multimodal) media. It also demonstrates that these ANNs can be multi-level, depending on the number of perturbations, since each perturbation adds a new hidden layer to the ANN. Such an approach has already been applied to a biological system [1], which worked as a random medium, to study the growth of brain tumor spheroids in the absent (unperturbed case) and the presence (perturbed case) of chemotherapy. In what follows, we illustrate another application of the random optical machine to the design of quantum gates. For this purpose, we do not use a random medium, but a multimodal one, such as a multimodal fiber, where the random optical machine is easier to implement [27, 409].

IMPLEMENTATION OF QUANTUM GATES

The development of multilevel quantum information processing systems has steadily grown over the past few years, with experimental realizations of multi-level, or qudit, logic gates for several widely used photonic degrees of freedom, such as orbital-angular-momentum and path encoding [416–419]. However, efforts are still needed for increasing the complexity of such systems while, still being practical, with the ultimate goal of realizing complex large-scale computing devices that operate in a technologically efficient manner.

Here we adopt reservoir computing-ML to design complex multi-level gates [417, 418, 420, 421], which form a building block for high-dimensional quantum information processing systems. While low-dimensional examples of such gates have been implemented using bulk and integrated optics, efficiently scaling them up to high dimensions remains a challenge. We explore methodologies to train the input and the output gates by using different implementations of ML concepts.

Figure 11.4 shows the scheme of a device including the complex medium, represented by the unitary operator $\hat{U}$ and two trainable input $\hat{S}^{\text{in}}$ and readout $\hat{S}^{\text{out}}$ operators. The use of an optical gate as in Fig. 11.4 is also related to a Quantum Key Distribution (QKD) with Physically Unclonable Function (PUF) [276, 422, 423]. A PUF may be realized by a random medium to authenticate an object or data. Top panels in Fig. 11.4a display the concept by introducing input/output readout operators that provide a programmable gate. Assuming (bottom panels in Fig. 11.4b) that one has two q-dits as input, one $|c\rangle$ acting as a "control", and the

other acting as the "challenge" $|\psi\rangle$. The challenge/response relation will depend on the control and the training. $|h^{(1,2)}\rangle$ are hidden states.

In our general framework, we have a random system modeled by a unitary random matrix. We want to use the random medium to perform a random optical machine in a Hilbert space containing many q-dits. The random medium is not necessarily a disordered system (for example, a dielectric assembly of scattering particles), but may also be a multimode fiber, or an array of waveguides. The input/output relation is represented by a linear unitary matrix operator U_M and only forward modes are considered. The U_M matrix has dimensions $M \times M$, with M the dimension of the *embedding space*.

The "reduced" state vector at input has dimensions $N \times 1$, with $N \leq M$. This models the case in which we use a subset of all the available modes. The input to the reservoir is a "rigged" state vector $\mathbf{x}$ with dimension M, where the missing complementing C components are replaced by C *ancillas* with $C = M - N$. Our goal is to use the random medium to perform a given operation denoted by a gate unitary matrix

$$T_M = S_M^{\text{out}} \cdot U_M \cdot S_M^{\text{in}}. \tag{11.19}$$

S_M^{in} and S_M^{out} are two "training" operators that are applied at input and output (see Fig. 11.4), and whose elements can be adjusted. We first consider the presence of the input operator $S_M^{\text{in}} = S_M$, and $S_M^{\text{out}} = \mathbb{1}_M$, which can be implemented by SLMs (we denote as $\mathbb{1}_M$ the identity matrix with dimension M).

We identify two cases:

(i) we know the matrix U_M,

(ii) we have to infer U_M from the input/output relations.

In the following, we show the way these two problems can be solved by an ANN, where we denote the two families as (i) *non-inferencing* and (ii) *inferencing* gates.

Non-inferencing Gates

We consider a target gate with complex-valued input state with dimension N, and components $x_1, x_2, ..., x_N$. We embed the input vector in a RHS with dimension $M \geq N$, thus the overall input vector is $\mathbf{x} = \{x_1, x_2, ..., x_N, x_{N+1}, ..., x_M\}$. We have a linear propagation through a medium with unitary complex transmission matrix U_M. The overall transmission matrix is $T_M = U_M \cdot S_M$, such that the output vector is $\mathbf{y} = T_M \cdot \mathbf{x} = U_M \cdot S_M \cdot \mathbf{x}$. The observed output vector is written as $P \cdot \mathbf{y}$,

where P is a $N-$projector operator with dimensions $N \times M$, such that $P = [\mathbb{1}_N|\mathbf{0}]$, with $\mathbb{1}_N$ the identity matrix of size $N \times N$, and $\mathbf{0}$ a null matrix of dimension $N \times C$. The goal is to find the matrix S_M such that

$$P \cdot U_M \cdot S_M = [X_N|\mathbf{0}], \tag{11.20}$$

where X_N is the $N \times N$ target gate and $\mathbf{0}$ is the null complement $N \times C$ at dimension M. Eq. (11.20) is a matrix equation, which guarantees that the overall system behaves as a X_N gate on the reduced input. Solving the matrix Eq. (11.20) may be demanding and non-trivial when the number of dimensions grows. In the following, we discuss the use of ML techniques.

The transmission matrix T_M in the rigged space from $\mathbf{x}$ to $\mathbf{y}$ can be written as blocks

$$T_M = \left[\begin{array}{c|c} X_N & \mathbf{0} \\ \hline \mathbf{0} & O_C \end{array}\right], \tag{11.21}$$

where O_C is a unitary matrix with dimensions $C \times C$ to be determined. If U_M and S_M are unitary, the resulting transmission matrix T_M is also unitary. However, if one uses Eq. (11.20), the problem may also have a nonunitary solution ("projected case") as some channels are dropped at the output. In other words, solving Eq. (11.21) is not equivalent to solving Eq. (11.20), and we adopt two different methodologies: one can look for unitary or nonunitary solutions by ANN.

By following previous work developed for real-valued matrices [424], we map the complex-valued matrix equation ((11.20)) into a recurrent ANN. In the *non-inferencing* case, the matrix U_M is known, and the solution is found by the recurrent ANN in Fig. 11.5. The recurrent ANN solves an unconstrained optimization problem by finding the minimum of the sum of the elements $e_{ij} > 0$ of an error matrix E. The error depends on a "state matrix" W_M, and one trains the elements w_{ij} of W_M to find the minimum

$$\min_{W_M} E[G(W_M)] = \min_{W_M} \sum_{i,j} e_{ij}[G(W_M)]. \tag{11.22}$$

In the adopted approach, the sum of the elements e_{ij} is minimum when the hidden layer elements g_{ij} of the matrix $G(W)$ are zero. E and G have to be suitably chosen to solve the considered problem. We found two possible G matrices: (i) the "projected" one

$$G_P = P \cdot U_M \cdot W_M - X_{N0}, \tag{11.23}$$

with $X_{N0} = [X_N|\mathbf{0}]$ as in Eq. (11.20) and, (ii) the "unitary" one (see eq. 11.21)

$$G_U = U_M \cdot W_M - T_M. \tag{11.24}$$

These two cases are discussed below.

To find the unknown training matrix S_M, one starts from an initial guess matrix $W_M(0)$. The guess is then recurrently updated, as in Fig. 11.5, until a stationary state $W_M(\infty)$ is reached. Once this optimization has converged, the solution is given by $S_M = W_M(\infty)$. The update equation is determined by a proper choice of the error matrix E.

As the matrices are complex-valued, e_{ij} is a function of g_{ij} and g_{ij}^*. We set $e_{ij} = e_{ij}(|g_{ij}|^2)$. The corresponding dynamic recurrent ANN equation, which for large time gives the solution to the optimization problem, is

$$\frac{dW_M}{dt} = -\mu U_M^\dagger \cdot F[G(W_M)], \tag{11.25}$$

where μ is the "learning rate", an optimization coefficient (hyperparameter) which is set to speed-up the convergence. The elements f_{ij} of the matrix F are $f_{ij} = \frac{de_{ij}}{dg_{ij}^*}$. Letting $e_{ij} = |g_{ij}|^2$, one has $f_{ij} = g_{ij}$.

Eq. ((11.25)) implies that the recurrent ANN is composed of two bidirectionally connected layers of neurons, the output layer with state matrix W, and the hidden layer with state matrix G. The training corresponds to sequential updates of F and W when solving the Ordinary Differential Equation (ODE) ((11.25)). As shown in [424], this recurrent ANN is asymptotically stable and its steady state matrix represents the solution (an example of training dynamics is in Fig. 11.5b).

We code the recurrent ANN by TF and use the ODEs integrator *odeint*. In the case $N = M$, as $X_N = X_M$ is a unitary operator, the solution of the recurrent ANN furnishes a unitary S_M matrix, which solves the problem. For $M > N$ the recurrent ANN furnishes a unitary solution S_M - and a unitary transfer function T_M - only if we embed the target gate X_N in a unitary operator as in ((11.21)) with O_C a randomly generated unitary matrix.

Single Non-inferencing Q-trit X Gate

We study the training of a gate X_3 defined by [417]

$$X_3 = \sum_{l=0}^{d-1} |l \oplus 1\rangle\langle l| = \begin{bmatrix} 0 & 1 & 0 \\ 0 & 0 & 1 \\ 1 & 0 & 0 \end{bmatrix}. \tag{11.26}$$

The gate X_3 is obtained by an embedding dimension $M = 5$ and unitary transfer function U_5, as in Fig. 11.5.

For $G = G_P$, the number of ODEs for the training of the network is minimal ($N = 3$), but the solution is not unitary, as some channels are

dropped out by the $N-$projector. The overall $M \times M$ transmission matrix, after the training, T_M is such that $T_M^\dagger \cdot T_M \neq I$, because the solution S_M is not unitary. However, the system always reaches a stationary case.

A unitary solution is found by letting $G = G_U$ and involving the maximum number M of ODEs in ((11.25)) with a unitary embedding of X_N as in ((11.21)), i.e., adopting a further - randomly generated - unitary matrix O_C. The key point is that the system *finds a solution for any random unitary rigging of the matrix* X_N, that is, for any randomly assigned matrix O_C. This implies that we can train all these systems to realize different multilevel gates.

Inferencing Gates

In the case that we do not know the transmission matrices of the system, we can still train the overall transmission matrix by using an ANN and infer U_M. Here we use an ANN to determine the training operators without measuring the transmission matrices. Figure 11.6 shows the scheme of the ANN, where the unitary matrix U_M is represented by its elements u_{ij}, and the w_{ij} are the adjustable weights. After the training, the resulting w_{ij} are the elements of the solution matrix S_M. For the sake of simplicity, we first consider $\hat{S}^{\text{out}} = \mathbb{1}_M$, as above. For a target X_N, we build the T_M as in (11.21) by randomly generating the unitary complement O_C. As T_M and U_M are unitary, the resulting S_M is also unitary. One can use a non-unitary T_M by choosing, for example, $O_C = 0$, correspondingly - after the training - S_M is not unitary.

We randomly generate a set of input states $\mathbf{x}_i$, with $i = 1, ..., n_{train}$. Each input state is labelled with the target output $\mathbf{y}_i = T_M \cdot \mathbf{x}_i$. We remark that $\mathbf{x}_i$ and $\mathbf{y}_i$ are vector with size M. A further set of n_{valid} validation rigged vectors is used to validate the training.

For any input $\mathbf{x}_i$ in the training set, we adjust the weights to minimize the error function

$$e_i = \frac{1}{N} \sum_N |\mathbf{y}_i - U_M \cdot W_M \cdot \mathbf{x}_i|^2, \tag{11.27}$$

with $\mathbf{y}_i = T_M \cdot \mathbf{x}_i$. After this training, we test the accuracy on the validation set. Each cycle of training and validation is denoted as *epoch*.

Figure 11.6 shows the ANN for $N = 3$, and $M = 5$. In our model, we build a matrix W_M of unknown weights. As we deal with complex quantities, W_M is written as $W_M = W'_M + \imath W''_M$, where W'_M and W''_M are real-valued matrices with elements forming the weights of the ANN. Using random matrices as initial states, we end the iteration when the validation cost is below a threshold ε_{valid}.

Single Q-trit Inferencing X Gate

Figure (11.6) shows the training of a single q-trit gate X_3 in 11.26. Similar results are obtained with other single q-dit gates as X^2 and Z. Training typically needs tens of iterations and scales well with the number of dimensions. Figure 11.6 shows an example with $N = 3$ and $M = 5$. Figure 11.6c shows that the number of training epoch n_{epochs} scales with the embedding space dimension M.

Generalized Q-trit Gate

We next consider the implementation of a generalized q-trit gate $\hat{\text{CNOT}}$, shown in Fig. 11.7. The gate is obtained by training a random system with a unitary transmission matrix U_9 by using an input layer S_9^{in}. In this case, we consider $N = M = 9$ corresponding to the dimensional space of two q-trits (one control and one challenge/response, denoted as *target*). Other controlled q-trits gates can be realized, as Feynman gates or GXOR [421].

Figure 11.7a shows the input/output matrix $\hat{S}^{\text{in}} = A$, obtained after the training when $\hat{S}^{\text{out}} = \mathbb{1}_9$. One can also figure out other configurations, for example by employing a double passage in the random system, such $\hat{S}^{\text{out}} = U_9$, with $U = U_9$. In this case, the previous input matrix $\hat{S}^{\text{in}} = A$ does not produce the correct result, as shown in Fig. 11.7b. One has to calculate a novel input matrix $\hat{S}^{\text{in}} = B$, as described in Figs. 11.7c,d.

This analysis may be the starting point for designing cryptographic quantum transmission systems with PUF.

CONCLUSIONS

Random materials, appearing as black boxes, transmit light through transmission channels, created by long-range intensity correlations. The result is that random media acts as an untrained ANN with a large number of weights, each one optimized iteratively by tuning input and readout. In essence, a random medium by itself is an extreme learning machine. When we weakly tamper the medium with external stimuli, we add layers to our ANN, and the architecture becomes deep. Thanks to this principle, here demonstrated, we created our reservoir computing random optical machine.

We have investigated the use of ML paradigms for designing linear multilevel quantum gates by using a complex transmitting multimodal system. In this application, the random optical machine is not necessarily a random medium, but may also be a multimode fiber, or an array of waveguides. The key point is the complexity of the radiation-matter interaction. We developed versatile algorithms and demonstrated their efficiency both for known and unknown random system unitary operators. We showed that single- and multi-qudit gates can be designed. We also considered the use of the ML training for QKDs with PUFs.

The overall methodology has been easily implemented by TF API, and can be directly adapted to experimentally retrieved data. The method can be generalized to more complex information protocols, and embedded in real-world multimodal systems. We believe that these results can give further momentum to the applications of AI and new computing paradigms, and to quantum technologies.

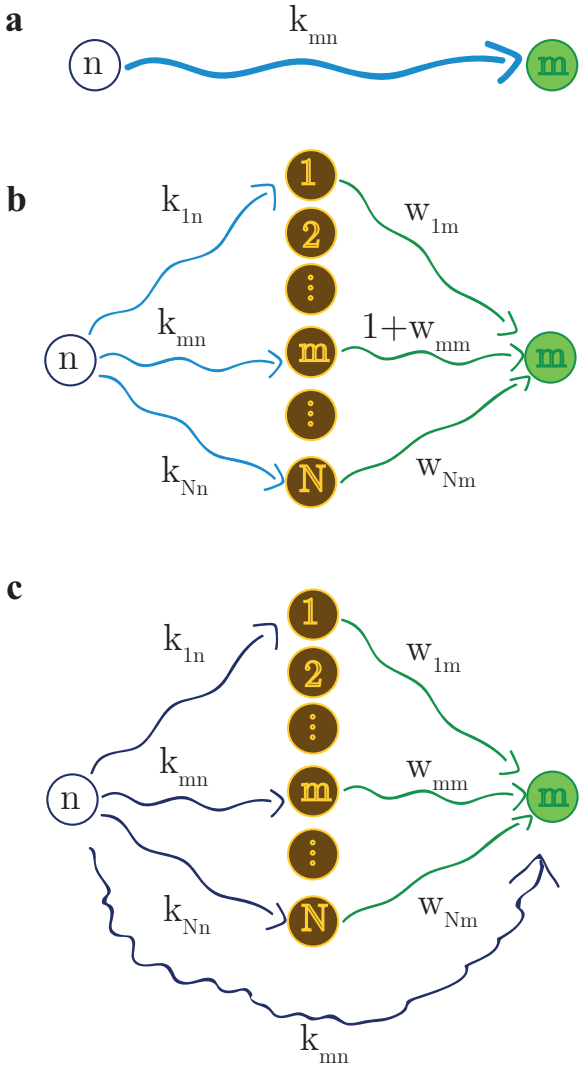

Figure 11.2: Schematics of the effect of the perturbation in the ANN. (a) Unperturbed transmission linking input channel n, and the output channel m. (b) In the presence of the perturbation, new links are created and all the channel in addition to the channel n contribute to the output m, see Eq. ((11.18)). (c) As in (b) an equivalent representation of Eq. ((11.18)).

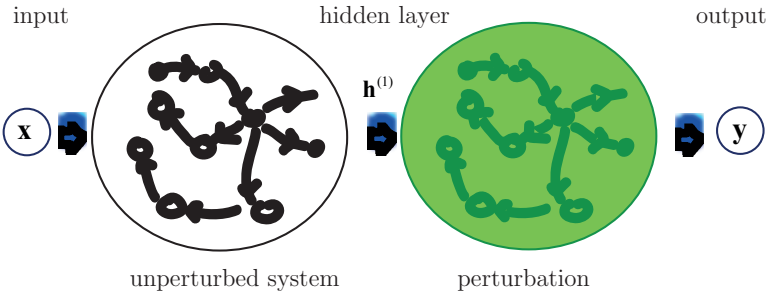

Figure 11.3: Synthetic representation of the effect of the perturbation to the input and output vector, through the formation of a hidden layer, with state vector $\mathbf{h}^{(1)}$.

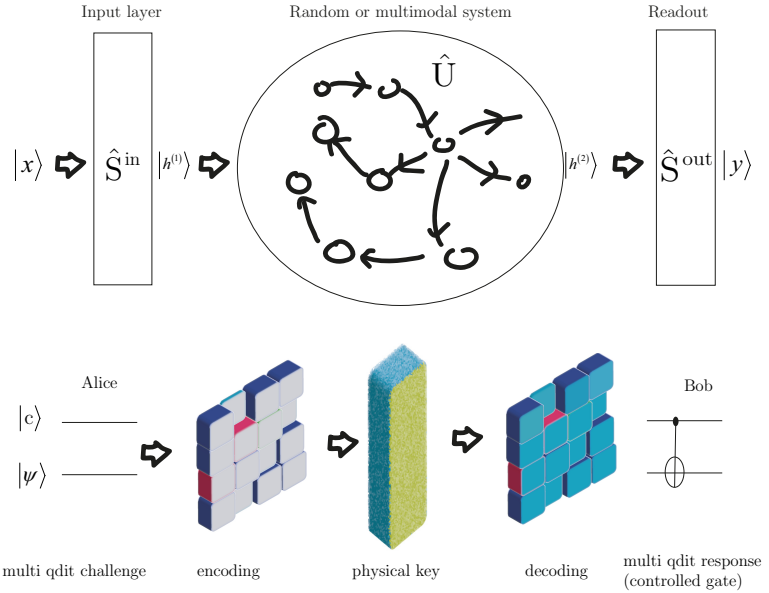

Figure 11.4: A general optical gate based on a complex random medium; the input state $\mathbf{x}$ is processed to the input layer with operator $\hat{S}^{\text{in}}$, the system is modeled by the unitary operator $\hat{U}$, and the ouput further elaborated by $\hat{S}^{\text{out}}$. When the complex system cannot be cloned, the overall gate is a cryptographic scheme in which the input and readout operators are keys to decode the transmission. An example of the controlled gate is sketched in the bottom panel. In the simplest formulation, one of the input and the readout operators can be omitted.

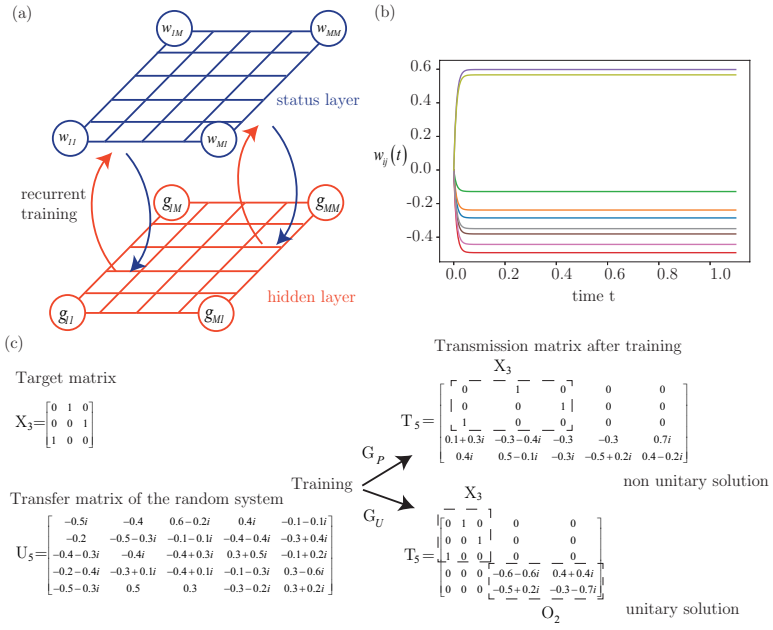

Figure 11.5: (a) Recurrent ANN for the matrix equation ((11.25)). The status nodes are denoted by the elements of the matrix W, and the hidden state of the system is in the nodes of the matrix F; (b) training dynamics for the case $N = M = 3$ with X_T corresponding to a single-qutrit X gate ($\mu = 100$); (c) resulting transfer function for the case $N = 3$ and $M = 5$ in the unitary and non-unitary case. In the latter case, the excess channels are ignored during the training. The resulting transmission channels T_M are displayed. O_2 is the unitary complements for $C = M - N = 2$ in the unitary case.

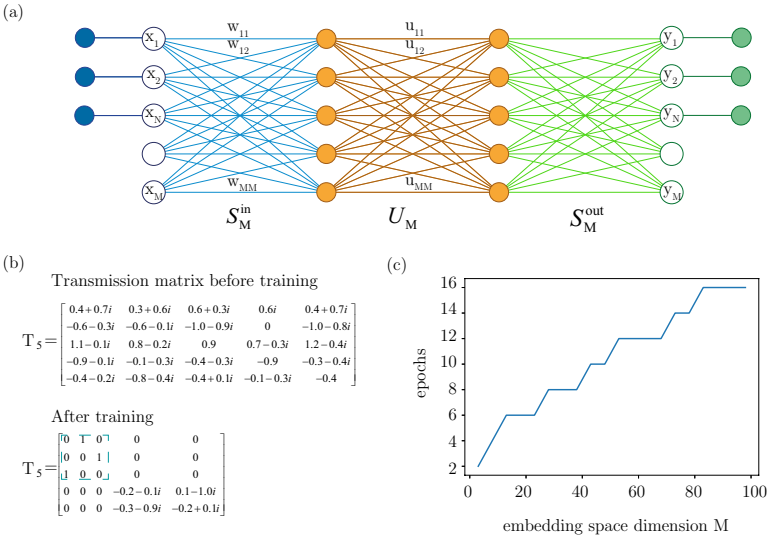

Figure 11.6: Example of inference training of a $M = 5$ random system to act as X_3 gate. (a) ANN model (in our example S_M^{out} is not used); (b) numerical examples for the transmission matrix $T_M = U_M \cdot S_M^{\text{in}}$ before and after training; (c) scaling properties in terms of training epochs. Parameters: $n_{train} = 100$, $n_{valid} = 50$, $e_{valid} = 10^{-3}$, $n_{epoch} = 6$.

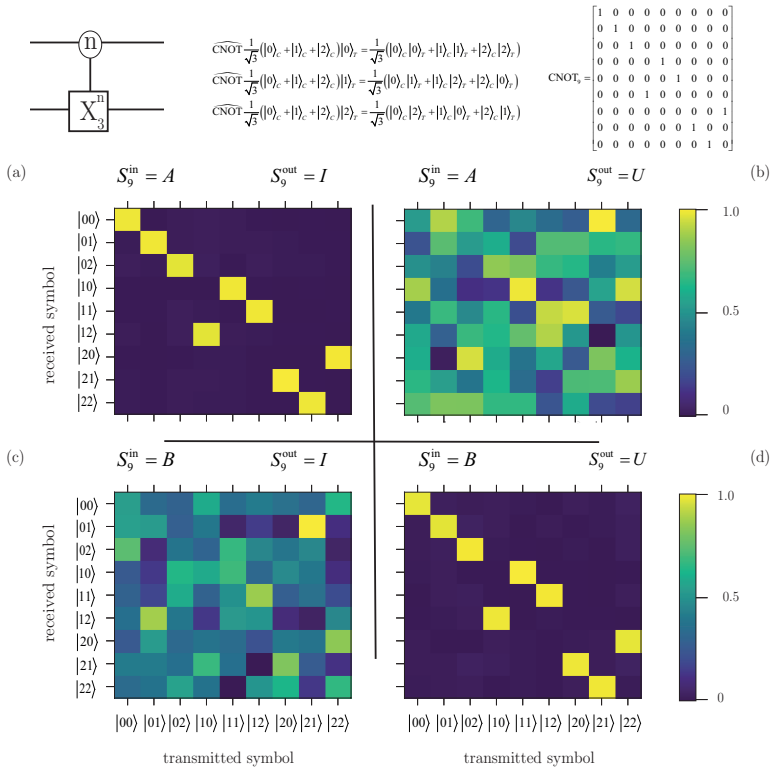

Figure 11.7: Training of a random system to realize a CNOT-like gate. Here $N = M = 9$, $n_{train} = 100$, $n_{valid} = 50$, $e_{valid} = 10^{-3}$, 12 epochs. C denotes the control q-trit, and T the transmitted q-trit. The circuit diagram and the transmission matrix of the gate are shown in top panel. Panel (a) corresponds to the trained transmission, when $S_9^{out} = \mathbb{1}_9$, for a randomly generated unitary matrix U_9, representing the complex system. The trained input operator is $S_9^{in} = A$. Panel (b) shows the output with $S_9^{in} = A$ and $S_9^{out} = U_9$ (double passage in the random system). Panel (c) shows the output with $S_9^{in} = B$ and $S_9^{out} = I_9$. B is the calculated input operator for $S_9^{out} = U_9$. Panel (d) is the output for $S_9^{in} = B$ and $S_9^{out} = U_9$. Information is decoded only if transmitter and receiver use the correct combination of input and output layers (panels (a) and (d)).

Part V

CONCLUSIONS AND OPEN QUESTIONS

12 CONCLUSIONS

In an era in which the long overdue promise of quantum technologies has not been fulfilled yet, the perspective of an *all-optical nonlinear computer*, which does computation at the speed of light, is more than appealing. Given that quantum technologies should be able to solve most of the main complexity science problems, but no significant progress can be seen in the near future, scientific community interest is moving towards other methodologies to realize super-fast computers. Indeed, new opto-electronic chips and machines have been recently developed [425, 426], and photonics is progressively more involved in the engineering of computational systems through artificial neural networks.

In this context, two neural network mathematical models are drawing the main research directions: the deep neural network and the reservoir computing. The optical realization of deep neural networks has been developed in many systems, as integrated circuits with coupled waveguides [325], pulse propagation in fibers [427] and continuous wave propagation in air [428]. For reservoir computing, we have devices made by multimodal fibers with delayed feedback [429, 430], diffractive resonator arrays via spatial light modulator [413, 431], and random media [27, 425, 432].

Beyond the engineering of conventional computational techniques, another field is gaining interest: the solutions of optimization problems, which have been analyzed both by classical and quantum models, including experimental implementations. In the field of quantum technologies, the most widespread approach is quantum annealing, which has its actualization in D-Wave processors. These devices are designed to find the ground states of Ising Hamiltonians with specific coupling constants. Classical minimization of the Ising models also solves optimization problems. Indeed, there is no proof that quantum annealing algorithms are more efficient than the classical ones. Classical Ising machines have been demonstrated by continuous waves propagating in air and designed via spatial light modulator [9], photonic integrated circuits [426], and pulse propagation in ring cavities [322].

However, we are still far away from the realization of a nonlinear all-optical device. This thesis is an in-depth study of classical and quantum complex nonlinear dynamics in optical systems, aiming at setting the basis to realize in future a machine that uses a highly nonlinear radiation-

matter interaction and iterative algorithms to solve NP-Complete problems.

After a general introduction to complexity science, we treated light complexity both in classical and in quantum systems. In Part ii, we investigated classical nonlinear dynamics in complex, extreme regimes. We dealt with new theoretical models for dispersive shock waves, rogue waves, Fermi-Pasta-Ulam-Tsingou recurrence, and soliton gas generation, and reported experimental results in thermal media and photorefractive crystals. Part iii was about quantum nonlinear systems described in a nonperturbative framework. By using the positive $\mathcal{P}$representation, we numerically solved stochastic nonlinear Schrödinger equations and studied quantum effects in solitons and rogue wave generation. In Part iv, we explored the use of waves for novel computational devices, able to solve complex optimization problems, like Ising machines random optical neural networks.

In this thesis, the complexity of light propagation in nonlinear media was examined from many points of view to try to answer a specific question: *can nonlinear waves do computation?* We think to have demonstrated, in various ways, that complexity can be controlled, and enlightening works in random media [1, 27] experimentally prove that randomness does generate a reservoir computing neural network.

This thesis also opens novel, inspiring questions: *What if we replace randomness with extreme nonlinear dynamics, or with quantum noise? What if the weights of the optical artificial neural network are given by an extreme radiation-matter interaction, which can be highly nonlinear, or even stochastic?* Maybe this could increase the neural network efficiency, maybe not. We hope to be able to respond certainly to all these open questions in the near future.

APPENDIX

IRREVERSIBLE EVOLUTION IN TIME ASYMMETRIC QUANTUM MECHANICS

Fundamental theorems of QM

In order to build a mathematical theory behind a generic quantum system, we need to define a Hausdorff vector space Ψ with a locally convex topology τ and a scalar product $(\cdot|\cdot)$. We need also an algebra $\mathcal{A}$ of τ-continuous linear operator on Ψ and a probability measure $\mathcal{P}$ on $\mathcal{A}$. By the scalar product $(\cdot|\cdot)$, we are able to build a norm $||\psi|| = \sqrt{(\psi|\psi)}$ $\forall\psi \in \Psi$ and a metric $d(\psi,\phi) = ||\phi - \psi||$ $\forall\,\phi,\psi \in \Psi$, that is induced by the norm, therefore we can settle a new topology τ_d on Ψ, given by the distance d. Now, we have a Euclidean space (Ψ,τ_d), which is also normed and separable. To be a physical space it needs the completeness.

Let $(\mathcal{H},\tau_{\mathcal{H}})$ be the completion of (Ψ,τ_d); $\mathcal{H}$ is a separable Hilbert space, and is the space used to formulate the known *time symmetric* quantum theory. The temporal symmetry in a Hilbert space arises from the following three theorems:

Theorem A.1.1 (Gleason). *[433] For every probability $\mathcal{P}(\Lambda)$, there exists a positive trace class operator ρ such that*

$$\mathcal{P}(\Lambda) = Tr(\Lambda\rho). \tag{A.1}$$

Theorem A.1.2 (Stone-Neumann). *[434] Let us consider the Schrödinger-Neumann equation for ρ previously defined*

$$\frac{\partial\rho(t)}{\partial t} = \frac{i}{\hbar}[H,\rho(t)], \tag{A.2}$$

with H Hamiltonian operator. The solutions of such an equation are time symmetric and they are given by the group of unitary operators $U^{\dagger}(t) = \exp -\frac{i}{\hbar}Ht$.

Theorem A.1.3 (Hegerfeldt). *[435] For every Hermitian and semi-bounded Hamiltonian H, either*

$$Tr(\Lambda(t)\rho) = Tr(\Lambda\rho(t)) = 0 \;\; \forall t \in \mathbb{R} \tag{A.3}$$

or

$$Tr(\Lambda(t)\rho) = Tr(\Lambda\rho(t)) > 0 \ \ \forall t \in \mathbb{R} \tag{A.4}$$

except on a set of Lebesgue measure zero.

These theorems imply that time asymmetric solutions of the Schrödinger equation

$$\imath\hbar\frac{\partial\phi(t)}{\partial t} = H\phi(t) \tag{A.5}$$

with time asymmetric boundary conditions are not allowed, hence we need to modify the mathematical description of the system.

Rigged Hilbert Space Topology

For every fixed $\psi_0 \in \Psi$, the translation $T : \Psi \to \Psi$ such that $\psi \to \psi + \psi_0$ is a linear homeomorphism of Ψ on itself. Therefore τ is uniquely determined by the neighborhood system $I(0)$ centered at the origin, because every other neighborhood of any point ψ of Ψ is obtained by translating a neighborhood of the origin of the vector ψ. (Ψ, τ) is said to be locally convex if $\mathcal{C} = \{C \in I(0) \mid C \text{is convex}\}$ is a neighborhood local basis. Since every open ball centered at the origin is convex, it is also a member of $\mathcal{C}$ if and only if $\exists A \in \tau \mid 0 \in A \subset B_r(0) \ \forall B_r(0)$. By this last condition, we build a locally convex topology τ on Ψ that is finer than the topology τ_d induced by the norm.

Let us suppose that (Ψ, τ) and $(\mathcal{H}, \tau_{\mathcal{H}})$ are the previously described spaces and, besides, τ is locally convex and finer than $\tau_{\mathcal{H}}$. Then we can define another completion Φ of Ψ, this time with respect to τ, and find another complete space (Φ, τ_Φ) that is different from $(\mathcal{H}, \tau_{\mathcal{H}})$. Precisely, $\Phi \subset \mathcal{H}$, and Φ is dense in $\mathcal{H}$. Moreover, $\Phi \subset \mathcal{H} \Rightarrow \mathcal{H}^* \subset \Phi^*$, where $\mathcal{H}^*$ and Φ^* are the dual spaces of $\mathcal{H}$ and Φ, respectively.

The definition of dual space is the basis to build a RHS and we need a more physically accessible dual space, according to [102, 103]. Let $\mathcal{E}$ be a Euclidean space. We identify the scalar product on $\mathcal{E}$ as $(\cdot|\cdot)$; instead $\langle\cdot|\cdot\rangle$ is the operatorial product on the dual space $\mathcal{E}^*$, namely $F(v) = \langle F|v\rangle$. We define our dual space $\Phi^\times$ as the space of *antilinear* and continuous functionals on Φ, that is

$$F \in \Phi^\times \iff F(\phi) = \langle\phi|F\rangle. \tag{A.6}$$

Thus every functional in $\Phi^\times$ has a sort of complex conjugate in Φ^*, and the Riesz-Frechet representation theorem on the Hilbert space $\mathcal{H}$ still works, hence $\mathcal{H} = \mathcal{H}^\times$. In this manner we obtain the *Gelfand triplet* $\Phi \subset \mathcal{H} \subset \Phi^\times$, which defines our RHS.

Gamow Vectors

It is well known that, in order to be observable, the Hamiltonian operator H of a quantum system must be self-adjoint on $\mathcal{H}$, so $H = H^\dagger$. Nevertheless $H \neq H^\times$ on $\Phi^\times$. Let us consider the secular equation

$$H^\times |E\rangle = E|E\rangle. \tag{A.7}$$

If $|E\rangle \in \Phi^\times \setminus \mathcal{H}$, we cannot affirm that the corresponding eigenvalue E is a real number. We define a generalized eigenvector $|E\rangle \in \Phi^\times$, which has complex eigenvalue, as a GV $|\phi_G\rangle = |E^\pm\rangle = |E_R \pm i\frac{\Gamma}{2}\rangle$ (subscript R is due to one of the first applications of this theory, that Bohm developed in scattering experiments [103], and it is related to the resonances of the system). From the Schrödinger equation (in units such that $\hbar = 1$), we get a unitary operator $U(t) = e^{-iHt}$ for the temporal evolution of any state in $\mathcal{H}$. We see that $U(t)^\times = e^{iH^\times t}$ is not unitary on $\Phi^\times$:

$$U(t)^\times |E_R \pm i\frac{\Gamma_n}{2}\rangle = e^{iE_R t} e^{\mp \frac{\Gamma_n}{2} t} |E_R \pm i\frac{\Gamma_n}{2}\rangle, \tag{A.8}$$

$U(t)^\times$ is not an isometry, because

$$||U(t)^\times |E_R \pm i\frac{\Gamma_n}{2}\rangle||^2 = e^{\mp \Gamma_n t} |||E_R \pm i\frac{\Gamma_n}{2}\rangle||^2. \tag{A.9}$$

Moreover

$$||U(t)^\times |E_R \pm i\frac{\Gamma_n}{2}\rangle|| \overset{t\to\pm\infty}{\longrightarrow} 0 \tag{A.10}$$

and

$$||U(t)^\times |E_R \pm i\frac{\Gamma_n}{2}\rangle|| \overset{t\to\mp\infty}{\longrightarrow} +\infty. \tag{A.11}$$

In a physical context, we need to identify Φ with the Schwartz space $S(\mathbb{R}^N)$, that is, the space of rapidly decreasing functions, and the Hilbert space $\mathcal{H}$ with the space of quadratically integrable functions $\mathcal{L}^2(\mathbb{R}^N)$, so these last two expressions suggest that we need to define the following new spaces:

$$\Phi_- = \left\{ \phi \in \Phi \mid f(E) = \langle \phi | E^- \rangle \in S(\mathbb{R}) \cap \mathcal{H}_-^2 \right\}, \tag{A.12}$$

$$\Phi_+ = \left\{ \phi \in \Phi \mid f(E) = \langle \phi | E^+ \rangle \in S(\mathbb{R}) \cap \mathcal{H}_+^2 \right\}; \tag{A.13}$$

where $\mathcal{H}_-^2$ and $\mathcal{H}_+^2$ are Hardy spaces bounded from below and from above, respectively. To sum up, $\Phi_\pm$ are dense in Φ, $\Phi = \Phi_- + \Phi_+$ ($\Phi_- \cap \Phi_+ \neq 0$ generally) and Φ is dense in $\mathcal{H}$, consequently

$$\Phi_- \overset{dense}{\subset} \Phi \overset{dense}{\subset} \mathcal{H} \overset{dense}{\subset} \Phi^\times \overset{dense}{\subset} \Phi_-^\times, \tag{A.14}$$

$$\Phi_+ \overset{dense}{\subset} \Phi \overset{dense}{\subset} \mathcal{H} \overset{dense}{\subset} \Phi^\times \overset{dense}{\subset} \Phi_+^\times. \tag{A.15}$$

We have now found two Gelfand triplets, $\Phi_- \subset \mathcal{H} \subset \Phi_-^\times$ and $\Phi_+ \subset \mathcal{H} \subset \Phi_+^\times$, where the evolution operator $U(t)$ acts as a semigroup, because it is well defined and continuous only for $t \leq 0$ on Φ_-, and only for $t \geq 0$ on Φ_+. The value $t = 0$ expresses the intrinsic irreversibility we have when, for example, we divide an experiment into a preparation stage and a registration stage. In this case, Φ_- will be the space of the initial states and Φ_+ will be the space of the detected states.

Quantization of a Damped Motion

For its simplicity and its relevance, the HO can be chosen to introduce the study of quantum mechanics in a time symmetric context [105, 106]. The classical HO Hamiltonian is

$$H = \frac{p^2}{2m} + \frac{m\omega^2}{2}x^2. \tag{A.16}$$

We quantize the HO by converting the canonical coordinates x, p into the operators $\hat{x}, \hat{p}$ such that

$$[\hat{x}, \hat{p}] = i\hbar, \tag{A.17}$$

and we find the spectrum of H:

$$H\psi(x) = E\psi(x), \quad E_n = \hbar\omega\left(n + \frac{1}{2}\right), \tag{A.18}$$

$$\psi_n(x) = \sqrt[4]{\frac{m\omega}{\hbar\pi}}\frac{1}{\sqrt{2^n n!}}H_n\left(\sqrt{\frac{m\omega}{\hbar}}x\right), \tag{A.19}$$

where $H_n(x) = (-1)^n x^2 \frac{d^n}{dx^n}e^{-x^2}$ are the Hermite polynomials.

In a time asymmetric context, considering the equation of a damped motion comes natural for its inherent irreversibility. In fact, if we consider the classical dynamical system in one dimension

$$\begin{cases} \frac{d}{dt}u(t) = -\gamma u(t) \\ u(0) = u_0 \end{cases} \tag{A.20}$$

where $\gamma > 0$ and $m = \hbar = 1$, we have

$$u(t) = e^{-\gamma t} u_0, \tag{A.21}$$

which represents a damping for $t \geq 0$. We quantize it exactly as we did for the HO, even if this one is not a Hamiltonian system. In a general n-dimensional space, one defines a dynamical system as

$$\frac{du}{dt} = X(u), \tag{A.22}$$

where X is a vector field. Using canonical coordinates $(u^1, ..., u^n, v^1, ..., v^n)$, we get the Hamiltonian

$$H(u, v) = \sum_{k=1}^{n} v_k X_k(u), \tag{A.23}$$

where X_k are the components of X in the coordinate basis, so for Eq.(A.20)

$$H(u, v) = -\gamma u v. \tag{A.24}$$

Since the quantization must take into account that $\hat{v}$ does not commute with $\hat{u}$, we have

$$\hat{H}(\hat{u}, \hat{v}) = -\frac{\gamma}{2}(\hat{u}\hat{v} + \hat{v}\hat{u}). \tag{A.25}$$

By performing the canonical transformation

$$\hat{u} = \frac{\gamma\hat{x} - \hat{p}}{\sqrt{2\gamma}}, \quad \hat{v} = \frac{\gamma\hat{x} + \hat{p}}{\sqrt{2\gamma}}, \tag{A.26}$$

one obtains the Hamiltonian of the RHO:

$$\hat{H}(\hat{x}, \hat{p}) = \frac{\hat{p}^2}{2} - \frac{\gamma^2\hat{x}^2}{2}. \tag{A.27}$$

Let us compare the HO and the RHO. We pass from the first one to the second one, by changing ω into the complex value $i\gamma$ [436]. This simple transformation allows us to move from a parabolic potential bounded from below to a parabolic barrier. This potential overturning produces a completely different physics: the HO models the behavior of a pointlike mass around a stable equilibrium and the RHO gives the dynamics around an unstable equilibrium, an intrinsically irreversible evolution (at variance with an oscillator, a falling body never goes back to its initial position).

In this section, we analyze the Hamiltonian of the damped motion, defined in (A.25). As proved in [105], $\hat{H}(\hat{u}, \hat{v})$ is self-adjoint on $\mathcal{L}^2(\mathbb{R})$ and parity invariant. We define the time reversal operator T such that

$$T\phi(t) := \phi(-t) \quad \Rightarrow TU(t) = U^\dagger(t)T \quad \Rightarrow U(t)TU(t) = T, \tag{A.28}$$

where $U(t) := e^{-iHt}$. T plays a fundamental role in this system, and coincides with the inverse FT, i.e. $T\phi(u,t) := \check{F}[\phi](u,t)$,where

$$\check{F}[\phi](x,t) = \frac{1}{\sqrt{2\pi}} \int_{\mathbb{R}} e^{ikx}\phi(k,t)dk. \tag{A.29}$$

Let us define two families of tempered distributions in $\Phi^{\times}$, the first one

$$\hat{u}|f_0^-\rangle := 0, \quad f_0^-(u) = \delta(u), \tag{A.30}$$

$$\forall n \in \mathbb{N}\ |f_n^-\rangle := \frac{(-i)^n}{\sqrt{n!}}\hat{v}^n|f_0^-\rangle \ \Rightarrow\ f_n^-(u) = \frac{(-1)^n}{\sqrt{n!}}\frac{d^n}{du^n}\delta(u), \tag{A.31}$$

and the second one

$$\hat{v}|f_0^+\rangle := 0, \quad f_0^+(u) = 1, \tag{A.32}$$

$$\forall n \in \mathbb{N}\ |f_n^+\rangle := \frac{1}{\sqrt{n!}}\hat{u}^n|f_0^+\rangle \ \Rightarrow\ f_n^+(u) = \frac{u^n}{\sqrt{n!}}. \tag{A.33}$$

Hereafter, following [99, 102, 103], we denote a tempered distribution $f_n^{\pm}$ a *resonance*. We can see that

$$H^{\times}|f_n^{\pm}\rangle = \pm E_n|f_n^{\pm}\rangle, \tag{A.34}$$

where $E_n := i\gamma\left(n + \frac{1}{2}\right) \in \mathbb{C}$. Given that $f_n^{\pm}$ are tempered distributions, their inverse FTs are well defined, and they are

$$\check{F}[f_n^-] = \frac{i^n}{\sqrt{2\pi}}f_n^+, \tag{A.35}$$

$$\check{F}[f_n^+] = i^n\sqrt{2\pi}f_n^-. \tag{A.36}$$

We show the *quasi-orthogonality* and the *quasi-completeness* of the resonances:

$$\langle f_n^-|f_m^+\rangle = \delta_{n,m}, \quad \sum_{n=0}^{\infty} f_n^-(u)f_n^+(y) = \delta(u-y). \tag{A.37}$$

In order to find real energy values, we need to analyze also the continuous spectrum. Since H is parity invariant, each generalized eigenvalue is doubly degenerate, thus

$$H^{\times}\psi_{\pm}^E = E\psi_{\pm}^E. \tag{A.38}$$

As one can see in [105], the generalized eigenfunctions are

$$\psi_{\pm}^{E}(u) = \frac{1}{\sqrt{2\pi\gamma}} u_{\pm}^{-\left(\frac{iE}{\gamma}+\frac{1}{2}\right)}, \tag{A.39}$$

where $u_{\pm}^{\lambda}$ are tempered distributions such that

$$u_{+}^{\lambda} := \begin{cases} u^{\lambda} & u \geq 0 \\ 0 & u < 0 \end{cases}, \; u_{-}^{\lambda} := \begin{cases} 0 & u < 0 \\ u^{\lambda} & u \leq 0 \end{cases}. \tag{A.40}$$

It is possible to prove both the orthonormality and the completeness of the eigenfunctions, namely

$$\sum_{\pm} \int [\psi_{\pm}^{E_1}(u)]^* \psi_{\pm}^{E_2}(u) du = \delta(E_1 - E_2); \tag{A.41}$$

$$\sum_{\pm} \int [\psi_{\pm}^{E}(u)]^* \psi_{\pm}^{E}(u') dE = \delta(u - u'). \tag{A.42}$$

Therefore we can apply the Gelfand-Maurin theorem [437] and write any function in $S(\mathbb{R})$ as

$$\phi(u) = \sum_{\pm} \int \psi_{\pm}^{E}(u) \langle \phi | \psi_{\pm}^{E} \rangle^* dE. \tag{A.43}$$

By repeating the same reasoning

$$H^{\times} \check{F} \left[\psi_{\pm}^{-E}\right] = E \check{F} \left[\psi_{\pm}^{-E}\right], \tag{A.44}$$

so one can prove also the orthonormality and the completeness of the inverse FTs of the eigenfunctions, whence

$$\phi(u) = \sum_{\pm} \int \check{F} \left[\psi_{\pm}^{-E}\right](u) \langle \phi | \check{F} \left[\psi_{\pm}^{-E}\right] \rangle^* dE. \tag{A.45}$$

We have just defined two groups of eigenfunctions, $\psi_{\pm}^{E}(u)$ and $\check{F}\left[\psi_{\pm}^{-E}\right](u)$, which represent the continuous spectrum of the Hamiltonian of a damped motion into the RHS. Moreover, we have just seen that they depend on the tempered distributions $u_{\pm}^{-\left(\frac{iE}{\gamma}+\frac{1}{2}\right)}$, which have simple poles in the complex plane when

$$E = -E_n = -i\gamma\left(n + \frac{1}{2}\right). \tag{A.46}$$

Thanks to the properties of the generalized function $u_{\pm}^{\lambda}$ [105], we can finally state what follows:

$$Res\left[\psi_{\pm}^{E}, -E_n\right] = \frac{(\pm 1)^n i\sqrt{\gamma}}{\sqrt{2\pi n!}} f_n^{-}, \tag{A.47}$$

$$Res\left[\check{F}[\psi_{\pm}^{-E}], E_n\right] = \frac{(\pm i)^n i\sqrt{\gamma}}{2\pi\sqrt{n!}} f_n^{+}. \tag{A.48}$$

By defining the following spaces, we get two Gelfand triplets:

$$\mathcal{H} = \mathcal{L}^2(\mathbb{R}), \quad \Phi = S(\mathbb{R}), \tag{A.49}$$

$$\Phi_{-} = \left\{\phi \in \Phi \mid f(E) = \langle \phi | \check{F}[\psi_{\pm}^{-E}]\rangle \in \mathcal{H}_{-}^{2}\right\}, \tag{A.50}$$

$$\Phi_{+} = \left\{\phi \in \Phi \mid f(E) = \langle \phi | \psi_{\pm}^{E}\rangle \in \mathcal{H}_{+}^{2}\right\}. \tag{A.51}$$

From this framework into the RHS $\Phi^{\times}$, we can infer the irreversible evolution of certain waves in Φ. We established above the connection between the continuous and the point spectrum. Now we make this link definitively clear and we show that the evolution operator acts as a semigroup on $\Phi_{\pm}$ for a well-defined orientation of the arrow of time. By recalling Eqs.(A.47) and (A.48), we apply the residue theorem to initial data in $\Phi_{\pm}$ [105] and get two different expansions in GV:

$$\phi^{+}(u) = \sum_{n=0}^{+\infty} \langle \phi^{+} | f_n^{+}\rangle f_n^{-}(u) \quad \forall\, \phi^{+} \in \Phi_{+}; \tag{A.52}$$

$$\phi^{-}(u) = \sum_{n=0}^{+\infty} \langle \phi^{-} | f_n^{-}\rangle f_n^{+}(u) \quad \forall\, \phi^{-} \in \Phi_{-}. \tag{A.53}$$

Thanks to the following definitions of two new function spaces, both of them subspaces of $S(\mathbb{R})$ and isomorphic by the inverse FT, we can establish the relation between Φ_{+} and Φ_{-}:
$\mathcal{D} = C_c^{\infty}(\mathbb{R})$ is the space of the infinitely differentiable functions with compact support;
$\mathcal{Z} = \left\{\check{F}[\phi] \,|\, \phi \in \mathcal{D}\right\}$, where $\check{F}$ is the inverse FT.
Since for each function $\phi \in \mathcal{Z}$, we have

$$\phi(u) = \sum_{n=0}^{+\infty} \frac{1}{n!} \frac{d^n}{du^n} \phi(u)|_{u=0} u^n = \sum_{n=0}^{+\infty} f_n^{+}(u) \langle f_n^{-} | \phi\rangle, \tag{A.54}$$

while, at the same time, every $\psi \in \mathcal{D}$ is the FT of a function in $\mathcal{Z}$, hence

$$\psi(u) = \frac{1}{\sqrt{2\pi}} \int_{\mathbb{R}} \check{F}[\psi](v) e^{-ivu} dv = \sum_{n=0}^{+\infty} f_n^-(u) \langle f_n^+ | \psi \rangle. \tag{A.55}$$

We can state that

$$\Phi_+ \equiv \mathcal{D}, \quad \Phi_- \equiv \mathcal{Z}. \tag{A.56}$$

At last, we study the evolution operator $U(t) = e^{-iHt}$. U is a unitary group on $\mathcal{H} = \mathcal{L}^2(\mathbb{R})$, given that if $\psi(u,0) \in \mathcal{L}^2(\mathbb{R})$ then

$$\psi(u,t) = U(t)\psi(u,0) = e^{\frac{\gamma}{2}t} \psi(e^{\gamma t} u, 0), \tag{A.57}$$

transformation that turns out to be an isometry on $\mathcal{L}^2(\mathbb{R})$. This means that if $\psi(u,t)$ solves the Schrödinger equation, then also $T\psi(u,t) = \psi(u,-t)$ does. Therefore the theory is time-reversal invariant on the Hilbert space $\mathcal{H}$, without letting us see the damping we expected. Where do we observe the temporal irreversibility? It lacks the analysis of U restricted to $\Phi_\pm$. If $\phi^+(u,0) \in \Phi_+$ then

$$\langle U(t)\phi^+ | \psi_\pm^E \rangle = \langle \phi^+ | U^\times(t) \psi_\pm^E \rangle = e^{iEt} \langle \phi^+ | \psi_\pm^E \rangle \ \in \mathcal{H}_+^2 \ \Leftrightarrow \ t \geq 0; \tag{A.58}$$

on the other hand, if $\phi^-(u,0) \in \Phi_-$ then

$$\begin{aligned} &\langle U(t)\phi^- | \check{F}[\psi_\pm^{-E}] \rangle = \langle U(-t) \check{F}[\phi^-] | \psi_\pm^{-E} \rangle = \\ &= \langle \check{F}[\phi^+] | U^\times(-t) \psi_\pm^{-E} \rangle = e^{iEt} \langle \check{F}[\phi^-] | \psi_\pm^{-E} \rangle = \\ &= e^{iEt} \langle \phi^- | \check{F}[\psi_\pm^{-E}] \rangle \ \in \mathcal{H}_-^2 \quad \Leftrightarrow \quad t \leq 0. \end{aligned} \tag{A.59}$$

We conclude that $U(t)$ establishes two semigroups:

$$U_+(t) : \Phi_+ \longrightarrow \Phi_+ \quad \forall t \geq 0 \tag{A.60}$$

and

$$U_-(t) : \Phi_- \longrightarrow \Phi_- \quad \forall t \leq 0. \tag{A.61}$$

We have just found a way to model irreversible phenomena. In fact, the action of U allows us to choose an orientation of the temporal arrow: if it goes forward from zero, then our initial data is in Φ_+, otherwise it is in Φ_-, indeed

$$\begin{aligned} \phi^+(u,t) &= \textstyle\sum_n e^{-\gamma(n+1/2)t} \langle \phi^+ | f_n^+ \rangle f_n^-(u) \\ \phi^-(u,t) &= \textstyle\sum_n e^{\gamma(n+1/2)t} \langle \phi^- | f_n^- \rangle f_n^+(u). \end{aligned} \tag{A.62}$$

Moreover, all the physics we get fixing a specific orientation of time's arrow is achievable fixing the other one too, because time reversal operator T establishes an isomorphism between Φ_+ and Φ_-, in fact

$$T\phi^+(u,t) = U(-t)T\phi^+(u,0) = \phi^-(u,-t). \tag{A.63}$$

Summarizing, we got an irreversible quantum system by observing that the evolution operator acts as a semigroup on $\Phi_\pm$, due to the presence of resonant states $f_n^\pm$. In this way, the instant $t = 0$ separates the evolution in two complementary directions: if one starts from Φ_+, one can stays forever in Φ_+ only evolving forward in time. In other words one chooses the temporal orientation, fixes the signature of $\Phi_\pm$, and cannot go backwards.

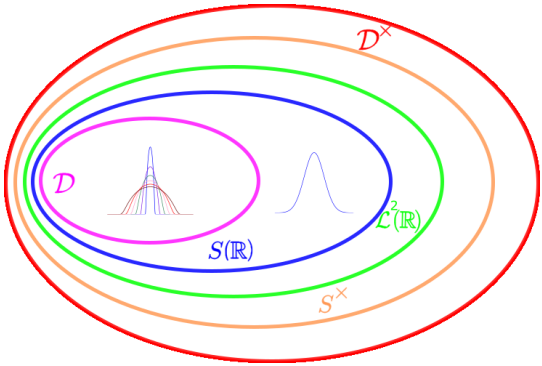

Figure A.1: Pictorial representation of Gelfand triplet defined in Eq.(A.15). Here $\Phi_+ \equiv \mathcal{D}$, $\Phi \equiv S(\mathbb{R})$ and $\mathcal{H} \equiv \mathcal{L}^2(\mathbb{R})$. One can get an Euler-Venn diagram also for the triplet in Eq.(A.14) by changing Φ_+ with Φ_- and $\mathcal{D}$ with $\mathcal{Z}$.

The Reversed Harmonic Oscillator: Remarkable Results

We consider the family of operators [106]

$$\hat{V}_\lambda = \exp\left\{\frac{\lambda}{2}(\hat{x}\hat{p} + \hat{p}\hat{x})\right\}. \tag{A.64}$$

In a system of measurement where $\hbar = 1$, we have $[\hat{x}, \hat{p}] = i$, so

$$\hat{V}_\lambda \phi(x) = e^{-i\frac{\lambda}{2}}\phi(e^{-i\lambda}x), \tag{A.65}$$

whence

$$\hat{V}_\lambda \hat{x} \hat{V}_\lambda^{-1} = e^{-i\lambda}\hat{x}, \quad \hat{V}_\lambda \hat{p} \hat{V}_\lambda^{-1} = e^{i\lambda}\hat{p}. \tag{A.66}$$

If we recall the Hamiltonian in the equation (A.19)

$$H_{HO} := \frac{\hat{p}^2}{2} + \frac{\gamma^2 \hat{x}^2}{2}, \tag{A.67}$$

it is easy to see that

$$\hat{V}_{\pm\frac{\pi}{4}} H \hat{V}_{\pm\frac{\pi}{4}}^{-1} = \pm \imath H_{HO} \tag{A.68}$$

and we can transform the results we already know for the HO in results for the RHO:

$$E_n^{HO} = \gamma(n + \frac{1}{2}),\ E_n = \imath E_n^{HO} \in \mathbb{C} \tag{A.69}$$

$$\psi_n^{HO} = \left(\frac{\gamma}{\pi}\right)^{1/4} (2^n n!)^{-1/2} e^{-\frac{\gamma}{2}x^2} H_n(\sqrt{\gamma}x) \tag{A.70}$$

$$f_n^{\pm} = \hat{V}_{\pm\frac{\pi}{4}}^{-1} \psi_n^{HO} \in S^\times(\mathbb{R}). \tag{A.71}$$

The Unitary Transformation: from (u, v) to (x, p) Framework

One passes from the HO to the RHO through the operator $\hat{V}_{\pm\frac{\pi}{4}}$, but can also pass from $H(\hat{u}, \hat{v})$ to $H(\hat{x}, \hat{p})$, i.e. from the damped motion to the RHO, through a canonical transformation and find a relation between the spectra of these two Hamiltonians.

The canonical transformation from (u, v) to (x, p) it is generated by the generating function

$$S(x, u) = \frac{\gamma}{2}x^2 - \sqrt{2\gamma}xu + \frac{1}{2}u^2, \tag{A.72}$$

with $p = \frac{\partial S}{\partial x}$, $v = -\frac{\partial S}{\partial u}$.

We define the unitary transformation

$$\mathcal{U} : \mathcal{L}^2(\mathbb{R}) \longrightarrow \mathcal{L}^2(\mathbb{R}) \tag{A.73}$$

such that

$$f(u) \longrightarrow (\mathcal{U}f)(x) = \tilde{C} \int_{\mathbb{R}} f(u) e^{iS(x,u)} du, \tag{A.74}$$

with $\tilde{C} := e^{-i\frac{\pi}{8}}\sqrt[4]{\frac{\gamma}{2\pi^2}}$ and we can prove that $\mathcal{U}$ is unitary by demonstrating that

$$|\tilde{C}|^2 \int_{\mathbb{R}} e^{i[S(x,u)-S(x',u)]}du = \delta(x-x'). \tag{A.75}$$

In order to get a relation of quasi-orthogonality and quasi-completeness for the resonances, we need to understand the nature of the operator $\hat{V}_\lambda$. It acts almost like the evolution operator U in Eq.(A.57), with a complex (instead of real) exponential, but this is enough only to say that $\hat{V}_\lambda$ is unitary for pure imaginary λ, not for every $\lambda \in \mathbb{C}$. In fact, for a generic $\lambda = \omega + i\gamma$, where $\omega, \gamma \in \mathbb{R}$, one has

$$\begin{aligned}\langle \hat{V}_\lambda \phi | \hat{V}_\lambda \psi \rangle = \int_{\mathbb{R}} dx \left[e^{\frac{\gamma - i\omega}{2}} \phi\left(e^{\gamma - i\omega}x\right)\right]^* e^{\frac{\gamma-i\omega}{2}} \psi\left(e^{\gamma-i\omega}x\right) = \\ = e^{i\omega}\int_{\mathbb{R}} dx\,[\phi(x)]^*\,\psi(x) = e^{i\omega}\langle\phi|\psi\rangle.\end{aligned} \tag{A.76}$$

Therefore it is not surprising that $f_n^\pm$ are only proportional to $\mathcal{U}[f_n^\pm(u)](x)$ and not exactly equal. In fact

$$f_n^\pm(x) = e^{in\frac{\pi}{4}}(2\pi)^{\pm\frac{1}{4}}\mathcal{U}[f_n^\pm(u)](x). \tag{A.77}$$

Nevertheless, we achieve the same relation of quasi-orthogonality and quasi-completeness we had before:

$$\langle f_n^\pm(x)|f_m^\mp(x)\rangle = \delta_{nm};\quad \sum_{n=0}^{+\infty}\left[f_n^\pm(x)\right]^* f_n^\mp(x') = \delta(x-x'). \tag{A.78}$$

Moreover

$$\left[f_n^\pm(x)\right]^* = f_n^\mp(x). \tag{A.79}$$

Recalling the equations (A.35), (A.36) and the meaning of the inverse FT for the damped motion represented by $\hat{H}(\hat{u},\hat{v})$ (the inverse FT coincides with the time reversal operator T in that system), one has $T = C$, where C is the complex conjugation operator, as shown in [106].

We want to find χ^E such that

$$H\chi^E = E\chi^E. \tag{A.80}$$

From [106] we get the complete derivation of the following solutions:

$$\chi_+^E(x) = \frac{\tilde{C}}{\sqrt{2\pi\gamma}} i^{\frac{\nu+1}{2}}\Gamma(\nu+1)D_{-\nu-1}(-\sqrt{-2\gamma i}x), \tag{A.81}$$

$$\chi_-^E(x) = \chi_+^E(-x), \tag{A.82}$$

where here $\nu = -\left(i\frac{E}{\gamma} + \frac{1}{2}\right)$ and

$$D_\nu(z) := \frac{e^{-\frac{z^2}{4}}}{\Gamma(-\nu)} \int_{\mathcal{R}} \xi_\pm^{-\nu-1} e^{\mp z\xi - \frac{1}{2}\xi^2} d\xi \tag{A.83}$$

is a Whittaker function [438].

If one remembers the equation (A.44), one knows that the set of eigenfunction is not complete yet. In fact, the two families of functions $\eta_\pm^E(x) := \left(\mathcal{U}\check{F}[\psi_\pm^{-E}]\right)(x)$ still miss, and we obtain

$$H\eta_\pm^E = -E\eta_\pm^E, \tag{A.84}$$

$$\eta_+^E(x) = \frac{\tilde{C}}{\sqrt{2\pi\gamma}} i^{\frac{\nu+1}{2}} \Gamma(-\nu) D_\nu(-\sqrt{2\gamma i}x), \tag{A.85}$$

$$\eta_-^E(x) = \eta_+^E(-x). \tag{A.86}$$

We observe that

$$\eta_\pm^E(x) = [\chi_\pm^E(x)]^*, \tag{A.87}$$

fact which confirms that the time reversal operator T acts like the complex conjugation C.

From the corresponding properties satisfied by $\psi_\pm^E(u)$ and from the unitary nature of $\mathcal{U}$ we have

$$\sum_\pm \int_{\mathbb{R}} [\chi_\pm^E(x)]^* \chi_\pm^{E'}(x) dx = \delta(E - E'); \tag{A.88}$$

$$\sum_\pm \int_{\mathbb{R}} [\chi_\pm^E(x)]^* \chi_\pm^E(x') dE = \delta(x - x'); \tag{A.89}$$

$$\sum_\pm \int_{\mathbb{R}} [\eta_\pm^E(x)]^* \eta_\pm^{E'}(x) dx = \delta(E - E'); \tag{A.90}$$

$$\sum_\pm \int_{\mathbb{R}} [\eta_\pm^E(x)]^* \eta_\pm^E(x') dE = \delta(x - x'). \tag{A.91}$$

At this point, we have all the tools we need to study the analytic properties of these four families of eigenfunctions. The outcome is that

$\chi^E_\pm(x)$ and $\eta^E_\pm(x)$ have simple poles at $E = -E_n$ and $E = E_n$, respectively. Furthermore,

$$Res[\chi^E_\pm(x); -E_n] = \frac{\tilde{C}}{\sqrt{2\pi\gamma}} \frac{(-1)^n}{n!} i^{-\frac{n}{2}} D_n(\mp\sqrt{-2\gamma i}x), \tag{A.92}$$

$$Res[\eta^E_\pm(x); E_n] = \frac{\tilde{C}}{\sqrt{2\pi\gamma}} \frac{(-1)^n}{n!} i^{\frac{n+1}{2}} D_n(\mp\sqrt{2\gamma i}x). \tag{A.93}$$

In [438], [439] and [440] one can find out that $D_n(y) = 2^{-\frac{n}{2}} e^{-\frac{y^2}{4}} H_n\left(\frac{z}{\sqrt{2}}\right)$. This, together with $H_n(-y) = (-1)^n H_n(y)$, allows us to obtain

$$Res[\chi^E_\pm(x); -E_n] \propto f^+_n(x) \tag{A.94}$$

and

$$Res[\eta^E_\pm(x); E_n] \propto f^-_n(x). \tag{A.95}$$

Following section A.1.4, we get $\Phi_\pm$ from the residues of the RHO eigenfunctions:

$$\mathcal{H} = \mathcal{L}^2(\mathbb{R}), \quad \Phi = S(\mathbb{R}), \tag{A.96}$$

$$\Phi_- = \left\{ \phi \in \Phi \mid f(E) = \langle \phi | \eta^E_\pm \rangle \in \mathcal{H}^2_- \right\}, \tag{A.97}$$

$$\Phi_+ = \left\{ \phi \in \Phi \mid f(E) = \langle \phi | \chi^E_\pm \rangle \in \mathcal{H}^2_+ \right\}. \tag{A.98}$$

The Evolution Operator Acting like a Semigroup

We study waves $\phi_\pm \in \Phi_\pm$ and the action of the evolution operator. We have $T = C$ and

$$T(\Phi_+) = \Phi_-. \tag{A.99}$$

Writing envelopes of $\phi_\pm$ in series of resonances:

$$\begin{array}{rcl} \phi^+(x) & = & \sum_{n=0}^{+\infty} \langle \phi^+ | f^+_n \rangle^* f^-_n(x) \ \ \forall\, \phi^+ \in \Phi_+, \\ \phi^-(x) & = & \sum_{n=0}^{+\infty} \langle \phi^- | f^-_n \rangle^* f^+_n(x) \ \ \forall\, \phi^- \in \Phi_-. \end{array} \tag{A.100}$$

Thanks to the Gelfand-Maurin spectral theorem

$$\begin{aligned} \phi^+(x) &= \sum_{\pm} \int_{\mathbb{R}} dE \chi^E_{\pm}(x) \langle \phi^+ | \psi^E_{\pm} \rangle^* \\ \phi^-(x) &= \sum_{\pm} \int_{\mathbb{R}} dE \eta^E_{\pm}(x) \langle \phi^- | \eta^E_{\pm} \rangle^*. \end{aligned} \tag{A.101}$$

In conclusion, even in this case, the temporal evolution operator $U(t) = e^{-iHt}$ establishes a unitary group on $\mathcal{H} = \mathcal{L}^2(\mathbb{R})$, and two semigroups:

$$U_+(t) : \Phi_+ \longrightarrow \Phi_+ \quad \forall t \geq 0; \tag{A.102}$$

$$U_-(t) : \Phi_- \longrightarrow \Phi_- \quad \forall t \leq 0. \tag{A.103}$$

Furthermore, if $\phi^+(x,0) \in \Phi_+$ then

$$\phi^+(x,t) = \sum_n e^{-\gamma(n+1/2)t} \langle \phi^+ | f^+_n \rangle^* f^-_n(x), \tag{A.104}$$

while, if $\phi^-(x,0) \in \Phi_-$ then

$$\phi^-(x,t) = \sum_n e^{\gamma(n+1/2)t} \langle \phi^- | f^-_n \rangle^* f^+_n(x). \tag{A.105}$$

We stress again that we got an irreversible quantum theory by studying the action of U on $\Phi_\pm$ as a semigroup. Time $t = 0$ splits the evolution in two diametrically opposed directions, and it becomes the instant which separates two different dynamics.

Functions with Compact Support

In this section we examine a function set in Φ_+. We start working in the (u,v) representation, where $H(\hat{u},\hat{v}) = -\frac{\gamma}{2}[\hat{u}\hat{v} + \hat{v}\hat{u}]$. We analyze the evolution in (u,v) and (x,p) planes. In (x,p) the Hamiltonian is $H = \frac{\hat{p}^2}{2} - \frac{\gamma^2 \hat{x}^2}{2}$ (we fix $\gamma = 1$ hereafter).

Wave Packets in (u,v) Plane

We previously proved that Φ_+ and Φ_- coincide with $\mathcal{D}$ and $\mathcal{Z}$, respectively. We choose the forward orientation of the temporal arrow, so we focus our attention on the triplet

$$\Phi_+ \subset \mathcal{H} \subset \Phi_+^\times, \tag{A.106}$$

that is $\mathcal{D} \subset \mathcal{L}^2(\mathbb{R}) \subset \mathcal{D}^\times$.

Let us consider the family of functions

$$\phi_\epsilon(u) = \begin{cases} K_\epsilon \exp\left[\frac{1}{\left(\frac{u}{\epsilon}\right)^2 - 1}\right] & |u| < \epsilon \\ 0 & |u| \geq \epsilon \end{cases} \tag{A.107}$$

where $\epsilon > 0$ and K_ϵ is such that $||\phi_\epsilon||_2 = 1$, i.e. $\left(\int_{\mathbb{R}} |\phi_\epsilon(u)|^2 dx\right)^{\frac{1}{2}} = 1$. $\phi_\epsilon(u)$ is a function of class $C^\infty(\mathbb{R})$, precisely

$$\phi_\epsilon(u) \in \mathcal{D} \;\; \forall\, \epsilon > 0. \tag{A.108}$$

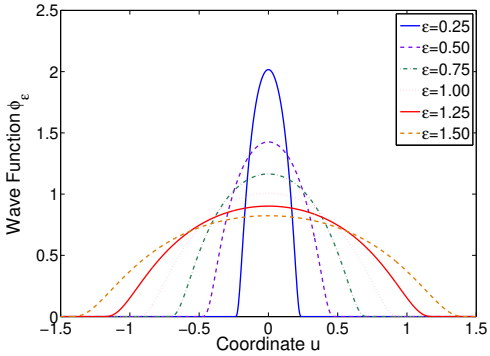

Figure A.2: Functions ϕ_ϵ with compact support defined in Eq.(A.107) for several ϵ values.

Starting from

$$\sum_{n=0}^{\infty} f_n^-(u) f_n^+(w) = \delta(u - w), \tag{A.109}$$

with $f_n^-(u) = \frac{(-1)^n}{\sqrt{n!}} \frac{d^n}{du^n}\delta(u)$ and $f_n^+(u) = \frac{u^n}{\sqrt{n!}}$, we have

$$\begin{aligned} &\phi_\epsilon(u) = \int_{\mathbb{R}} dw \delta(u - w)\phi_\epsilon(w) = \\ &= \int_{\mathbb{R}} dw \sum_{n=0}^{\infty} f_n^-(u) f_n^+(w)\phi_\epsilon(w) = \sum_{n=0}^{\infty} f_n^-(u)\langle \phi_\epsilon | f_n^+ \rangle, \end{aligned} \tag{A.110}$$

since $\phi_\epsilon \in \mathcal{D}$. In deriving Eq.(A.110), as discussed in Sec. A.1.4 and in [106], the residue theorem allows us to swap the integral and the summation. This is not valid for general functions in Φ not belonging to Φ_+. We define the N-order *background function* as

$$\phi_N^{BG}(u,t) := \phi(u,t) - \sum_{n=0}^{N} f_n^-(u)\langle U(t)\phi | f_n^+ \rangle^* \;\in\; \Phi^\times; \tag{A.111}$$

consequently

$$\phi(u,t) = \sum_{n=0}^{N} f_n^-(u)\langle U(t)\phi|f_n^+\rangle^* + \phi_N^{BG}(u,t) \quad \forall\phi \in \Phi. \tag{A.112}$$

For $\phi \in \Phi_+$, $\phi^{BG}_{N\to+\infty} = 0$ and $U(t)$ acts as a semigroup. The evolution is a superposition of exponentially decaying functions. On the contrary, for $\phi \notin \Phi_+$, $\phi^{BG}_{N\to+\infty}$ does not converge and the evolution includes non exponentially decaying components.

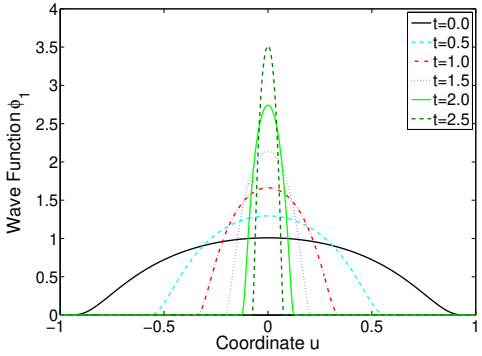

Figure A.3: One-dimensional evolution of $|\phi_1(u,t)|$ [Eq.(A.107) with $\epsilon = 1$].

We numerically simulate the Schrödinger equation $\imath\frac{\partial\psi}{\partial t} = H\psi$ for the Hamiltonian $H = \imath\gamma\left(u\frac{\partial}{\partial u} + \frac{1}{2}\right)$ (with γ=1), with initial condition $\psi(u,t=0) = \phi_\epsilon(u)$. Figures A.3 and A.4 show the resulting "focusing" evolution.

Figure A.5 reports the evolution of the coefficients $C_N(t) := \langle U(t)\phi_1|f_N^+\rangle^*$. These brackets exponentially decay, with quantized decay rates. Into a semilogarithmic scale, the decay rates correspond to straight lines with different slopes.

Wave Packets in (x,p) Plane

We pass from the (u,v) to (x,p) by the unitary transformation $\mathcal{U}$:

$$\phi_\epsilon(x) = \mathcal{U}[\phi_\epsilon(u)](x) = \sum_{n=0}^{\infty}\mathcal{U}[f_n^-(u)](x)\langle\mathcal{U}\phi_\epsilon|\mathcal{U}f_n^+\rangle = \sum_{n=0}^{\infty} f_n^-(x)\langle\phi_\epsilon|f_n^+\rangle, \tag{A.113}$$

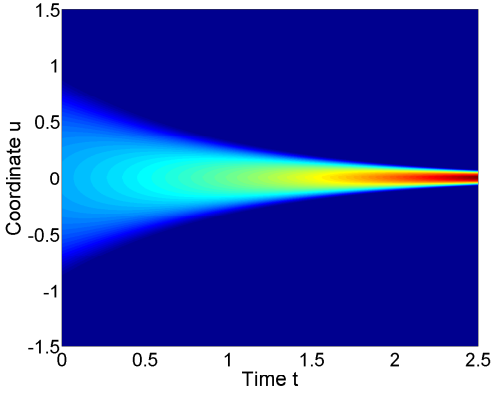

Figure A.4: Evolution of $|\phi_1(u,t)|$ [Eq.(A.107) with $\epsilon = 1$].

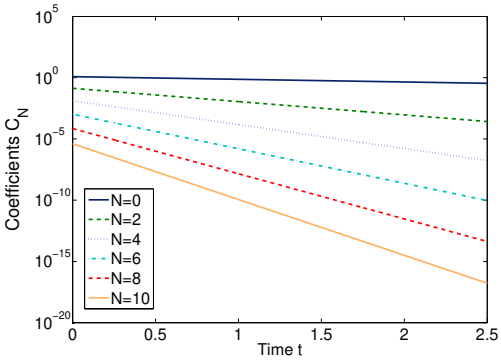

Figure A.5: Numerically calculated projections $C_N(t) := \langle U(t)\phi_1 | f_N^+ \rangle^*$ on the N order resonances of a function with compact support [Eq.(A.107) with $\epsilon = 1$] in the (u,v) representation, in a semilogarithmic scale.

with $f_n^{\pm}(x) = \hat{V}^{-1}_{\pm\frac{\pi}{4}} \psi_n^{HO}(x)$.

We numerically analyze the transformed functions. In Fig. A.6, one can see several $(\mathcal{U}\phi_\epsilon)(x)$. We remark that functions ϕ_ϵ, which have compact support in (u,v), do not have compact support in (x,p) phase plane.

We numerically study the evolution of wave packets in (x,p). We solve numerically $i\frac{\partial\psi}{\partial t} = H\psi$ with initial condition $\psi(x,t=0) = (\mathcal{U}\phi_\epsilon)(x)$ and

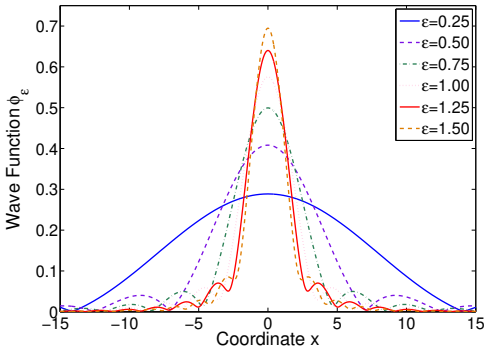

Figure A.6: Transformed ϕ_ϵ [Eq.(A.113) for various ϵ].

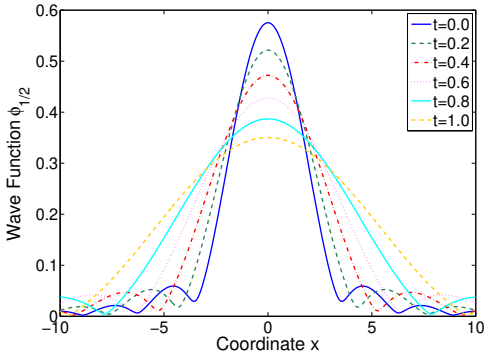

Figure A.7: One-dimensional evolution of a transformed function with compact support [Eq.(A.113), $\epsilon = 1/2$] with a RHO potential.

a RHO potential. Figures A.7 and A.8 show the resulting "defocusing" evolution.

Gaussian Function

We examine the Gelfand triplet in Eq.(A.15) defined in sections A.1.4 and A.1.5, in the case of the Gaussian function as element of the Hilbert space but not belonging neither to Φ_+ nor to Φ_- (see figure 1). For this kind of functions, the expansion in Gamow states must be truncated

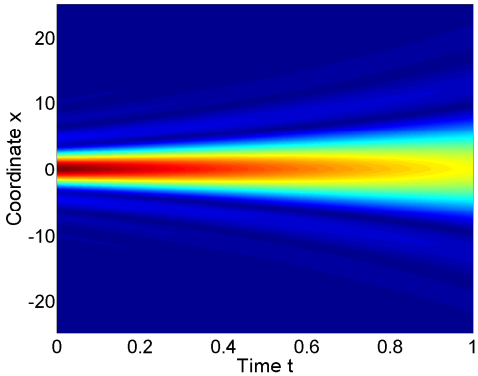

Figure A.8: Evolution of a transformed function with compact support [Eq.(A.113), $\epsilon = 1/2$] with a RHO potential.

and completed by an additional background function, not decaying exponentially, as discussed in Sec. A.1.8.2. We illustrate theoretically and numerically the properties of the background function, specifically studying a Gaussian function $\phi(u) = \frac{e^{-\frac{u^2}{2}}}{\sqrt[4]{\pi}}$ and its transformed $\mathcal{U}[\phi](x)$. We analyze the evolution both in (u, v) and (x, p) planes.

Let us define a normalized Gaussian function

$$\phi(u) = \frac{1}{\sqrt[4]{\pi}} e^{-\frac{u^2}{2}} \in S(\mathbb{R}). \tag{A.114}$$

$\phi(u)$ does not belong to $\mathcal{D}$ or to $\mathcal{Z}$ because the Fourier transformed of a Gaussian function is still a Gaussian function and $\mathcal{D} \cap \mathcal{Z} = \emptyset$. Since $\sum_{n=0}^{+\infty} f_n^+(u) f_n^-(w) = \delta(u - w)$, we have

$$\phi(u) = \int_{\mathbb{R}} dw \sum_{n=0}^{+\infty} f_n^-(u) f_n^+(w) \phi(w) \quad \forall \phi \in \Phi. \tag{A.115}$$

The integral and the summation in Eq.(A.115) cannot be swapped in general, at variance with the case of $\phi_\epsilon(u)$ previously considered. Without loss of generality, we write

$$\phi(u) = \sum_{n=0}^{N} f_n^-(u) \langle \phi | f_n^+ \rangle^* + \phi_N^{BG}(u), \tag{A.116}$$

where $\phi_N^{BG}(u)$ is the N-order background.

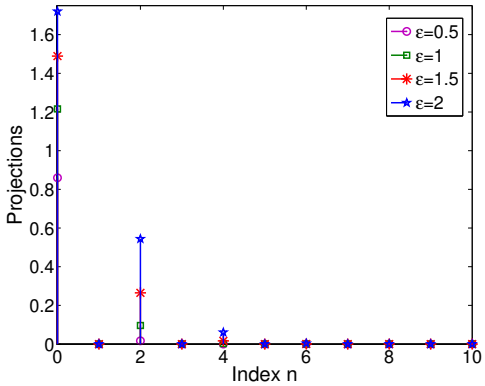

Figure A.9: Projections $\langle \phi_1 | f_n^+ \rangle^*$ of a function with compact support [defined in Eq.(A.107), $\epsilon = 1$].

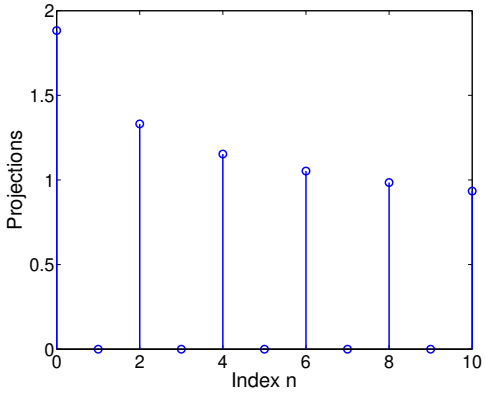

Figure A.10: Projections $\langle \phi | f_n^+ \rangle^*$ of the Gaussian function.

Since $\phi(u) = \phi(-u)$, while $f_n(u) = -f_n(-u)$ for odd n, we have

$$\langle \phi | f_n^+ \rangle = \begin{cases} \frac{2^{\frac{n+1}{2}} \Gamma\left(\frac{n+1}{2}\right)}{\sqrt[4]{\pi}\sqrt{n!}} & \text{for even} n \\ 0 & \text{for odd} n \end{cases} . \tag{A.117}$$

Both $\langle \phi | f_n^+ \rangle$ and $\langle \phi_\epsilon | f_n^+ \rangle$ decrease for even n, but the Gaussian $\langle \phi | f_n^+ \rangle$ decay much more slowly, as one can see by comparing figures 9 and

10. However, this is not a mathematical proof of the existence of the background. The presence of the background is proved through the study of the initial datum: $\phi_\epsilon(u)$ is an initial state that is composed only by a discrete sum of resonances without any component in the continuum, because it belongs to $\mathcal{D}$; on the contrary $\phi(u)$ is an initial state with a component of continuous radiation that is the background.

We analyze the evolved N-order background wave for a Gaussian initial data. We want to study its limit as $N \to +\infty$. We have

$$\begin{aligned}
&\phi_N^{BG}(u,t) = \phi(u,t) - \textstyle\sum_{n=0}^{N} f_n^-(u)\langle f_n^+|U(t)|\phi\rangle = \\
&= U(t)\phi(u) - \textstyle\sum_{n=0}^{N} f_n^-(u)\langle f_n^+|U(t)^\times|\phi\rangle = \\
&= U(t)\phi(u) - \textstyle\sum_{n=0}^{N} e^{-\frac{\gamma}{2}(2n+1)t} f_n^-(u)\langle f_n^+|\phi\rangle.
\end{aligned} \tag{A.118}$$

We notice that the limit as N approaches infinity could diverge or not exist. This happens in most cases, and specifically for the Gaussian function. In fact, in Eq.(A.117), we can approximate the Gamma function

$$\Gamma(z) = \sqrt{2\pi} z^{z-\frac{1}{2}} e^{-z} \left[1 + O\left(\frac{1}{z}\right)\right] \tag{A.119}$$

and the factorial

$$n! = \sqrt{2\pi} n^{n+\frac{1}{2}} e^{-n} \left[1 + O\left(\frac{1}{n}\right)\right] \tag{A.120}$$

for large values of z and n, thanks to the Stirling's formula [438]. We find, for even n

$$\langle\phi|f_n^+\rangle = \frac{2^{\frac{n+1}{2}}\Gamma\left(\frac{n+1}{2}\right)}{\sqrt[4]{\pi}\sqrt{n!}} \simeq \frac{2^{\frac{3}{4}}\left(1+\frac{1}{n}\right)^{\frac{n}{2}}}{\sqrt[4]{e^2 n}} \simeq \frac{2^{\frac{3}{4}}}{\sqrt[4]{n}}, \tag{A.121}$$

hence $\langle\phi|f_n^+\rangle$ approaches zero with order $\frac{1}{4}$, too slowly to let the series converge $\forall t \geq 0$, $\forall u \in \mathbb{R}$, so the limit $N \to +\infty$ does not exist globally. This confirms that an expansion like Eq.(A.113) with an infinite number of GV is meaningless for a Gaussian function, and a background term is needed.

Figures A.11 and A.12 show a portrayal of the Gaussian function evolution. In Fig. A.13 and in Fig. A.14 one can observe the decay of the coefficients.

The (u, v) phase space remains the simplest configuration for numerical tests of the theory. Since one runs into a high computational complexity when analyses the background evolution, we choose (u, v) phase space to compare the evolution of a Gaussian function with a specific ϕ_ϵ. We best fit the normalized Gaussian function by a function ϕ_ϵ in order to

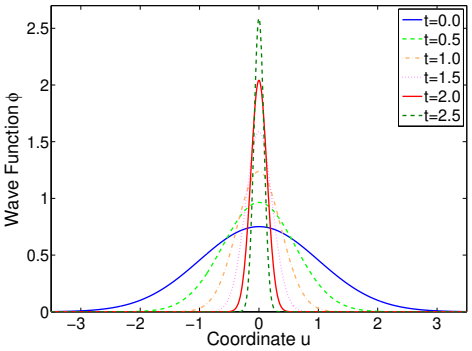

Figure A.11: One-dimensional evolution of the Gaussian wave $\phi(u) = \frac{e^{-\frac{u^2}{2}}}{\sqrt[4]{\pi}}$.

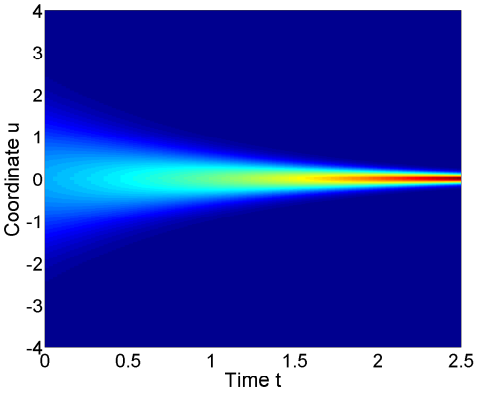

Figure A.12: Evolution of the Gaussian wave $\phi(u) = \frac{e^{-\frac{u^2}{2}}}{\sqrt[4]{\pi}}$.

compare the background function with the difference between these two waves. Figure A.15 shows $\phi(u)$ and its best fit by $\phi_\epsilon(u)$, obtained for $\epsilon = \epsilon_0 = 1,802425$. Fig. A.16 compares the calculated evolution of $\phi(u)$ and ϕ_{ϵ_0}. We should see the dispersive component that occurs on the boundaries of the Gaussian evolution. However, appreciating the dispersive behavior is difficult in a linear scale; we report a comparison between ϕ_{20}^{BG} and $\phi - \phi_{\epsilon_0}$ in Fig. A.17 in a semilogarithmic scale. The

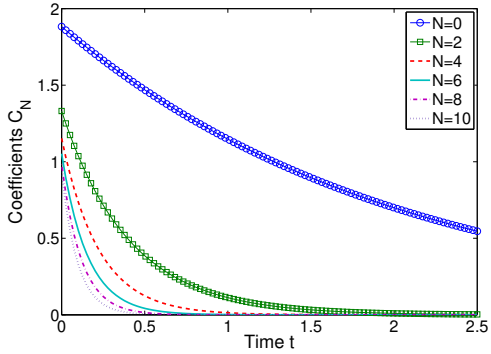

Figure A.13: Evolution of the projections $C_N(t) := \langle U(t)\phi | f_N^+ \rangle^*$ on the N order resonances of the Gaussian wave $\phi(u) = \frac{e^{-\frac{u^2}{2}}}{\sqrt[4]{\pi}}$ in the (u,v) representation, in a linear scale.

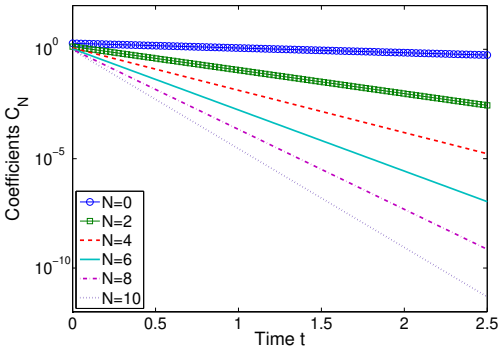

Figure A.14: Evolution of the projections on the N order resonances $C_N(t) := \langle U(t)\phi | f_N^+ \rangle^*$ of the Gaussian wave $\phi(u) = \frac{e^{-\frac{u^2}{2}}}{\sqrt[4]{\pi}}$ in the (u,v) representation, in a semilogarithmic scale.

continuous lines represent the Gaussian background for several time values, while the dashed lines give the difference between the Gaussian and the function with compact support. One can now see without difficulties that the outlines on the boundaries are well overlapped, so the long time evolution of a Gaussian background, that is, the dispersive

tail of a function not belonging to Φ_+, can be approximated to the rest between the function we are studying and an appropriately chosen function ϕ_ϵ.

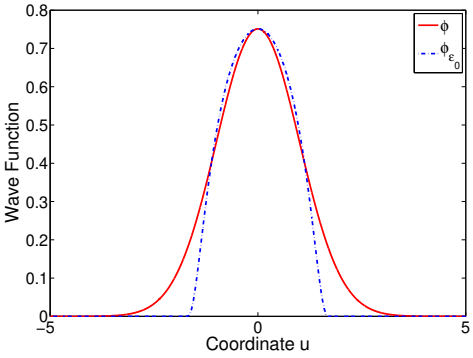

Figure A.15: Fit of the Gaussian function $\phi(u) = \frac{e^{-\frac{u^2}{2}}}{\sqrt[4]{\pi}}$ by the function $\phi_{\epsilon_0}(u)$ ($\epsilon_0 = 1.802425$).

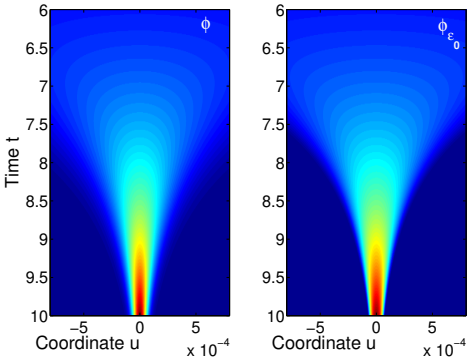

Figure A.16: Comparison of the Gaussian evolution $\phi(u,t)$ with $\phi_{\epsilon_0}(u,t)$. $\phi_{\epsilon_0}(u,t)$ focalizes without any loss or dispersion of energy, while the Gaussian presents a dispersive background (see also Fig. A.17).

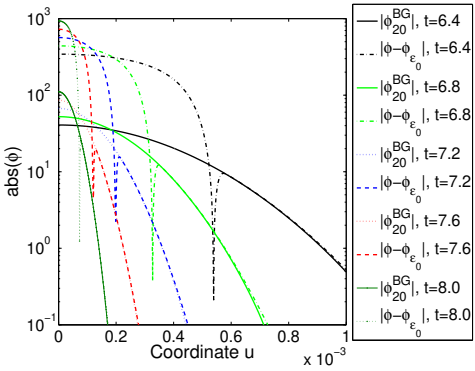

Figure A.17: We want to analyze if a region where $\phi_N^{BG}(u,t) \simeq \phi(u,t) - \phi_{\epsilon_0}(u,t)$ exists. A comparison between $\phi_{20}^{BG}(u,t)$ and $\phi(u,t) - \phi_{\epsilon_0}(u,t)$ is here reported in semilogarithmic scale: these two wave packets are well overlapped on their borders.

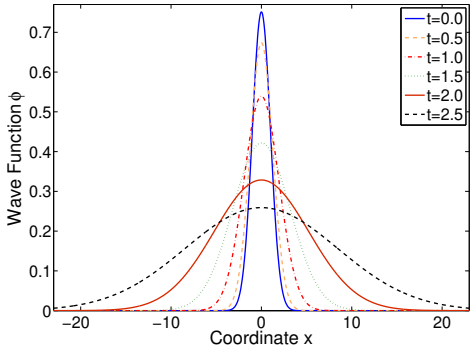

Figure A.18: One-dimensional evolution of the Gaussian wave $\phi(x) = \frac{e^{-\frac{x^2}{2}}}{\sqrt[4]{\pi}}$ under a RHO potential.

We want now complete our analysis by considering the $(x,p)-$system. By the transformation $\mathcal{U}$ we see that $\phi(x) = [\mathcal{U}\phi(u)](x)$ is a Gaussian function anyway, because

$$[\mathcal{U}\phi(u)](x) = \pi^{-\frac{1}{4}}\tilde{C}\int_{\mathbb{R}} e^{-\frac{u^2}{2}} e^{iS(x,u)} du = \left(\frac{\gamma}{\pi}\right)^{\frac{1}{4}} e^{-\frac{\gamma}{2}x^2}. \qquad \text{(A.122)}$$

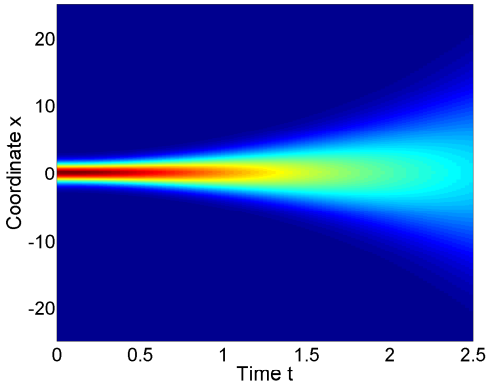

Figure A.19: Evolution of the wave $|\phi|$ with initial condition $\phi(x) = \frac{e^{-\frac{x^2}{2}}}{\sqrt[4]{\pi}}$.

The focusing dynamics in the (u, v) space corresponds to a defocusing propagation in the (x, p) space as shown in Fig. A.18 and in Fig. A.19.

MATHEMATICAL DEFINITIONS

This appendix is written to let the reader find the mathematical definitions used in Sec. A.1 quickly. It presents only a list of definitions, without any ambition to explain the mathematics that is behind. For more details, one can see [441–444].

Definition A.2.1. Given a set X, a **topology** τ is a collection of elements of the power set $P(X)$ such that:

- $\emptyset, X \in \tau$;
- $\cup_{n=1}^{\infty} A_n \in \tau \; \forall \{A_n\}_{n\in\mathbb{N}} \subset \tau$;
- $\cup_{n=1}^{N} A_n \in \tau \; \forall \{A_1, ..., A_N\} \subset \tau$.

The members of τ are called **open sets**.

Definition A.2.2. Given two topologies τ_1 and τ_2 on the same set X, we say that τ_1 is **finer** or **stronger** than τ_2 if $\tau_2 \subset \tau_1$.

Definition A.2.3. Let $f : X \to Y$ be a function between two topological spaces (X, τ_X) and (Y, τ_Y). f is said to be **continuous** if and only if

$$f^{-1}(A) \in \tau_X \;\; \forall A \in \tau_Y. \tag{A.123}$$

Definition A.2.4. Let $f : X \to Y$ be a function between two topological spaces (X, τ_X) and (Y, τ_Y). f is called a **homeomorphism** if and only if f is a bijective continuous function with continuous inverse function.

Definition A.2.5. Let (X, τ) be a vector space with a topology τ. If τ makes the vector addition and the scalar multiplication be continuous on X, then we say that (X, τ) is a **topological vector space**.

Definition A.2.6. A subset $\mathcal{B}$ of the topology τ is a **basis** (or a **base**) of τ if

$$\forall A \in \tau \ \ \exists \{B_i\}_{i \in I \subseteq \mathbb{N}} \subset \mathcal{B} \ \mid \ A = \cup_{i \in I} B_i. \tag{A.124}$$

Definition A.2.7. Given $x \in X$, a **neighborhood** U of x is a subset of X such that $\exists A \in \tau \ \mid \ x \in A \subseteq U$.

Definition A.2.8. Given $x \in X$ and given the neighborhood system centered at x

$$I(x) = \{U \subseteq X \mid U \text{isaneighbourhoodof} x\}, \tag{A.125}$$

a **neighborhood local basis** is a subset J of $I(x)$ such that $\forall U \in I(x) \ \ \exists A \in J \ \mid \ A \subset U$.

Definition A.2.9. A topological space (X, τ) is a **Hausdorff space** if

$$\forall x, y \in X \ \ \exists \, U \in I(x), V \in I(y) \ \mid \ U \cap V = \emptyset. \tag{A.126}$$

Definition A.2.10. Let (X, τ) be a topological vector space. A subset C of X is said to be **convex** if the segments $\{(1-t)x + ty \mid 0 \leq t \leq 1\}$ are contained in C for any $x, y \in C$.

Definition A.2.11. Let (X, τ) be a topological vector space. (X, τ) is said to be **locally convex** if $\mathcal{C} = \{C \in I(0) \ \mid \ C \text{isconvex}\}$ is a neighborhood local basis.

Definition A.2.12. Let $\{\psi_n\}_{n \in \mathbb{N}}$ be a sequence of elements of X, where (X, τ) is a topological vector space. Let $\mathcal{B}$ be a neighborhood local basis that is centered at 0. $\{\psi_n\}_{n \in \mathbb{N}}$ is said to be a **Cauchy sequence** if

$$\forall B \in \mathcal{B} \ \ \exists \nu \in \mathbb{N} \ \mid \ \phi_m - \phi_n \in B \ \ \forall m, n > \nu. \tag{A.127}$$

Definition A.2.13. A topological vector space is said to be **complete** when it contains the limit elements of every its Cauchy sequence.

Definition A.2.14. Let (X, τ) be a topological vector space. A topological vector space Y is the X **completion** according to τ if it is the smallest vector space that contains every members of X and each limit element of Cauchy sequences in X.

Definition A.2.15. Let X be a set. A **metric** (or a **distance**) on X is a function $d : X \times X \to \mathbb{R}$ that satisfies the following three conditions:

- $d(x,y) \geq 0 \; \forall x, y \in X$ and $d(x,y) = 0 \; \Leftrightarrow x = y$;
- $d(x,y) = d(y,x) \; \forall x, y \in X$;
- $d(x,z) \leq d(x,y) + d(y,z) \; \forall x, y, z \in X$.

Definition A.2.16. Given a metric space (X,d), we define an **open ball** of radius $r \in \mathbb{R}^+$ centered at $x_0 \in X$ as the set

$$B_r(x_0) = \{x \in X \mid d(x_0, x) < r\}. \tag{A.128}$$

Definition A.2.17. Let (X,d) be a metric space. d induces a **metric topology** τ_d on X, which is generated by the basis $\mathcal{B} = \{B_r(x) \mid x \in X, \;\; r \in \mathbb{R}^+\}$. In τ_d, the subset $J = \{B_r(0) \mid r \in \mathbb{R}^+\}$ of $\mathcal{B}$ is a neighborhood centered at the origin.

Definition A.2.18. Let X be a set. A **norm** on X is a function $||\cdot|| : X \to \mathbb{R}$ that satisfies the following three conditions:

- $||x|| \geq 0 \; \forall x \in X$ and $||x|| = 0 \; \Leftrightarrow x = 0$;
- $||ax|| = |a| \; ||x|| \; \forall x \in X, \; \forall \text{scalar} a$;
- $||x + y|| \leq ||x|| + ||y|| \; \forall x, y \in X$.

Definition A.2.19. In a topological space (X,τ), a point $x_0 \in X$ is the **limit** of the sequence $\{x_n\}_{n \in \mathbb{N}}$ if

$$\forall U \in I(x_0) \;\; \exists \nu \in \mathbb{N} \;\mid\; x_n \in U \;\; \forall n > \nu. \tag{A.129}$$

Definition A.2.20. $A \subset X$ is **dense** in (X,τ) if every point $x \in X$ either belongs to A or is a limit point of a sequence in A.

Definition A.2.21. A topological vector space that is normed and complete with respect to the norm is called **Banach space**.

Definition A.2.22. A topological vector space with a scalar product is called **Euclidean space**.

Definition A.2.23. A Banach space with a scalar product is called **Hilbert space**.

Definition A.2.24. Given a set X, an **algebra** $\mathcal{A}$ is a collection of elements of the power set $P(X)$ such that:

- $\emptyset \in \mathcal{A}$;

- $A^c \in \mathcal{A} \ \ \forall A \in \mathcal{A}$;
- $A \cup B \in \mathcal{A} \ \ \forall A, B \in \mathcal{A}$.

Definition A.2.25. Given a set X, a **σ-algebra** $\mathcal{A}$ is a collection of elements of the power set $P(X)$ such that:

- $\emptyset \in \mathcal{A}$;
- $A^c \in \mathcal{A} \ \ \forall A \in \mathcal{A}$;
- $\cup_{n=1}^{\infty} A_n \in \mathcal{A} \ \forall \{A_n\}_{n\in\mathbb{N}} \subset \mathcal{A}$.

The members of $\mathcal{A}$ are called **measurable sets**.

Remark A.2.1. Each σ-algebra is an algebra.

Definition A.2.26. Given an algebra $\mathcal{A}$, a **measure** on $\mathcal{A}$ is a function $\mu : \mathcal{A} \to \bar{\mathbb{R}}$ that satisfies the following three conditions:

- $\mu(\emptyset) = 0$;
- $\mu(A) \geq 0 \ \ \forall A \in \mathcal{A}$;
- $\mu(\cup_{n=1}^{\infty} A_n) = \sum_{n=1}^{\infty} \mu(A_n) \ \ \forall \{A_n\}_{n\in\mathbb{N}} \subset \mathcal{A} \ \mid \ \cup_{n=1}^{\infty} A_n \subset (A), \ \ A_k \cap A_j = \emptyset \ \forall k \neq j$.

Definition A.2.27. Given a set X, an algebra $\mathcal{A}$ on X and a measure μ on $\mathcal{A}$, a **measure space** is the triplet $(X, \mathcal{A}, \mu)$.

Definition A.2.28. Let $(X, \mathcal{A}, \mu)$ be a measure space. If $\mu(X) = 1$, $(X, \mathcal{A}, \mu)$ is a **probability space** and μ is called a **probability measure**.

Definition A.2.29. Given a vector space V on a field $\mathbb{K}$, $V^* = \{F : V \to \mathbb{K} \mid F\text{iscontinuousandlinear}\}$ is called a **dual space** of V, and any $F \in V^*$ is called a **linear functional**. Moreover, if W is a vector subspace of V, then $V^* \subset W^*$.

The one which follows is a fundamental theorem about the representation of the dual space of a Hilbert space.

Theorem A.2.1 (Riesz-Fréchet)**.** *Let $\mathcal{H}$ be a Hilbert space. Given any $F \in \mathcal{H}^*$, there exists a unique $f \in \mathcal{H}$ such that*

$$\langle F|\phi\rangle = (f|\phi) \ \ \forall \phi \in \mathcal{H}, \tag{A.130}$$

where $\langle F|\phi\rangle := F(\phi)$ is the operatorial product. Moreover,

$$||F||_{\mathcal{H}^*} = \sup_{||\phi||_{\mathcal{H}} \leq 1} |\langle F|\phi\rangle| = ||f||_{\mathcal{H}}. \tag{A.131}$$

Definition A.2.30. Let us consider a continuous linear operator $A : \mathcal{H} \to \mathcal{H}$, where $\mathcal{H}$ is a Hilbert space. Then the **adjoint** of A is the continuous linear operator $A^\dagger : \mathcal{H} \to \mathcal{H}$ satisfying

$$(Ax|y) = (x|A^\dagger y) \; \forall x, y \in H. \tag{A.132}$$

If $A = A^\dagger$ it is a **Hermitian** (or **self-adjoint**) operator. Moreover, if A is a Hermitian continuous operator, its spectrum is real.

Definition A.2.31. A continuous linear operator $U : \mathcal{H} \to \mathcal{H}$ is said to be **unitary** if and only if $U^\dagger = U^{-1}$. Moreover, an operator U is unitary on $\mathcal{H}$ if and only if U is an isometry, i.e. $||Ux|| = ||x||$.

Definition A.2.32. Let us define the **Hardy space** $\mathcal{H}^p_+$ ($\mathcal{H}^p_-$), $p \in (0; +\infty)$ for the upper half space (for the lower half space) as the space of the holomorphic functions $f : \mathbb{C} \to \mathbb{C}$ such that $||f|| := \sup_{y>0} \left[\int_{\mathbb{R}} |f|\right]^{1/p}$ $\left(||f|| := \sup_{y<0} \left[\int_{\mathbb{R}} |f|\right]^{1/p}\right)$ is a finite real number.

BIBLIOGRAPHY

[1] D. Pierangeli et al. "Deep optical neural network by living tumour brain cells." In: ArXiv e-prints (2019). arXiv: 1812.09311 [physics.med-ph].

[2] G. Marcucci et al. "Anisotropic Optical Shock Waves in Isotropic Media with Giant Nonlocal Nonlinearity." In: ArXiv e-prints (2019). arXiv: 1909.04506 [physics.optics].

[3] G. Marcucci et al. "Programming Multi-level Quantum Gates in Disordered Computing Reservoirs via Machine Learning." In: ArXiv e-prints (2019). arXiv: 1905.05264 [quant-ph].

[4] G. Marcucci et al. "Quantum Control of Quantum Solitons." In: Advanced Photonics 2018. Optical Society of America, 2018, NpM2I.3.

[5] G. Marcucci et al. "Metriplectic Structure of a Radiation-Matter Interaction Toy Model." In: ArXiv e-prints (2018). arXiv: 1804.00526 [physics.gen-ph].

[6] G. Marcucci et al. "Simulating general relativity and non-commutative geometry by non-paraxial quantum fluids." In: New J. Phys. Accepted Manuscript (2019).

[7] G. Marcucci et al. "Topological Control of Extreme Waves." In: Nat. Commun. 10 (2019), p. 5090.

[8] G. Marcucci et al. "Optical spatial shock waves in nonlocal nonlinear media." In: Adv. Phys. X 4 (2019), p. 1662733.

[9] D. Pierangeli et al. "Large-Scale Photonic Ising Machine by Spatial Light Modulation." In: Phys. Rev. Lett. 122 (2019), p. 213902.

[10] D. Pierangeli et al. "Observation of Fermi-Pasta-Ulam-Tsingou Recurrence and Its Exact Dynamics." In: Phys. Rev. X 8 (2018), p. 041017.

[11] "Machine learning inverse problem for topological photonics." In: Comm. Phys. 1 (2018), p. 57.

[12] L. Di Mauro Villari et al. "Sine-Gordon soliton as a model for Hawking radiation of moving black holes and quantum soliton evaporation." In: J. Phys. Commun. 2 (2018), p. 055016.

[13] G. Marcucci et al. "Time Asymmetric Quantum Mechanics and Shock Waves: Exploring the Irreversibility in Nonlinear Optics." In: Ann. Phys. 529 (2017), p. 1600349.

[14] G. Marcucci et al. "Irreversible evolution of a wave packet in the rigged-Hilbert-space quantum mechanics." In: Phys. Rev. A 94 (2016), p. 052136.

[15] M. C. Braidotti et al. "Nonlinear Gamow vectors in nonlocal optical propagation." In: Nuovo Cimento 39 C.281 (02 2016).

[16] S. Gentilini et al. "Physical realization of the Glauber quantum oscillator." In: Sci. Rep. 5 (2015), p. 15816.

[17] S. Gentilini et al. "Nonlinear gamow vectors, shock waves, and irreversibility in optically nonlocal media." In: Phys. Rev. A 92 (2015), p. 023801.

[18] M. C. Braidotti et al. "Irreversibility and Squeezing of Shock Waves." In: Nonlinear Guided Wave Optics. IOP Publishing, 2017. Chap. 3.

[19] F. Heylighen et al. "Complexity and Philosophy." In: ed. by J. Bogg et al. Oxford UK: Radcliffe Publishing, 2007. Chap. 8, p. 117.

[20] I. Prigogine et al. Order Out of Chaos. New York: Bantam Books, 1984.

[21] M. M. Waldrop. Complexity. New York: Simon & Schuster Paperbacks, 1992.

[22] M. Gell-Mann. Complex adaptive systems. Addison-Wesley, 1994.

[23] J. H. Holland. Hidden Order. Helix Books. New York: Basic Books, 1996.

[24] J. B. Hartle. "The Quantum Mechanics of Cosmology." In: ArXiv (2018). arXiv: 1805.12246 [gr-qc].

[25] C. G. Langton. "Computation at the edge of chaos: phase transitions and emergent computation." In: Physica D 42 (1990), p. 12.

[26] J. Satsuma et al. "B. Initial Value Problems of One-Dimensional Self-Modulation of Nonlinear Waves in Dispersive Media." In: Prog. Theor. Phys. Suppl. 55 (1974), p. 284.

[27] A. Saade et al. "Random projections through multiple optical scattering: Approximating Kernels at the speed of light." In: 2016 IEEE (ICASSP). 2016, p. 6215.

[28] G. A. Pavliotis et al. Multiscale Methods. Springer-Verlag Berlin Heidelberg, 2008.

[29] T. Hori et al. "Experimental and numerical analysis of widely broadened supercontinuum generation in highly nonlinear dispersion shifted fiber with a femtosecond pulse." In: J. Opt. Soc. Am. B 21 (2004), p. 1969.

[30] C. Cheng et al. "Nonlinear copropagation of two optical pulses of different frequencies in photonic crystal fibers." In: Appl. Phys. B 80 (2005), p. 291.

[31] G. P. Agrawal. Nonlinear Fiber Optics. 4th. Academic Press, 2016.

[32] S. R. Friberg et al. "Breakup of bound higher-order solitons." In: Opt. Lett. 17 (1992), p. 979.

[33] J. M. Dudley et al. "Modulation instability, Akhmediev Breathers and continuous wave supercontinuum generation." In: Opt. Express 17 (2009), p. 21497.

[34] M. Conforti et al. "Auto-modulation versus breathers in the nonlinear stage of modulational instability." In: Opt. Lett. 43 (2018), p. 5291.

[35] P. G. Grinevich et al. "The finite gap method and the analytic description of the exact rogue wave recurrence in the periodic NLS Cauchy problem. 1." In: Nonlinearity 31 (2018), p. 5258.

[36] P. G. Grinevich et al. "The exact rogue wave recurrence in the NLS periodic setting via matched asymptotic expansions, for 1 and 2 unstable modes." In: Phys. Lett. A 382 (2018), p. 973.

[37] A. Mussot et al. "Fibre multi-wave mixing combs reveal the broken symmetry of Fermi-Pasta-Ulam recurrence." In: Nat. Photon. 12 (2018), p. 303.

[38] R. W. Boyd. Nonlinear Optics. 3rd. Academic Press, 2008.

[39] A. V. Gurevich et al. "Nonstationary structure of a collisionless shock wave." In: Sov. Phys. JETP 38 (1974), p. 291.

[40] G. B. Whitham. Linear and Nonlinear Waves. New York: Wiley, 1999.

[41] G. A. El. "Resolution of a shock in hyperbolic systems modified by weak dispersion." In: Chaos 15 (2005), p. 037103.

[42] C. Barsi et al. "Dispersive shock waves with nonlocal nonlinearity." In: Opt. Lett. 32 (2007), p. 2930.

[43] M. A. Hoefer et al. "Interactions of Dispersive Shock Waves." In: Physica D 236 (2007), p. 44.

[44] M. A. Hoefer et al. "Piston Dispersive Shock Wave Problem." In: Phys. Rev. Lett. 100 (2008), p. 084504.

[45] M. Crosta et al. "The Whitham approach to dispersive shocks in systems with cubic–quintic nonlinearities." In: New J. Phys. 14 (2012), p. 093019.

[46] M. Conforti et al. "Resonant radiation shed by dispersive shock waves." In: Phys. Rev. A 89 (2014), p. 013807.

[47] A. Moro et al. "Mechanism of wave breaking from a vacuum point in the defocusing nonlinear Schrödinger equation." In: Phys. Rev. E 89 (2014), p. 023202.

[48] G. A. El et al. "Dispersive shock waves and modulation theory." In: Physica D 333 (2016), p. 11.

[49] G. A. El et al. "Radiating dispersive shock waves in non-local optical media." In: Proc. R. Soc. A 472 (2016), p. 20150633.

[50] D. H. Peregrine. "Calculations of the development of an undular bore." In: J. Fluid Mech. 25 (1966), p. 321.

[51] R. J. Taylor et al. "Observation of Collisionless Electrostatic Shocks." In: Phys. Rev. Lett. 24 (1970), p. 206.

[52] N. F. Smyth et al. "Hydraulic Jump and Undular Bore Formation on a Shelf Break." In: J. Phys. Ocean. 18 (1988), p. 947.

[53] J. E. Rothenberg et al. "Observation of the Formation of an Optical Intensity Shock and Wave Breaking in the Nonlinear Propagation of Pulses in Optical Fibers." In: Phys. Rev. Lett. 62 (1989), p. 531.

[54] B. Wetzel et al. "Experimental Generation of Riemann Waves in Optics: A Route to Shock Wave Control." In: Phys. Rev. Lett. 117 (2016), p. 073902.

[55] B. Damski. "Formation of shock waves in a Bose-Einstein condensate." In: Phys. Rev. A 69 (2004), p. 043610.

[56] A. M. Kamchatnov et al. "Dissipationless shock waves in Bose-Einstein condensates with repulsive interaction between atoms." In: Phys. Rev. A 69 (2004), p. 063605.

[57] V. M. Pérez-García et al. "Feshbach Resonance Induced Shock Waves in Bose-Einstein Condensates." In: Phys. Rev. Lett. 92 (2004), p. 220403.

[58] T. P. Simula et al. "Observations on Sound Propagation in Rapidly Rotating Bose-Einstein Condensates." In: Phys. Rev. Lett. 94 (2005), p. 080404.

[59] M. A. Hoefer et al. "Dispersive and classical shock waves in Bose-Einstein condensates and gas dynamics." In: Phys. Rev. A 74 (2006), p. 023623.

[60] J. J. Chang et al. "Formation of Dispersive Shock Waves by Merging and Splitting Bose-Einstein Condensates." In: Phys. Rev. Lett. 101 (2008), p. 170404.

[61] E. Bettelheim et al. "Nonlinear Quantum Shock Waves in Fractional Quantum Hall Edge States." In: Phys. Rev. Lett. 97 (2006), p. 246401.

[62] G. A. El et al. "Theory of optical dispersive shock waves in photorefractive media." In: Phys. Rev. A 76 (2007), p. 053813.

[63] L. Romagnani et al. "Observation of Collisionless Shocks in Laser-Plasma Experiments." In: Phys. Rev. Lett. 101 (2008), p. 025004.

[64] M. D. Maiden et al. "Observation of Dispersive Shock Waves, Solitons, and Their Interactions in Viscous Fluid Conduits." In: Phys. Rev. Lett. 116 (2016), p. 174501.

[65] S. A. Akhmanov et al. "Nonlinear Defocusing of Laser Beams." In: Sov. J. Exp. Theor. Phys. Lett. 6 (1967), p. 38.

[66] N. Ghofraniha et al. "Shocks in Nonlocal Media." In: Phys. Rev. Lett. 99 (2007), p. 043903.

[67] W. Wan et al. "Dispersive superfluid-like shock waves in nonlinear optics." In: Nat. Phys. 3 (2007), p. 46.

[68] C. Conti et al. "Observation of a Gradient Catastrophe Generating Solitons." In: Phys. Rev. Lett. 102 (2009), p. 083902.

[69] N. Ghofraniha et al. "Shock Waves in Disordered Media." In: Phys. Rev. Lett. 109 (2012), p. 243902.

[70] J. Garnier et al. "Incoherent Dispersive Shocks in the Spectral Evolution of Random Waves." In: Phys. Rev. Lett. 111 (2013), p. 113902.

[71] S. Gentilini et al. "Shock waves in thermal lensing." In: Phys. Rev. A 87 (2013), p. 053811.

[72] S. Gentilini et al. "Optical shock waves in silica aerogel." In: Opt. Express 22 (2014), p. 1667.

[73] V. Smith et al. "Dark Soliton Attraction and Optical Spatial Shock Waves Observed in M-cresol/Nylon Solutions." In: CLEO: 2014. Optical Society of America, 2014, FW3D.1.

[74] G. Xu et al. "From coherent shocklets to giant collective incoherent shock waves in nonlocal turbulent flows." In: Nat. Commun. 6 (2015), p. 8131.

[75] M. C. Braidotti et al. "Gamow vectors explain the shock profile." In: Opt. Express 24 (2016), p. 21963.

[76] G. Xu et al. "Incoherent shock waves in long-range optical turbulence." In: Physica D 333 (2016), p. 310.

[77] A. Zannotti et al. "Pearcey solitons in curved nonlinear photonic caustic lattices." In: J. Opt. 19 (2017), p. 094001.

[78] R. Gautam et al. "Optical force induced nonlinearity and self guiding of light in human red blood cell suspensions." In: Light Sc. Appl. 8 (2019), p. 31.

[79] Clifford S. Gardner et al. "Method for Solving the Korteweg-deVries Equation." In: Phys. Rev. Lett. 19 (1967), p. 1095.

[80] G. Fibich. The Nonlinear Schrödinger Equation. Springer-Verlag Berlin Heidelberg, 2015.

[81] C. A. Carter et al. "Comparison of models describing the thermal lens effect." In: Appl. Opt. 23 (1984), p. 476.

[82] O. Bang et al. "Collapse arrest and soliton stabilization in nonlocal nonlinear media." In: Phys. Rev. E 66 (2002), p. 046619.

[83] M. Peccianti et al. "Nonlocal spatial soliton interactions in nematic liquid crystals." In: Opt. Lett. 27 (2002), p. 1460.

[84] C. Conti et al. "Observation of Optical Spatial Solitons in a Highly Nonlocal Medium." In: Phys. Rev. Lett. 92 (2004), p. 113902.

[85] Q. Guo et al. "Large phase shift of nonlocal optical spatial solitons." In: Phys. Rev. E 69 (2004), p. 016602.

[86] C. Rotschild et al. "Solitons in Nonlinear Media with an Infinite Range of Nonlocality: First Observation of Coherent Elliptic Solitons and of Vortex-Ring Solitons." In: Phys. Rev. Lett. 95 (2005), p. 213904.

[87] A. I. Yakimenko et al. "Stable vortex solitons in nonlocal self-focusing nonlinear media." In: Phys. Rev. E 71 (2005), p. 065603.

[88] A. Minovich et al. "Experimental reconstruction of nonlocal response of thermal nonlinear optical media." In: Opt. Lett. 32 (2007), p. 1599.

[89] V. Folli et al. "Frustrated Brownian Motion of Nonlocal Solitary Waves." In: Phys. Rev. Lett. 104 (2010), p. 193901.

[90] V. Folli et al. "Anderson localization in nonlocal nonlinear media." In: Opt. Lett. 37 (2012), p. 332.

[91] F. Maucher et al. "Stability of solitary waves in random nonlocal nonlinear media." In: Phys. Rev. A 85 (2012), p. 063803.

[92] V. Folli et al. "Random walk of solitary and shock waves in nonlocal disordered media." In: New J. Phys. 15 (2013), p. 085026.

[93] V. Smith et al. "Giant tunable self-defocusing nonlinearity and dark soliton attraction observed in m-cresol/nylon thermal solutions." In: Opt. Mater. Express 4 (2014), p. 1807.

[94] A. Alberucci et al. "Spatial optical solitons in highly nonlocal media." In: Phys. Rev. A 91 (2015), p. 013841.

[95] A. Alberucci et al. "Breather solitons in highly nonlocal media." In: J. Opt. 18 (2016), p. 125501.

[96] T. P. Horikis et al. "Light Meets Water in Nonlocal Media: Surface Tension Analogue in Optics." In: Phys. Rev. Lett. 118 (2017), p. 243903.

[97] T. P. Horikis et al. "Patterns of water in light." In: Proc. R. Soc. A 475 (2019), p. 20190110.

[98] A. Bohm. "Resonance poles and Gamow vectors in the rigged Hilbert space formulation of quantum mechanics." In: J. Math. Phys. 22 (1981), p. 2813.

[99] A. Bohm et al. "Gamow Vectors and Decaying States." In: Am. J. Phys. 57 (1989), p. 1103.

[100] C. G. Bollini et al. "Gamow States as Continuous Linear Functionals over Analytical Test Functions." In: J. Math. Phys. 37 (1996), p. 4235.

[101] M. Castagnino et al. "Rigged Hilbert spaces and time-asymmetry: the case of the upside-down simple harmonic oscillator." In: Int. Jour. Theo. Phys. 36 (1997), p. 2349.

[102] A. Bohm et al. "Quantum Theory in the Rigged Hilbert Spaces - Irreversibility from Causality." In: Lect. N. Phys. 504 (1998), p. 179.

[103] A. Bohm. "Time Asymmetric Quantum Physics." In: Phys. Rev. A60 (1999), p. 861.

[104] R. de la Madrid et al. "A Pedestrian Introduction to Gamow Vectors." In: Am. J. Phys. 70 (2002), p. 626.

[105] D. Chruściński. "Quantum Mechanics of Damped Systems." In: J. Math. Phys. 44 (2003), p. 3718.

[106] D. Chruściński. "Quantum Mechanics of Damped Systems 2." In: J. Math. Phys. 45 (2004), p. 841.

[107] O. Civitarese et al. "Physical and Mathematical Aspects of Gamow States." In: Phys. Rep. 396 (2004), p. 41.

[108] A. Picozzi. "Towards a nonequilibrium thermodynamic description of incoherent nonlinear optics." In: Opt. Express 15 (2007), p. 9063.

[109] S. Can et al. "Observation of the kinetic condensation of classical waves." In: Nat. Phys. 8 (2012), p. 470.

[110] A. Picozzi et al. "Optical wave turbulence: Towards a unified nonequilibrium thermodynamic formulation of statistical nonlinear optics." In: Phys. Rep. 542 (2014), p. 1.

[111] A. Fusaro et al. "Emergence of long-range phase coherence in nonlocal fluids of light." In: Phys. Rev. A 95 (2017), p. 063818.

[112] C. J. Wetterer et al. "Correction of thermal blooming by optical phase conjugation." In: Opt. Lett. 14 (1989), p. 874.

[113] P. Brochard et al. "Thermal nonlinear refraction in dye solutions: a study of the transient regime." In: J. Opt. Soc. Am. B 14 (1997), p. 405.

[114] E. C. Kemble. "A contribution to the Theory of the B.W.K. Method." In: Phys. Rev. 48 (1935), p. 549.

[115] A. W. Snyder et al. "Accessible Solitons." In: Science 276 (1997), p. 1538.

[116] E. Celeghini et al. "Applications of rigged Hilbert spaces in quantum mechanics and signal processing." In: J. Math. Phys. 57 (2016), p. 072105.

[117] G. Gamow. "Zur Quantentheorie des Atomkernes." In: Z. Phys. 51 (1928), p. 204.

[118] G. Gamow. "The Quantum Theory of Nuclear Disintegration." In: Nature 122 (1928), p. 805.

[119] M. Lisak et al. "Dissipative damping of dark solitons in optical fibers." In: Opt. Lett. 16 (1991), p. 1936.

[120] Y. V. Kartashov et al. "Brownian soliton motion." In: Phys. Rev. A 77 (2008), p. 051802.

[121] R. L. Honeycutt. "Stochastic Runge-Kutta algorithms. I. White noise." In: Phys. Rev. A 45 (1992), p. 600.

[122] R. L. Honeycutt. "Stochastic Runge-Kutta algorithms. II. Colored noise." In: Phys. Rev. A 45 (1992), p. 604.

[123] A. Venkateswara Rao et al. "Preparation and characterization of hydrophobic silica aerogels." In: Mat. Chem. Phys. 53 (1998), p. 13.

[124] P. Latimer. "Light Scattering and Absorption as Methods of Studying Cell Population Parameters." In: Ann. Rev. Biophys. Bioeng. 11 (1982), p. 129.

[125] A. Ashkin et al. "Optical trapping and manipulation of single cells using infrared laser beams." In: Nature 330 (1987), p. 769.

[126] A. Bezryadina et al. "Nonlinear Self-Action of Light through Biological Suspensions." In: Phys. Rev. Lett. 119 (2017), p. 058101.

[127] J. Dervaux et al. "Light-controlled flows in active fluids." In: Nat. Phys. 13 (2017), p. 306.

[128] C. Conti et al. "Optical Spatial Solitons in Soft Matter." In: PRL 95 (2005), p. 183902.

[129] R. El-Ganainy et al. "Soliton dynamics and self-induced transparency in nonlinear nanosuspensions." In: Opt. Express 15 (2007), p. 10207.

[130] E. Greenfield et al. "Shockwave based nonlinear optical manipulation in densely scattering opaque suspensions." In: Opt. Express 21 (2013), p. 23785.

[131] W. Man et al. "Optical Nonlinearities and Enhanced Light Transmission in Soft-Matter Systems with Tunable Polarizabilities." In: Phys. Rev. Lett. 111 (2013), p. 218302.

[132] J. M. Steinke et al. "Comparison of Mie theory and the light scattering of red blood cells." In: Appl. Opt. 27 (1988), p. 4027.

[133] N. Ghosh et al. "Simultaneous determination of size and refractive index of red blood cells by light scattering measurements." In: Appl. Phys. Lett. 88 (2006), p. 084101.

[134] L. Miccio et al. "Red blood cell as an adaptive optofluidic microlens." In: Nat. Commun. 6 (2015), p. 6502.

[135] R. Gautam et al. "Characterization of Storage-Induced Red Blood Cell Hemolysis Using Raman Spectroscopy." In: Lab. Med. 49 (2018), p. 298.

[136] T. Dauxois. "Fermi, Pasta, Ulam, and a mysterious lady." In: Phys. Today 61 (2008), p. 55.

[137] J. Ford. "The Fermi-Pasta-Ulam problem: paradox turns discovery." In: Phys. Rep. 213 (1992), p. 271.

[138] G. Gallavotti. "The Fermi-Pasta-Ulam Problem: A Status Report." In: Lecture Notes in Physics. Vol. 728. Springer-Verlag Berlin Heidelberg, 2008.

[139] G. P. Berman et al. "The Fermi-Pasta-Ulam problem: fifty years of progress." In: Chaos 15 (2005), p. 015104.

[140] G. Benettin et al. "The Fermi-Pasta-Ulam problem and its underlying integrable dynamics." In: J. Stat. Phys. 152 (2013), p. 195.

[141] M. Onorato et al. "Route to Thermalization in the α-Fermi-Pasta-Ulam System." In: Proc. Nat. Acad. Sci. 112 (2015), p. 4208.

[142] M. Guasoni et al. "Incoherent Fermi-Pasta-Ulam Recurrences and Unconstrained Thermalization Mediated by Strong Phase Correlations." In: Phys. Rev. X 7 (2017), p. 011025.

[143] Y. V. Lvov et al. "Double Scaling in the Relaxation Time in the β-Fermi-Pasta-Ulam-Tsingou Model." In: Phys. Rev. Lett. 120 (2018), p. 144301.

[144] S. Wabnitz et al. "Instability and noise-induced thermalization of Fermi-Pasta-Ulam recurrence in the nonlinear Schrödinger equation." In: Phys. Lett. A 378 (2014), p. 2750.

[145] O. Kimmoun et al. "Modulation Instability and Phase-Shifted Fermi-Pasta-Ulam Recurrence." In: Sci. Rep. 6 (2016), p. 28516.

[146] S. Trillo et al. "Experimental Observation and Theoretical Description of Multisoliton Fission in Shallow Water." In: Phys. Rev. Lett. 117 (2016), p. 144102.

[147] M. Wu et al. "Experimental Observation of Fermi-Pasta-Ulam Recurrence in a Nonlinear Feedback Ring System." In: Phys. Rev. Lett. 98 (2007), p. 047202.

[148] C. Bao et al. "Observation of Fermi-Pasta-Ulam Recurrence Induced by Breather Solitons in an Optical Microresonator." In: Phys. Rev. Lett. 117 (2016), p. 163901.

[149] G. Van Simaeys et al. "Experimental Demonstration of the Fermi-Pasta-Ulam Recurrence in a Modulationally Unstable Optical Wave." In: Phys. Rev. Lett. 87 (2001), p. 033902.

[150] A. Mussot et al. "Fermi-Pasta-Ulam Recurrence in Nonlinear Fiber Optics: The Role of Reversible and Irreversible Losses." In: Phys. Rev. X 4 (2014), p. 011054.

[151] M. J. Ablowitz et al. "Discrete and continuous nonlinear Schrödinger systems." In: London Math. Soc. 302 (2004).

[152] B. Kibler et al. "The Peregrine soliton in nonlinear fibre optics." In: Nat. Phys. 6 (2010), p. 790.

[153] B. Frisquet et al. "Collision of Akhmediev Breathers in Nonlinear Fiber Optics." In: Phys. Rev. X 3 (2013), p. 041032.

[154] M. Erkintalo et al. "Higher-Order Modulation Instability in Nonlinear Fiber Optics." In: Phys. Rev. Lett. 107 (2011), p. 253901.

[155] A. Chabchoub et al. "Rogue Wave Observation in a Water Wave Tank." In: Phys. Rev. Lett. 106 (2011), p. 204502.

[156] A. Chabchoub et al. "Super Rogue Waves: Observation of a Higher-Order Breather in Water Waves." In: Phys. Rev. X 2 (2012), p. 011015.

[157] B. Kibler et al. "Super-regular Breathers in Optics and Hydrodynamics: Omnipresent Modulation Instability beyond Simple Periodicity." In: Phys. Rev. X 5 (2015), p. 041026.

[158] M. Onorato et al. "Rogue Waves and Their Generating Mechanisms in Different Physical Contexts." In: Phys. Rep. 528 (2013), p. 47.

[159] J. M. Dudley et al. "Instabilities, breathers and rogue waves in optics." In: Nat. Photon. 8 (2014), p. 755.

[160] N. Akhmediev et al. "Roadmap on optical rogue waves and extreme events." In: J. Opt. 18 (2016), p. 063001.

[161] D. Pierangeli et al. "Spatial Rogue Waves in Photorefractive Ferroelectrics." In: Phys. Rev. Lett. 115 (2015), p. 093901.

[162] D. Pierangeli et al. "Enhancing optical extreme events through input wave disorder." In: Phys. Rev. A 94 (2016), p. 063833.

[163] P. Suret et al. "Single-shot observation of optical rogue waves in integrable turbulence using time microscopy." In: Nat. Commun. 7 (2016), p. 13136.

[164] P. Berman et al. "The limit of stochasticity for a one-dimensional chain of interacting oscillators." In: Sov. Phys. JETP 60 (1984), p. 1116.

[165] E. Infeld. "Quantitive Theory of the Fermi-Pasta-Ulam Recurrence in the Nonlinear Schrödinger Equation." In: Phys. Rev. Lett 47 (1981), p. 717.

[166] N. N. Akhmediev et al. "Exact first-order solutions of the nonlinear Schrödinger equation." In: Theor. Math. Phys. 72 (1987), p. 809.

[167] E. DelRe et al. "Photorefractive Solitons and Their Underlying Nonlocal Physics." In: Prog. Opt. 53 (2009). Ed. by E. Wolf, p. 153.

[168] E. DelRe et al. "Approach to space-charge field description in photorefractive crystals." In: J. Opt. Soc. Am. B 15 (1998), p. 1469.

[169] E. DelRe et al. "Optical nonlinearity and existence conditions for quasi-steady-state photorefractive solitons." In: J. Opt. Soc. Am. B 23 (2006), p. 2323.

[170] J. Fatome et al. "Observation of Optical Undular Bores in Multiple Four-Wave Mixing." In: Phys. Rev. X 4 (2014), p. 021022.

[171] Q. Lu et al. "Visualization of spatial-temporal evolution of light-induced refractive index in Mn:Fe:KTN Co-doped crystal based on digital holographic interferometry." In: IEEE Photon. J. 7 (2015), p. 2600711.

[172] F. Di Mei et al. "Intrinsic negative mass from nonlinearity." In: Phys. Rev. Lett. 116 (2016), p. 153902.

[173] D. Pierangeli et al. "Super-crystals in composite ferroelectrics." In: Nat. Commun. 7 (2016), p. 10674.

[174] C. Barsi et al. "Imaging through nonlinear media using digital holography." In: Nat. Photon. 3 (2009), p. 211.

[175] S. A. Chin et al. "Anatomy of the Akhmediev breather: Cascading instability, first formation time, and Fermi-Pasta-Ulam recurrence." In: Phys. Rev. E 92 (2015), p. 063202.

[176] J.M. Martinis et al. "Rabi Oscillations in a Large Josephson-Junction Qubit." In: Phys. Rev. Lett. 89 (2002), p. 117901.

[177] N. Devine et al. "Recurrence phase shift in Fermi-Pasta-Ulam nonlinear dynamics." In: Phys. Lett. A 375 (2011), p. 4158.

[178] J. M. Soto-Crespo et al. "Adiabatic transformation of continuous waves into trains of pulses." In: Phys. Rev. A 96 (2017), p. 023825.

[179] D. Pierangeli et al. "Turbulent Transitions in Optical Wave Propagation." In: Phys. Rev. Lett. 117 (2016), p. 183902.

[180] D. Pierangeli et al. "Observation of replica symmetry breaking in disordered nonlinear wave propagation." In: Nat. Commun. 8 (2017), p. 1501.

[181] N.N. Akhmediev et al. "Pseudo-recurrence in Two-Dimensional Modulation Instability with a Saturable Self-Focusing Nonlinearity." In: Phys. Rev. Lett. 65 (1990), p. 1423.

[182] B. Rumpf et al. "Coherent Structures and Entropy in Constrained, Modulationally Unstable, Nonintegrable Systems." In: PRL 87 (2001), p. 054102.

[183] D. R. Solli et al. "Optical rogue waves." In: Nature 450 (2007), p. 1054.

[184] C. Bonatto et al. "Deterministic Optical Rogue Waves." In: PRL 107 (2011), p. 053901.

[185] M.J. Ablowitz et al. Solitons. Cambridge University Press, 1991.

[186] Y. S. Kivshar et al. Optical Solitons. Academic Press, Elsevier Science, 2003.

[187] N. Bulso et al. "Effective dissipation and nonlocality induced by nonparaxiality." In: Phys. Rev. A 89 (2014), p. 023804.

[188] Y. V. Kartashov et al. "Two-dimensional dispersive shock waves in dissipative optical media." In: Opt. Lett. 38 (2013), p. 7900.

[189] M. Erkintalo et al. "On the statistical interpretation of optical rogue waves." In: Eur. Phys. J. Sp. Top. 185 (2010), p. 135.

[190] N. Akhmediev et al. "Recent progress in investigating optical rogue waves." In: J. Opt. 15 (2013), p. 060201.

[191] D. S. Agafontsev et al. "Integrable turbulence and formation of rogue waves." In: Nonlinearity 28 (2015), p. 2791.

[192] S. Toenger et al. "Emergent rogue wave structures and statistics in spontaneous modulation instability." In: Sci. Rep. 5 (2015), p. 10380.

[193] A. Tikan et al. "Universality of the Peregrine Soliton in the Focusing Dynamics of the Cubic Nonlinear Schrödinger Equation." In: Phys. Rev. Lett. 119 (2017), p. 033901.

[194] A. A. Gelash et al. "Strongly interacting soliton gas and formation of rogue waves." In: Phys. Rev. E 98 (2018), p. 042210.

[195] A. Gelash et al. "Bound state soliton gas dynamics underlying the noise-induced modulational instability." In: ArXiv e-prints (2019). arXiv: 1907.07914 [nlin.SI].

[196] V. E. Zakharov et al. "Behavior of Light Beams in Nonlinear Media." In: J. Exp. Theor. Phys. 33 (1971), p. 77.

[197] G. A. El et al. "Kinetic Equation for a Dense Soliton Gas." In: Phys. Rev. Lett. 95 (2005), p. 204101.

[198] I. Redor et al. "Experimental Evidence of a Hydrodynamic Soliton Gas." In: Phys. Rev. Lett. 122 (2019), p. 214502.

[199] W. Wan et al. "Diffraction from an edge in a self-focusing medium." In: Opt. Lett. 35 (2010), p. 2819.

[200] G. A. El et al. "Dam break problem for the focusing nonlinear Schrödinger equation and the generation of rogue waves." In: Nonlinearity 29 (2016), p. 2798.

[201] F. Audo et al. "Experimental observation of the emergence of Peregrine-like events in focusing dam break flows." In: Opt. Lett. 43 (2018), p. 2864.

[202] G. Biondini. "Riemann problems and dispersive shocks in self-focusing media." In: Phys. Rev. E 98 (2018), p. 052220.

[203] G. Biondini et al. "Nonlinear interactions between solitons and dispersive shocks in focusing media." In: Phys. Rev. E 99 (2019), p. 022215.

[204] M. Bertola et al. "Rogue waves in multiphase solutions of the focusing nonlinear Schrödinger equation." In: Proc. R. Soc. A 472 (2016), p. 20160340.

[205] G. Xu et al. "Dispersive Dam-Break Flow of a Photon Fluid." In: Phys. Rev. Lett. 118 (2017), p. 254101.

[206] S. Randoux et al. "Nonlinear spectral analysis of Peregrine solitons observed in optics and in hydrodynamic experiments." In: Phys. Rev. E 98 (2018), p. 022219.

[207] G. Xu et al. "Phase evolution of Peregrine-like breathers in optics and hydrodynamics." In: Phys. Rev. E 99 (2019), p. 012207.

[208] J. N. Kutz. Data-Driven Modeling and Scientific Computing. Oxford University Press, 2013.

[209] J. C. Howell et al. "Realization of the Einstein-Podolsky-Rosen Paradox Using Momentum- and Position-Entangled Photons from Spontaneous Parametric Down Conversion." In: Phys. Rev. Lett. 92 (2004), p. 210403.

[210] J. Leach et al. "Quantum Correlations in Optical Angle–Orbital Angular Momentum Variables." In: Science 329 (2010), p. 662.

[211] M. Förtsch et al. "A versatile source of single photons for quantum information processing." In: Nat. Commun. 4 (2013), p. 1818.

[212] C. Couteau. "Spontaneous parametric down conversion." In: C. Phys. 59 (2018), p. 291.

[213] P. D. Drummond et al. The Quantum Theory of Nonlinear Optics. Cambridge University Press, 2014.

[214] P. D. Drummond et al. "Quantum Field Theory of Squeezing in Solitons." In: J. Opt. Soc. Am. B 4 (1987), p. 1565.

[215] A. Gilchrist et al. "Positive P representation: Application and validity." In: Phys. Rev. A 55 (1997), p. 3014.

[216] C. Gardiner et al. Quantum Noise. 3rd. Springer-Verlag Berlin Heidelberg, 2004.

[217] A. Greiner et al. "Numerical integration of stochastic differential equations." In: J. Stat. Phys. 51 (1988), p. 95.

[218] Y. Lai et al. "Quantum theory of solitons in optical fibers. I. Time-dependent Hartree approximation." In: Phys. Rev. A 40 (1989), p. 844.

[219] Y. Lai et al. "Quantum theory of solitons in optical fibers. II. Exact solution." In: Phys. Rev. A 40 (1989), p. 854.

[220] M. Hillery et al. "Quantization of electrodynamics in nonlinear dielectric media." In: Phys. Rev. A 30 (1984), p. 1860.

[221] P. D. Drummond et al. "Quantum solitons in optical fibres." In: Nature 365 (1993), p. 307.

[222] S. Schmitt et al. "Photon-Number Squeezed Solitons from an Asymmetric Fiber-Optic Sagnac Interferometer." In: Phys. Rev. Lett. 81 (1998), p. 2446.

[223] R. J. C. Spreeuw. "A Classical Analogy of Entanglement." In: Found. Phys. 28 (1998), p. 361.

[224] F. Töppel et al. "Classical entanglement in polarization metrology." In: New J. Phys. 16 (2014), p. 073019.

[225] S. Berg-Johansen et al. "Classically entangled optical beams for high-speed kinematic sensing." In: Optica 2 (2015), p. 864.

[226] D. Guzman-Silva et al. "Demonstration of local teleportation using classical entanglement." In: Laser & Phot. Rev. 10 (2016), p. 317.

[227] D. D'Alessandro. Introduction to Quantum Control and Dynamics. New York: Chapman and Hall, 2007.

[228] I. R. Petersen et al. "Quantum control theory and applications: a survey." In: IET Control Theory Appl. 4 (2010), p. 2651.

[229] M. V. Berry. "Transitionless quantum driving." In: J. Phys. A 42 (2009), p. 365303.

[230] A. Del Campo. "Shortcuts to Adiabaticity by Counterdiabatic Driving." In: Phys. Rev. Lett. 111 (2013), p. 100502.

[231] M. Okuyama et al. "From Classical Nonlinear Integrable Systems to Quantum Shortcuts to Adiabaticity." In: Phys. Rev. Lett. 117 (2016), p. 070401.

[232] K. Jacobs et al. "Feedback Control of Nonlinear Quantum Systems: A Rule of Thumb." In: Phys. Rev. Lett. 99 (2007), p. 020501.

[233] C. Brif et al. "Control of quantum phenomena: past, present and future." In: New J. Phys. 12 (2010), p. 075008.

[234] C. Altafini et al. “Modeling and Control of Quantum Systems: An Introduction.” In: IEEE Trans. Aut. C. 57 (2012), p. 1898.

[235] C. P. Koch. “Controlling open quantum systems: tools, achievements, and limitations.” In: J. Phys. Condens. Matter 28 (2016), p. 213001.

[236] N. Khaneja et al. In: J. Magn. Reson. 172 (2005), p. 296.

[237] M. Hallaji et al. “Quantum control of population transfer between vibrational states in an optical lattice.” In: ArXiv e-prints (2015). arXiv: 1510.09186.

[238] S. Machnes et al. In: Phys. Rev. A 84 (2011), p. 2176.

[239] S. Kallush et al. In: Phys. Rev. A 83 (2011), p. 063412.

[240] A. Rahmani et al. In: Phys. Rev. Lett. 107 (2011), p. 016402.

[241] N. Wu et al. In: Phys. Rev. B 91 (2015), p. 041115.

[242] P. Doria et al. “Optimal Control Technique for Many-Body Quantum Dynamics.” In: Phys. Rev. Lett. 106 (2011), p. 190501.

[243] N. Rach et al. “Dressing the chopped-random-basis optimization: A bandwidth-limited access to the trap-free landscape.” In: Phys. Rev. A 92 (2015), p. 062343.

[244] T. Caneva et al. “Optimal Control at the Quantum Speed Limit.” In: Phys. Rev. Lett. 103 (2009), p. 240501.

[245] C. Lovecchio et al. “Optimal preparation of quantum states on an atom-chip device.” In: Phys. Rev. A 93 (2016), p. 010304.

[246] S. Rosi et al. In: Phys. Rev. A 88 (2013), p. 021601.

[247] S. van Frank et al. “Optimal control of complex atomic quantum systems.” In: Sci. Rep. 6 (2016), p. 34187.

[248] R. Heck et al. “Do physicists stop searches too early? A remote-science, optimization landscape investigation.” In: ArXiv e-prints (2017). arXiv: 1709.02230.

[249] S. Kallush et al. In: New J. Phys. 16 (2014), p. 15008.

[250] S Lloyd et al. “Information Theoretical Analysis of Quantum Optimal Control.” In: Phys. Rev. Lett. 113 (2014), p. 010502.

[251] Jens Jakob W H Sørensen et al. “Exploring the Quantum Speed Limit with Computer Games.” In: Nature 532 (2016), p. 210.

[252] M. Bukov et al. “Machine Learning Meets Quantum State Preparation. The Phase Diagram of Quantum Control.” In: ArXiv e-prints (2017). arXiv: 1705.00565.

[253] M. Pysher et al. "Parallel Generation of Quadripartite Cluster Entanglement in the Optical Frequency Comb." In: Phys. Rev. Lett. 107 (2011), p. 030505.

[254] M. Chen et al. "Experimental Realization of Multipartite Entanglement of 60 Modes of a Quantum Optical Frequency Comb." In: Phys. Rev. Lett. 112 (2014), p. 120505.

[255] J. G. Titchener et al. "Two-photon tomography using on-chip quantum walks." In: Opt. Lett. 41.17 (2016), pp. 4079–4082.

[256] C. Reimer et al. "Generation of multiphoton entangled quantum states by means of integrated frequency combs." In: Science 351 (2016), p. 1176.

[257] M. Kues et al. "On-chip generation of high-dimensional entangled quantum states and their coherent control." In: Nature 546 (2017), p. 622.

[258] G. P. Agrawal. Applications of Nonlinear Fiber Optics. 2nd. New York: Academic Press, 2008.

[259] P. D. Drummond et al. "Quantum simulations in phase-space: from quantum optics to ultra-cold physics." In: Phys. Scripta 91 (2016), p. 073007.

[260] T. Caneva et al. "Chopped random-basis quantum optimization." In: Phys. Rev. A 84 (2011), p. 022326.

[261] S. K. Turitsyn et al. In: Phys. Rep. 521 (2012), p. 135.

[262] S. A. Derevyanko et al. "Capacity estimates for optical transmission based on the nonlinear Fourier transform." In: Nat. Commun. 7 (2016), p. 12710.

[263] D. Y. Tang et al. "Observation of High-Order Polarization-Locked Vector Solitons in a Fiber Laser." In: Phys. Rev. Lett. 101 (2008), p. 153904.

[264] H. Zhang et al. "Dark pulse emission of a fiber laser." In: PRA 80 (2009), p. 045803.

[265] H. Zhang et al. "Vector dark domain wall solitons in a fiber ring laser." In: Opt. Expr. 18 (2010), p. 4428.

[266] L. Barbiero et al. "Quantum bright solitons in a quasi one dimensional optical lattice." In: Phys. Rev. A 89 (2014), p. 063605.

[267] L. Barbiero et al. "Quantum bright solitons in the Bose-Hubbard model with site-dependent repulsive interactions." In: Phys. Rev. A 90 (2014), p. 063611.

[268] F. Calogero et al. "Comparison between the exact and Hartree solutions of a one-dimensional many-body problem." In: Phys. Rev. A 11 (1975), p. 265.

[269] R. V. Mishmash et al. "Quantum Entangled Dark Solitons Formed by Ultracold Atoms in Optical Lattices." In: Phys. Rev. Lett. 103 (14 2009), p. 140403.

[270] D. Delande et al. "Many-Body Matter-Wave Dark Soliton." In: PRL 112 (4 2014), p. 040402.

[271] R. K. Lee et al. "Quantum correlations in soliton collisions." In: Phys. Rev. A 71 (2005), p. 035801.

[272] R. Fedele et al. "A method for filtering and controlling soliton states of Bose-Einstein condensates." In: Phys. Scripta 2005 (2005).

[273] S. R. Friberg et al. "Quantum-nondemolition measurement of the photon number of an optical soliton." In: Phys. Rev. Lett. 69 (1992), p. 3165.

[274] S. R. Friberg et al. "Observation of Optical Soliton Photon-Number Squeezing." In: Phys. Rev. Lett. 77 (1996), p. 3775.

[275] A. Sizmann. In: Appl. Phys. B 65 (1997), p. 745.

[276] M. Leonetti et al. "Secure information transport by transverse localization of light." In: Sci. Rep. 6 (2016), p. 29918.

[277] S. A. Goorden et al. "Quantum-secure authentication of a physical unclonable key." In: Optica 1 (2014), p. 421.

[278] L. Di Mauro Villari et al. "Quantum soliton evaporation." In: Phys. Rev. A 98 (2018), p. 043859.

[279] R. J. Glauber. "Coherent and Incoherent States of the Radiation Field." In: Phys. Rev. 131 (1963), p. 2766.

[280] E. C. G. Sudarshan. "Equivalence of Semiclassical and Quantum Mechanical Descriptions of Statistical Light Beams." In: PRL 10 (1963), p. 277.

[281] G. De Chiara et al. "Optimal control of atom transport for quantum gates in optical lattices." In: Phys. Rev. A 77 (2008), p. 052333.

[282] P. Walczak et al. "Optical Rogue Waves in Integrable Turbulence." In: Phys. Rev. Lett. 114 (2015), p. 143903.

[283] M. Onorato et al. Rogue and shock waves in nonlinear media. Springer.

[284] M. Artin. Algebra. 2nd. Pearson Modern Classics for Advanced Mathematics Series. Pearson, 2018.

[285] A. Church. "Review of Turing 1936." In: J. Symb. Log. 2 (1937), p. 42.

[286] A. Lukkarinen et al. "Mechanisms of fluid spreading: Ising model simulations." In: Phys. Rev. E 51 (1995), p. 2199.

[287] A. Zunger et al. "Obtaining Ising-like expansions for binary alloys from first principles." In: Model. Simul. Mater. Sci. Eng. 10 (2002), p. 685.

[288] Ido Kanter. "Potts-glass models of neural networks." In: PRA 37 (1988), p. 2739.

[289] G. A. Kohring et al. "Parallelism on the Intel 860 Hypercube: Ising Magnets, hydrodynamical Cellular Automata and Neural Networks." In: Int. J. Mod. Phys. C 03 (), p. 1165.

[290] S. Istrail. "Statistical mechanics, three-dimensionality and NP-completeness: I. Universality of intracatability for the partition function of the Ising model across non-planar surfaces (extended abstract)." In: STOC. 2000.

[291] F. Barahona. "On the computational complexity of Ising spin glass models." In: J. Phys. A 15 (1982), p. 3241.

[292] A. Lucas. "Ising formulations of many NP problems." In: Fr. Phys. 2 (2014), p. 5.

[293] M. R. Garey et al. "Computers and Intractability: A Guide to the Theory of NP-Completeness." In: WH Freeman, 1979.

[294] Y. Fu et al. "Application of statistical mechanics to NP-complete problems in combinatorial optimisation." In: J. Phys. A 19 (1986), p. 1605.

[295] S. Kirkpatrick et al. "Optimization by Simulated Annealing." In: Science 220 (1983), p. 671.

[296] T. Kadowaki et al. "Quantum annealing in the transverse Ising model." In: Phys. Rev. E 58 (1998), p. 5355.

[297] M. Mézard et al. Information, Physics, and Computation. Oxford, UK: Oxford University Press, 2009.

[298] E. Torrontegui et al. "Chapter 2 - Shortcuts to Adiabaticity." In: Advances in Atomic, Molecular, and Optical Physics. Ed. by E. Arimondo et al. Vol. 62. Advances In Atomic, Molecular, and Optical Physics. Academic Press, 2013, p. 117.

[299] P. Salamon et al. "Maximum work in minimum time from a conservative quantum system." In: Phys. Chem. Chem. Phys. 11 (2009), p. 1027.

[300] M. Ohzeki et al. “Quantum Annealing: an Introduction and New Developments.” In: J. Comp. Theor. Nano. 8 (2011), p. 963.

[301] P. Hauke et al. “Perspectives of quantum annealing: Methods and implementations.” In: arXiv e-prints (2019). arXiv: 1903.06559 [quant-ph].

[302] B. Altshuler et al. “Anderson localization makes adiabatic quantum optimization fail.” In: Proc. Nat. Ac. Sci. 107 (2010), p. 12446.

[303] N. G. Dickson et al. “Does Adiabatic Quantum Optimization Fail for NP-Complete Problems?” In: Phys. Rev. Lett. 106 (2011), p. 050502.

[304] V. Bapst et al. “The quantum adiabatic algorithm applied to random optimization problems: The quantum spin glass perspective.” In: Phys. Rep. 523 (2013), p. 127.

[305] G. De las Cuevas et al. “Simple universal models capture all classical spin physics.” In: Science 351 (2016), p. 1180.

[306] K. Kim et al. “Quantum simulation of frustrated Ising spins with trapped ions.” In: Nature 465 (2010), p. 590.

[307] J. W. Britton et al. “Engineered two-dimensional Ising interactions in a trapped-ion quantum simulator with hundreds of spins.” In: Nature 484 (2012), p. 489.

[308] X. Ma et al. “Quantum simulation of the wavefunction to probe frustrated Heisenberg spin systems.” In: Nat. Phys. 7 (2011), p. 399.

[309] M. W. Johnson et al. “Quantum annealing with manufactured spins.” In: Nature 473 (2011), p. 194.

[310] “An electromechanical Ising Hamiltonian.” In: Sci. Adv. 2 (2016), e1600236.

[311] B. Sutton et al. “Intrinsic optimization using stochastic nanomagnets.” In: Sci. Rep. 7 (2017), p. 44370.

[312] N. G. Berloff et al. “Realizing the classical XY Hamiltonian in polariton simulators.” In: Nat. Mater. 16 (2017), p. 1120.

[313] N. Ghofraniha et al. “Experimental evidence of replica symmetry breaking in random lasers.” In: Nat. Commun. 6 (2015), p. 6058.

[314] F. Tommasi et al. “Robustness of replica symmetry breaking phenomenology in random laser.” In: Sci. Rep. 6 (2016), p. 37113.

[315] S. Basak et al. “Large fluctuations at the lasing threshold of solid- and liquid-state dye lasers.” In: Sci. Rep. 6 (2016), p. 32134.

[316] A. L. Moura et al. "Replica Symmetry Breaking in the Photonic Ferromagneticlike Spontaneous Mode-Locking Phase of a Multimode Nd:YAG Laser." In: Phys. Rev. Lett. 119 (2017), p. 163902.

[317] M. Nixon et al. "Observing Geometric Frustration with Thousands of Coupled Lasers." In: Phys. Rev. Lett. 110 (2013), p. 184102.

[318] W. Ettoumi et al. "Laser filamentation as a new phase transition universality class." In: Phys. Rev. Lett. 114 (2015), p. 063903.

[319] D. Pierangeli et al. "Observation of replica symmetry breaking in disordered nonlinear wave propagation." In: Nat. Commun. 8 (2017), p. 1501.

[320] A. Marandi et al. "Network of time-multiplexed optical parametric oscillators as coherent Ising machine." In: Nat. Photon. 8 (2014), p. 937.

[321] P.L. McMahon et al. "A fully-programmable 100-spin coherent Ising machine with all-to-all connections." In: Science 354 (2016), p. 614.

[322] T. Inagaki et al. "A coherent Ising machine for 2000-node optimization problems." In: Science 354 (2016), p. 603.

[323] T. Inagaki et al. "Large-scale Ising spin network based on degenerate optical parametric oscillators." In: Nat. Photon. 10 (2016), p. 415.

[324] Y. Takeda et al. "Boltzmann sampling for an XY model using a non degenerate optical parametric oscillator network." In: Q. Sci. Tech. 3 (2018), p. 014004.

[325] Y. Shen et al. "Deep learning with coherent nanophotonic circuits." In: Nat. Photon. 11 (2017), p. 441.

[326] N. C. Harris et al. "Quantum transport simulations in a programmable nanophotonic processor." In: Nat. Photon. 11 (2017), p. 447.

[327] C. Roques-Carmes et al. "Photonic Recurrent Ising Sampler." In: arXiv:1811.02705 (2018).

[328] S. R. Huisman et al. "Programmable Multiport Optical Circuits in Opaque Scattering Materials." In: Opt. Express 23 (2015), p. 3102.

[329] R. Fickler et al. "Custom-Tailored Spatial Mode Sorting by Controlled Random Scattering." In: Phys. Rev. B 95 (2017), p. 161108.

[330] P. del Hougne et al. "Leveraging Chaos for Wave-Based Analog Computation: Demonstration with Indoor Wireless Communication Signals." In: Phys. Rev. X 8 (2018), p. 041037.

[331] D.C. Mattis. "Solvable spin systems with random interactions." In: Phys. Lett. A 56 (1976), p. 421.

[332] H. Nishimori. Statistical Physics of Spin Glasses. Vol. 111. Clarendon Press-Oxford, 2001.

[333] "Phase control algorithms for focusing light through turbid media." In: Opt. Commun. 281 (2008), p. 3071.

[334] A. D. King et al. "Emulating the coherent Ising machine with a mean-field algorithm." In: arXiv:1806.08422 (2018).

[335] A. Jesacher et al. "Wavefront correction of spatial light modulators using an optical vortex image." In: Opt. Express 15 (2007), p. 5801.

[336] F. Wyrowski. "Diffractive optical elements: iterative calculation of quantized, blazed phase structures." In: J. Opt. Soc. Am. A 7 (1990), p. 961.

[337] G. Parisi. Statistical field theory. Vol. 66. Frontiers in Physics. Addison-Wesley, 1988.

[338] D.P. Landau. "Finite-size behavior of the Ising square lattice." In: Phys. Rev. B 13 (1976), p. 2997.

[339] K. Binder et al. Monte Carlo Simulation in Statistical Physics. Springer, 1997.

[340] A. Jesacher et al. "Near-perfect hologram reconstruction with a spatial light modulator." In: Opt. Express 16 (2008), p. 2597.

[341] Y. Liu et al. "Focusing light inside dynamic scattering media with millisecond digital optical phase conjugation." In: Optica 4 (2017), p. 280.

[342] D. F. Kibler et al. "Machine Learning As an Experimental Science." In: Proc. EWSL. EWSL'88. Glasgow, UK: Pitman Publishing, Inc., 1988, p. 81.

[343] C.M. Bishop. Pattern recognition and machine learning. Springer, 2006.

[344] R. Duda. Pattern Classification. Wiley, 2001.

[345] K. Murphy. Machine learning: A Probabilistic Perspective. The MIT Press, 2012.

[346] L. Zdeborova. "Machine learning: New tool in the box." In: Nat. Phys. 13 (2017), p. 420.

[347] J. Carrasquilla et al. "Machine learning phases of matter." In: Nat. Phys. 13 (2017), p. 431.

[348] Y. Zhang et al. "Quantum Loop Topography for Machine Learning." In: Phys. Rev. Lett. 118 (2017), p. 216401.

[349] L. Lu et al. "Topological photonics." In: Nat. Photon. 8 (2014), p. 821.

[350] Y. Wu et al. "Applications of topological photonics in integrated photonic devices." In: Adv. Opt. Mater. 5 (2017), p. 1700357.

[351] T. Ozawa et al. "Topological Photonics." In: ArXiv e-prints (2018). arXiv: 1802.04173.

[352] F. D. M. Haldane et al. "Possible Realization of Directional Optical Waveguides in Photonic Crystals with Broken Time-Reversal Symmetry." In: Phys. Rev. Lett. 100 (2008), p. 013904.

[353] S. Raghu et al. "Analogs of quantum-Hall-effect edge states in photonic crystals." In: Phys. Rev. A 78 (2008), p. 033834.

[354] Z. Wang et al. "Reflection-Free One-Way Edge Modes in a Gyromagnetic Photonic Crystal." In: Phys. Rev. Lett. 100 (2008), p. 013905.

[355] M. C. Rechtsman et al. "Photonic Floquet topological insulators." In: Nature 496 (2013), p. 196.

[356] M. Z. Hasan et al. "Topological insulators." In: Rev. Mod. Phys. 82 (2010), p. 3045.

[357] M. Hafezi et al. "Imaging topological edge states in silicon photonics." In: Nat. Photon. 7 (2013), p. 1001.

[358] T. Kitagawa et al. "Observation of topologically protected bound states in photonic quantum walks." In: Nat. Commun. 3 (2012), p. 882.

[359] B. Bahari et al. "Nonreciprocal lasing in topological cavities of arbitrary geometries." In: Science 358 (2017), p. 636.

[360] M. A. Bandres et al. "Topological insulator laser: Experiments." In: Science (2018).

[361] G. Harari et al. "Topological insulator laser: Theory." In: Science (2018).

[362] P. St-Jean et al. "Lasing in topological edge states of a one dimensional lattice." In: Nature Photonics 11 (2017), pp. 651–656.

[363] N. X. A. Rivolta et al. "Topological edge modes with PT-symmetry in a quasiperiodic structure." In: Phys. Rev. A 96 (2017), p. 023864.

[364] L. Pilozzi et al. "Topological lasing in resonant photonic structures." In: Phys. Rev. B 93 (2016), p. 195317.

[365] O. Zilberberg et al. "Photonic topological boundary pumping as a probe of 4D quantum Hall physics." In: Nature 553 (2018), p. 59.

[366] M. Lohse et al. "Exploring 4D quantum Hall physics with a 2D topological charge pump." In: Nature 553 (2018), p. 55.

[367] Y. E. Kraus et al. "Topological Equivalence between the Fibonacci Quasicrystal and the Harper Model." In: Phys. Rev. Lett. 109 (2012), p. 116404.

[368] S. Aubry et al. "Analyticity breaking and anderson localization in incommensurate lattices." In: Ann. Israel. Phys. Soc. 3 (1980), p. 133.

[369] P. G. Harper. "Single Band Motion of Conduction Electrons in a Uniform Magnetic Field." In: Proc. Phys. Soc. 68 (1955), p. 874.

[370] A. V. Poshakinskiy et al. "Radiative Topological States in Resonant Photonic Crystals." In: Phys. Rev. Lett. 112 (2014), p. 107403.

[371] W. C. Chew. Waves and Fields in Inhomogeneous Media. Wiley-IEEE Press, 1999.

[372] D. R. Hofstadter. "Energy levels and wave functions of Bloch electrons in rational and irrational magnetic fields." In: Phys. Rev. B 14 (1976), p. 2239.

[373] Y. Hatsugai. "Edge states in the integer quantum Hall effect and the Riemann surface of the Bloch function." In: Phys. Rev. B 48 (1993), p. 11851.

[374] C. Tauber et al. "Topological edge states in two-gap unitary systems: a transfer matrix approach." In: New J. Phys. 17 (2015), p. 115008.

[375] G.M. Graf et al. "Bulk-Edge Correspondence for Two-Dimensional Topological Insulators." In: Commun. Math. Phys. 324 (2013), p. 851.

[376] A. V. Poshakinskiy et al. "Phase spectroscopy of topological invariants in photonic crystals." In: Phys. Rev. A 91 (2015), p. 043830.

[377] G.M. Graf et al. "Bulk-Edge correspondence for two-dimensional Floquet topological insulators." In: ArXiv e-prints (2017). arXiv: 1707.09212 [physics.optics].

[378] T. Kitagawa et al. "Observation of topologically protected bound states in photonic quantum walks." In: Nat. Commun. 3 (2012), p. 882.

[379] H. Kabir et al. "Neural Network Inverse Modeling and Applications to Microwave Filter Design." In: IEEE 56 (2008), p. 867.

[380] G. Gosal et al. “Transmitarray Antenna Design Using Forward and Inverse Neural Network Modeling.” In: IEEE, Ant. wirel. prop. lett. 15 (2016), p. 1483.

[381] A. Aoad et al. “Knowledge based response correction method for design of reconfigurable N-shaped microstrip patch antenna using inverse ANNs.” In: Int. J. Num. Mod. 30 (2017), e2129.

[382] D. Liu et al. “Training Deep Neural Networks for the Inverse Design of Nanophotonic Structures.” In: ACS Photon. 5 (2018), p. 1365.

[383] J. Adler et al. “Solving ill-posed inverse problems using iterative deep neural networks.” In: Inv. Prob. 33 (2017), p. 124007.

[384] Y. V. Kartashov et al. “Bistable Topological Insulator with Exciton-Polaritons.” In: Phys. Rev. Lett. 119 (2017), p. 253904.

[385] D. Mihalache et al. “Stable topological modes in two-dimensional Ginzburg-Landau models with trapping potentials.” In: PRA 82 (2010), p. 023813.

[386] J. Jünemann et al. “Exploring Interacting Topological Insulators with Ultracold Atoms: The Synthetic Creutz-Hubbard Model.” In: Phys. Rev. X 7 (2017), p. 031057.

[387] M. Mancini et al. “Observation of chiral edge states with neutral fermions in synthetic Hall ribbons.” In: Science 349 (2015), p. 1510.

[388] M. Parto et al. “Complex Edge-State Phase Transitions in 1D Topological Laser Arrays.” In: arXiv:1709.00523 (2018).

[389] L. Pilozzi et al. “Topological cascade laser for frequency comb generation in PT-symmetric structures.” In: Opt. Lett. 42 (2017), p. 5174.

[390] S. Longhi. “Parity-Time Symmetry meets Photonics: A New Twist in non-Hermitian Optics.” In: ArXiv e-prints (2018). arXiv: 1802.05025 [physics.optics].

[391] J. M. Zeuner et al. “Observation of a Topological Transition in the Bulk of a Non-Hermitian System.” In: Phys. Rev. Lett. 115 (2015), p. 040402.

[392] A. P. Gibson et al. “Recent advances in diffuse optical imaging.” In: Phys. Med. Bio. 50 (2005), R1.

[393] C. Rockstuhl et al. “Comparison and optimization of randomly textured surfaces in thin-film solar cells.” In: Opt. Express 18 (2010), A335.

[394] A. P. Mosk et al. “Controlling waves in space and time for imaging and focusing in complex media.” In: Nat. Photon. 6 (2012), p. 283.

[395] F. Riboli et al. “Engineering of light confinement in strongly scattering disordered media.” In: Nat. Mater. 13 (2014), p. 720.

[396] R. Uppu et al. “Asymmetric Cryptography with Physical Unclonable Keys.” In: arXiv e-prints (2018). arXiv: 1802.07573.

[397] F. Lemoult et al. “Manipulating Spatiotemporal Degrees of Freedom of Waves in Random Media.” In: Phys. Rev. Lett. 103 (2009), p. 173902.

[398] T. W. Kohlgraf-Owens et al. “Transmission matrices of random media: means for spectral polarimetric measurements.” In: Opt. Lett. 35 (2010), p. 2236.

[399] F. van Beijnum et al. “Frequency bandwidth of light focused through turbid media.” In: Opt. Lett. 36 (2011), p. 373.

[400] Y. Guan et al. “Polarization control of multiply scattered light through random media by wavefront shaping.” In: Opt. Lett. 37 (2012), p. 4663.

[401] M. W. Matthés et al. “Turning Optical Complex Media into Universal Reconfigurable Linear Operators by Wavefront Shaping.” In: arXiv e-prints (2018). arXiv: 1810.05688 [physics.optics].

[402] P. Zhao et al. “Universal linear optical operations on discrete phase-coherent spatial modes.” In: arXiv e-prints (2018). arXiv: 1801.05092 [physics.optics].

[403] S. M. Popoff et al. “Measuring the Transmission Matrix in Optics: An Approach to the Study and Control of Light Propagation in Disordered Media.” In: Phys. Rev. Lett. 104 (2010), p. 100601.

[404] A. Fleming et al. “Perturbation of Transmission Matrices in Nonlinear Random Media.” In: Ann. Phys. 531 (2019), p. 1900091.

[405] T. Čižmár et al. “In situ wavefront correction and its application to micromanipulation.” In: Nat. Photon. 4 (2010), p. 388.

[406] I. M. Vellekoop et al. “Exploiting disorder for perfect focusing.” In: Nat. Photon. 4 (2010), p. 320.

[407] E. G. van Putten et al. “Scattering Lens Resolves Sub-100 nm Structures with Visible Light.” In: Phys. Rev. Lett. 106 (2011), p. 193905.

[408] M. Kim et al. “Relation between transmission eigenchannels and single-channel optimizing modes in a disordered medium.” In: Opt. Lett. 38 (2013), p. 2994.

[409] S. Rotter et al. “Light fields in complex media: Mesoscopic scattering meets wave control.” In: Rev. Mod. Phys. 89 (2017), p. 015005.

[410] M. P. van Albada et al. “Observation of long-range intensity correlation in the transport of coherent light through a random medium.” In: Phys. Rev. Lett. 64 (1990), p. 2787.

[411] J. Aulbach et al. “Control of Light Transmission through Opaque Scattering Media in Space and Time.” In: Phys. Rev. Lett. 106 (2011), p. 103901.

[412] F. Duport et al. “All-optical reservoir computing.” In: Opt. Express 20 (2012), p. 22783.

[413] G. Van der Sande et al. “Advances in photonic reservoir computing.” In: Nanophoton. 6 (2017), p. 561.

[414] E. N. Economou. Green’s Functions in Quantum Physics. Springer-Verlag Berlin Heidelberg, 1979.

[415] Olivier J. F. Martin et al. “Generalized Field Propagator for Electromagnetic Scattering and Light Confinement.” In: Phys. Rev. Lett. 74 (1995), p. 526.

[416] S. R. Huisman et al. “Programmable multiport optical circuits in opaque scattering materials.” In: Opt. Express 23 (2015), p. 3102.

[417] A. Babazadeh et al. “High-Dimensional Single-Photon Quantum Gates: Concepts and Experiments.” In: Phys. Rev. Lett. 119 (2017), p. 180510.

[418] M. Malik et al. “Multi-photon entanglement in high dimensions.” In: Nat. Photon. 10 (2016), p. 248.

[419] C. Taballione et al. “8×8 reconfigurable quantum photonic processor based on silicon nitride waveguides.” In: Opt. Express 27 (2019), p. 26842.

[420] A. Muthukrishnan et al. “Multivalued logic gates for quantum computation.” In: Phys. Rev. A 62 (2000), p. 052309.

[421] Y. M. Di et al. “Elementary gates for ternary quantum logic circuit.” In: arXiv e-prints (2011). arXiv: 1105.5485 [quant-ph].

[422] S. A. Goorden et al. “Quantum-secure authentication of a physical unclonable key.” In: Optica 1 (2014), p. 421.

[423] T. B. H. Tentrup et al. “Spatially encoded light for Large-alphabet Quantum Key Distribution.” In: arXiv e-prints (2018). arXiv: 1808.02823 [quant-ph].

[424] J. Wang. “Recurrent neural networks for solving linear matrix equations.” In: Comput. Math. Appl. 26.9 (1993), p. 23.

[425] J. Dong et al. “Optical Reservoir Computing Using Multiple Light Scattering for Chaotic Systems Prediction.” In: IEEE 26 (2020), p. 1.

[426] M. Prabhu et al. “A Recurrent Ising Machine in a Photonic Integrated Circuit.” In: arXiv e-prints (2019). arXiv: 1909.13877 [physics.optics].

[427] P. Fan et al. “Light Propagation Prediction through Multimode Optical Fibers with a Deep Neural Network.” In: 2018 IEEE (IAEAC). 2018, p. 1080.

[428] X. Lin et al. “All-optical machine learning using diffractive deep neural networks.” In: Science 361 (2018), p. 1004.

[429] L. Larger et al. “Photonic information processing beyond Turing: an optoelectronic implementation of reservoir computing.” In: Opt. Express 20 (2012), p. 3241.

[430] A. Argyris et al. “Photonic machine learning implementation for signal recovery in optical communications.” In: Sci Rep 8 (2018), p. 8487.

[431] J. Bueno et al. “Reinforcement learning in a large-scale photonic recurrent neural network.” In: Optica 5 (2018), p. 756.

[432] J. Dong et al. “Scaling up Echo-State Networks with multiple light scattering.” In: 2018 IEEE (SSP). 2018, p. 448.

[433] A.M. Gleason. “Measures on the Closed Subspaces of a Hilbert Space.” In: J. Math. and Mech. 6 (1957), p. 885.

[434] M. H. Stone. “On One-Parameter Unitary Groups in Hilbert Space.” In: Ann. of Math. 33 (1932), p. 643.

[435] G. C. Hegerfeldt. “Causality problems for Fermi’s two-atom system.” In: Phys. Rev. Lett. 72 (1994), p. 596.

[436] G. Barton. “Quantum Mechanics of The Inverted Oscillator Potential.” In: Ann. Phys. 166 (1986), p. 322.

[437] M. Gadella et al. “On the Mathematical Basis of the Dirac Formulation of Quantum Mechanics.” In: Int. J. Theor. Phys 42 (2003), p. 2225.

[438] I. Gradshteyn et al. Table of Integrals, Series and Products. Academic Press, 1965.

[439] P. M. Morse et al. Methods of Theoretical Physics. McGraw-Hill, 1953.

[440] M. Abramowitz et al. Handbook of Mathematical Functions. Dover Publications, 1972.

[441] H. Brezis. Functional Analysis. Springer-Verlag Berlin Heidelberg, 2010.

[442] J. R. Munkres. Topology. II. Prentice Hall, Inc., 2000.

[443] H. L. Royden. Real Analysis. III. Macmillian Publishing Company, 1988.

[444] W. Rudin. Real and Complex Analysis. III. McGraw-Hill, Inc., 1987.